KINETICS OF CHEMICAL EXCHANGE DURING MELTING OF PLANETARY INTERIORS

by

JAMES ASHTON VAN ORMAN

B.S. Geology
Florida State University, 1994

Submitted to the Department of
Earth, Atmospheric and Planetary Sciences
in Partial Fulfillment of the Requirements for the Degree of

DOCTOR OF PHILOSOPHY

in

GEOCHEMISTRY

at the

MASSACHUSETTS INSTITUTE OF TECHNOLOGY

September, 2000

Signature of Author_____
Department of Earth, Atmospheric and Planetary Sciences
August 4, 2000

Certified by_____
Timothy L. Grove
Thesis Supervisor

Accepted by_____
Ronald G. Prinn
Department Chairman

KINETICS OF CHEMICAL EXCHANGE DURING MELTING OF PLANETARY INTERIORS

by

JAMES ASHTON VAN ORMAN

Submitted to the Department of
Earth, Atmospheric and Planetary Sciences
in Partial Fulfillment of the Requirements for the Degree
of Doctor of Philosophy in Geochemistry

ABSTRACT

Experimental and numerical modeling studies are used to place constraints on the kinetics of chemical exchange during partial melting within the mantles of the terrestrial planets. Chapter 1 presents experiments on the diffusion rates of La, Ce, Nd, Dy and Yb in diopside at pressures of 0 to 2.5 GPa and temperatures of 1050 to 1450 °C. The results demonstrate a large variation in diffusivity among the rare earth elements, with the diffusion coefficient for La a factor of ~35 smaller than for Yb at a given temperature and pressure. Chapter 2 presents experiments on the diffusion of Sm, Dy and Yb in pyrope at 2.8 GPa and 1200-1450 °C. No significant difference in diffusivity is found among these elements, and their absolute diffusion rates are similar to those of the heavy rare earth elements in diopside at the same pressure and temperature. Chapter 3 presents a numerical model for diffusion-controlled fractionation of trace elements during adiabatic decompression melting of a polyphase solid. The model is used to simulate the fractionation of rare earth elements between solid and melt during partial melting of Earth's upper mantle. Diffusion is found to exert a strong control on the evolution of the system at conditions typical of melting beneath ocean spreading centers, leading to less efficient fractionation of the rare earth elements than under conditions of local chemical equilibrium. Chapter 4 presents experiments on the diffusion of U and Th in diopside at 1 atm pressure. Uranium and thorium are found to diffuse at similar rates, and diffusive fractionation between these elements is therefore unlikely to be significant during partial melting in Earth's upper mantle. Thorium and radium may be diffusively fractionated, however, enhancing the production of $^{226}Ra/^{230}Th$ radioactive disequilibrium during partial melting while inhibiting chromatographic fractionation during melt transport. Chapter 5 presents phase equilibrium and dissolution kinetics experiments that constrain hypotheses for the origin of lunar high-Ti ultramafic glasses. The experimental results demonstrate that assimilation of ilmenite-bearing cumulates is not a viable mechanism for production of the high-Ti glasses. It is proposed that the source of the high-Ti ultramafic glasses formed by shallow level mixing and reaction of late-stage magma ocean liquids with underlying olivine-orthopyroxene cumulates, followed by sinking of these dense hybrid materials into the lunar mantle.

Thesis Supervisor: Timothy L. Grove
Title: Professor of Geology

ACKNOWLEDGMENTS

I am indebted to my thesis committee, Tim Grove, Nobu Shimizu, Stan Hart, Fred Frey, Brian Evans, and Daniele Cherniak, for their constructive criticism and for many fruitful discussions over the years. I am particularly grateful to Tim, who got me started on this project and provided all of the resources necessary to see it through. Tim allowed me the freedom to run with my ideas, but was ready with advice when I needed it. Nobu Shimizu introduced me to the "joy" of secondary ion mass spectrometry, and has been unfailingly generous with his time, advice, and support. Kip Hodges provided guidance during my first year, and his seminars helped spark my interest in diffusion. I have also benefited from numerous discussions with Greg Hirth, Peter Kelemen, Kelin Whipple, and Sam Bowring.

This thesis could not have been completed without technical assistance from many people. Graham Layne offered crucial advice on SIMS depth profiling techniques and was always patient when I called with questions early on a weekend morning. Neel Chatterjee kept the electron microprobe lab running smoothly and assisted with some of the analyses. George Harlow donated some of the diopside single crystals used in this study; the pyrope crystals were donated by Eric Essene, Youxue Zhang, and Liping Wang. Jun Korenaga provided helpful advice on the numerical modeling of diffusion/advection problems. Rosie Hegg made the 12th floor run without a hitch, which is no small task.

I have learned a lot from my fellow graduate students, postdocs, and staff. They are responsible, in large part, for making MIT a stimulating, and fun, place to work. I enjoyed numerous discussions with my officemates, Steve Parman and Ken Koga, and appreciated their susceptibility to arm twisting when I wanted to play basketball. I am also grateful to Ken and Estelle Rose for providing five-star accommodations on my many trips to Woods Hole. Glenn Gaetani and Tom Wagner showed me the ropes in the experimental lab, and I continue to learn a great deal from both of them. I appreciate the friendship of Alberto Saal, as well as his political savvy and his constant reminders to stay relaxed. Fellow lunatic Lindy Elkins has added abundant energy and enthusiasm to the 12th floor, as well as a steady supply of furry four-legged creatures. Over the last year Steve Singletary offered daily exhortations to keep on writing, although part of me suspects that this was part of his plan to grab the window seat in our office. I am lucky that my final thesis push overlapped with those of Steve Parman, Kirsten Nicolaysen, and Eric Kirby—lots of fun, wasn't it guys? I have benefited in many ways from my interactions with Othmar Muentener, Astrid Holzheid, Karen Viskupic, Shane Pelechaty, Mike Pope, Valerie Chauvagnac, Meg Coleman, Mark Schmitz, Anke Friedrich, Audrey Huerta, Jesse Dann, Debbie Hassler, Mark Martin, Gunter Siddiqi, and Jörg Renner. Thanks everybody!

I am grateful to my family for their confidence in me and for their continuous support. And finally, I thank Beverly Saylor; her companionship, encouragement and understanding have made the last five years truly enjoyable.

TABLE OF CONTENTS

INTRODUCTION

Basaltic magmas provide a primary source of information on the constitution and dynamics of terrestrial planet interiors. Elements are fractionated between the melt and solid during melting, and this modifies the composition of the melt from that of the solid source. To interpret the chemical information that basaltic magmas provide, the processes of chemical fractionation must be understood. Our understanding of the thermodynamic controls on chemical fractionation has advanced considerably in the recent past. A considerable body of data exists on phase equilibria and partitioning in relevant systems, and models based on these data have been successful in recovering the global compositional variation in mid-ocean ridge basalts on Earth (Klein and Langmuir, 1987; Kinzler and Grove, 1992a,b; Langmuir et al., 1992). Understanding of the kinetic controls on chemical fractionation is not nearly so advanced. Recent theoretical treatments of solid-melt separation during decompression melting have introduced the possibility that melting in Earth's upper mantle may take place under disequilibrium conditions (Qin, 1992; Iwamori, 1993a,b; Hart, 1993; Spiegelman and Kenyon, 1992). The extent to which disequilibrium may influence the chemical exchange process during melting depends on the time available for interaction between melt and solid before they separate, and the time required for chemical species to be transported from the interior of solid grains to their interface with the melt. Very limited information exists on the rates at which elements migrate in silicate minerals under conditions relevant to melting, and the lack of this basic kinetic data has limited the application of disequilibrium melting models to partial melting in planetary interiors.

The first two chapters of this dissertation provide experimental data on diffusion rates of the rare earth elements (REE) in high-Ca pyroxene and garnet. Rare earth elements are widely used as tracers of igneous processes, and high-Ca pyroxene and garnet are the principal solid hosts of these elements within the melting regime in Earth's upper mantle. Solid-state diffusion is the slowest mechanism for transport of elements in the mantle, and in many situations will control the rate of equilibration between solid and melt. Chapter 1 presents experiments on the

diffusion of La, Ce, Nd, Dy and Yb in high-Ca pyroxene at temperatures of 1050 to 1450 °C and pressures of 0 to 2.5 GPa. These are the first diffusion data that have been reported for these elements in pyroxene. The experimental results demonstrate a large variation in diffusivity among the REE that can lead to diffusive fractionation of these elements during melting. Diffusion rates are strongly correlated with ionic radius; La, the largest of the rare earth elements, diffuses ~35 times more slowly than Yb at a given temperature and pressure. The relationship between the diffusion coefficient and ionic radius is shown to be consistent with a simple model that considers the elastic strain associated with an atomic jump. Chapter 2 presents experiments on rare earth element diffusion in pyrope garnet at pressures and temperatures within its stability field (2.8 GPa and 1200-1450 °C). Unlike clinopyroxene, there is no significant difference in diffusion rates among the REE in garnet.

Implications of the rare earth element diffusion data for chemical fractionation during melting in Earth's upper mantle are discussed in Chapter 3. A numerical model is developed to describe diffusion-controlled chemical exchange between melt and a solid composed of several phases, each with different diffusion and partitioning properties. This model is used to simulate the distribution of rare earth elements among the solid, residual melt, and segregated melt during adiabatic decompression melting in the mantle. Under conditions typical of melting beneath ocean spreading centers, diffusion in high-Ca pyroxene is predicted to have a strong influence on the chemical evolution of the system. The slowly diffusing light REE are held within the cores of high-Ca pyroxene grains at abundance levels considerably higher than at equilibrium, and this leads to less efficient fractionation of the REE between solid and melt than under equilibrium conditions. Comparison of the model predictions with rare earth element data from abyssal peridotites of the America-Antarctic and Southeast Indian ridge systems (Johnson et al., 1990; Johnson and Dick, 1992) demonstrates that the effective grain radius beneath these spreading centers must be < 3 mm, and the residual melt fraction must be < 0.03.

Chapter 4 presents data on the diffusion rates of U and Th in diopside, and discusses their implications for U-series disequilibrium in mid-ocean ridge basalts (MORB). Uranium

and thorium are found to diffuse at rates similar to the light rare earth elements in diopside, and may not be distributed between solid and melt in equilibrium proportions during near-fractional melting of spinel peridotite. Although diffusion of U and Th may be too slow to allow complete equilibration between high-Ca pyroxene and melt during partial melting, diffusive fractionation between these two elements is unlikely to be important because their diffusion rates are similar at peridotite melting temperatures. Diffusive fractionation of Ra from Th may be important, however, especially if Ra diffusion rates are similar to those of other large divalent cations like Sr (Sneeringer et al., 1984) and Pb (Cherniak, 1998). Slow diffusion of Th and relatively rapid diffusion of Ra would enhance Ra/Th fractionation during partial melting, and inhibit chromatographic separation of Ra and Th during melt transport. It is suggested that the negative correlation between [^{226}Ra] and [^{230}Th] observed in the MORB data set (Kelemen et al., 1997) may be a natural consequence of disequilibrium chemical fractionation during partial melting, without the requirement of separate porosity regimes for the production of ^{226}Ra and ^{230}Th excesses.

Chapter 5 presents phase equilibrium and dissolution kinetics experiments that constrain hypotheses for the origin of lunar high-Ti ultramafic glasses. Unlike the first four chapters, which are concerned with the relatively slow kinetics of chemical exchange across a solid/melt interface, this chapter focuses on the kinetics of mass transfer associated with dissolution (phase change from solid to melt). Dissolution in most regimes is controlled by diffusion in the melt, and may be many orders of magnitude faster than chemical exchanges limited by diffusion in the solid. The experimental results demonstrate that assimilation of ilmenite-bearing cumulates is not a viable mechanism for production of the high-Ti ultramafic glasses. Instead, the very high titanium contents of these magmas (up to 16.4 wt.%; Delano, 1986) must be derived from the source. It is proposed that the source of the high-Ti glasses may have formed by shallow level mixing and reaction of late-stage magma ocean liquids with underlying olivine-orthopyroxene cumulates, followed by sinking of these dense hybrid materials into the lunar mantle.

REFERENCES

Cherniak D. J. (1998) Pb diffusion in clinopyroxene. *Chem. Geol.* **150**, 105-117.

Hart S. R. (1993) Equilibration during mantle melting: A fractal tree model, *Proc. Natl. Acad. Sci.* **90**, 11,914-11,918.

Iwamori H. (1993a) Dynamic disequilibrium melting model with porous flow and diffusion controlled chemical equilibration. *Earth Planet. Sci. Lett.* **114**, 301-313.

Iwamori H. (1993b) A model for disequilibrium mantle melting incorporating melt transport by porous and channel flows. *Nature* **366**, 734-737.

Johnson K. T. M. and Dick H. J. B. (1992) Open system melting and temporal and spatial variation of peridotite and basalt at the Atlantis-II fracture-zone. *J. Geophys. Res.* **97**, 9219-9241.

Johnson K. T. M., Dick H. J. B. and Shimizu N. (1990) Melting in the oceanic upper mantle: an ion microprobe study of diopsides in abyssal peridotites. *J. Geophys. Res.* **95**, 2661-2678.

Kelemen P. B., Hirth G., Shimizu N., Spiegelman M., and Dick H. J. B. (1997) A review of melt migration processes in the adiabatically upwelling mantle beneath ocean spreading ridges. *Phil. Trans. R. Soc. Lond. A* **355**, 283-318.

Kinzler R. J. and Grove T. L. (1992a) Primary magmas of mid-ocean ridge basalts, 1. Experiments and methods. *J. Geophys. Res.* **97**, 6885-6906.

Kinzler R. J. and Grove T. L. (1992b) Primary magmas of mid-ocean ridge basalts, 2. Applications. *J. Geophys. Res.* **97**, 6907-6926.

Klein E. M. and Langmuir C. H. (1987) Global correlations of ocean ridge basalt chemistry with axial depth and crustal thickness. *J. Geophys Res* **92**, 8089-8115.

Langmuir C. H., Klein, E. M. and Plank T. (1992) Petrological systematics of mid-ocean ridge basalts: Constraints on melt generation beneath ocean ridges. In J. Phipps-Morgan et al., eds., *Mantle Flow and Melt Generation, AGU Monograph 71*, 183-280.

Qin Z. (1992) Disequilibrium partial melting model and its implications for trace element fractionations during mantle melting. *Earth Planet. Sci. Lett.* **112**, 75-90.

Sneeringer M., Hart S. R. and Shimizu N. (1984) Strontium and samarium diffusion in diopside. *Geochim. Cosmochim. Acta* **48**, 1589-1608.

Spiegelman M. and Kenyon P. (1992) The requirements for chemical disequilibrium during magma migration. *Earth Planet. Sci. Lett.* **109**, 611-620.

REFERENCES

Cherniak D. J. (1998) Pb diffusion in clinopyroxene. *Chem. Geol.* **150**, 105-117.

Hart S. R. (1993) Equilibration during mantle melting: A fractal tree model, *Proc. Natl. Acad. Sci.* **90**, 11,914-11,918.

Iwamori H. (1993a) Dynamic disequilibrium melting model with porous flow and diffusion controlled chemical equilibration. *Earth Planet. Sci. Lett.* **114**, 301-313.

Iwamori H. (1993b) A model for disequilibrium mantle melting incorporating melt transport by porous and channel flows. *Nature* **366**, 734-737.

Johnson K. T. M. and Dick H. J. B. (1992) Open system melting and temporal and spatial variation of peridotite and basalt at the Atlantis-II fracture-zone. *J. Geophys. Res.* **97**, 9219-9241.

Johnson K. T. M., Dick H. J. B. and Shimizu N. (1990) Melting in the oceanic upper mantle: an ion microprobe study of diopsides in abyssal peridotites. *J. Geophys. Res.* **95**, 2661-2678.

Kelemen P. B., Hirth G., Shimizu N., Spiegelman M., and Dick H. J. B. (1997) A review of melt migration processes in the adiabatically upwelling mantle beneath ocean spreading ridges. *Phil. Trans. R. Soc. Lond. A* **355**, 283-318.

Kinzler R. J. and Grove T. L. (1992a) Primary magmas of mid-ocean ridge basalts, 1. Experiments and methods. *J. Geophys. Res.* **97**, 6885-6906.

Kinzler R. J. and Grove T. L. (1992b) Primary magmas of mid-ocean ridge basalts, 2. Applications. *J. Geophys. Res.* **97**, 6907-6926.

Klein E. M. and Langmuir C. H. (1987) Global correlations of ocean ridge basalt chemistry with axial depth and crustal thickness. *J. Geophys Res* **92**, 8089-8115.

Langmuir C. H., Klein, E. M. and Plank T. (1992) Petrological systematics of mid-ocean ridge basalts: Constraints on melt generation beneath ocean ridges. In J. Phipps-Morgan et al., eds., *Mantle Flow and Melt Generation, AGU Monograph 71*, 183-280.

Qin Z. (1992) Disequilibrium partial melting model and its implications for trace element fractionations during mantle melting. *Earth Planet. Sci. Lett.* **112**, 75-90.

Sneeringer M., Hart S. R. and Shimizu N. (1984) Strontium and samarium diffusion in diopside. *Geochim. Cosmochim. Acta* **48**, 1589-1608.

Spiegelman M. and Kenyon P. (1992) The requirements for chemical disequilibrium during magma migration. *Earth Planet. Sci. Lett.* **109**, 611-620.

CHAPTER 1.

RARE EARTH ELEMENT DIFFUSION IN DIOPSIDE: INFLUENCE OF TEMPERATURE, PRESSURE AND IONIC RADIUS

ABSTRACT

Volume diffusion rates for five rare earth elements (La, Ce, Nd, Dy and Yb) have been measured in natural diopside crystals at pressures of 0.1 MPa to 2.5 GPa and temperatures of 1050 to1450 °C. Polished, pre-annealed diopside single crystals were coated with a thin film of rare earth element oxides, then held at constant temperature and pressure for times ranging from 20 to 882 hours. Diffusion profiles in quenched samples were measured by SIMS (secondary ion mass spectrometry) depth profiling. At 1 atm pressure, with the oxygen fugacity controlled near the quartz-fayalite-magnetite buffer, the following Arrhenius relations were obtained for diffusion normal to (001) (diffusion coefficient D in $m^2\ s^{-1}$):

$$\log_{10} D_{Yb} = (-4.64 \pm 0.42) - \left(411 \pm 12\ kJ\ mol^{-1}/2.303RT\right)$$
$$\log_{10} D_{Dy} = (-3.31 \pm 1.44) - \left(461 \pm 41\ kJ\ mol^{-1}/2.303RT\right)$$
$$\log_{10} D_{Nd} = (-2.95 \pm 2.64) - \left(496 \pm 77\ kJ\ mol^{-1}/2.303RT\right)$$
$$\log_{10} D_{Ce} = (-4.10 \pm 1.08) - \left(463 \pm 31\ kJ\ mol^{-1}/2.303RT\right)$$
$$\log_{10} D_{La} = (-4.22 \pm 2.66) - \left(466 \pm 78\ kJ\ mol^{-1}/2.303RT\right)$$

Diffusion rates decrease with pressure, with similar activation volumes for Yb (9.5 ± 2.0 $cm^3\ mol^{-1}$) and Ce (10.2 ± 3.2 $cm^3\ mol^{-1}$).

The data show a systematic increase in diffusivity with decreasing ionic radius. Diffusion rates for La (0.116 nm radius in eight-fold coordination) and Yb (0.099 nm) differ by a factor of ~35. The relationship between diffusivity and ionic radius is consistent with a model in which elastic strain energy plays a critical role in governing the motion of an ion through the crystal lattice.

INTRODUCTION

High-Ca pyroxene is an important host for rare earth elements in the upper mantle, and the partitioning and diffusion properties of this mineral have a central role in determining the distribution of REE between solid and melt during adiabatic decompression melting. This study presents experiments on the diffusional transport of REE in diopside, a representative high-Ca pyroxene with the chemical formula $CaMgSi_2O_6$. The influence of temperature, pressure and oxygen fugacity on rare earth element diffusion rates are examined under conditions relevant to melting beneath oceanic spreading centers and hot spots.

Although the rare earth elements share similar properties, small differences in ionic radii can lead to pronounced differences in geochemical behavior. One example is the strong preferential partitioning of heavy REE relative to light REE into high-Ca pyroxene. Differences in ionic radius may similarly affect diffusion rates, with the potential to induce diffusive fractionation of the rare earth elements. We have examined the relationship between diffusivity and ionic radius by measuring the diffusion rates of five rare earth elements, La, Ce, Nd, Dy and Yb, spanning ionic radii of 0.099 to 0.116 nm. The data show a systematic increase in diffusion rates with decreasing ionic radius, and this trend is shown to be consistent with a model in which a large fraction of the migration energy is expended in elastic strain of the crystal lattice.

The diffusion data presented in this chapter have application to problems that involve transfer of rare earth elements among minerals and fluids in Earth's mantle and crust. The influence of diffusion in high-Ca pyroxene on the distribution of REE between melt and solid during adiabatic decompression melting is discussed in Chapter 3. Two other applications are discussed in this chapter. The data are used to evaluate the amplitude of Nd isotopic heterogeneity that can be sustained at the scale of individual mineral grains in the upper mantle, and to assess kinetic controls on the uptake of REE by clinopyroxene phenocrysts during basalt crystallization.

EXPERIMENTAL METHODS

Diffusion coefficients were determined from isothermal annealing experiments in which an oriented, polished diopside single crystal was coated with a thin layer of REE oxides and then held at constant temperature and pressure for times of 20 to 882 hours. Diffusion profiles in quenched samples were measured by SIMS (Secondary Ion Mass Spectrometry) depth profiling, and diffusion coefficients were determined by fitting the profiles to an appropriate solution of the diffusion equation. Most experiments were designed to examine diffusion of two or three rare earth elements in the same experiment. This approach reduces the uncertainty in the relative diffusion rates of the elements, and is more efficient than performing a separate set of experiments for each element. In order to determine whether multi-component coupling effects among the REE may be important (in other words, whether the concentration gradient in one rare earth element may affect the diffusive flux of another), a set of experiments was performed in which Ce was the only diffusing element.

The influence of temperature on diffusion of the rare earth elements was evaluated by performing a set of experiments at atmospheric pressure between 1050 and 1300 °C. The oxygen fugacity in these experiments was controlled near the quartz-fayalite-magnetite (QFM) buffer, similar to the f_{O_2} inferred for MORB (Christie et al., 1986). One experiment was also performed with the oxygen fugacity held four log units above the QFM buffer, as a preliminary investigation of the influence of f_{O_2} on diffusion. To evaluate the influence of pressure on diffusion of the REE, a set of high pressure experiments was performed to measure Ce and Yb diffusivities at pressures of 1.3 to 2.5 GPa and temperatures of 1250 to1450 °C.

In the present study we have focused on diffusion normal to the (001) plane. Previous studies of Sr, Ca and Pb diffusion in diopside (Sneeringer et al. 1984; Dimanov et al., 1996; Dimanov and Jaoul, 1998; Cherniak, 1998) have found little anisotropy, and we tentatively expect that the REE, which partition onto the same crystallographic site (M2), behave similarly in this respect.

Starting Material

The starting material for the diffusion experiments consisted of gem-quality diopside single crystals from the Kunlun Mts., China. These crystals are from the same locality as those used by Van Orman et al. (1998) in a study of U and Th diffusion in diopside. The crystals were free of cracks and visible inclusions and homogeneous in major element composition, as determined by electron microprobe (Table 1). Well-developed growth faces allowed the crystals to be oriented optically with respect to their crystallographic axes. Each crystal was cut perpendicular to the *c* axis into ~0.5 mm thick wafers, and one side of each wafer was mechanically polished with diamond and alumina pastes, then chemically polished with an alkaline colloidal silica (0.06 μm) suspension. The polished diopside wafers were rinsed in purified water, then pre-annealed for 1 to 2 days at 1150-1200 °C under a controlled atmosphere. The purpose of this pre-conditioning step is to heal surface damage caused by polishing and to equilibrate point defects at temperature and f_{O_2} conditions near those to be used in the diffusion experiments.

1 atm diffusion anneals

The tracer layer was deposited by evaporating an aqueous solution onto the polished, pre-annealed surface of the diopside. Four different tracer solutions were used, containing Ce, Ce+Yb, La+Nd+Dy, and Yb, respectively, each in dilute (~0.05 M) nitric acid with ~300-500 ppm REE. The solutions were mixed in 1:1 proportions with methanol, which acted as a surfactant, and a few drops (~10 μl) were delivered to the polished diopside surface with a microsyringe. After allowing the solution to evaporate on a hot plate at 120 °C, the nitrates were decomposed by heating the sample in a furnace for ten minutes at 800 °C, leaving a thin layer of REE oxides on the surface. This thin oxide layer, consisting of microgranular particles distributed uniformly over the diopside surface, provided the tracer source for the diffusion experiments. The total concentration of REE in the tracer layer was approximately 0.2 μg/mm^2.

Samples were placed in open Pt crucibles with the coated side facing up and held in the hotspot of a Deltech DT31VT vertical gas mixing furnace for times ranging from 23 to 882 hours. The temperature and oxygen fugacity were adjusted to run conditions before introducing the sample into the furnace, and were held constant during the diffusion anneal. Temperature was monitored continuously with a Pt-$Pt_{90}Rh_{10}$ thermocouple calibrated against the melting points of NaCl, Au, and Pd on the IPTS 1968 temperature scale, and fluctuated within less than ± 2 °C over the course of each experiment. Oxygen fugacity was controlled by mixing CO_2 and H_2 gases and was monitored using a solid ZrO_2-CaO electrolyte oxygen sensor calibrated against the Fe-FeO, Ni-NiO, and Cu-Cu_2O buffers. Variation in f_{O_2} during an experiment was within less than ± 0.1 log unit. Removing the sample from the furnace and allowing it to cool in air served to quench an experiment.

After the diffusion anneal, samples were rinsed ultrasonically in purified H_2O and examined under a reflected light microscope and by SEM. Recrystallization and surface migration took place within the tracer layer during the diffusion anneal, evidenced by the formation of coarser REE oxide crystals and more isolated islands of coating compared to the starting samples. The surface of the diopside maintained a mirror finish, and there was no evidence for chemical reaction with the REE oxide coating.

High pressure diffusion anneals

High pressure diffusion anneals were performed in 0.5 inch solid-medium piston-cylinder devices (Boyd and England, 1960). A polished diopside wafer, pre-annealed under QFM buffered conditions at 1150-1200 °C and coated with Ce and Yb oxides using the method described above, was loaded with packed graphite powder into a cylindrical 0.175" diameter Pt capsule. The coated surface of the diopside was positioned in the center (hotspot) of the capsule. Most of the experiments were run with the sample in direct contact with graphite powder, but two experiments were run with the sample wrapped in Pt foil within graphite, and one sample was placed in a $Au_{80}Pd_{20}$ inner capsule that was surrounded by powdered NaCl

within the Pt outer capsule. After drying for 24-48 hours at 120 °C, the Pt outer capsule was welded shut, placed into a high-density alumina sleeve, and centered in a straight walled graphite furnace using crushable MgO spacers. This assembly was then inserted into a sintered barium carbonate sleeve, which served as the pressure medium. Pressure for our piston cylinder assembly has been calibrated using the Ca-Tschermakite breakdown reaction (Hays, 1966). The friction correction was found to be less than 0.1 GPa at 1.3 GPa and 1350 °C, and the pressures reported in Table 4 do not include a friction correction.

Temperature was continuously monitored and controlled with a $W_{97}Re_3$-$W_{75}Re_{25}$ thermocouple that was separated from the Pt capsule by a thin crushable MgO wafer. The temperature difference between the center of the capsule and the position of the thermocouple has been determined to be 20 °C using offset thermocouples, and temperatures reported in Table 4 are corrected for this difference. No correction for the effect of pressure on thermocouple emf has been applied. Runs were pressed cold to 0.7 GPa and then heated at 100 °C/min to 865 °C, where they were held for 6 minutes. They were then pumped to run pressure and heated to run temperature at a rate of 50 °C/min. Experiments were held at constant temperature and pressure for times ranging from 20 to 76 hours and were quenched by shutting off the power. Diopside single crystals were carefully removed from the capsule after the high pressure runs and ultrasonically rinsed in purified water. Some crystals were cracked in a few places, but in each sample large crack free regions were available for analysis by SIMS depth profiling.

Analyses

Diffusion profiles in the annealed diopside crystals were measured using the Cameca Ims 3f ion microprobe at the Woods Hole Oceanographic Institution. The samples were mounted in epoxy with the polished, tracer-coated surface exposed and covered with a thin (~20 nm) gold film. A primary beam of O^- ions, accelerated under a potential of 8.2 kV and with the total current held constant at 10 to 40 nA, was focused onto the sample surface to a diameter of

20-30 μm. The primary beam was rastered over a square area on a region of the diopside surface that was flat and free of large patches of REE oxides. Secondary ions produced as the primary beam sputtered through the diopside crystal were analyzed in a magnetic sector mass spectrometer. The secondary voltage was offset by –50 V, with a ± 20 V energy window, to reduce the contribution of molecular ions. Isotopes of the REE were monitored throughout the depth profiling analysis by repeatedly cycling through a sequence of ascending masses. ^{30}Si and ^{44}Ca were also monitored to check the stoichiometry of the analyses and to keep track of any instrumental drift. Beyond the first one or two cycles, ^{30}Si and ^{44}Ca intensities were constant. The measured intensities for each mass were adjusted to the midpoint of the cycle by linear interpolation so that concentrations for each element would refer to the same depth. No standardization was used to convert secondary ion intensities to absolute concentrations; diffusion coefficients were calculated directly from profiles of REE/^{30}Si intensity ratios.

A circular field aperture was inserted into the secondary ion optics to restrict data collection to the flat central portion of the sputtered area and thus to minimize contamination of the diffusion profile with material from the tracer layer. In most analyses the sputtered area was 150 x 150 μm^2, and sampling was restricted to a central circular region 68 μm in diameter, but for some samples it was necessary to reduce the sampled area to an 8 μm circle in order to avoid coarse REE oxide crystals. Even with the field aperture, it was impossible to completely eliminate contamination from the surface tracer material during collection of the upper part of the diffusion profile. Small, heterogeneously distributed REE oxide crystals were present everywhere on the diopside surface, and these were inevitably sampled along with the diopside over the first several cycles. It was possible to identify the contaminated part of the diffusion profile, as discussed below, and these data points were not included when calculating diffusion coefficients.

Following the depth profiling analysis, the gold coat was removed by ultrasonicating the sample in an aqueous potassium iodide solution (Ryerson and McKeegan, 1994), and the depth

of the sputtered pit was measured using a Sloan Dektak 8000 surface-contact profilometer equipped with a 2.5 μm diamond-tipped stylus. Several scans of each pit were made, from at least 3 different directions, and the mean depth over the central ~70 μm of the sputtered area was considered. The uncertainty in the depth estimate was set primarily by the roughness and curvature of the diopside surface, and was estimated to be between 20 and 40 nm in most cases. Pits that were sputtered under the same beam conditions for different times yielded consistent estimates of the sputtering rate. This confirms that the sputtering rate during a depth profiling analysis was constant, and that diffusion profiles measured as a function of sputtering time could be scaled linearly to depth.

Determination of diffusion coefficients

Diffusion in our experiments can be modeled as one-dimensional diffusion into a semi-infinite medium, with a constant concentration boundary condition at the interface between the diopside and the tracer layer. The solution to the diffusion equation under these conditions is:

$$\frac{C(x,t) - C_0}{C_i - C_0} = erf\left(\frac{x}{2\sqrt{Dt}}\right), \qquad (1)$$

where C refers to the concentration at depth x after annealing time t, C_0 is the concentration at the interface, C_i is the initial concentration in the diopside crystal, and D is the diffusion coefficient. Diffusivities were evaluated by plotting the inverse error function of the left-hand side of Eq. 1 versus depth (Fig. 1a). This results in a straight line of slope $(4Dt)^{-1/2}$ if the data satisfy the conditions of the diffusion model. The erf^{-1} profiles are fit by linear least squares regression, with the value of C_0 adjusted by an iterative procedure until the fitted line passes through the origin. Only the linear segment of the inverse error function profiles is considered in the fitting procedure. The shallow portion of most erf^{-1} profiles is steep and curved, and is considered to represent contamination from the REE oxide surface layer. Depth profiles measured on samples that were coated with REE oxides but not annealed ("zero-time" experiments) were very similar in length and in form to the near surface segment of the profiles

from annealed samples, with high surface REE intensities falling to background levels over a depth of 50-75 nm. The linear portion of the erf^{-1} profiles in most annealed samples begins at a depth of 120 nm or less, and can be as shallow as 20 nm on exceptionally "clean" surfaces. Diffusion coefficients could be extracted only from diffusion profiles that extended significantly beyond the contaminated region and exhibited a distinct linear segment on the inverse error function plot.

RESULTS

The results of diffusion anneals performed under atmospheric pressure are listed in Tables 2 and 3, and the high pressure results are presented in Table 4. Two or more depth profiles were typically measured on each sample, and the diffusion coefficients reported in Tables 2-4 represent the mean of values determined from these repeat analyses. Diffusion coefficients obtained from different profiles on the same sample agreed to better than $\pm 25\%$ in nearly every case, and always to better than $\pm 40\%$. Much of the variation in diffusion coefficients can be attributed to error in the measurement of SIMS pit depths, which typically led to an uncertainty in D of $\pm 20\%$.

A time series study was performed at 1 atm and 1200 °C, and the results are plotted in Fig. 2. Diffusion coefficients from these experiments, with anneal times ranging from 119 to 456 hours, are in excellent agreement; the total range of diffusion coefficients among the experiments is similar to the interprofile variation within a single sample. This demonstrates that diffusion coefficients are independent of anneal time and is consistent with transport by volume diffusion.

There is no significant effect on Ce diffusion of the simultaneous transport of Yb. Diffusion coefficients determined from experiments in which Ce was the only rare earth element present in the tracer layer were indistinguishable from those determined from experiments in which both Ce and Yb diffused into the diopside.

One experiment was performed to measure the diffusivity of Yb with the oxygen fugacity held four log units above the QFM buffer at 1200 °C. The diffusion coefficient determined from this experiment was more than a factor of 3 higher than in the three experiments performed at the QFM buffer, suggesting a positive dependence of D on f_{O_2} (Fig. 3). This result is important because it suggests that the point defects responsible for diffusion of the REE are those present to compensate the charge of an impurity whose valence is sensitive to oxygen fugacity (e.g. Fe^{3+}). The positive dependence of D on f_{O_2} is consistent with diffusion by a vacancy mechanism, with the dominant vacancies being those present to compensate Fe^{3+} impurities on M1 sites, as discussed below.

Figure 4 is an Arrhenius plot summarizing the results of diffusion experiments performed along the QFM buffer at 1 atm. The diffusion data for each element are consistent with an Arrhenius relationship, $D = D_0 e^{-E/RT}$, where D_0 is the pre-exponential factor, E is the activation energy, and R is the gas constant. Values of D_0 and E were determined by linear least squares regression and are listed in Table 5. The uncertainties reported in Table 5 are those obtained from the linear regression (1 σ). Diffusion coefficients among the rare earth elements are strongly dependent on ionic radius, with D_{Yb} (0.0985 nm in eight-fold coordination) being ~3 times greater than D_{Dy} (0.103 nm), ~20 times greater than D_{Nd} (0.111 nm) and D_{Ce} (0.114 nm), and ~35 times greater than D_{La} (0.116 nm). This trend of decreasing diffusivity with increasing ionic radius is consistent with an elastic strain model for diffusion, as discussed below.

In the high pressure experiments, a systematic difference in diffusion rates is observed between samples annealed in contact with Pt or AuPd and those annealed in contact with graphite. This difference appears to be related to loss of Fe from diopside crystals that were annealed in noble metal capsules, and because of these difficulties we have considered only data from runs in graphite capsules to evaluate the influence of pressure on diffusion of Ce and Yb.

Diffusion coefficients determined from experiments run in noble metal capsules are internally consistent—a sample run in a sealed AuPd inner capsule within a molten NaCl medium yielded the same value of D_{Yb} as a run in which the sample was wrapped in Pt foil and surrounded by graphite. Samples annealed within a molten salt confining medium should have experienced isostatic stress, and the consistency among these results shows that deviatoric stresses that might be experienced by samples held within a graphite medium have no significant effect on diffusion. Samples that were held in direct contact with graphite, with no intervening Pt foil, also yield internally consistent diffusion coefficients, but D_{Ce} and D_{Yb} from these runs are a factor of 3-4 higher than in runs performed in noble metal containers. We measured SIMS depth profiles of ^{56}Fe in two samples that had been annealed in contact with a noble metal (B474 and B553), with the secondary ion voltage displaced by –110 V to reduce molecular interferences. In both samples, the concentration of Fe decreases smoothly toward the interface with the noble metal (Fig. 5). Immediately adjacent to the interface the relative loss of Fe is ~90%. In both samples the Fe loss profiles conform to an error function solution to the diffusion equation, and similar diffusion coefficients of $7.0 \pm 3.2 \times 10^{-20}$ m^2/s and $4.9 \pm 2.0 \times 10^{-20}$ m^2/s are obtained for runs B474 and B553, respectively. The diffusivity of Fe is very similar to that of Yb in these experiments. The relative difference in Ce and Yb diffusion rates is similar to that observed in the graphite capsule experiments, and in the 1 atm experiments.

The reduction in Ce and Yb diffusivities in samples run in noble metal capsules may be related to changes in defect chemistry associated with the loss of Fe. The positive dependence of D on oxygen fugacity observed in the 1 atm experiments suggests that the dominant vacancies in the Kunlun Mts. diopside are those that have been created to compensate Fe^{3+}. Loss of Fe^{3+} and associated vacancies would lead directly to a decrease in diffusivity by reducing the number of vacant sites available for Ce and Yb atoms to hop to.

Diffusion data from the high pressure experiments performed in graphite capsules and from 1 atm anneals performed along the QFM buffer were multiply regressed against P and T^{-1}

(Figs. 6 and 7). The data are consistent with an Arrhenius relationship $D = D_0 e^{-(E+PV)/RT}$, where V is the activation volume. Values of D_0, E and V determined from the regressions are listed in Table 6, along with their 1 σ uncertainties. The values of D_0 and E are nearly identical to those determined from the 1 atm data set alone, but have somewhat lower uncertainties.

In Figure 7 the 1 atm and high pressure diffusion data are shown together on a plot of log D vs. inverse temperature, with the high pressure data corrected to 1 atm using the activation volumes for Ce and Yb determined above. The 1 atm and high-pressure data are in excellent agreement, and there are no changes in slope that would suggest a change in diffusion mechanism between 1050 and1450 °C.

Activation volumes for Ce and Yb are similar, and over the temperature range investigated amount to a decrease in diffusivity by a factor of ~6.5 as pressure is increased from 1 atm to 2.5 GPa. The reported uncertainties in the activation volumes are those determined from statistical fits to the data, and do not include systematic errors that may arise from differences in oxygen fugacity or other parameters between the 1 atm and high pressure experiments. The oxygen fugacity in the high pressure experiments, if buffered by the presence of graphite in equilibrium with a CO_2-CO-O_2 fluid, would be about two orders of magnitude lower than the f_{O_2} of 1 atm experiments that were performed along the QFM buffer (Huebner, 1971). According to our preliminary results on the f_{O_2} dependence of Yb diffusion at 1 atm, a 2 log unit shift in oxygen fugacity would shift diffusion coefficients upward by ~0.25 log units. Correcting the high pressure diffusion coefficients to the same oxygen fugacity would reduce the calculated activation volume for Yb by 38%, from 9.5 to 5.9 cm^3/mol, and for Ce by 44%, from 10.2 to 5.7 cm^3/mol.

The only previous determination of the pressure dependence of diffusion in pyroxene was made by Sneeringer et al. (1984), who found an apparent *negative* activation volume for Sr diffusion in synthetic diopside. Sneeringer et al. (1984) also found a relatively large anisotropy in the activation volume, with diffusion parallel to *a* and *b* having a stronger pressure

dependence than diffusion parallel to *c*. The scatter in the data is relatively large, and a small positive activation volume for the *c* direction (the same crystallographic direction investigated in this study) is within the uncertainty in the Sr diffusion measurements. The high pressure experiments of Sneeringer et al. (1984) were performed by placing two diopside crystals, one doped with Sr and the other undoped, together within a high-pressure cell. It is possible that the boundary between the two crystals migrated during the diffusion anneal, and that this enhanced the re-distribution of Sr during the diffusion anneal (see Hay and Evans, 1987, for a discussion of enhanced solute transport associated with grain boundary migration). Such non-diffusive transport might account for the apparent positive dependence of Sr diffusivity on pressure.

Comparison with other diffusion data

The only previous experimental study of rare earth element diffusion in diopside was that of Sneeringer et al. (1984) and Sneeringer (1981), who measured Sm diffusion rates in a synthetic diopside single crystal. Figure 8 shows an Arrhenius plot comparing the Sm diffusion data with our 1 atm data for La, Ce, Nd, Dy and Yb. On the basis of the relationship observed in our data set between D and ionic radius, we would expect D_{Sm} to be less than D_{Dy} and greater than D_{Nd}. The 1 atm Arrhenius curve of Sneeringer (1981) is slightly lower than our curve for Nd. Given the relatively large scatter in the Sm diffusion data (up to an order of magnitude at a given temperature), these results are in reasonable agreement with our data. The high pressure Sm data of Sneeringer et al. (1984) are about an order of magnitude higher than our data for Dy at 1 atm, and the difference increases if our data are corrected to higher pressures.

Figure 9 shows a comparison of our 1 atm diffusion data for the rare earth elements with diffusion data for other elements in diopside. Arrhenius curves for most elements, including the REE, U, Th, Ca and O, fall within a relatively narrow band spanning about two orders of magnitude at a given temperature. Lead and strontium (in natural diopside crystals) fall about two orders of magnitude above this band, and Si falls below. Much of the variation in

diffusivity among these elements may be explained as a consequence of the different sites that the ions occupy (the tetrahedral site in diopside has a much deeper energy well than the M1 or M2 site (Smyth and Bish, 1988), which probably explains the slow diffusivity of Si relative to cations that partition onto the metal sites) and the size and charge of the ion relative to the ideal size and charge of the site. Diffusion rates are also influenced by the composition of the pyroxene. Strontium diffusion in natural diopside crystals, with the dominant impurity being Fe at the level of 1.5 wt.% FeO*, is two orders of magnitude faster than Sr diffusion in nominally pure synthetic diopside crystals (Sneeringer et al., 1984). Calcium self-diffusion rates in natural diopside crystals containing ~1-2 wt.% FeO are also faster than in pure synthetic diopside, by about an order of magnitude (Dimanov et al., 1996). In contrast to the relatively large compositional dependence of diffusion found by Sneeringer et al. (1984) and Dimanov et al. (1996) for Sr and Ca diffusion, Cherniak (1998) found similar diffusion rates for Pb in two natural diopside crystals containing ~1 wt.% and ~17 wt.% FeO, respectively. Although further experimental work must be done in order to characterize the influence of pyroxene composition on diffusion rates, it may be that cation diffusion rates are reduced drastically only when impurity concentrations are very low. Increasing the Fe concentration beyond 1 wt.% does not appear to increase cation diffusion rates significantly, which may suggest that Fe^{3+}–associated cation vacancies are present at nearly saturated levels even in pyroxene crystals with relatively low Fe contents.

DISCUSSION

Coupled element exchange during "tracer" diffusion

Coupled substitution is required to balance the extra positive charge that is introduced when a trivalent rare earth element is exchanged with a divalent cation on the diopside M2 site. Unfortunately, we cannot directly infer the coupled substitution responsible for the uptake of REE in our experiments. The concentration of REE is on the order of a few thousand ppm at most, and at these low abundances it is not possible to resolve coupled variations in major

element concentration that would indicate which substitution is taking place. However, because the tracer layer contained only rare earth element oxides, with no charge balancing species such as Al or Na present, it is likely that the introduction of REE into the diopside in our experiments involved an Eskola-type exchange, with charge balance achieved through the formation of vacancies on M1 or M2 sites. Two possible exchange reactions can be written as follows:

$$REE_2O_3 + 2Ca_{M2}^{\times} + Mg_{M1}^{\times} \rightarrow 2\mathrm{REE}_{M2}^{\cdot} + V_{M1}^{\cdot\cdot} + MgO + 2CaO \qquad (2)$$

or,

$$REE_2O_3 + 3Ca_{M2}^{\times} \rightarrow 2\mathrm{REE}_{M2}^{\cdot} + V_{M2}^{\cdot\cdot} + 3CaO \qquad (3)$$

using Kröger-Vink notation (e.g. Kröger, 1974). In this notation X_Y^Z refers to an element X or vacancy V on a crystallographic site Y, with Z referring to the excess charge relative to that of the normally occupied site. A dot ($\cdot$) denotes one excess positive charge, a prime ($'$) stands for one excess negative charge, and a cross ($\times$) indicates that the site is negatively charged. Equation 2 describes the substitution of two REE^{3+} ions for two Ca^{2+} ions on the M2 site, with the formation of a vacancy on the M1 (Mg) site. Mg and Ca are transported out of the diopside crystal and deposited on the surface as MgO and CaO. The reaction described by Eq. (3) is similar but involves formation of a vacancy on M2 (Ca) rather than M1. We can not rule out other exchanges, such as a Tschermak's (REEAl-CaSi) or jadeite (REENa-CaCa) type substitution. However, because no Na or Al is available in the tracer layer in our experiments, such exchanges would necessarily be accompanied by a net decrease in the number of lattice units in the diopside crystal, and outward transport of Si and other components. We consider this unlikely, because the self-diffusivity of Si in diopside (Bejina and Jaoul, 1996) is an order of magnitude slower than the La diffusivity we have measured and more than two orders of magnitude slower than Yb. If a Tschermak's or jadeite substitution were responsible for uptake of REE in our experiments, we would expect transport to have been limited by diffusion of Si and for all of the rare earth elements to have diffusion profiles of similar length. The fact that

we observed large differences in diffusivity among the REE indicates that transport is limited by the mobility of the rare earth elements themselves.

Diffusion mechanism

The positive dependence of D_{Yb} on oxygen fugacity is consistent with diffusion by a vacancy mechanism. Under oxidizing conditions excess oxygen may be incorporated into the diopside structure, creating cation vacancies that are electronically compensated by Fe^{3+} on M1 sites ($Fe^{\cdot}_{M1}$). This reaction can be described by the following equation:

$$8Fe^{\times}_{M1} + 2O_2 = 4O^{\times}_{O} + V^{\cdot\cdot}_{M2} + V^{\cdot\cdot}_{M1} + V^{\cdot\cdot\cdot\cdot}_{Si} + 8Fe^{\cdot}_{M1} \qquad (4)$$

with the corresponding mass action law:

$$\left[V^{\cdot\cdot}_{M2}\right]\left[V^{\cdot\cdot}_{M1}\right]\left[V^{\cdot\cdot\cdot\cdot}_{Si}\right]\left[Fe^{\cdot}_{M1}\right]^8 = K\left[Fe^{\times}_{M1}\right]^8 f_{O_2}^2 \qquad (5)$$

If the electroneutrality condition $\left[Fe^{\cdot}_{M1}\right] = 2\left[V^{\cdot\cdot}_{M2}\right] + 2\left[V^{\cdot\cdot}_{M1}\right] + 4\left[V^{\cdot\cdot\cdot\cdot}_{Si}\right]$ is satisfied and the concentrations of M1, M2 and Si vacancies are approximately equal (as would be the case if most vacancies were produced by reaction (5)), then $\left[V^{\cdot\cdot}_{M2}\right] \propto f_{O_2}^m$, with $m = +2/11$. If diffusion of the rare earth elements is governed by M2 vacancies, the diffusion coefficients should have the same proportionality with f_{O_2}. Our preliminary investigation of the f_{O_2} dependence of Yb diffusivity at 1200 °C suggests that $m \approx 0.13$, slightly lower than the value of ~0.18 predicted from the point defect model. Cherniak (1999) has investigated the influence of f_{O_2} on diffusion of Pb in four different high-Ca clinopyroxene samples spanning a wide range of compositions. A positive dependence of the diffusion coefficient on f_{O_2} was observed in all cases, with $m \approx$ 0.18 for a near end-member diopside sample. In contrast to the results of Cherniak (1999) for Pb and our preliminary result for Yb, Dimanov and co-workers have found that diffusion of Ca in diopside is *inversely* proportional to f_{O_2}, with $m \approx -0.19$. This result suggests that Ca diffuses by an interstitial rather than a vacancy mechanism; the observed dependence on oxygen fugacity is consistent with a point defect model in which Ca interstitials are formed in response

to oxygen desorption and associated reduction of $Fe^{\cdot}_{M1}$ to $Fe^{\times}_{M1}$ (Jaoul and Raterron, 1994; Dimanov and Jaoul, 1998). Apparently the energy required for an M2 cation to move to an adjacent vacancy is not very different from that required for a jump to an interstitial site, and as a result the diffusion mechanism that an ion prefers is very sensitive to its size and charge.

The diffusion coefficient measured in annealing experiments can be related to atomic jump parameters by the following equation (e.g. Flynn, 1972):

$$D = n\gamma a^2 f \nu_o \exp\left(\frac{S_m}{R}\right)\exp\left(\frac{-(E_m + PV_m)}{RT}\right), \qquad (6)$$

where n is the mole fraction of vacancies or interstitial sites that govern diffusion, γ is a geometrical factor, a is the atomic jump distance, f is a correlation factor, and ν_o is the jump attempt frequency (which is close to the vibrational frequency of an atom in its lattice site). S_m, E_m and V_m are the entropy, energy and volume of motion, respectively. Because our 1 atm experiments were performed along the QFM buffer rather than at constant oxygen fugacity, the apparent activation energies we have measured for diffusion of the REE do not represent motion energies alone, but include the influence of f_{O_2} on diffusivity. At constant f_{O_2} the activation energies for the REE would be less by mH_{QFM}, where H_{QFM} is the enthalpy of the QFM reaction, equal to +493 kJ/mol (Huebner, 1971). If m = +0.13, the activation energy at constant f_{O_2} would be 64 kJ/mol less than along the QFM buffer, and if m = +2/11 as expected from the point defect model, the activation energy at constant f_{O_2} would be 90 kJ/mol less than along the QFM buffer. The activation energy at constant f_{O_2} is still not equivalent to the motion energy E_m, because there is also a contribution from the enthalpy of the vacancy formation reaction (Eq. 5). Unfortunately, the thermodynamic data needed to estimate the enthalpy of this reaction are not available. Thermodynamic data do exist for a similar reaction in olivine (Nakamura and Schmalzried, 1983; Hirsch and Shankland, 1993), and the enthalpy is found to be small—approximately +13 kJ/mol. Taking this as an estimate for the enthalpy of the reaction expressed in Eq. 5, the motion energy for Yb in diopside would be ~[411-(90+13)] =

308 kJ/mol. It is interesting to compare this to the calculated motion energy for Ca diffusion in diopside by a vacancy mechanism. Azough et al. (1998), using the Mott-Littleton approach with empirical interatomic potentials, found that the most favorable Ca jump requires ~190 kJ/mol. This is close to 2/3 of the motion energy we estimate for Yb diffusion, which is the ratio expected if the motion energy is proportional to the charge of the cation.

AN ELASTIC DIFFUSION MODEL

Because diffusion data for minerals remain sparse, there is considerable interest in obtaining an empirical or theoretical relationship that can be used to predict the diffusion parameters of ions that have not yet been studied in the laboratory. In this section we introduce an elastic strain model for diffusion and discuss its application to diopside and other silicate minerals.

Relation between D and ionic radius

Mullen (1966) derived a theoretical expression relating the motion energy of an impurity in an ionic solid to the difference between the ionic radius of the impurity and the ideal site radius. Ions are represented as hard spheres linked by Einstein springs, and the motion energy is taken to be the work required to move ions into a configuration (the so-called "saddle-point" configuration) that allows motion of a jumping ion along a straight-line path to an adjoining vacancy (Mullen, 1966). The motion energy is assumed to be purely due to elastic strain and does not include the change in Coulomb energy between the equilibrium configuration and the saddle-point configuration. With these assumptions, a relation between the motion energy and the ionic radius is given by the following equation (combining Mullen's Eqs. 2 and 4):

$$E_m = E_m^\circ\left\{1+2\left[\delta\left(1-1/\sqrt{2}\right)^{-1}-\delta^2\left(1-1/\sqrt{2}\right)^{-2}\right]\right\}. \qquad (7)$$

The parameter E_m° in Eq. 7 refers to the motion energy for an ion with ideal radius, and δ is a size factor defined as $(r_i\text{-}r_{site})/r_o$, where r_i is the radius of the impurity ion, r_{site} is the ideal site

radius, and r_o is the average cation-anion bond length for the site. The Mullen equation predicts a parabolic relation between the motion energy and the ionic radius for ions occupying a particular site. The maximum motion energy is predicted for an ion with $\delta = 0.147$. The REE in diopside have values of δ between 0.0440 (for La) and –0.0260 (for Yb), assuming an ideal M2 site radius of 0.105 nm (Blundy and Wood, 1994) and an average M2-O bond length of 0.250 nm (Smyth and Bish, 1988). If E_m° for a trivalent ion has a value of ~330 kJ/mol (estimated from the inferred motion energies for the REE, interpolated to $\delta = 0$), the motion energy is predicted to increase by ~140 kJ/mol from Yb to La. There does appear to be an increase in the activation energy (and by extension, the motion energy) with increasing ionic radius among the REE in diopside, but the trend is poorly resolved due to relatively large uncertainties in the activation energies.

The relative variation in diffusivity among the rare earth elements at a particular temperature is much greater than the variation in activation energy, and the Mullen equation can be compared to the data more readily if it is recast in terms of D rather than E_m. This can be done provided that a relationship can be formulated between D_0 and ionic radius. In many materials, including silicate minerals (Hart, 1981) and melts (Hofmann, 1980), a positive correlation is found among D_0 and E. Zener (1952) showed that such a correlation is expected if a large part of the energy expended during an atomic jump is due to lattice strain. In this case a relation between the motion entropy and the temperature coefficient of the bulk (or shear) modulus μ is expected, as described by the following equation:

$$\ln D_0 \propto S_m \approx -\{\partial(\mu/\mu_\circ)/\partial T\}E_m. \qquad (8)$$

D_0 is a composite term comprising several atomic jump parameters (the first 6 terms in Eq. 6, for extrinsic diffusion), but most of them are related to the mineral structure and only S_m and ν_o depend on the properties of the jumping ion. If it is assumed that variations in ν_o among the REE are small and that variation in D_0 is due primarily to differences in S_m (in other words, that the jump attempt frequencies among the REE are similar, but that the success of a jump is

determined by the size of the ion), then the Mullen equation (Eq. 7) can be combined with the Zener relation (Eq. 8) to give:

$$\ln D = \ln D^{\delta=0} - 2b\left[\delta\left(1-1/\sqrt{2}\right)^{-1} - \delta^2\left(1-1/\sqrt{2}\right)^{-2}\right], \qquad (9)$$

where

$$b \approx \frac{E_m^\circ}{R}\left[\frac{\partial(\mu/\mu_\circ)}{\partial T} + \frac{1}{T}\right]. \qquad (10)$$

Equation 9 describes a parabola on a plot of ln$D$ vs. δ, with a minimum at $\delta = 0.147$. For the diopside M2 site, the minimum in diffusivity is predicted for an ion with radius ~0.142 nm. The REE are all much smaller than this "minimum diffusivity" radius and thus their diffusion coefficients are expected to decrease monotonically with increasing ionic radius. This prediction is in accord with the results of our experiments. Figure 10 shows our experimental results for diffusion of La, Ce, Nd, Dy and Yb at 1 atm and 1200 °C on a plot of ln D vs. δ. The curve through the data was obtained by a least squares fit to Eq. 9, with $\ln D^{\delta=0}$ and b as the only adjustable parameters. The parameter b controls the "tightness" of the parabola—the larger the value of b, the tighter the parabola—and $\ln D^{\delta=0}$ determines the vertical placement of the curve. The parabola is not adjusted along the δ axis; its horizontal position on the plot is fixed by specifying the ideal M2 site radius (0.105 nm; Blundy and Wood, 1994) and mean M2-O bond length (0.250 nm; Smyth and Bish, 1988). The values of b and $\ln D^{\delta=0}$ obtained from the fit are given in Table 7.

The Mullen/Zener model appears to provide an excellent description of REE diffusion rates in diopside at 1200 °C. As shown in Fig. 11, it also describes the temperature dependence of REE diffusion quite well. The lines shown in Fig. 11 are not fits to the data but were obtained from the Mullen/Zener model, as follows. The motion energy for each element is assumed to follow Eq. 7, with E_m° = 330 kJ/mol. Because the diffusion data were obtained along the QFM buffer rather than at constant oxygen fugacity, the activation energy

(represented by the slope of the Arrhenius line) is taken to equal (E_m°+92+13) kJ/mol. Relative values of $\ln D_0$ are given by Eq. 8, using the value of $-\partial(\mu/\mu_0)/\partial T$ obtained from the fit of Eqs. 9 and 10 to the data at 1200 °C. The Arrhenius curves obtained from the Mullen/Zener model (Fig. 11) pass through nearly all of the data points for each element within error, and agree with the data nearly as well as Arrhenius curves fitted to the data by least-squares regression (Fig. 4). The Mullen/Zener model thus appears to provide a useful means for estimating the Arrhenius parameters of rare earth elements (as well as other trivalent elements that partition onto the M2 site) that have not yet been determined experimentally.

Diffusion data are also available for ions with a range of ionic radii in the silicate minerals zircon and anorthite. Diffusion coefficients for the REE in zircon (Cherniak et al., 1997a) and the alkaline earth elements in anorthite (LaTourrette and Wasserburg, 1998) at 1200 °C were fit to Eq. 9, and the results are shown in Fig. 12 along with those for the REE in diopside. Each data set is fit quite well by the Mullen/Zener model, and the relative values of b for each mineral (Table 7) are consistent with the relationship given in Eq. 10. The dependence of diffusivity on the size factor δ is greatest for zircon, which also has the largest motion energy (and the stiffest lattice). Diffusion in plagioclase has the weakest dependence on ionic radius among the three minerals, and the smallest activation energy for diffusion (as well as the most compliant lattice). Although there is a general correspondence between the data and the predictions of the Mullen/Zener model, the value of b predicted from Eq. 10 is a factor of ~2-3 greater than the value obtained from the fit to the diffusion data (Table 7). In other words, the dependence of diffusivity on ionic radius that is predicted from the Mullen/Zener model, using experimentally determined motion energies and temperature derivatives of the elastic moduli, is greater than that observed in the diffusion data.

Relation between D and ionic charge

The change in electrostatic energy required to move an ion to an adjacent vacant site in a solid is, to a first approximation, linearly related to ionic charge (e.g. Anderson and Stuart,

1954). Taking the motion energy to be proportional to cation charge, and assuming that the motion energy and motion entropy are linearly related according to Eq. 7, a relationship among the diffusion coefficient D, ionic charge z and size factor δ can be formulated as follows:

$$\ln D_z = \ln D_{z_{ref}}^{\delta=0} + b\left(1 - \frac{z}{z_{ref}}\right) - 2b\left(\frac{z}{z_{ref}}\right)\left[\delta\left(1-1/\sqrt{2}\right)^{-1} - \delta^2\left(1-1/\sqrt{2}\right)^{-2}\right], \quad (11)$$

where b is as defined above (Eq. 10) with E_m° equal to the motion energy for a cation with ideal radius and the reference charge z_{ref}. This relationship can be compared to the diffusion data for divalent, trivalent and tetravalent cations in diopside and zircon using the values of $\ln D_{z=3}^{\delta=0}$ and b determined from the REE diffusion data (Fig. 13). The diffusion data shown in Fig. 13 are corrected to $\delta = 0$ using the relationship given by Eq. 11. The lines represent solutions to Eq. 11, and intersect $\ln D_{z=3}^{\delta=0}$ with a slope of $-b/3$. Although there is considerable scatter in the data for divalent ions in diopside and tetravalent ions in zircon, the model captures the general trends for the two minerals remarkably well. Equation 11 predicts that a mineral in which D depends strongly on ionic radius should also exhibit a strong dependence of D on ionic charge. Diopside and zircon are consistent with this relationship; diffusion rates in zircon are more sensitive to both size and charge than are diffusion rates in diopside.

Activation volume

An elastic strain energy model relating the activation volume and activation energy for diffusion was introduced by Keyes (1963) and has been discussed further by Flynn (1972) and Sammis et al. (1981). If the lattice distortions involved in the motion of an ion are perfectly elastic, then a lower bound on the activation volume is obtained by assuming that the lattice strain is purely shear, and an upper bound is obtained by assuming that strain is entirely dilatational. In the case of shear strain, the activation volume is given by:

$$V_m = E_m\left[\left(\frac{\partial(\ln G)}{\partial P}\right)_T - \frac{1}{K_T}\right]\left[1 - \left(\frac{\partial(\ln G)}{\partial(\ln T)}\right)_P - \beta T\right]^{-1} \quad (12)$$

where G is the shear modulus, K_T is the isothermal bulk modulus, and β is the coefficient of thermal expansion (Sammis et al., 1981). If the strain energy is assumed to be purely dilatational, then:

$$V_m = E_m\left[\left(\frac{\partial(\ln K_T)}{\partial P}\right)_T - \frac{1}{K_T}\right]\left[1-\left(\frac{\partial(\ln K_T)}{\partial(\ln T)}\right)_P - \beta T\right]^{-1}. \qquad (13)$$

Using values given by Anderson (1989) for the elastic moduli and their temperature and pressure derivatives, and the thermal expansion coefficient for diopside given by Fei (1995), Eqs. 12 and 13 yield estimates of 6.1 and 11.2 cm^3/mol, respectively, for the activation volume of Yb diffusion. These estimates are in agreement with the measured activation volume of 9.5 ± 2.0 cm^3/mol. For Ce, the measured activation volume of 10.2 ± 3.2 cm^3/mol also falls within the predicted range of 7.0 to 12.8 cm^3/mol (for a Ce motion energy of 358 kJ/mol).

Applications of the Data

The diffusion data presented above are applicable to a wide range of kinetic problems in high temperature geochemistry. Rare earth element diffusion rates in diopside are slow enough that melts may not completely equilibrate with high-Ca pyroxene during partial melting of the upper mantle. Diffusive fractionation of the REE during adiabatic decompression melting is discussed in Chapter 3. Koga et al. (1999) discuss the diffusion-limited redistribution of trace elements, and the inheritance of "garnet signatures" in pyroxene grains, that may take place when upwelling mantle passes through the garnet–spinel facies transition. In this section the REE diffusion data are used to evaluate the length scale over which Nd isotopic heterogeneity can be maintained in the upper mantle, and to assess kinetic controls on REE uptake during basalt crystallization.

Isotopic heterogeneity

A large body of data from mid-ocean ridge basalts (MORB) and ocean island basalts (OIB) shows that the Earth's mantle is heterogeneous in isotopic composition (see Zindler and Hart, 1986; Allegre et al., 1986; Hart et al., 1992; Hofmann, 1997; and references therein).

Hofmann and Hart (1978) argued for a mantle that is heterogeneous on a regional scale but homogeneous on a local (grain size) scale. The original argument for local isotopic equilibrium was based on a diffusion data set that was quite sparse; in 1978 no experimental data were available for diffusion of radioisotopes in major upper mantle minerals. In 1984, Sneeringer et al. showed that diffusion of Sr in clinopyroxene is rapid enough at temperatures near the solidus of peridotite to easily maintain grain-scale $^{87}Sr/^{86}Sr$ homogeneity. Here we revisit the question of local equilibrium for Nd isotopes. The calculations that follow assume that isotopic equilibration is governed by volume diffusion in the minerals. Mineral grains are also assumed to maintain communication with each other through a network of high diffusivity paths (e.g. grain boundaries or melt tubules along 3-grain junctions), with no intervening solid barriers to diffusional exchange between individual mineral grains. If clinopyroxene grains are "armored" by olivine or orthopyroxene, which dissolve very little Nd, then isotopic equilibration could be significantly slower than in the case considered here. On the other hand, equilibration could be considerably faster if recrystallization or some other process acts to short-circuit volume diffusion.

Because diffusion of Nd is slower in clinopyroxene than in garnet (Chapter 2 of this thesis; Coghlan, 1990; Ganguly et al., 1998), cpx probably controls the rate of equilibration of Nd isotopes in mantle rocks. In garnet lherzolite at temperatures near the solidus (~1450 °C at a pressure of 2.5 GPa) the diffusion coefficient for Nd in diopside is estimated to be ~1.8 x 10^{-19} m^2/s, assuming an activation volume of 10 cm^3/mol. Under these conditions, a spherical cpx grain 5 mm in diameter can remain closed to Nd isotope exchange for only ~1 My. In this time, garnet and cpx with Sm/Nd ratios that differ by a factor of ~3-4 can maintain differences in $^{143}Nd/^{144}Nd$ of only ~10^{-6}. This local scale heterogeneity is very small compared to variations in $^{143}Nd/^{144}Nd$ of 10^{-4} to 10^{-3} among MORB and OIB. Thus the common assumption that Nd isotopes are locally in equilibrium during melting of garnet lherzolite appears to be a good one.

Melting of eclogite may be a different story. The solidus of eclogite could be as low as 1150 °C at 1.5 GPa pressure (e.g. Hirschmann and Stolper, 1996), and at these conditions the diffusion coefficient for Nd in diopside is estimated to be ~2 x 10^{-22} m^2/s. Significant isotopic disequilibrium could be maintained between 5 mm cpx and garnet grains for times on the order of a billion years, which could lead to differences in $^{143}Nd/^{144}Nd$ between cpx and garnet of ~10^{-3}. This degree of local disequilibrium is quite large compared to the variation in Nd isotopic ratios observed in oceanic basalts. If eclogitic material makes an important contribution to basaltic magmas, the assumption of local isotopic equilibrium in the source may not be valid.

Disequilibrium REE uptake by clinopyroxene phenocrysts

Clinopyroxene phenocrysts grown from silicate melts commonly exhibit disequilibrium features such as oscillatory zoning or sectoral enrichment. The underlying cause of disequilibrium may be related to boundary layer effects in the melt adjacent to the growing crystal (e.g. Albarede and Bottinga, 1972) or to enrichment/adsorption at the crystal surface (Shimizu, 1981; Watson and Liang, 1995; Watson, 1996). Preservation of the chemical zoning produced by either process is controlled by volume diffusion in the crystal. In the case of disequilibrium uptake due to surface enrichment phenomena, preservation of zoning depends on the value of the "growth" Peclet number, Pe = Vl/D, where V is the crystal growth rate, l is the enriched surface layer thickness, and D is the diffusion coefficient in the crystal (Watson, 1996). Watson and Liang (1995) and Watson (1996) showed that perceptible disequilibrium uptake is possible if the Peclet number is greater than ~0.1. Phenocryst growth rates in basaltic lava lakes have been estimated to be 10^{-12} to 10^{-11} m/s from direct sampling of phenocryst size distributions over time (Kirkpatrick et al., 1977). Assuming a surface enrichment layer on order of a single silicate monolayer (~0.5 nm), these crystal growth rates are rapid enough to allow significant disequilibrium uptake of REE. For phenocrysts growing at a rate of 5 x 10^{-12} m/s at a temperature of 1100 °C, Peclet numbers for the REE range from 0.5 for Yb to 22 for La. Uptake of the HREE may thus take place under near-equilibrium conditions, while uptake of

LREE may be dominated by surface enrichment effects. The REE patterns preserved in clinopyroxene phenocrysts, under typical conditions of basalt crystallization, will be sensitive not only to variations in bulk and surface partitioning but to phenocryst growth rates. Zoning of REE in clinopyroxene phenocrysts is expected under many conditions of basalt crystallization, and may provide a sensitive record of cooling and crystallization rates.

REFERENCES

Albarede F. and Bottinga Y. (1972) Kinetic disequilibrium in trace element partitioning between phenocrysts and host lava. *Geochim. Cosmochim. Acta* **36**, 141-156.

Allègre C. J., Hamelin B., Provost A. and Dupré B. (1986) Topology in isotopic multispace and origin of mantle chemical heterogeneities. *Earth Planet. Sci. Lett.* **81**, 319-337.

Anderson D. L. (1989) *Theory of the Earth*. Blackwell Scientific, Oxford.

Azough F., Freer R., Wright K., and Jackson R. (1998) A computer simulation study of point defects in diopside and the self-diffusion of Mg and Ca by a vacancy mechanism. *Mineral. Mag.* **62**, 599-606.

Bass J. D. (1995) Elasticity of minerals, glasses, and melts. In Ahrens, T. J., ed., *Mineral Physics and Crystallography: A Handbook of Physical Constants*. American Geophysical Union, Washington, DC.

Bejina F. and Jaoul O. (1996) Silicon self-diffusion in quartz and diopside measured by nuclear micro-analysis methods. *Phys. Earth Planet. Inter.* **97**, 145-162.

Blundy J. and Wood B. (1994) Prediction of crystal-melt partition coefficients from elastic moduli. *Nature* **372**, 452-454.

Boyd F. R. and England J. L. (1960) Apparatus for phase equilibrium studies at pressures up to 50 kbars and temperatures up to 1750 °C. *J. Geophys. Res.* **65**, 741-748.

Brady J. B. and McCallister R. H. (1983) Diffusion data for clinopyroxenes from homogenization and self-diffusion experiments. *Am. Mineral.* **68**, 95-105.

Cherniak D. J. (1998) Pb diffusion in clinopyroxene. *Chem. Geol.* **150**, 105-117.

Cherniak D. J. (1999) Pb diffusion in Cr diopside and augite, and consideration of the dependence on oxygen fugacity of Pb diffusion in pyroxene. *Eos Trans. AGU* **80**, S373.

Cherniak D. J., Hanchar J. M. and Watson, E. B. (1997a) Rare-earth diffusion in zircon. *Chem. Geol.* **134**, 289-301.

Cherniak D. J., Hanchar J. M. and Watson, E. B. (1997b) Diffusion of tetravalent cations in zircon. *Contrib. Mineral. Petrol.* **127**, 383-390.

Christie D. M., Carmichael I. S. E., and Langmuir C. H. (1986) Oxidation-state of midocean ridge basalt glasses. *Earth Planet. Sci. Lett.* **79**, 397-411.

Coghlan R. A. N. (1990) Studies of diffusional transport: grain boundary transport of oxygen in feldspars, strontium and the REE's in garnet, and thermal histories of granitic intrusions in south-central Maine using oxygen isotopes. Ph.D. thesis, Brown University, Providence, Rhode Island.

Dimanov A. and Ingrin J. (1995) Premelting and high-temperature diffusion of Ca in synthetic diopside: an increase of the cation mobility. *Phys. Chem. Minerals* **22**, 437-442.

Dimanov A. and Jaoul O. (1998) Calcium self-diffusion in diopside at high temperature: implications for transport properties. *Phys. Chem. Minerals* **26**, 116-127.

Dimanov A., Jaoul O. and Sautter V. (1996) Calcium self-diffusion in natural diopside single crystals. *Geochim. Cosmochim. Acta* **60**, 4095-4106.

Fei Y. (1995) Thermal expansion. In Ahrens, T. J., ed., *Mineral Physics and Crystallography: A Handbook of Physical Constants*. American Geophysical Union, Washington, DC.

Flynn C. P. (1972) *Point Defects and Diffusion*. Oxford Univ. Press, Oxford.

Ganguly J., Tirone M. and Hervig R. L. (1998) Diffusion kinetics of samarium and neodymium in garnet, and a method for determining cooling rates of rocks. *Science* **281**, 805-807.

Hart S. R. (1981) Diffusion compensation in natural silicates. *Geochim. Cosmochim. Acta* **45**, 279-291.

Hart S. R., Hauri E. H., Oschmann L. A. and Whitehead J. A. (1992) Mantle plumes and entrainment: Isotopic evidence. *Science* **256**, 517-520.

Hay R. S. and Evans B. (1987) Chemically induced grain boundary migration in calcite: temperature dependence, phenomenology, and possible applications to geologic systems. *Contrib. Mineral. Petrol.* **97**, 127-141.

Hays J. F. (1966) Lime-alumina-silica. *Carnegie Inst. Wash. Yearbk.* **65**, 234-236.

Hirsch L. M. and Shankland T. J. (1993) Quantitative olivine-defect chemical model: Insights on electrical conduction, diffusion, and the role of Fe content. *Geophys. J. Int.* **114**, 21-35.

Hirschmann M. M. and Stolper E. M. (1996) A possible role for garnet pyroxenite in the origin of the "garnet signature" in MORB. *Contrib. Mineral. Petrol.* **124**, 185-208.

Hofmann A. W. (1980) Diffusion in natural silicate melts: a critical review. In Hargraves R. B., ed.. *Physics of Magmatic Processes*, Princeton Univ. Press, Princeton.

Hofmann A. W. (1997) Mantle geochemistry: The message from oceanic volcanism. *Nature* **385**, 219-229.

Hofmann A. W. and Hart S. R. (1978) An assessment of local and regional isotopic equilibrium in the mantle. *Earth Planet. Sci. Lett.* **38**, 44-62.

Huebner J. S. (1971) Buffering techniques for hydrostatic systems at elevated pressures. In Ulmer, G. C., ed., *Research Techniques for High Pressure and High Temperature*. Springer-Verlag, New York.

Jaoul O. and Raterron P. (1994) High-temperature deformation of diopside crystal 3. Influences of pO_2 and SiO_2 precipitation. *J. Geophys. Res.* **99**, 9423-9439.

Keyes, R. W. (1963) Continuum models of the effect of pressure on activated processes. In Paul W. and Warschauer D. M., eds., *Solids Under Pressure*, McGraw-Hill, New York.

Koga K. T., Shimizu N. and Grove T. L. (1999) Disequilibrium trace element redistribution during garnet to spinel facies transition. In Gurney J. J., Gurney J. L., Pascoe M. D., and Richardson S. H., eds., Proceedings of the 7th International Kimberlite Conference, v. 1, p. 444-451.

Kröger, F. A. (1974) *The Chemistry of Imperfect Crystals, 2nd ed.* North-Holland, New York.

LaTourrette T. and Wasserburg G. J. (1998) Mg diffusion in anorthite: implications for the formation of early solar system planetesimals. *Earth Planet. Sci. Lett.* **158**, 91-108.

Mullen J. G. (1966) Theory of diffusion in ionic crystals. *Phys. Rev.* **143**, 658-662.

Ryerson F. J. and McKeegan K. D. (1994) Determination of oxygen self-diffusion in akermanite, anorthite, diopside, and spinel: Implications for oxygen isotopic anomalies and the thermal histories of Ca-Al-rich inclusions. *Geochim. Cosmochim. Acta* **58**, 3713-3734.

Sammis C. G., Smith J. C. and Schubert G. (1981) A critical assessment of estimation methods for activation volume. *J. Geophys. Res.* **86**, 10707-10718.

Sautter V., Jaoul O. and Abel F. (1988) Aluminum diffusion in diopside using the $^{27}Al(p,\gamma)^{28}Si$ nuclear reaction: preliminary results. *Earth Planet. Sci. Lett.* **89**, 109-114.

Shannon R. D. (1976) Revised effective ionic radii and systematic studies of interatomic distances in halides and chalcogenides. *Acta Crystall.* **A32**, 751-767.

Shimizu N. (1981) Trace element incorporation into growing augite phenocryst. *Nature* **289**, 575-577.

Smyth J. R. and Bish D. L. (1988) *Crystal Structures and Cation Sites of the Rock Forming Minerals.* Allen & Unwin, Boston.

Sneeringer M. A. (1981) Strontium and samarium diffusion in diopside. Ph.D. Thesis, MIT.

Sneeringer M., Hart S. R. and Shimizu N. (1984) Strontium and samarium diffusion in diopside. *Geochim. Cosmochim. Acta* **48**, 1589-1608.

Van Orman J. A., Grove T. L. and Shimizu N. (1998) Uranium and thorium diffusion in diopside. *Earth Planet. Sci. Lett.* **160**, 505-519.

Watson E. B. (1996) Surface enrichment and trace-element uptake during crystal growth. *Geochim. Cosmochim. Acta* **60**, 5013-5020.

Watson E. B. and Liang Y. (1995) A simple model for sector zoning in slowly grown crystals: Implications for growth rate and lattice diffusion, with emphasis on accessory minerals in crustal rocks. *Amer. Mineral.* **80**, 1179-1187.

Wuensch B. J. (1982) Diffusion in stoichiometric close-packed oxides. In Beniere F. and Catlow C. R. A., eds., *Mass Transport in Oxides*, NATO-ASI series.

Zener C. (1952) Theory of diffusion. In Shockley W., Hollomon J. H., Maurer R., and Seitz F., eds., *Imperfections in Nearly Perfect Crystals*, 289-314, Wiley, New York.

Zindler A. and Hart S. R. (1986) Chemical geodynamics. *Ann. Rev. Earth Planet. Sci.* **14**, 493-571.

Table 1. Kunlun Mts. diopside composition.

Oxide	Weight %[a]
SiO_2	55.75 (0.34)
TiO_2	0.04 (0.01)
Al_2O_3	0.88 (0.17)
Cr_2O_3	0.02 (0.01)
FeO*	0.70 (0.07)
MnO	0.05 (0.02)
MgO	17.73 (0.36)
CaO	24.53 (0.29)
Na_2O	0.48 (0.09)
Tot	100.2 (0.6)

a. Average of 15 electron microprobe analyses of three different crystals. Numbers in parentheses represent one standard deviation.

Table 2. Summary of 1 atm run conditions and diffusion data for Ce and Yb.

Run #	T (°C)	Anneal time (hrs)	logf_{O2} (bars)	Diffusion Coefficients (x10^{21} m^2/s) Ce	Yb
CeYb6	1300	23.2	-7.8	31.9 ± 11.5	537 ± 96
CeYb9	1275	76.9	-7.7	25.0 ± 10.1	465 ± 86
CeYb3	1250	74.7	-7.9	11.5 ± 2.8	143 ± 37
CeYb2	1250	190.8	-7.9	6.83 ± 1.35	142 ± 60
CeYb7	1225	183.3	-8.5	5.83 ± 2.26	130 ± 27
CeYb8	1200	455.6	-8.6	2.53 ± 0.47	43.7 ± 8.6
CeYb10	1200	235.0	-8.6	4.45 ± 0.92	54.7 ± 11.3
CeYb4	1200	191.4	-8.4	4.01 ± 1.42	49.8 ± 17.7
Ce1	1200	118.9	-8.4	4.53 ± 2.10	
Yb1	1200	145.6	-4.5		158 ± 34
CeYb12	1175	170.3	-8.4		27.0 ± 8.8
Ce3	1150	577.8	-9.1	0.68 ± 0.12	
CeYb1	1150	455.6	-9.2	0.62 ± 0.36	24.2 ± 9.1
CeYb11	1125	477.8	-9.7		13.7 ± 2.6
CeYb5	1100	425.0	-9.8		4.62 ± 1.6
CeYb15	1050	794.4	-10.5		1.41 ± 0.20

Table 3. Summary of 1 atm run conditions and diffusion data for La, Nd and Dy.

Run #	T (°C)	Anneal time (hrs)	$\log f_{O_2}$ (bars)	Diffusion Coefficients ($x10^{21}$ m^2/s) La	Nd	Dy
LaNdDy4	1300	25.1	-7.3	21.5 ± 7.6	38.1 ± 13.0	190 ± 65
LaNdDy2	1275	76.9	-7.7	10.0 ± 4.0	22.5 ± 9.2	170 ± 69
LaNdDy10	1250	95.5	-7.9	4.46 ± 3.10	10.2 ± 7.1	97.2 ± 43.0
LaNdDy7	1250	42.5	-8.2			72.8 ± 49.2
LaNdDy1	1200	455.6	-8.6	1.82 ± 0.62	2.95 ± 1.00	17.9 ± 6.1
LaNdDy3	1200	235.0	-8.6			24.8 ± 9.5
LaNdDy6	1175	170.3	-8.4			12.4 ± 6.0
LaNdDy9	1100	882.2	-9.8			1.30 ± 0.76

Diffusion coefficients were obtained by fitting the diffusion profiles to Eqn. (1) by non-linear least squares regression.

Table 4. Summary of high pressure run conditions and diffusion data for Ce and Yb.

Run #	Capsule	T (°C)	P (GPa)	duration (hr)	D_{Ce} (x 10^{21} m^2/s)	D_{Yb} (x 10^{21} m^2/s)
B588	graphite	1450	1.8	25.1	183 ± 136	3100 ± 1570
B584	graphite	1350	1.3	20.2		665 ± 224
C163	graphite	1350	1.5	70.0	33 ± 19	322 ± 176
C177	graphite	1350	2.5	72.2		202 ± 73
C207	graphite	1300	1.5	67.2		166 ± 89
B596	graphite	1250	1.8	75.8		60 ± 34
B475	Pt	1450	1.8	68.1	66 ± 29	781 ± 355
B474	Pt	1350	1.8	68.1	10 ± 7	71 ± 34
B553	AuPd	1350	1.8	42.2		73 ± 23

Table 5. Arrhenius parameters ($D = D_0 e^{-E/RT}$) for diffusion at 1 atm along the QFM buffer. Uncertainties (1 σ) were determined from the linear regression.

Element	$\log_{10} D_0$ (m^2/s)	E (kJ/mol)
Yb	-4.64 ± 0.42	411 ± 12
Dy	-3.31 ± 1.44	461 ± 41
Nd	-2.95 ± 2.64	496 ± 77
Ce	-4.10 ± 1.08	463 ± 31
La	-4.22 ± 2.66	466 ± 78

Table 6. Arrhenius parameters ($D = D_0 e^{-(E+PV)/RT}$) for pressures of 0.1 MPa to 2.5 GPa and temperatures of 1050-1450 °C. Uncertainties (1 σ) were determined from the linear regression.

Element	$\log_{10} D_0$ (m^2/s)	E (kJ/mol)	V (cm^3/mol)
Yb	-4.63 ± 0.39	411 ± 11	9.5 ± 2.0
Ce	-4.12 ± 0.94	463 ± 27	10.2 ± 3.2

Table 7. Parameters in Mullen/Zener model.

	r_{site} (nm)	[6] r_0 (nm)	$\partial(\mu/\mu_o)/\partial T$ (x10^4 K^{-1})	[9] E_m° (kJ/mol)	[10] $\ln D^{\delta=0}$	[10] b	[11] b^*
[1]Diopside, 3+	[4]0.105	0.250	[7]-1.3	330	-45.78	8.1	22
[2]Zircon, 3+	[5]0.084	0.220	[8]-0.89	670	-37.25	25	48
[3]Anorthite, 2+	[4]0.120	0.253	--	250	-41.48	2.1	--

1. This study.
2. Cherniak et al. (1997a).
3. LaTourrette and Wasserburg (1998).
4. Ideal cation site radius (Blundy and Wood, 1994).
5. Ideal site radius calculated as the mean cation-oxygen bond distance (r_0) minus the ionic radius of O^{2-} (0.138 nm).
6. Values from Smyth and Bish (1988).
7. Anderson (1989) p. 105. Average of temperature derivatives of shear modulus and bulk modulus.
8. Bass (1995). Average of temperature derivatives of shear modulus and bulk modulus.
9. Migration enthalpy at $\delta = 0$ (estimated from measured activation enthalpies).
10. Determined from least squares fit to Eq. 7 of diffusion coefficients at 1200 °C.
11. Calculated from Eq. (8).

FIGURE CAPTIONS

Figure 1. Typical diffusion profiles (Experiment LaNdDy2—1275 °C, 0.1 MPa, 76.9 hr). a) Plot of $\text{erf}^{-1}[(C_0\text{-}C)/C_0]$ versus depth in nanometers. C represents [REE/^{30}Si] in counts per second, and C_0 is the interface concentration (adjusted in the fitting procedure so that the linear portion of each diffusion profile passes through the point (0,0)). Profiles for La, Nd and Dy overlap in the shallow region, but fall along distinct linear trends beyond a depth of ~90 nm. The shallow part of the profile is considered to reflect sampling of heterogeneously distributed REE oxide crystals remaining on the diopside surface after the experiment, and only the linear portion of the profile is fitted to obtain the diffusion coefficient. In b) the concentration data are plotted versus depth, along with fitted error function curves.

Figure 2. Time series showing diffusion coefficients for Yb, Dy and Ce versus run duration, for experiments run at 1 atm and 1200 °C. The diffusion coefficient for each element is independent of anneal time, a necessary condition for mass transport by volume diffusion.

Figure 3. Plot of $\log D_{Yb}$ versus oxygen fugacity at 1200 °C. Yb diffusivity increases with oxygen fugacity, suggesting that an impurity whose valence is sensitive to f_{O_2} (e.g. Fe) controls the point defects that are responsible for Yb diffusion in diopside.

Figure 4. Arrhenius plot showing diffusion coefficients versus T^{-1} for experiments run at 1 atm total pressure, with oxygen fugacity controlled along the QFM buffer. Open circles—Yb; filled circles—Dy; 'x'—Nd; open squares—Ce; '*' —La. Arrhenius parameters are given in Table 5.

Figure 5. SIMS depth profiles for Fe, Yb and Ce from a high pressure experiment performed in a Pt container (B474—1350 °C, 1.8 GPa). Fe is lost from the diopside to the Pt. Concentrations refer to element/^{30}Si intensity ratios.

Figure 6. Plot of Yb and Ce diffusion coefficients versus pressure, at 1350 °C. Data obtained at other temperatures have been corrected to 1350 °C using the temperature dependence for diffusion determined from multiple linear regression of the data (Table 6). Only data from 1 atm experiments and high pressure experiments performed in graphite capsules are shown; 1 atm data are shown as a single point representing the mean value of *D*.

Figure 7. Arrhenius plot comparing high- and low-pressure diffusion data for Yb and Ce. The high pressure data (filled circles) have been corrected to 1 atm pressure using the activation volumes determined from multiple linear regression of the data (Table 6).

Figure 8. Arrhenius plot comparing REE diffusion data from this study (at 1 atm) with Sm diffusion data for synthetic diopside. The 1 atm Sm diffusion data are from Sneeringer (1981) and the high pressure data are from Sneeringer et al. (1984).

Figure 9. Arrhenius plot of cation diffusion data in high-Ca clinopyroxene. References for the data are as follows: Sr (in both natural (n) and synthetic (s) diopside crystals) and Sm (synthetic)—Sneeringer et al., 1984; Pb—Cherniak, 1998; Ca—Dimanov and Jaoul, 1998; Ca-Mg interdiffusion—Brady and McCallister, 1983; O—Ryerson and McKeegan, 1994; Al—Sautter et al., 1988; U and Th—Van Orman et al., 1998; Si—Bejina and Jaoul, 1996; Yb, Dy and La—this study.

Figure 10. Plot of ln*D* versus the ionic size factor $\delta = (r_i - r_{site})/r_o$ for REE diffusion in diopside at 1200 °C and 0.1 MPa. r_i is the radius of the trivalent ion in eight-fold coordination

(Shannon, 1976), r_{site} is the ideal site radius (0.105 nm; Blundy and Wood, 1994), and r_o is the average cation-anion bond length (0.250 nm; Smyth and Bish, 1988). The curve is a least squares fit to Eq. 7 with $\ln D^{\delta=0}$ and b as the only adjustable parameters.

Figure 11. Comparison of 1 atm diffusion data for the rare earth elements in diopside with Arrhenius curves obtained from the Mullen/Zener elastic diffusion model.

Figure 12. Plot of $\ln D_{1473K}$ versus δ for alkaline earth elements in anorthite (LaTourrette and Wasserburg, 1998), REE in zircon (Cherniak et al., 1997a), and REE in diopside (this study). Curves are least squares fits to Eq. 7; parameters obtained from the fits are given in Table 6.

Figure 13. Plot of $\ln D_{1473K}^{\delta=0}$ versus ionic charge for cations that partition onto the eight-fold site in diopside and zircon. Diffusion coefficients are corrected to $\delta = 0$ using Eq. 10. The two lines on the plot are not fits to the data, but instead show the trends expected from Eq. 10, given the values of $\ln D_{z=3}^{\delta=0}$ and b determined from fits of the REE data to Eq. 7 (see Table 6). Open circles—diopside; filled circles—zircon. References for zircon diffusion data: REE—Cherniak et al., 1997a; U, Th and Hf —Cherniak et al., 1997b. References for diopside diffusion data: U, Th—Van Orman et al., 1998; REE—this study; Pb—Cherniak, 1998; Sr—Sneeringer et al., 1984; Ca—Dimanov and Jaoul, 1998.

Figure 1a

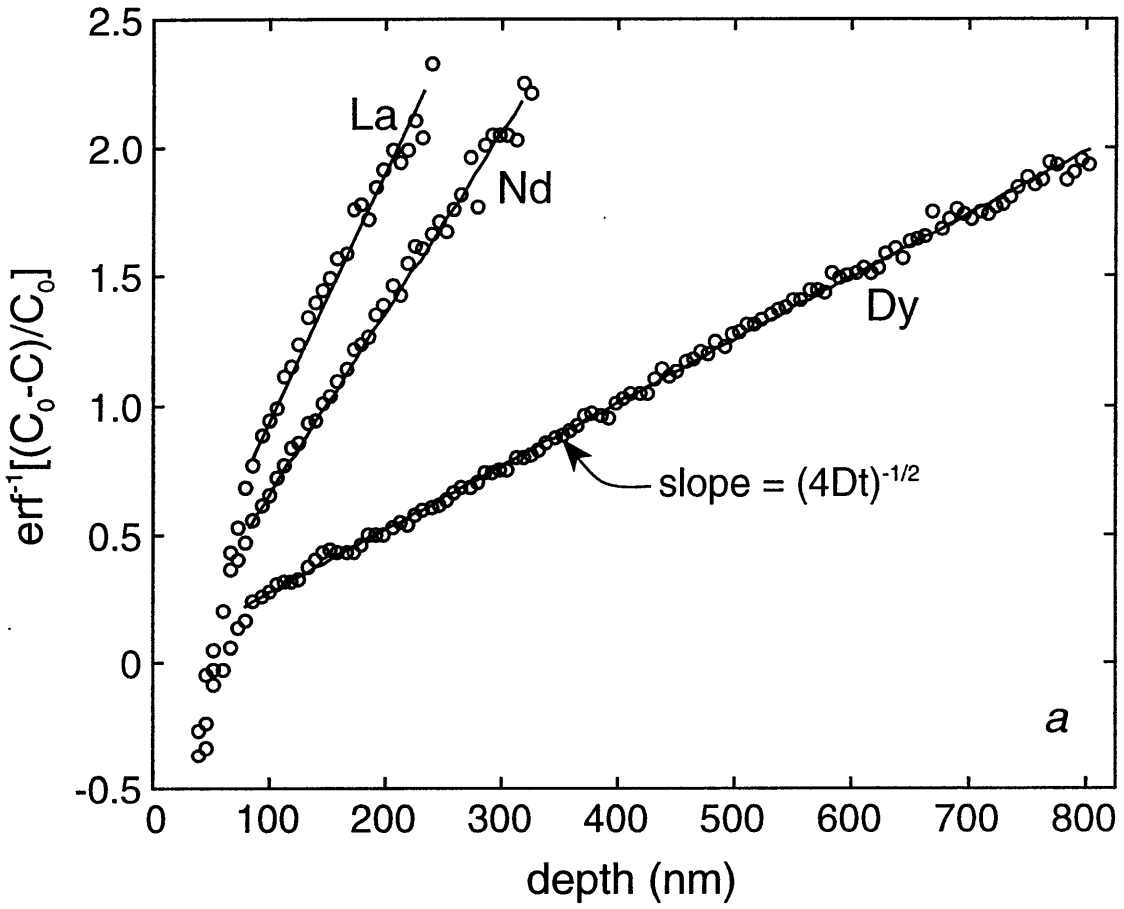
2.5
2.0
1.5
1.0
0.5
0
-0.5
0
100
200
300
400
500
600
700
800
depth (nm)
erf^{-1}[(C$_0$-C)/C$_0$]
La
Nd
Dy
slope = (4Dt)$^{-1/2}$
a

Figure 1b

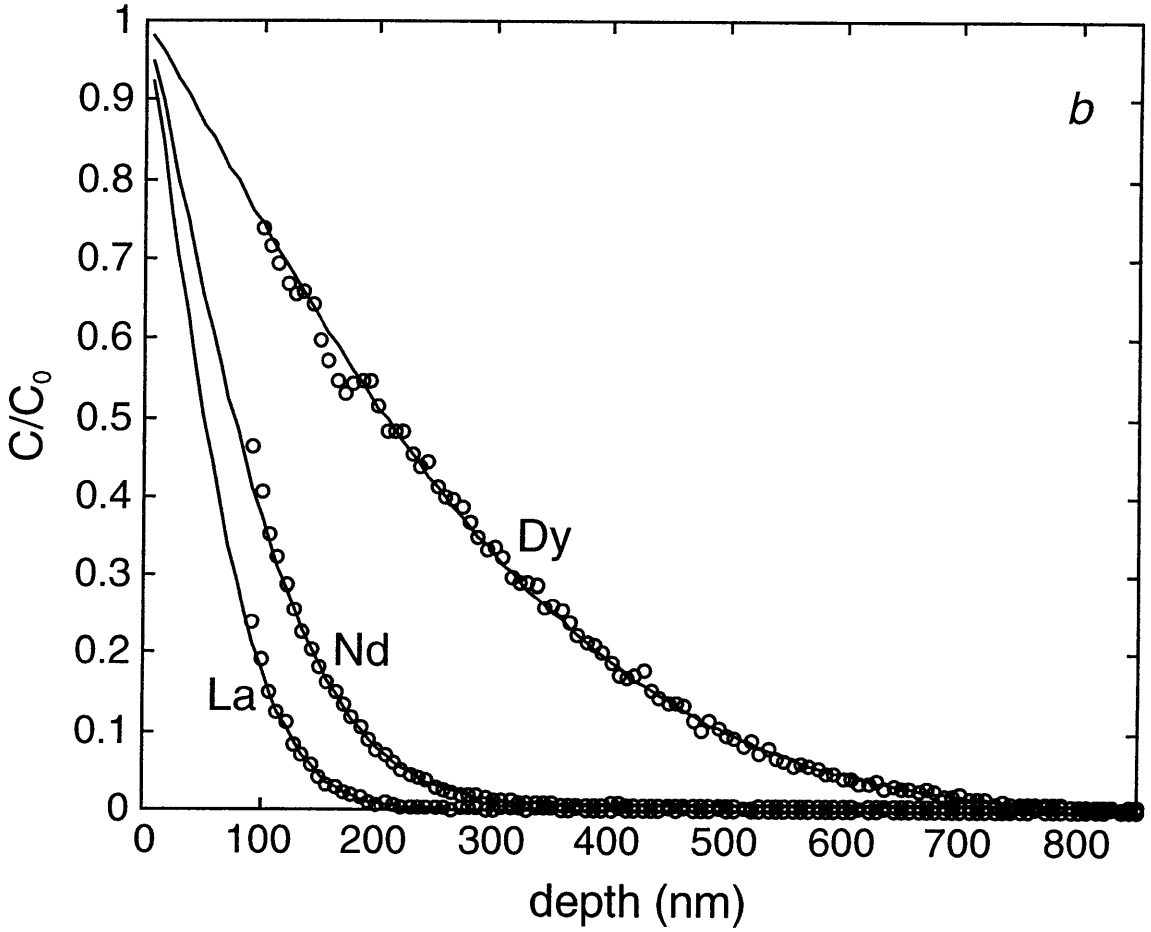
1
0.9
0.8
0.7
0.6
0.5
0.4
0.3
0.2
0.1
0
C/C0
b
Dy
Nd
La
0
100
200
300
400
500
600
700
800
depth (nm)

Figure 2

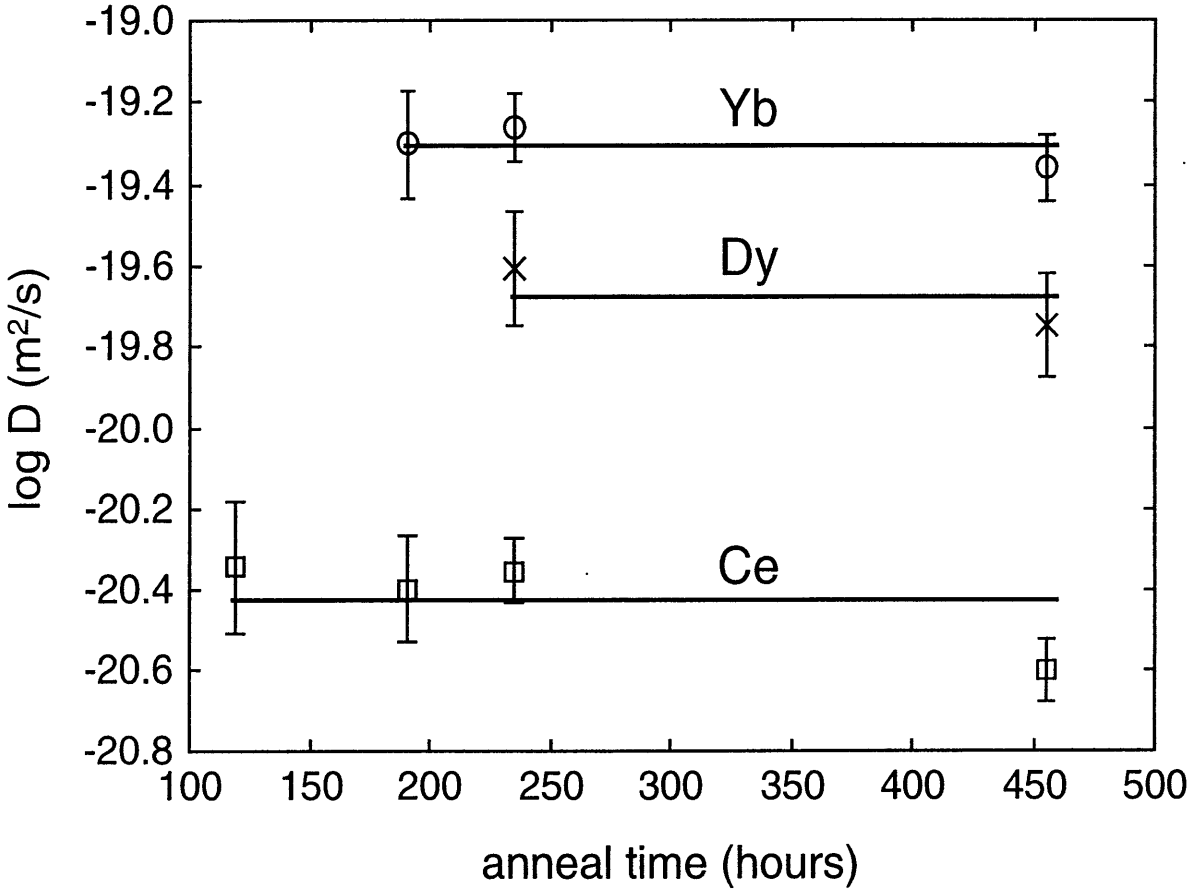
-19.0
-19.2
-19.4
-19.6
-19.8
-20.0
-20.2
-20.4
-20.6
-20.8
log D (m²/s)
Yb
Dy
Ce
100
150
200
250
300
350
400
450
500
anneal time (hours)

Figure 3

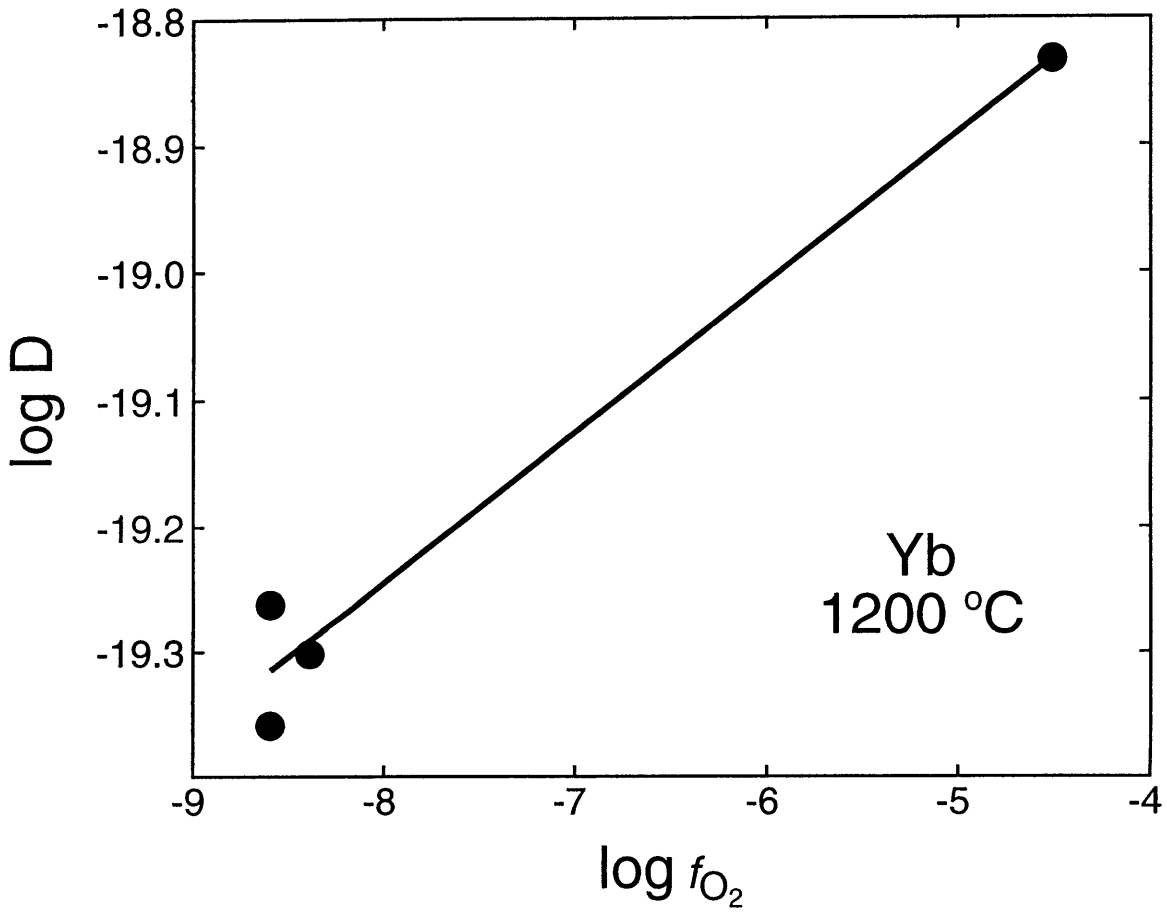

Figure 4

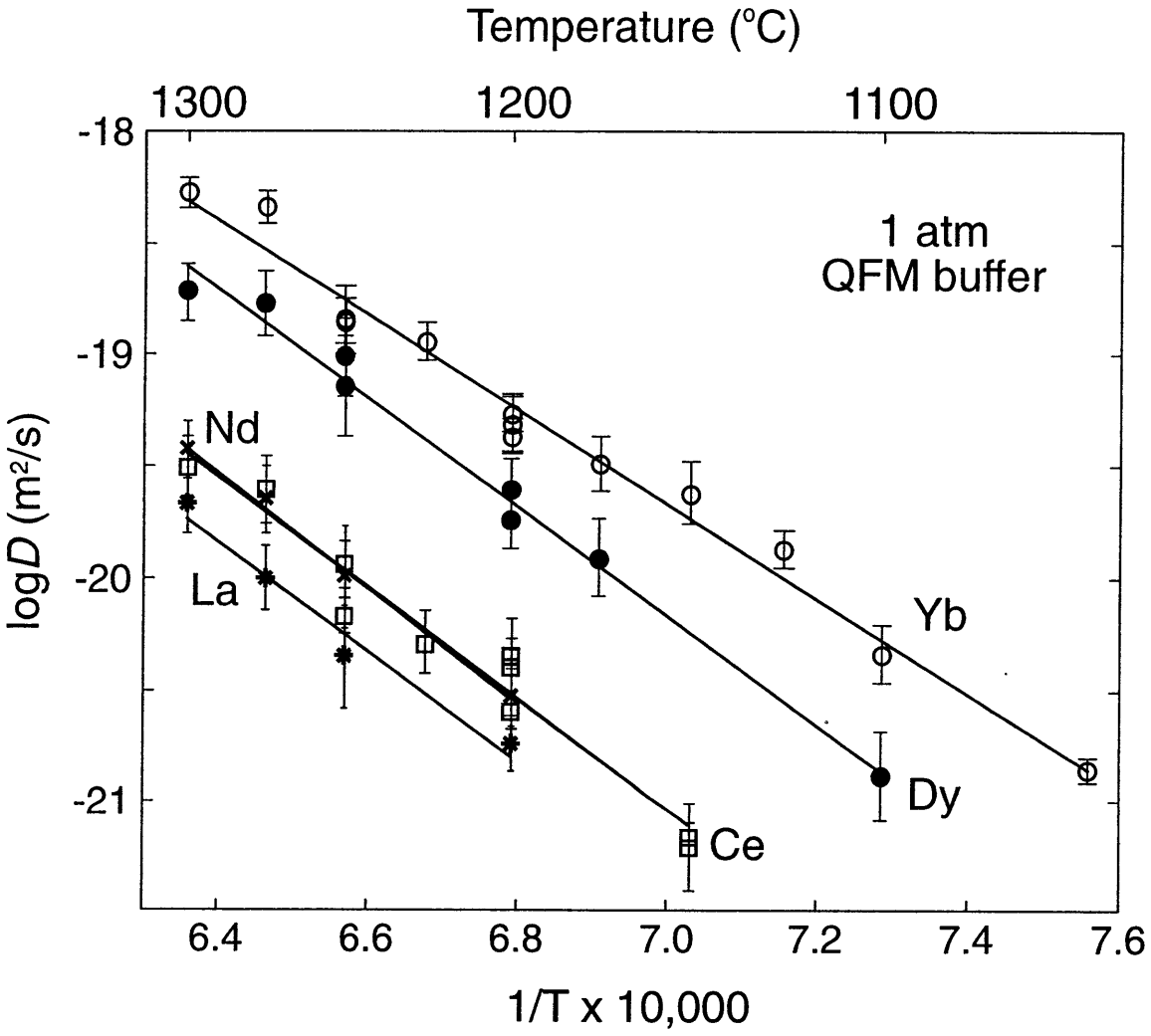
Temperature (°C)
1300
1200
1100
-18
-19
-20
-21
log$D$ (m²/s)
1 atm
QFM buffer
Nd
La
Yb
Dy
Ce
6.4
6.6
6.8
7.0
7.2
7.4
7.6
1/T x 10,000

Figure 5

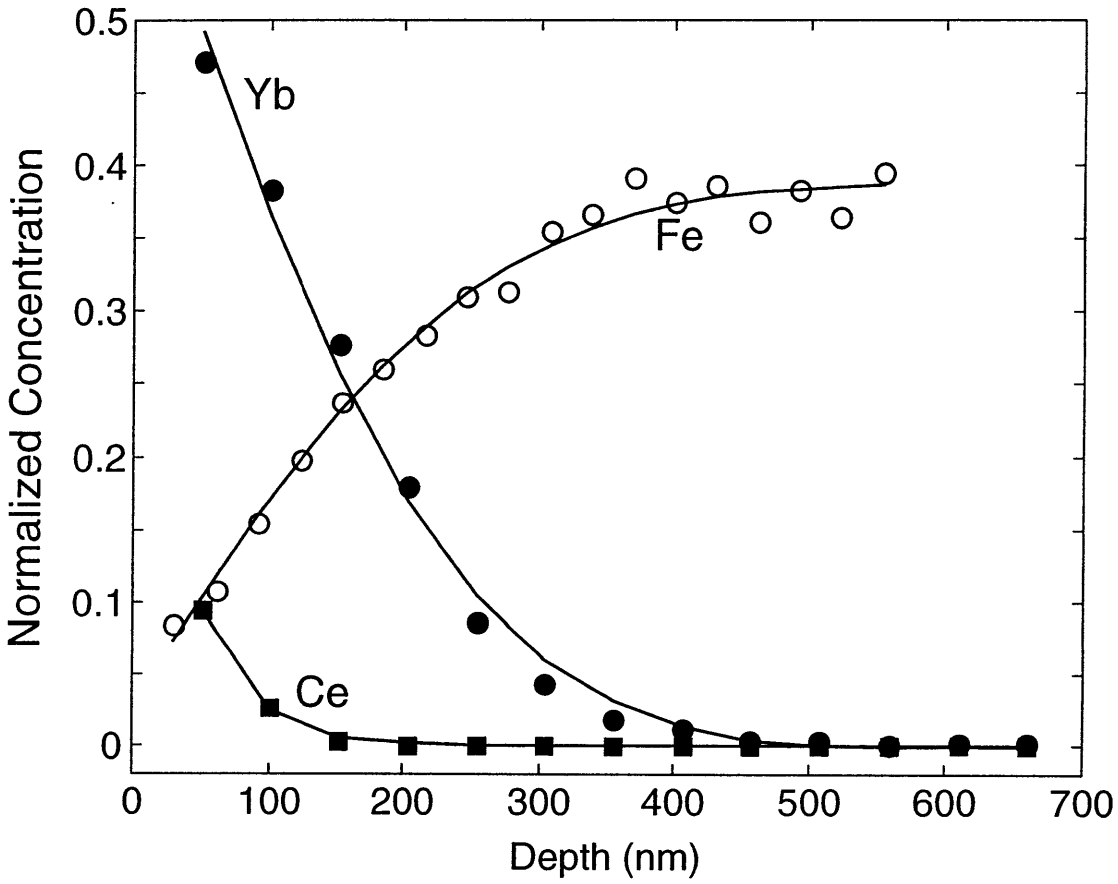
0.5
0.4
0.3
0.2
0.1
0
Normalized Concentration
Yb
Fe
Ce
0
100
200
300
400
500
600
700
Depth (nm)

Figure 6

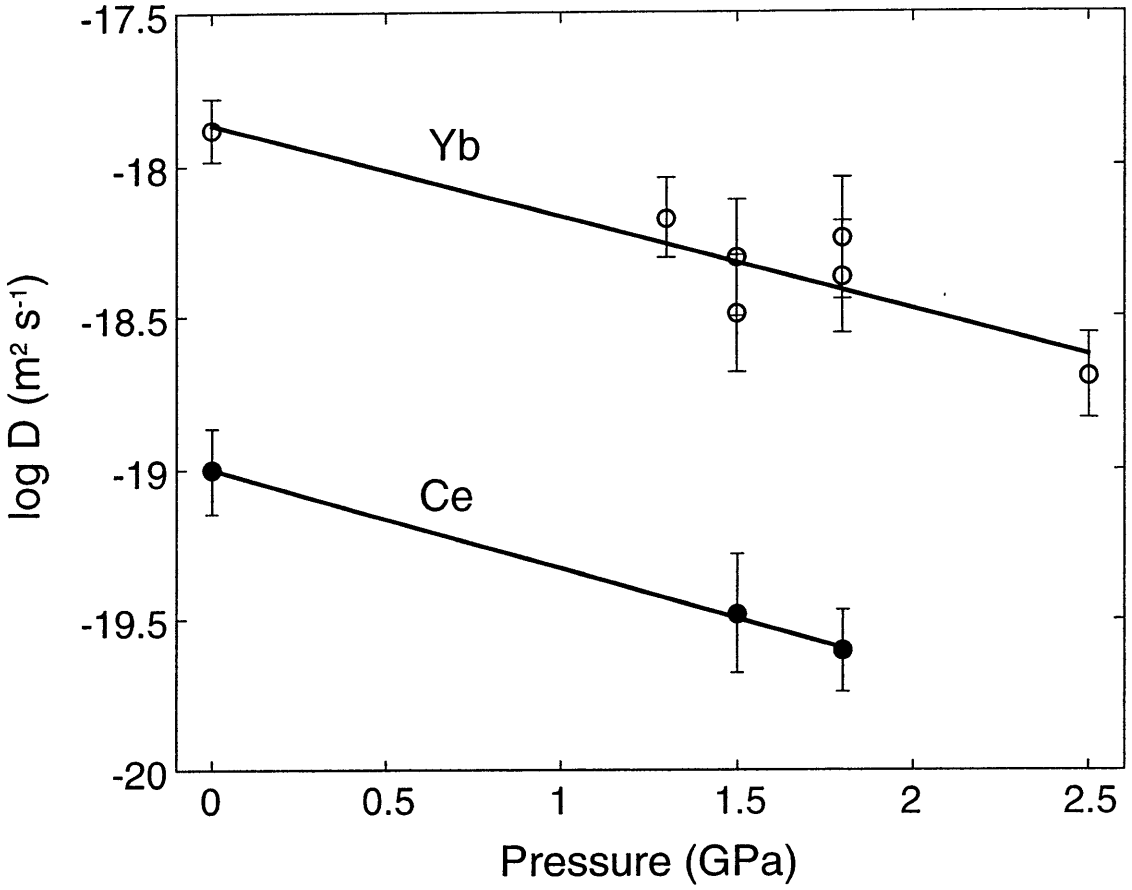

Figure 7

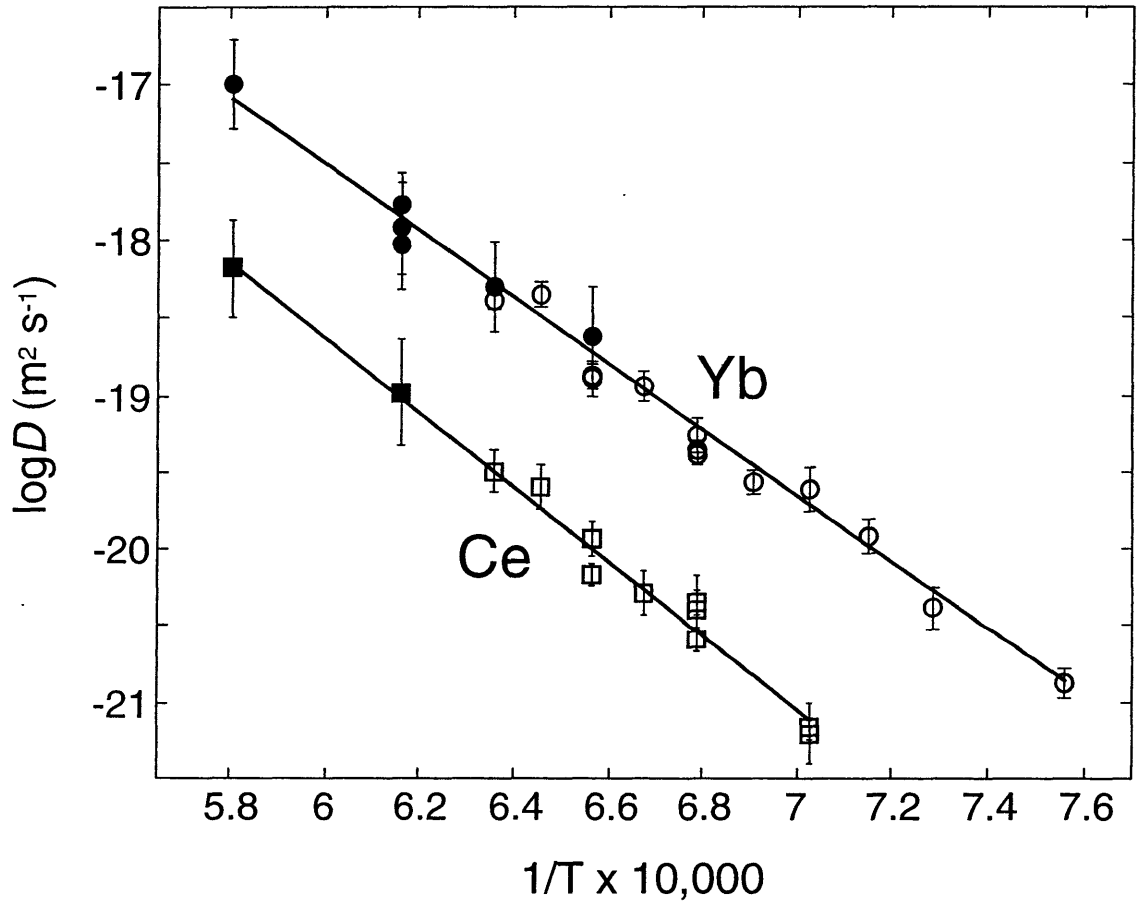

Figure 8

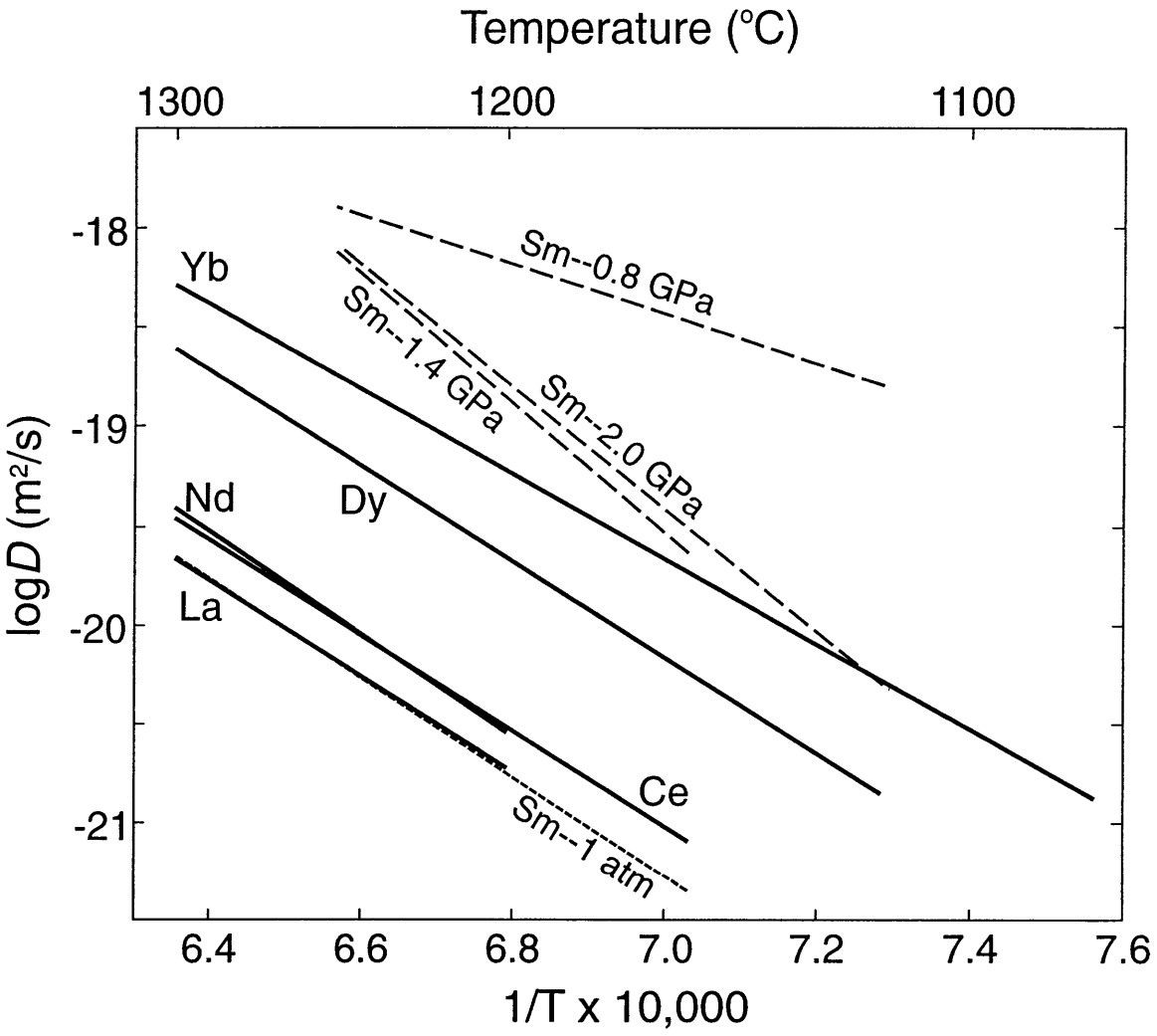
Temperature (°C)
1300
1200
1100
-18
-19
-20
-21
log D (m²/s)
Yb
Nd
Dy
La
Ce
Sm--0.8 GPa
Sm--1.4 GPa
Sm--2.0 GPa
Sm--1 atm
6.4
6.6
6.8
7.0
7.2
7.4
7.6
1/T x 10,000

Figure 9

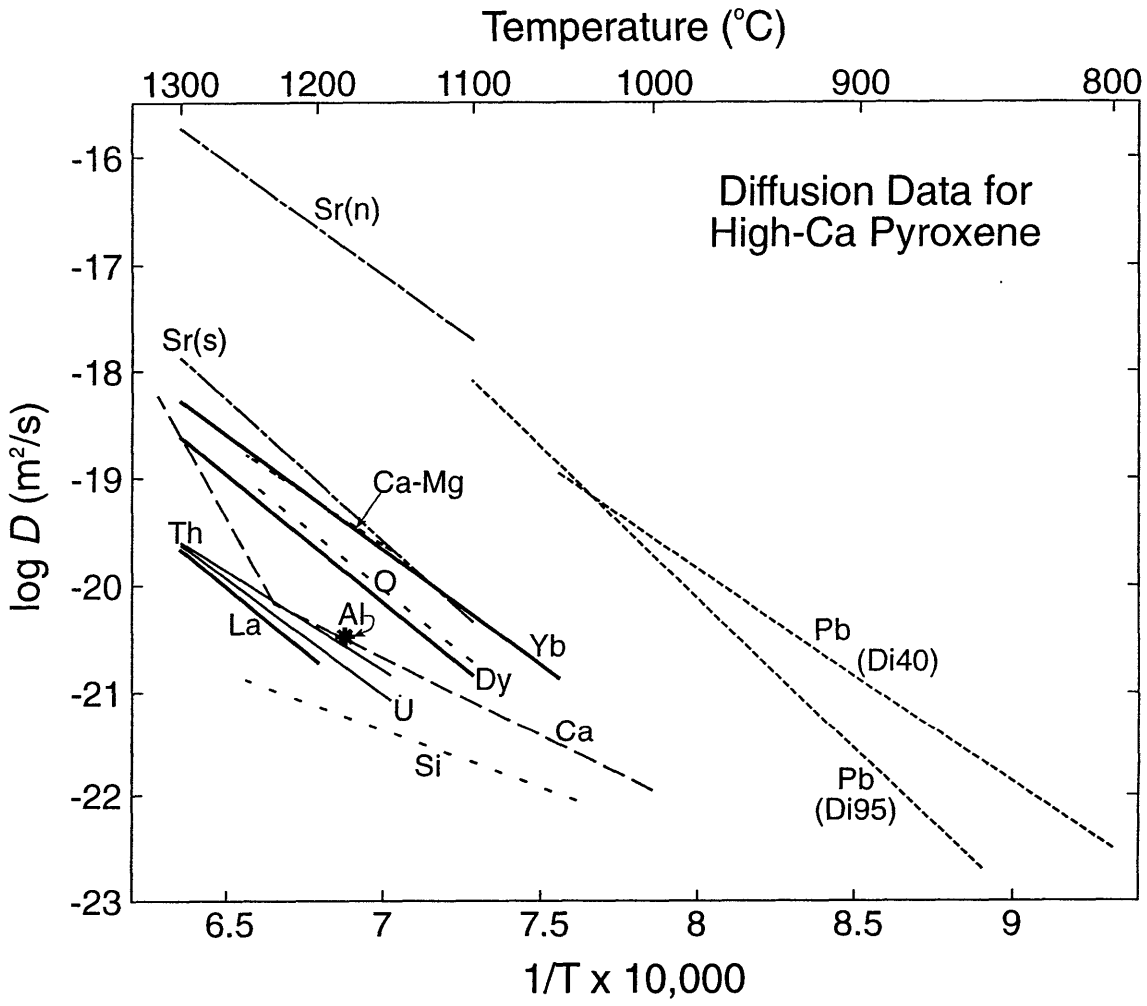
Temperature (°C)
1300
1200
1100
1000
900
800
Diffusion Data for
High-Ca Pyroxene
Sr(n)
Sr(s)
Ca-Mg
Th
O
Al
La
Yb
Dy
U
Ca
Si
Pb
(Di40)
Pb
(Di95)
log D (m²/s)
-16
-17
-18
-19
-20
-21
-22
-23
6.5
7
7.5
8
8.5
9
1/T x 10,000

Figure 10

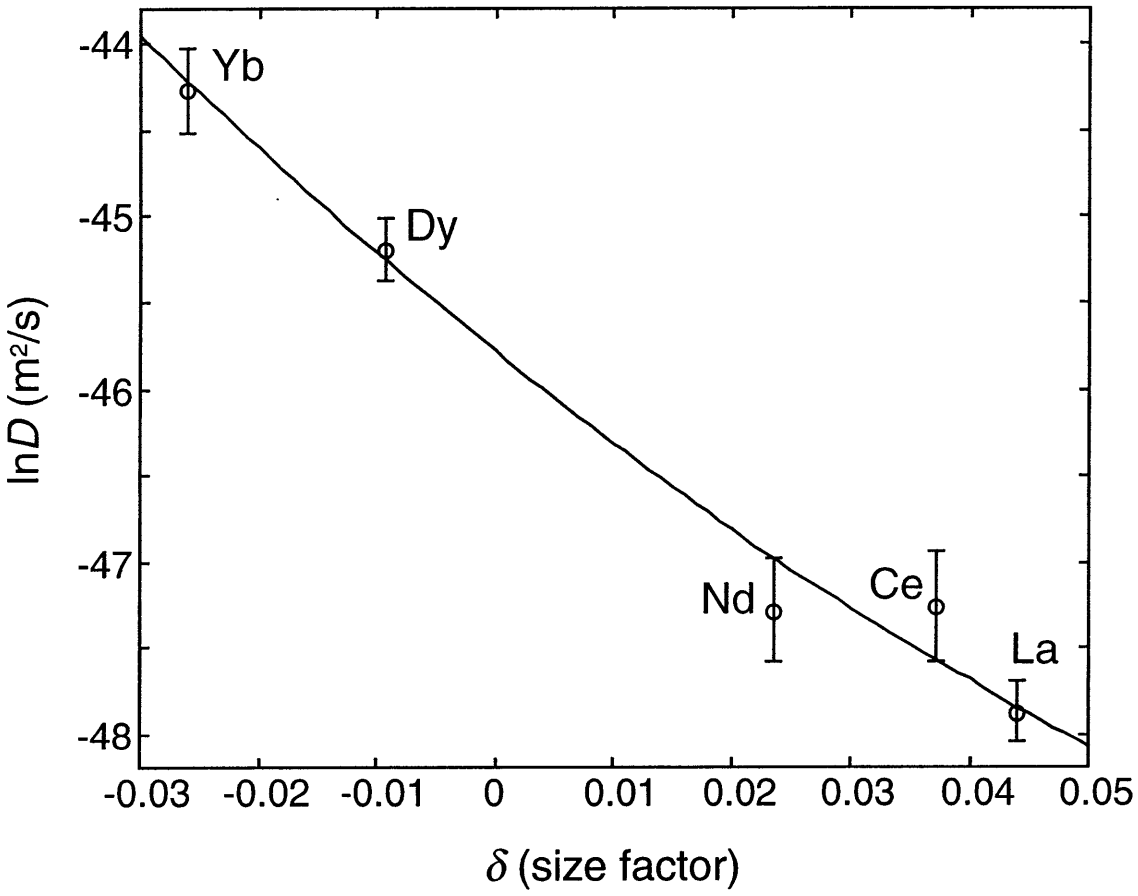
-44
-45
-46
-47
-48
ln$D$ (m^2/s)
Yb
Dy
Nd
Ce
La
-0.03
-0.02
-0.01
0
0.01
0.02
0.03
0.04
0.05
δ (size factor)

Figure 11

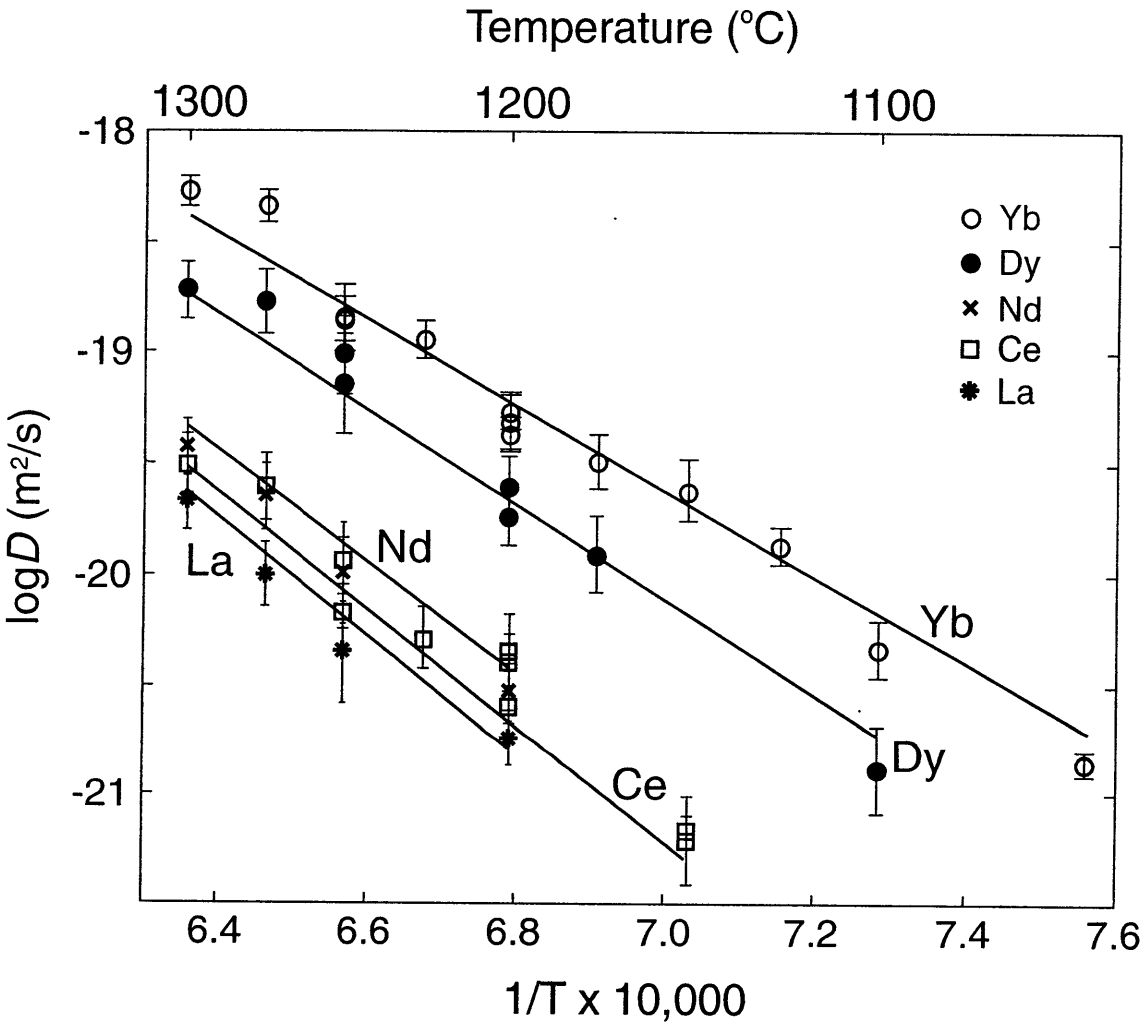
Temperature (°C)
1300
1200
1100
-18
-19
-20
-21
log D (m²/s)
Yb
Dy
Nd
Ce
La
La
Nd
Yb
Dy
Ce
6.4
6.6
6.8
7.0
7.2
7.4
7.6
1/T x 10,000

Figure 12

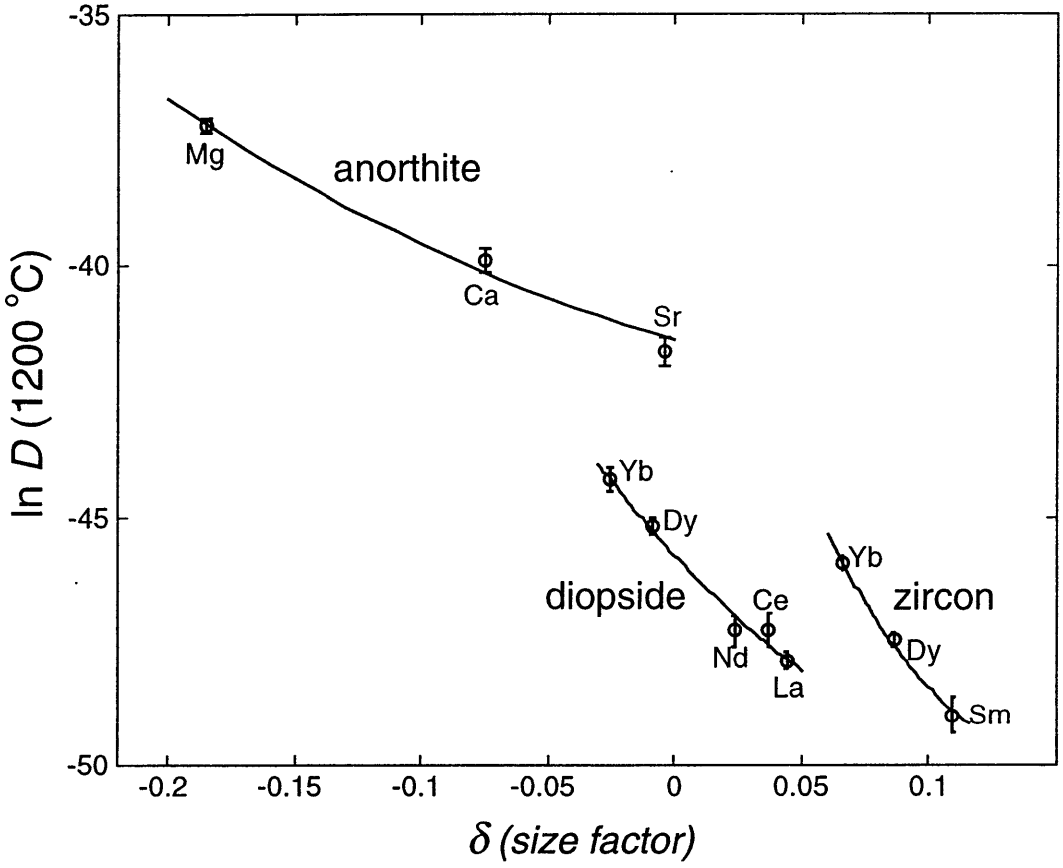
-35
-40
-45
-50
ln D (1200 °C)
-0.2
-0.15
-0.1
-0.05
0
0.05
0.1
δ (size factor)
Mg
anorthite
Ca
Sr
Yb
Dy
diopside
Ce
Nd
La
Yb
zircon
Dy
Sm

Figure 13

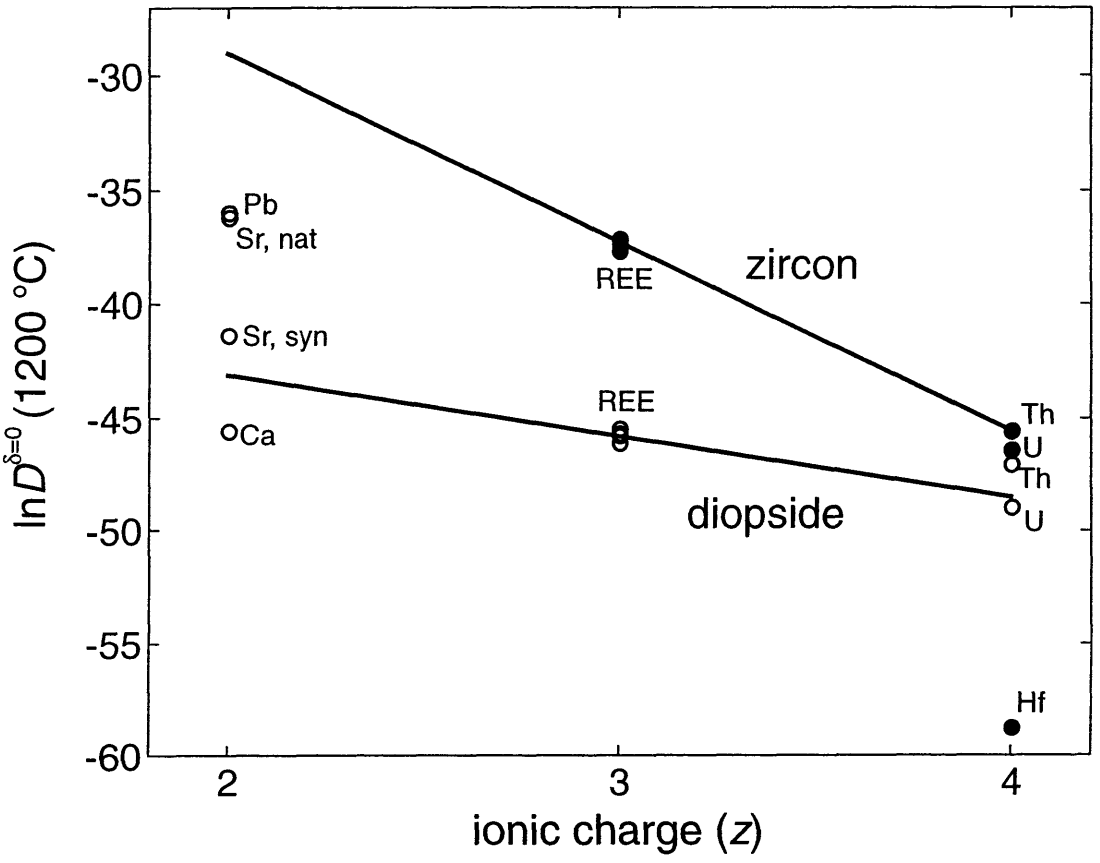
-30
-35
-40
-45
-50
-55
-60
2
3
4
ionic charge (z)
lnD^δ=0 (1200 °C)
Pb
Sr, nat
Sr, syn
Ca
REE
REE
zircon
diopside
Th
U
Th
U
Hf

CHAPTER 2.

RARE EARTH ELEMENT DIFFUSION IN A NATURAL PYROPE SINGLE CRYSTAL AT 2.8 GPA

ABSTRACT

Volume diffusion rates of Sm, Dy and Yb have been measured in a natural pyrope single crystal ($Py_{71}Alm_{16}Gr_{13}$) at 2.8 GPa and 1200-1450 °C. Pieces of a single gem-quality pyrope megacryst were polished, coated with a thin layer of REE oxide, then annealed in a piston cylinder device for times between 2.6 and 90 hours. Diffusion profiles in the annealed samples were measured by SIMS depth profiling. The dependence of diffusion on temperature can be described by the following Arrhenius equations (diffusion coefficients in m^2/s):

$$\log_{10} D_{Sm} = (-9.05 \pm 0.97) - \left(304 \pm 30\ kJ\ mol^{-1}/2.303RT\right)$$
$$\log_{10} D_{Dy} = (-9.09 \pm 0.97) - \left(300 \pm 30\ kJ\ mol^{-1}/2.303RT\right)$$
$$\log_{10} D_{Yb} = (-7.74 \pm 0.97) - \left(343 \pm 30\ kJ\ mol^{-1}/2.303RT\right)$$

Diffusion coefficients for Sm, Dy and Yb are indistinguishable within the measurement uncertainty; there is no significant influence of ionic radius on diffusion rates in garnet. At temperatures near the solidus of garnet lherzolite (~1450 °C at 2.8 GPa), REE diffusion rates in pyrope are similar to Yb and Dy in diopside, and an order of magnitude faster than Nd, Ce and La in diopside. At lower temperatures relevant to metamorphism in the crust, REE diffusion rates in garnet are several orders of magnitude faster than in diopside. Closure temperatures for the REE are calculated to be between 765 and 920 °C for pyrope spheres 1 mm in diameter cooling at 1 to 100 °C My^{-1}; in diopside the closure temperature for Nd is about 200 °C higher.

INTRODUCTION

Pyrope-rich garnet is the stable aluminous phase in peridotite at depths below ~75 km. Melting commonly begins at depths where garnet is stable (Shimizu and Arculus, 1975; Frey et al., 1978; Salters and Hart, 1989; Beattie, 1993; LaTourrette et al., 1993), and in this regime garnet exerts an important control on the distribution of rare earth elements between solid and melt. This chapter presents experimental data on the diffusion rates of REE in a natural pyrope single crystal under pressure and temperature conditions relevant to melting beneath ocean spreading centers (2.8 GPa and 1200-1450 °C). The implications of the data for diffusion-controlled fractionation of the REE during melting within the garnet stability field are discussed in Chapter 3.

Garnet is also an important phase in many crustal rocks, and zoning within metamorphic garnets often preserves a record of the temperatures, pressures, and fluid interactions experienced by the host rock over its history. Information on the timescales of the processes recorded by zoned garnet crystals can be obtained provided that diffusion rates are known for the appropriate *P*, *T* conditions. The Sm/Nd isotopic system in garnet is often used for radiometric dating and the data presented here can be used to predict closure temperatures for this system.

EXPERIMENTAL METHODS

One section of a single pyrope megacryst was used for the diffusion experiments. The sample was taken from an ultramafic diatreme of the Colorado Plateau, and contained no visible cracks or inclusions. Another piece cut from the same crystal was used by Wang et al. (1996) in a study of hydrogen diffusion in pyrope, and the major and minor element composition of the crystal is given in that paper (their sample Py-6). The initial content of H_2O was 102 ± 10 ppm (Wang et al., 1996; FTIR measurement); no attempt was made to measure the hydrogen content after the REE diffusion anneals. The pyrope crystal was ground flat, in a random

orientation, and polished to 0.06 μm alumina, then rinsed ultrasonically in a purified water bath. No further surface preparation was undertaken, and the sample was not pre-annealed because pyrope is unstable at atmospheric pressure.

A dilute nitric acid solution containing Ce, Sm, Dy and Yb in equimolar proportions, with a total concentration of 750 ppm REE, was dropped onto the polished surface and then denitrified by heating at 800 °C for a few minutes. A thin layer of microcrystalline oxide particles remained on the surface, and this provided the tracer source for the diffusion experiments. After deposition of the tracer layer, a diamond wafering saw was used to cut the pyrope sample into ~12 pieces, each roughly cubical with an edge length of about one millimeter.

The diffusion anneals were performed in 0.5 inch solid-medium piston-cylinder devices (Boyd and England, 1960) using techniques similar to those reported in Chapter 1. A coated pyrope cube was loaded with graphite powder into a 0.175" platinum outer capsule, taking care to position the coated surface in the center of the capsule. Four experiments were run with the pyrope cube in direct contact with the graphite powder. In two other experiments, the coated surface of the pyrope was placed against a polished disk of vitreous carbon (Alfa Aesar type II), and the pyrope/vitreous-carbon pair was separated from the graphite powder with two pieces of platinum foil. Each sample assembly was dried for one to two days at 120 °C, then the Pt outer capsule was welded shut, gently pounded flat, and placed within a high density alumina sleeve. The sample was centered within a graphite furnace using MgO spacers and then inserted into a $BaCO_3$ sleeve that served as the pressure medium. Each run was pressed cold to 0.7 GPa, then heated to 865 °C at 50 °C /minute. After a 6 minute dwell, the sample was compressed to 2.8 GPa while heating to the final run temperature at a rate of 100 °C/minute. Runs were held at constant temperature and pressure for times between 2.6 and 90 hours, then quenched by shutting off the power. After quenching, the pyrope cube was carefully extracted from the Pt capsule by scraping away the graphite. Pyrope cubes that were run in direct contact with graphite powder could generally be extracted as whole pieces, while samples that were in contact

with the vitreous carbon disk parted along planes parallel to the pyrope/carbon interface. In every case the coated surface of the pyrope crystal was preserved intact.

Pyrope crystals that were annealed in graphite bore the imprint of the polycrystalline graphite confining medium on their coated surfaces. The surface was visibly roughened, and Dektak profilometer scans showed that the mean surface roughness had increased from 5-10 nm in unannealed samples to 30-50 nm after the anneal. Samples that were annealed in contact with the vitreous carbon disk maintained a mirror finish on their coated surfaces after the experiment, and the surface roughness did not increase significantly.

The samples were mounted in epoxy with the tracer-coated surface exposed and covered with a thin (~20 nm) gold film in preparation for SIMS depth profiling analysis. Analyses were performed using the Cameca IMS 3f ion microprobe at the Woods Hole Oceanographic Institution, using the same general procedure discussed in Chapter 1. A 10 nA O^- primary beam was rastered over a square area 50 μm on a side, and sampling was restricted to a circle 8 μm in diameter through the use of a mechanical field aperture. ^{30}Si, ^{44}Ca, ^{140}Ce, ^{147}Sm or ^{152}Sm, ^{164}Dy and ^{174}Yb intensities were monitored, with the secondary voltage offset by –50V to reduce molecular interferences. The gold coat was removed after the analysis by ultrasonicating the sample in a potassium iodide solution, and the depths of the sputtered pits were measured using a Dektak 8000 diamond-tipped stylus profilometer.

Diffusion coefficients were determined by fitting the REE concentration profiles to an error function solution to the diffusion equation. In fitting the profiles, the pyrope crystal was considered to represent a semi-infinite medium, and the concentration at the interface between the pyrope and REE oxide layer was assumed to have been constant throughout the experiment. Representative diffusion profiles from a sample annealed in a graphite capsule at 1450 °C are shown in Fig. 1. The relative abundances of Yb, Dy and Sm in the annealed pyrope crystals are qualitatively consistent with experimental studies on the partitioning of rare earth elements into garnet (e.g. Hauri et al., 1994; van Westrenen et al., 1999).

Because of the low solubility of Ce in pyrope, ^{140}Ce intensities in the annealed samples were very low, and Ce diffusion profiles could not be detected reliably. ^{140}Ce counts were quite low even near the surface (Fig. 1), and in each sample fell to background levels within the first two cycles, corresponding to a depth of 100 nm or less. Diffusion coefficients for Ce could not be estimated from any of the experiments.

RESULTS

The results of the diffusion experiments are listed in Table 1. At each temperature the diffusion coefficients for Sm, Dy and Yb are indistinguishable from each other within the measurement uncertainty. This is in striking contrast to our results for rare earth element diffusion in diopside (Chapter 1), where diffusivities were found to differ by a factor of ~3 between Yb and Dy, and by a factor of ~35 between Yb and La.

Two experiments performed at 1400 °C for times 2.6 and 24 hours yielded similar diffusion coefficients (Fig. 2). The close agreement between these experiments indicates that the diffusion coefficients are independent of time, and suggests that transport of REE into the pyrope crystal was indeed accomplished by lattice diffusion. No difference in diffusivity was observed between experiments in which the sample was in contact with graphite powder and experiments that used a polished vitreous carbon disk (Table 1). The greater surface roughness of the samples annealed in graphite powder resulted in poorer depth resolution, but had no significant effect on the diffusion coefficients.

Diffusion coefficients are plotted as a function of inverse temperature in Fig. 3. The data for each element define a linear trend on the plot and are consistent with an Arrhenius relationship, $D = D_0 e^{-H/RT}$. Values of the pre-exponential factor D_0 and activation enthalpy H ($\equiv E+PV$) are similar for each element, and are listed in Table 2.

DISCUSSION

Figure 4 shows an Arrhenius plot comparing our data with other rare earth element diffusion data in garnets. The diffusion data of Harrison and Wood (1980) for samarium in pure pyrope are more than two orders of magnitude higher than our data under similar pressure and temperature conditions. Harrison and Wood calculated apparent diffusion coefficients from the time required to attain steady state partitioning between ~10 micron pyrope crystals and a silicate melt (at 3.0 GPa). The high apparent diffusivities and low activation energies that they obtained suggest that recrystallization, rather than diffusion, may have been the primary mechanism for Sm transfer between crystals and melt in their experiments. Coghlan (1990) determined Nd and Er diffusion coefficients in almandine ($Alm_{67}Sp_{28}An_3Py_2$) single crystals from hydrothermal experiments at 0.1 GPa and 800-1000 °C, using an isotopically enriched aqueous tracer solution as the diffusion source. Coghlan's data, extrapolated to the temperatures of our experiments, are in reasonable agreement with our data.

Ganguly et al. (1998) measured Sm and Nd diffusion coefficients in metastable almandine ($Alm_{75}Py_{22}$) single crystals at 1 bar and 777-877 °C, using thin film and ion probe depth profiling techniques similar to those we have employed. The extension of their Arrhenius trend, uncorrected for pressure, plots more than an order of magnitude above our data. While no experimental estimate of the activation volume for REE diffusion in garnet is available, the activation volume for Mg tracer diffusion is ~8 cm^3/mol (Chakraborty and Rubie, 1996) and for Ca-(Mg,Fe) interdiffusion is11.2 cm^3/mol (Freer and Edwards, 1999). If the activation volume for rare earth element diffusion is similar (~10 cm^3/mol), then the Arrhenius curve of Ganguly et al. (1998), corrected to 2.8 GPa, lies about one order of magnitude above our data. This discrepancy may arise from the error involved in extrapolating the data over a large temperature (and pressure) interval, or may indicate a dependence of REE diffusion rates on the composition of the garnet. Chakraborty and Rubie (1996) reported a small but significant increase in Mg tracer diffusion rates with increasing almandine content, and if this trend also applies to REE diffusion it may account for the difference between our measurements and those of Ganguly et

al. (1998). The activation enthalpy of 254 kJ/mol calculated by Ganguly et al. (1998) for Nd and Sm diffusion at 1 bar is similar to the activation enthalpies we have obtained, and even more so if the effect of pressure is considered. Corrected to 1 bar using an activation volume of 10 cm^3/mol, our activation enthalpies are in the range 272-315 kJ/mol.

Also shown in Fig. 4 are diffusion data for La, Nd, Dy and Yb in yttrium aluminum garnet (YAG) determined by Cherniak (1998). The data for REE diffusion in YAG are similar to our data at temperatures of 1300-1400 °C but the activation enthalpies for YAG are much higher (~540-600 kJ/mol), and diffusion rates in YAG at lower temperatures are significantly slower than in aluminosilicate garnets.

None of the studies of rare earth element diffusion in garnet show any significant effect of ionic radius on diffusion rates. This is surprising, because according to the elastic strain model presented in Chapter 1 a significant dependence of D on ionic radius is expected. The eight-fold site onto which rare earth elements partition in pyrope is similar in size to the eight-fold site in high-Ca pyroxene (Smyth and Bish, 1988; Blundy and Wood, 1994; van Westrenen et al., 1999) and the temperature dependence of the bulk and shear moduli in garnet and pyroxene are also similar (Bass, 1995). On the basis of these considerations, diffusion rates in garnet might be expected to have a dependence on ionic radius similar to that observed in diopside. One possible explanation for the absence of a relationship between D and ionic radius in pyrope is that REE diffusion is limited by the coupled transport of another ion or defect. If the rare earth elements are incorporated into pyrope via a REEAl-MgSi exchange, for example, transport may be limited by the interdiffusion of Al and Si rather than by diffusion of the REE themselves. Although it is possible that coupled transport limits the diffusion of REE in pyrope, it does not explain the lack of a D–ionic radius dependence in yttrium aluminum garnet (Cherniak, 1998), in which REE^{3+} exchange directly for Y^{3+} with no coupled transport required. Diffusion of divalent cations in aluminosilicate garnets also involves a direct exchange, and only very small differences in diffusion rates are observed among Fe, Mg, Mn and Ca in aluminosilicate garnets (Chakraborty and Ganguly, 1992; Freer and Edwards, 1999).

These observations suggest that the insensitivity of diffusion rates in garnet to the radius of the diffusing ion does not result from the influence of a coupled exchange, but instead is related to the structure and properties of the garnet lattice. It does not appear that the elastic properties of the eight-fold site in pyrope are anomalous. Trace element partitioning trends in garnet conform very well to an elastic strain model (van Westrenen et al., 1999), and the dependence of the partition coefficient on ionic radius is actually more pronounced in garnet than it is in diopside. Instead, it appears that there is something about the geometry of the path that an ion takes when jumping to an adjacent vacancy in garnet that makes the jump frequency insensitive to the size of the ion. Computer simulations of the type performed by Wright et al. (1995) to investigate the mechanism of oxygen diffusion in garnet may help to shed light on this issue. A computational investigation of the migration pathway and migration energy for cations of various sizes should lend insight into underlying reasons for the lack of a perceivable relationship between diffusivity and cation radii.

There does appear to be a decrease in diffusivity with increasing ionic charge in garnet. Figure 5 shows our data for rare earth element diffusion along with two different data sets for divalent cation diffusion collected under similar *P–T* conditions (Chakraborty and Ganguly, 1992; Freer and Edwards, 1999). Divalent cation diffusion rates are more than two orders of magnitude faster than trivalent REE diffusion rates at the same pressure and temperature. This large difference in diffusivity between REE and divalent cations has important implications for the interpretation of thermal histories of metamorphic rocks. It suggests that the Sm-Nd isotopic system in garnet is considerably more resistant to diffusional resetting than major element cation exchanges used for thermometry (e.g. Fe-Mg exchange between garnet and biotite). The temperature recorded by the garnet biotite exchange thermometer may be much lower than the temperature corresponding to the Sm-Nd age.

In Figure 6 rare earth element diffusion rates in pyrope are compared to REE diffusion rates in diopside. At temperatures of 1300-1400 °C, diffusion rates of Yb, Dy and Sm in pyrope are similar to Yb and Dy diffusion rates in diopside, and are about an order of

magnitude faster than Nd, Ce and La in diopside. At lower temperatures the Arrhenius curves diverge. Rare earth element diffusion rates in pyrope, extrapolated to 900 °C, are more than an order of magnitude faster than Yb, and three orders of magnitude faster than Nd, in diopside. Closure temperatures for the REE in garnet are significantly lower than in diopside (Fig. 7). For spherical crystals 1 mm in diameter cooling at 1 to 100 °C My^{-1}, the closure temperature for Nd in pyrope is in the range 765-920 °C, and for diopside is about 200 °C higher. The closure temperatures for Nd in garnet that we have estimated here based on our experimental data are similar to the empirical estimate of Jagoutz (1988) for slowly cooled eclogite xenoliths from Tanzania (~850 °C), and higher than the estimate of Mezger et al. (1992) for amphibolites and granulites (~600 °C).

The experimental data presented in this chapter and in Chapter 1 indicate that at temperatures below ~1400 °C, clinopyroxene will limit the diffusive mass transfer of REE in rocks that contain both garnet and clinopyroxene. This is consistent with geochemical observations in granulites from the Bergen Arcs in western Norway (Burton et al., 1995), where garnet adjacent to clinopyroxene preserves significantly older Sm/Nd ages than garnet adjacent to any other mineral. Major element zoning profiles preserved in eclogite xenoliths where garnet has exsolved from clinopyroxene are also consistent with the experimental finding that diffusion rates in clinopyroxene are more sluggish than in garnet. Eclogites from the Roberts Victor kimberlite (Sautter and Harte, 1990) preserve compositional gradients in clinopyroxene that are much steeper than in adjacent garnet lamellae.

Observations in some peridotite xenoliths appear to suggest that clinopyroxene equilibrates more rapidly than co-existing garnet. While garnet crystals in peridotite xenoliths commonly exhibit zoning in major and trace elements, chemical zoning is usually absent in high-Ca pyroxene crystals from the same rocks (e.g. Griffin et al., 1989; Smith et al., 1991; Smith and Boyd, 1992). There are at least two possible interpretations for this apparently contradictory observation. One is that diffusion profiles actually do exist in the clinopyroxene, but that their length is too short to be detected. A second possibility is that clinopyroxene

crystals in these rocks are not primary, but have precipitated from a silicate melt or undergone recrystallization in the presence of a fluid (e.g. Shimizu, 1999). All of the peridotite samples in which garnet zoning has been observed, in the absence of any detectable chemical zoning in co-existing pyroxene, preserve clear evidence for interaction with metasomatic fluids. Clinopyroxene may react with the fluid by a dissolution/precipitation process, while interaction between garnet and fluid may take place primarily via solid-state diffusion. Another possibility is that the garnet zoning profiles are strictly growth features, and do not represent diffusion at all.

In any case, the body of experimental data on cation diffusion in clinopyroxene and garnet clearly shows that clinopyroxene has the more sluggish diffusion kinetics at low temperatures. This experimental constraint in itself provides an important bound on the interpretation of data from natural samples. Quantitative constraints on the time-scales of cooling and metasomatism in the upper mantle may be obtained by applying the rare earth element diffusion data presented here to garnet zoning profiles in peridotite xenoliths.

REFERENCES

Bass J. D. (1995) Elasticity of minerals, glasses, and melts. In Ahrens, T. J., ed., *Mineral Physics and Crystallography: A Handbook of Physical Constants*, 45-63. American Geophysical Union, Washington, DC.

Beattie P. (1993) Uranium-thorium disequilibria and partitioning on melting of garnet peridotite. *Nature* **363**, 63-65.

Blundy J. and Wood B. (1994) Prediction of crystal-melt partition coefficients from elastic moduli. *Nature* **372**, 452-454.

Burton K. W., Kohn M. J., Cohen A. S. and O'Nions R. K. (1995) The relative diffusion of Pb, Nd, Sr and O in garnet. *Earth Planet. Sci. Lett.* **133**, 199-211.

Chakraborty S. and Ganguly J. (1992) Cation diffusion in aluminosilicate garnets: experimental determination in spessartine-almandine diffusion couples, evaluation of effective binary diffusion coefficients, and applications. *Contrib. Miineral. Petrol.* **111**, 74-86.

Chakraborty S. and Rubie D. C. (1996) Mg tracer diffusion in aluminosilicate garnets at 750-850 °C, 1 atm and 1300 °C, 8.5 GPa. *Contrib. Mineral. Petrol.* **122**, 406-414.

Cherniak D. J. (1998) Rare earth element and gallium diffusion in yttrium aluminum garnet. *Phys. Chem. Minerals* **26**, 156-163.

Coghlan R. A. N. (1990) Studies of diffusional transport: grain boundary transport of oxygen in feldspars, strontium and the REE's in garnet, and thermal histories of granitic intrusions in south-central Maine using oxygen isotopes. Ph.D. thesis, Brown University, Providence, Rhode Island.

Dodson, M. H. (1973) Closure temperature in cooling geochronological and petrological systems. *Contrib. Mineral. Petrol.* **40**, 259-274.

Freer R. and Edwards A. (1999) An experimental study of Ca-(Fe,Mg) interdiffusion in silicate garnets. *Contrib. Mineral. Petrol.* **134**, 370-379.

Frey F. A., Green D. H. and Roy S. D. (1978) Integrated models of basalt petrogenesis; a study of quartz tholeiites to olivine mellilites from Southeastern Australia utilizing geochemical and experimental petrological data. *J. Petrol.* **19**, 463-513.

Ganguly J. and Tirone M. (1998) Diffusion closure temperature and age of a mineral with arbitrary extent of diffusion: theoretical formulation and applications. *Earth Planet. Sci. Lett.* **170**, 131-140.

Griffin W. L., Smith D., Boyd F. R., Cousens D. R., Ryan C. G., Sie S. H. and Suter F. (1989) Trace-element zoning in garnets from sheared mantle xenoliths. *Geochim. Cosmochim. Acta* **53**, 561-567.

Hauri E. H., Wagner T. P. and Grove T. L. (1994) Experimental and natural partitioning of Th, U, Pb and other trace elements between garnet, clinopyroxene and basaltic melts. *Chem. Geol.* **117**, 149-166.

Jagoutz E. (1988) Nd and Sr systematics in an eclogite xenolith from Tanzania: Evidence for frozen mineral equilibria in continental lithosphere. *Geochim. Cosmochim. Acta* **52**, 1285-1293.

LaTourrette T. Z., Kennedy A. K. and Wasserburg G. J., (1993) Thorium-uranium fractionation by garnet: Evidence for a deep source and rapid rise of oceanic basalts. *Science* **261**, 739-742.

Mezger K., Essene E. J. and Halliday A. N. (1992) Closure temperatures of the Sm-Nd system in metamorphic garnets. *Earth Planet. Sci. Lett.* **113**, 397-409.

Salters V. J. M. and Hart S. R. (1989) The hafnium paradox and the role of garnet in the source of mid-ocean-ridge basalts. *Nature* **343**, 420-422.

Sautter V. and Harte B. (1990) Diffusion gradients in an eclogite xenolith from the Roberts Victor kimberlite pipe: (2) kinetics and implications for petrogenesis. *Contrib. Mineral. Petrol.* **105**, 637-649.

Shannon R. D. (1976) Revised effective ionic radii and systematic studies of interatomic distances in halides and chalcogenides. *Acta Crystall. A* **32**, 751-767.

Shimizu N. (1999) Young geochemical features in cratonic peridotites from Southern Africa and Siberia. In Fei Y., Bertka C. M. and Mysen B. O., eds., *Mantle Petrology: Field Observations and High Pressure Experimentation.* The Geochemical Society Spec. Publ. **6**, 47-55.

Shimizu N. and Arculus R. J. (1975) Rare earth element concentrations in a suite of basanitoids and alkali olivine basalts from Grenada, Lesser Antilles. *Contrib. Mineral. Petrol.* **50**, 231-240.

Smith D. and Boyd F. R. (1992) Compositional zonation in garnets in peridotite xenoliths. *Contrib. Mineral. Petrol.* **112**, 134-147.

Smith D., Griffin W. L., Ryan C. G. and Sie S. H. (1991) Trace-element zonation in garnets from The Thumb: heating and melt infiltration below the Colorado Plateau. *Contrib. Mineral. Petrol.* **107**, 60-79.

Smyth J. R. and Bish D. L. (1988) *Crystal Structures and Cation Sites of the Rock Forming Minerals.* Allen & Unwin, Boston.

Van Orman J. A., Grove T. L. and Shimizu N. (1998) Uranium and thorium diffusion in diopside. *Earth Planet. Sci. Lett.* **160**, 505-519.

Van Westrenen W., Blundy J. D. and Wood B. J. (1999) Crystal-chemical controls on trace element partitioning between garnet and anhydrous silicate melt. *Am. Min.* **84**, 838-847.

Wang L., Zhang Y. and Essene E. J. (1996) Diffusion of the hydrous component in pyrope. *Am. Mineral.* **81**, 706-718.

Wright K., Freer R. and Catlow C. R. A. (1995) Oxygen diffusion in grossular and some geological implications. *Am. Mineral.* **80**, 1020-1025.

Table 1. Summary of run conditions and diffusion data for Sm, Dy and Yb in pyrope at 2.8 GPa.

Run #	Capsule	T (°C)	duration (hr)	D_{Sm} (x 10^{21} m^2/s)	D_{Dy} (x 10^{21} m^2/s)	D_{Yb} (x 10^{21} m^2/s)
C229	Graphite	1450	4.0	370 ± 109	433 ± 128	434 ± 128
B619	Graphite	1400	24.0	315 ± 137	484 ± 210	485 ± 210
B738	Vitreous C	1400	2.6	332 ± 98	454 ± 134	599 ± 171
D30	Graphite	1350	20.2	171 ± 50	144 ± 43	140 ± 42
C223	Graphite	1300	90.0	124 ± 75	126 ± 67	155 ± 103
B740	Vitreous C	1200	40.3	12.7 ± 3.8	17.2 ± 5.1	12.0± 3.5

Table 2. Arrhenius parameters ($D = D_0 e^{-H/RT}$) for diffusion in pyrope at 2.8 GPa.

Element	$\log_{10} D_0$ (m^2/s)	H (kJ/mol)
Yb	-7.74 ± 0.97	343 ± 30
Dy	-9.09 ± 0.97	300 ± 30
Sm	-9.05 ± 0.97	304 ± 30

FIGURE CAPTIONS

Figure 1. Typical diffusion profiles (a) and their error function inversions (b). Experiment C229—1450 °C, 4 hours.

Figure 2. Time series at 1400 °C. Diffusion coefficients for Yb, Dy and Sm are independent of the anneal duration, consistent with transport by lattice diffusion.

Figure 3. Arrhenius plot showing Yb, Dy and Sm diffusion coefficients from this study versus T^{1}. Values of D_0 and H are given in Table 2.

Figure 4. Comparison of diffusion data obtained in this study with other published data for rare earth elements in silicate and aluminate garnets.

Figure 5. Arrhenius plot comparing REE diffusion data obtained in this study with diffusion data for divalent cations obtained under similar conditions. All data are corrected to 2.8 GPa using the expressions given in the data sources—Chakraborty and Ganguly, 1992; Freer and Edwards, 1999.

Figure 6. Comparison of REE diffusion rates in pyrope (this study; solid lines) and diopside (Chapter 1; dashed lines). Diopside data are corrected to 2.8 GPa.

Figure 7. Closure temperatures for Nd in pyrope and diopside, calculated using the Dodson equation for spherical grains (Dodson, 1973). Dashed lines—diopside; solid lines—pyrope. Numbers on curves indicate the grain diameter in millimeters.

Figure 1a

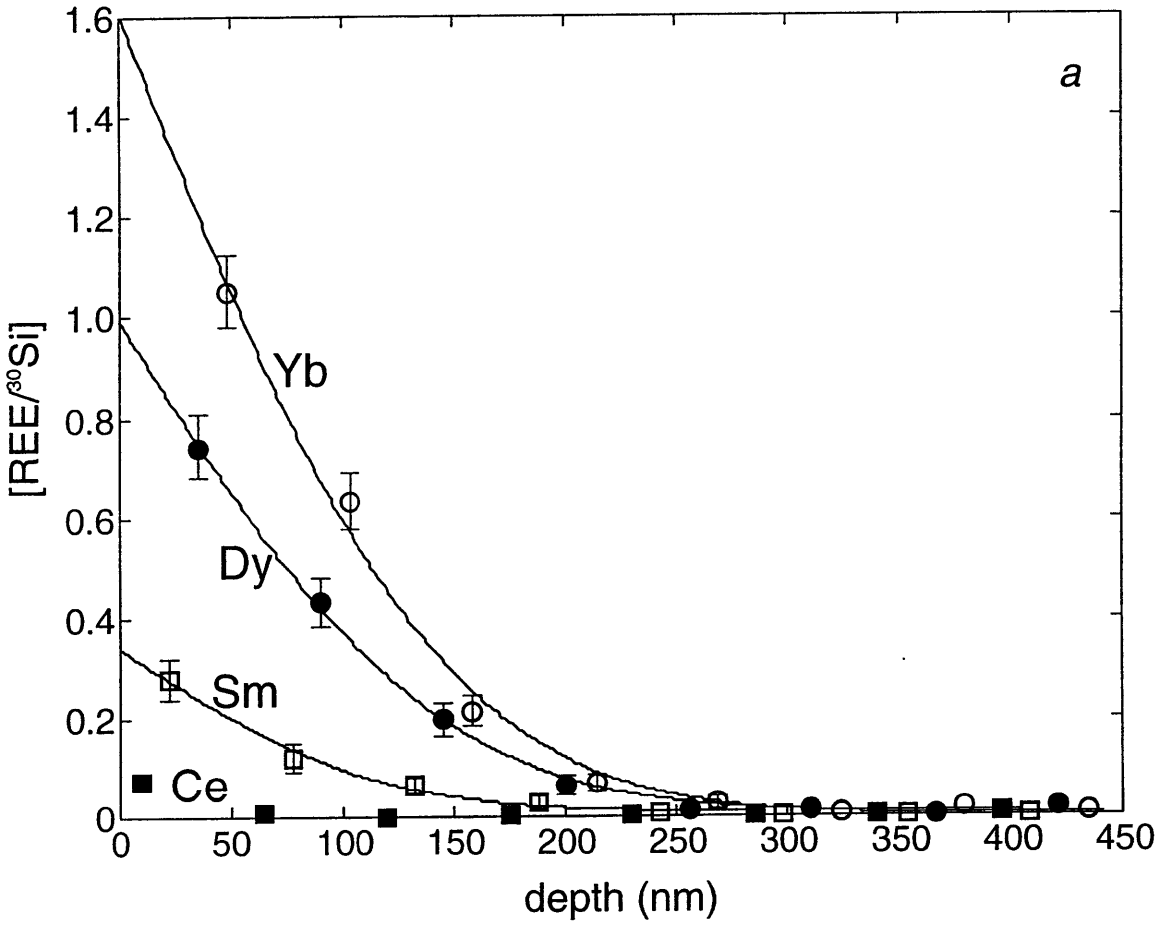
a
Yb
Dy
Sm
Ce
[REE/30Si]
depth (nm)
0
0.2
0.4
0.6
0.8
1.0
1.2
1.4
1.6
0
50
100
150
200
250
300
350
400
450

Figure 1b

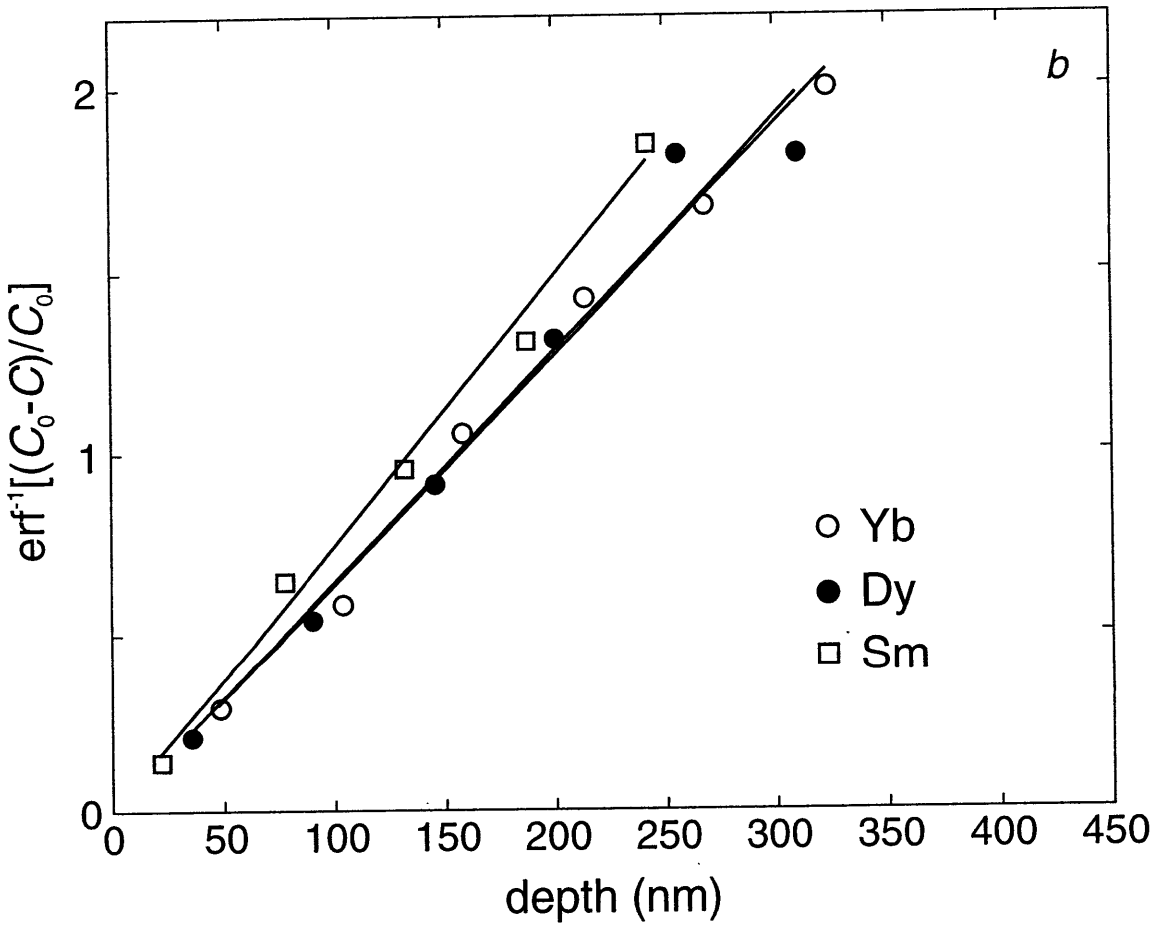
b
2
1
0
0
50
100
150
200
250
300
350
400
450
depth (nm)
erf^{-1}[(C_0-C)/C_0]
Yb
Dy
Sm

Figure 2

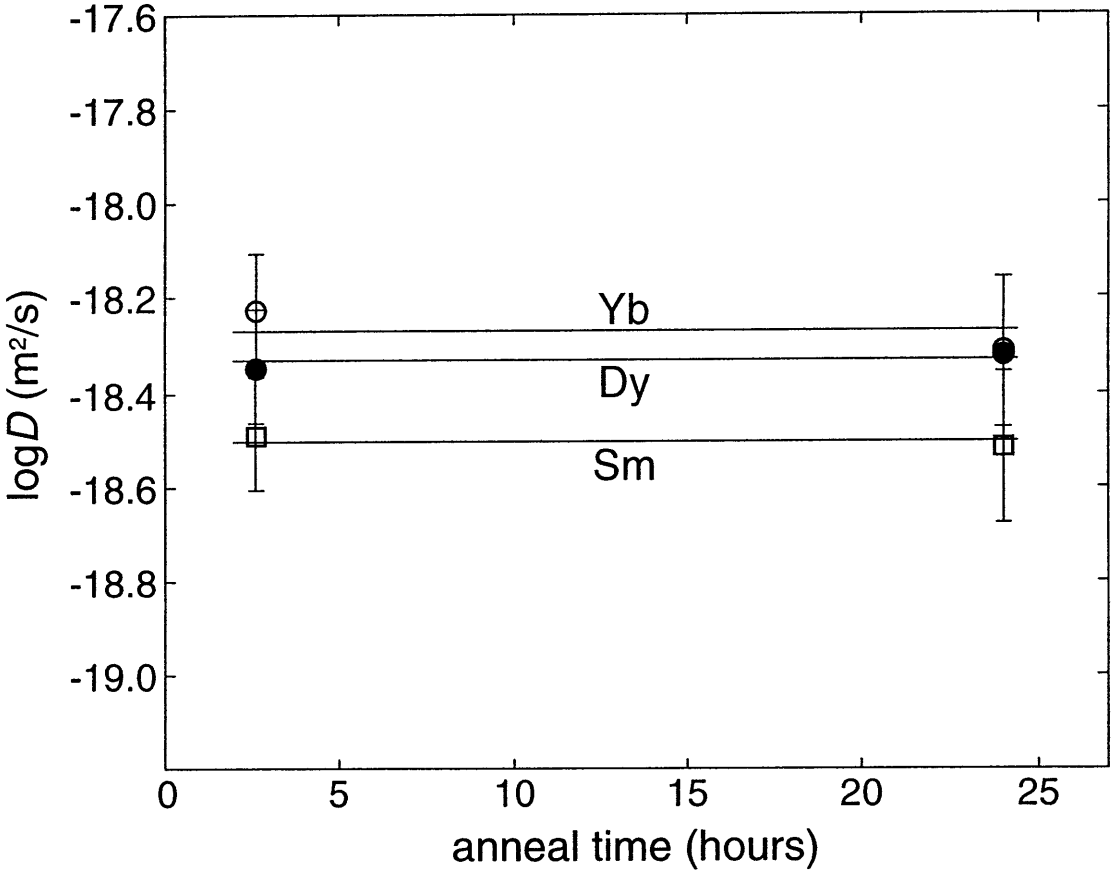
-17.6
-17.8
-18.0
-18.2
-18.4
-18.6
-18.8
-19.0
log$D$ (m^2/s)
Yb
Dy
Sm
0
5
10
15
20
25
anneal time (hours)

Figure 3

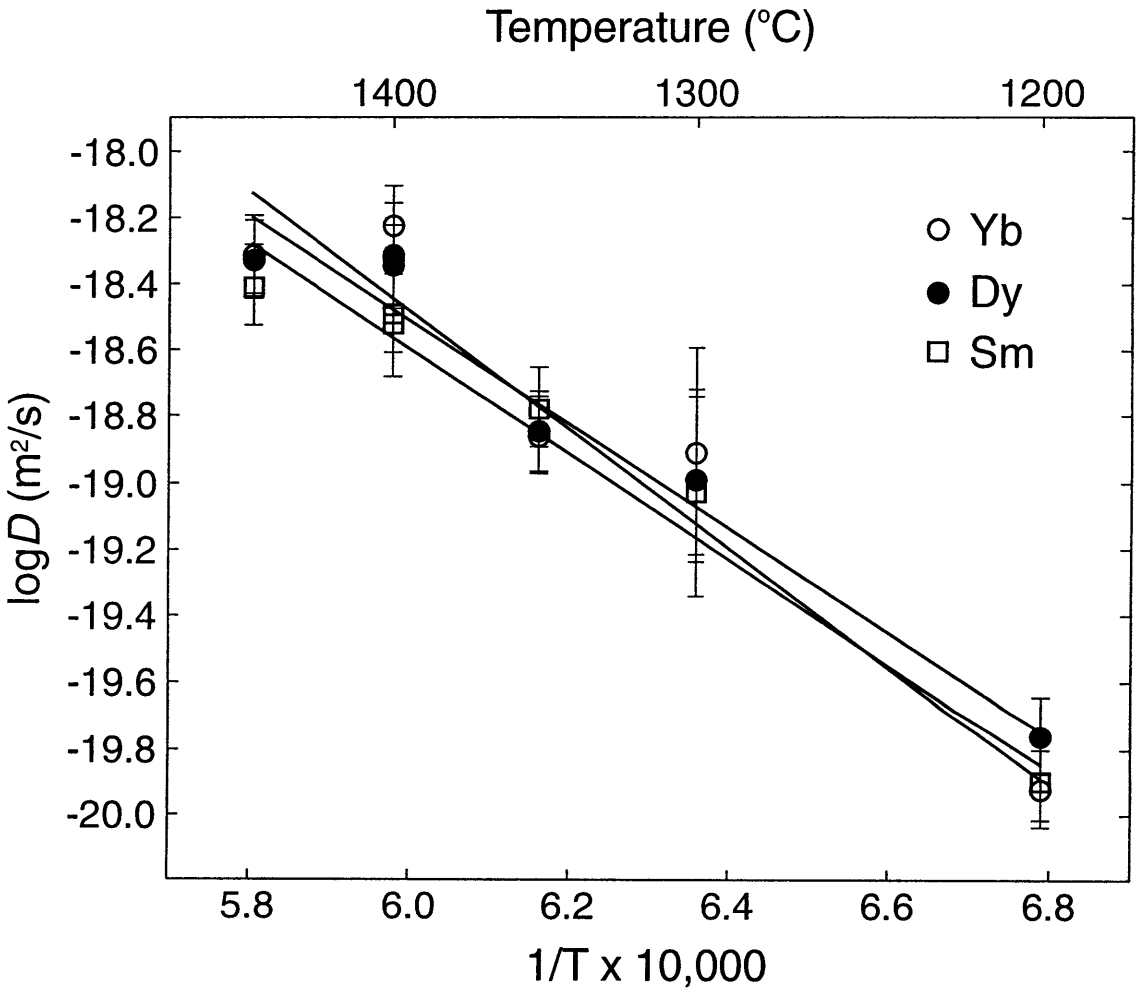
Temperature (°C)
1400
1300
1200
-18.0
-18.2
-18.4
-18.6
-18.8
-19.0
-19.2
-19.4
-19.6
-19.8
-20.0
log D (m²/s)
Yb
Dy
Sm
5.8
6.0
6.2
6.4
6.6
6.8
1/T x 10,000

Figure 4

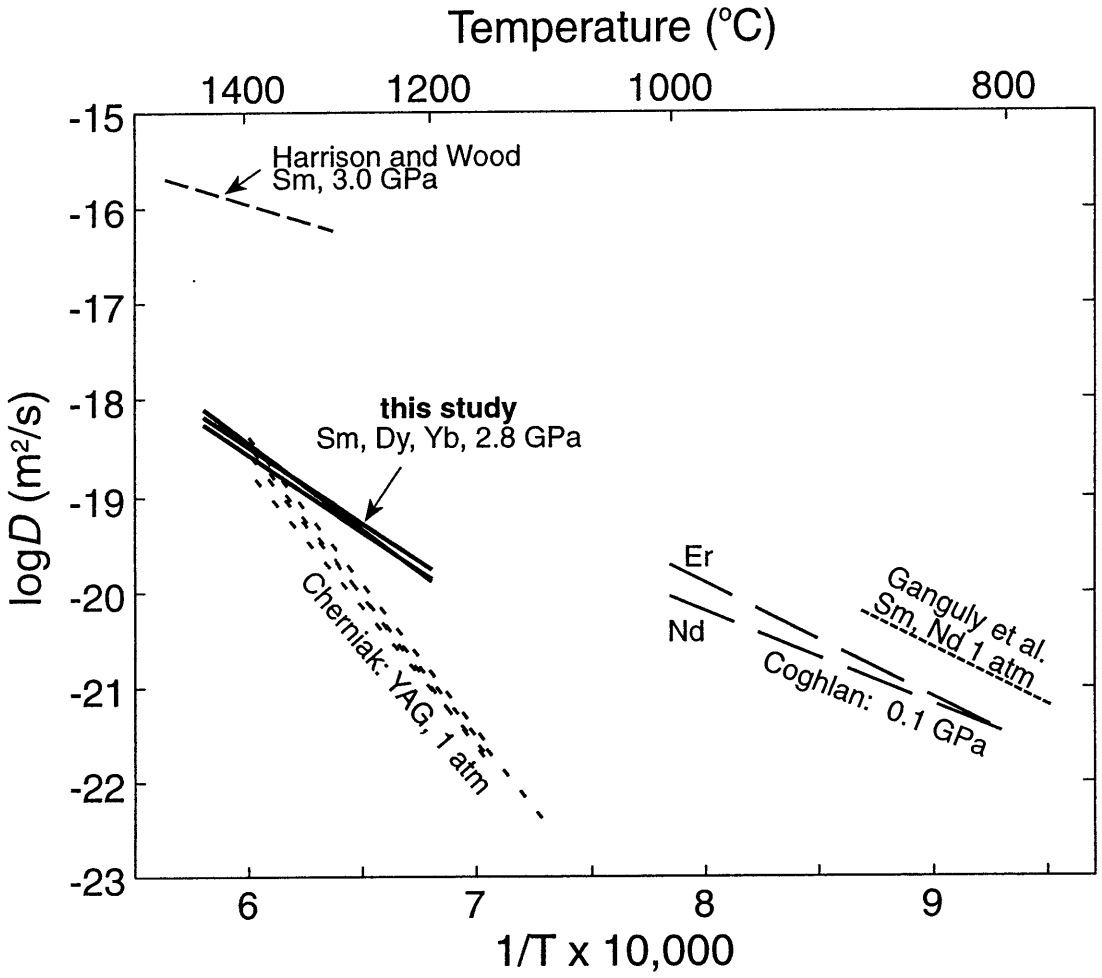
Temperature (°C)
1400
1200
1000
800
-15
-16
-17
-18
-19
-20
-21
-22
-23
log D (m²/s)
Harrison and Wood
Sm, 3.0 GPa
this study
Sm, Dy, Yb, 2.8 GPa
Er
Nd
Ganguly et al.
Sm, Nd 1 atm
Coghlan: 0.1 GPa
Cherniak: YAG, 1 atm
6
7
8
9
1/T x 10,000

Figure 5

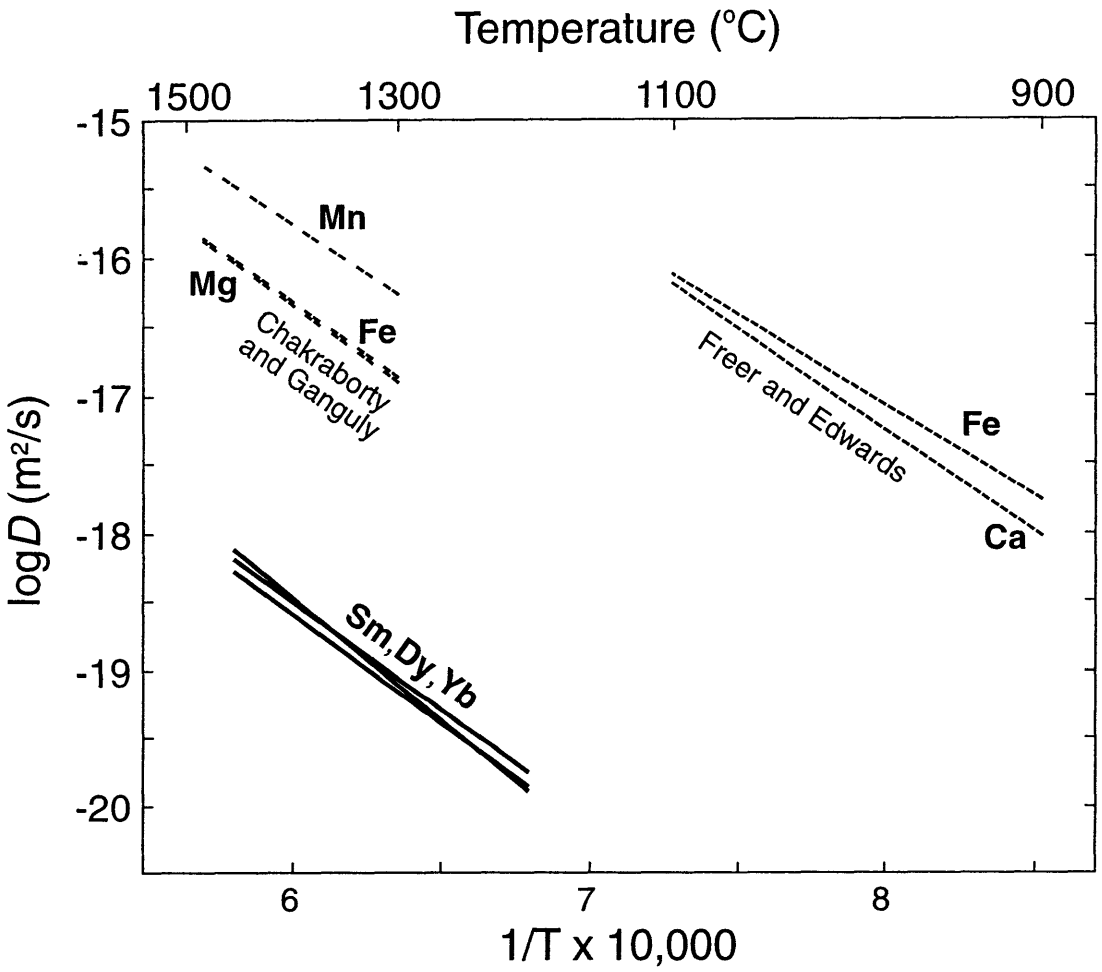
Temperature (°C)
1500
1300
1100
900
-15
-16
-17
-18
-19
-20
log D (m²/s)
Mn
Mg
Fe
Chakraborty and Ganguly
Fe
Ca
Freer and Edwards
Sm, Dy, Yb
6
7
8
1/T x 10,000

Figure 6

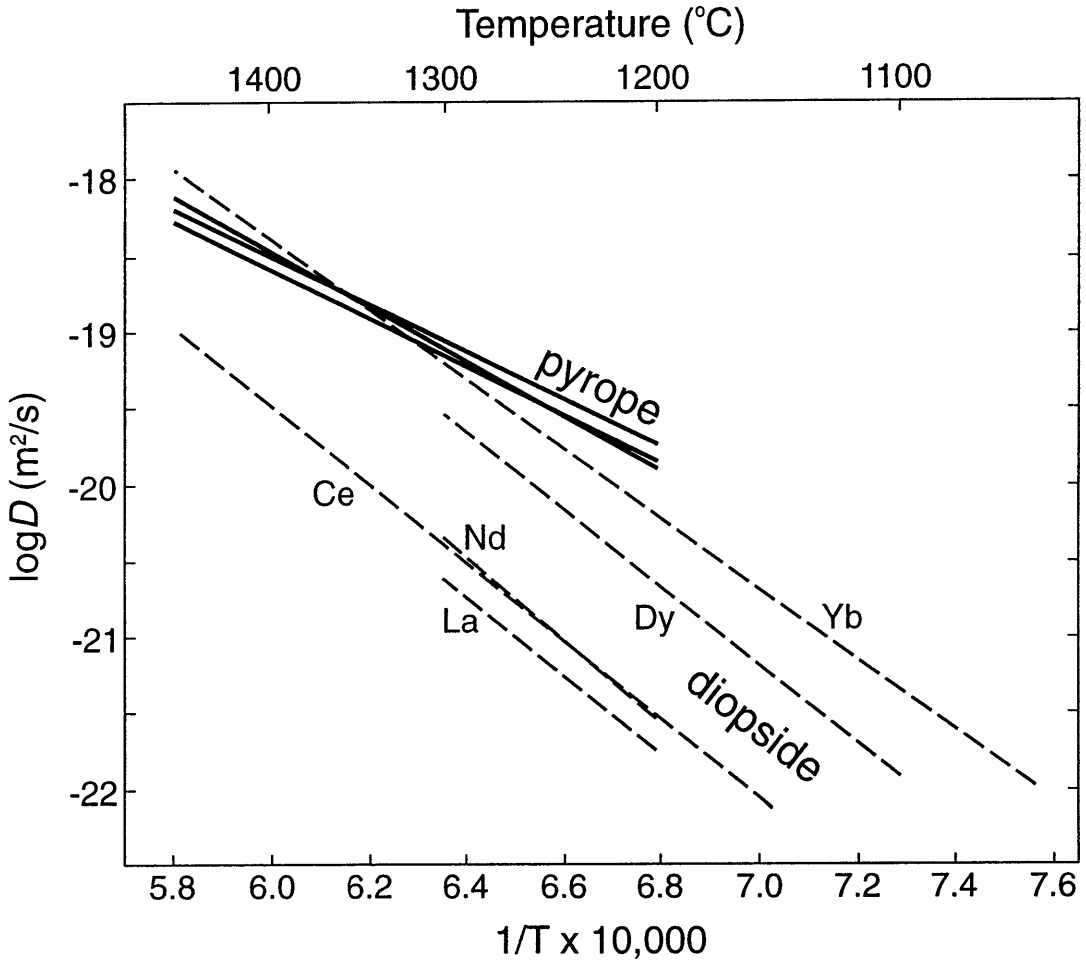
Temperature (°C)
1400
1300
1200
1100
-18
-19
-20
-21
-22
log$D$ (m²/s)
pyrope
Ce
Nd
La
Dy
Yb
diopside
5.8
6.0
6.2
6.4
6.6
6.8
7.0
7.2
7.4
7.6
1/T x 10,000

Figure 7

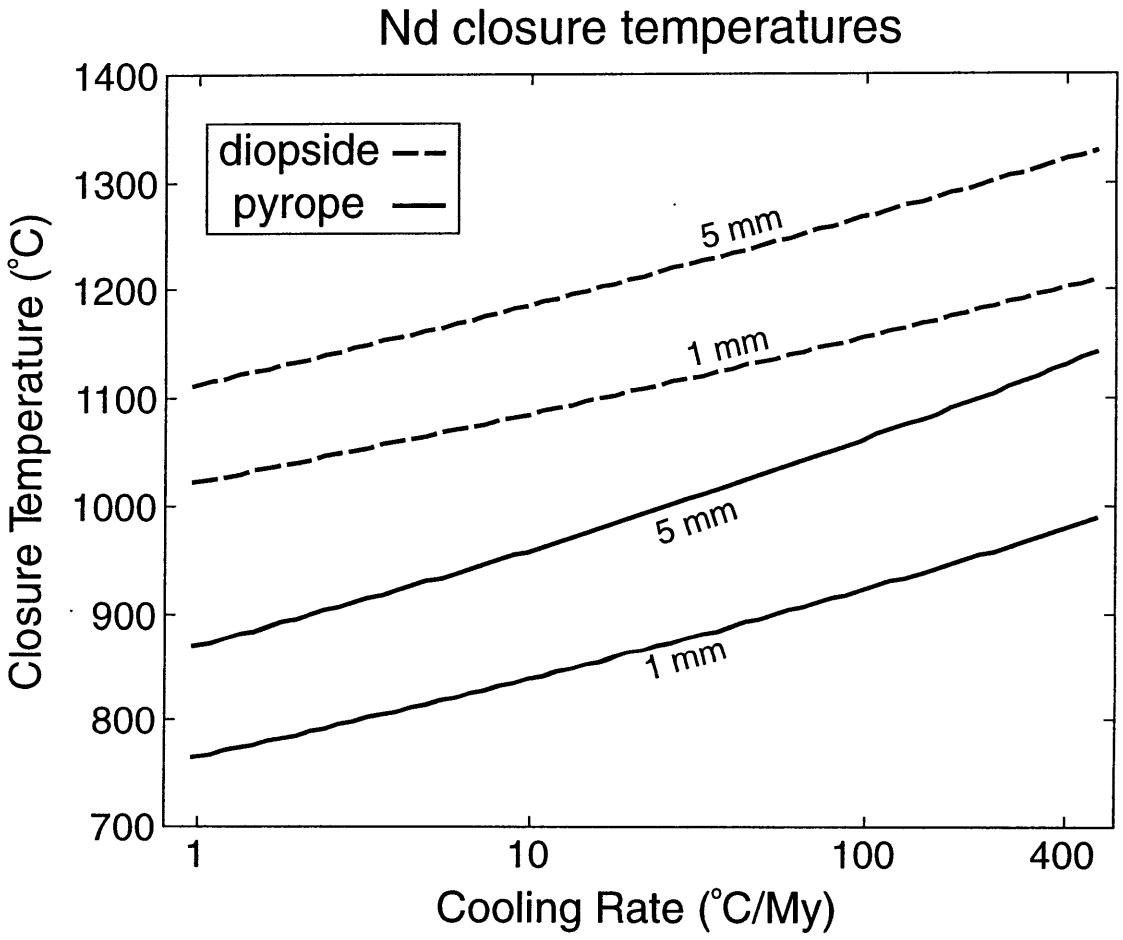
Nd closure temperatures
diopside
pyrope
5 mm
1 mm
5 mm
1 mm
Closure Temperature (°C)
1400
1300
1200
1100
1000
900
800
700
1
10
100
400
Cooling Rate (°C/My)

CHAPTER 3.

A MODEL FOR DIFFUSION-CONTROLLED CHEMICAL EXCHANGE DURING MANTLE MELTING, WITH IMPLICATIONS FOR RARE EARTH ELEMENT FRACTIONATION

ABSTRACT

A numerical model is developed to describe diffusion-controlled exchange of trace elements between solid and melt during dynamic partial melting. The model differs from previous disequilibrium melting models by treating the solid as a polyphase aggregate and accounting for mass transfer between the melt and each solid phase. Based on diffusion data for clinopyroxene and garnet presented in Chapters 1 and 2, the model is used to assess rare earth element fractionation during adiabatic decompression melting in Earth's upper mantle. For conditions typical of near-fractional melting beneath slow spreading centers (melting rate $\sim 5 \times 10^{-8}$ yr^{-1}), diffusion is found to significantly affect REE fractionation if the initial radius of clinopyroxene grains is ~1 mm or greater. The effect of diffusion is to reduce the relative fractionation of light and heavy REE; this effect becomes more pronounced with increased melting rate, increased grain size, and increased efficiency of melt segregation. Comparison of the model predictions with REE data from abyssal peridotites dredged on the America-Antarctic and Southwest Indian ridge systems shows that the residual porosity beneath these ridges must be less than ~0.03 and that the effective grain radius must be less than ~3 mm.

INTRODUCTION

The solid and liquid products of partial melting in Earth's upper mantle preserve information on the chemical composition of the mantle and on the dynamics of the melting process itself. To interpret the chemical information that is recorded in igneous rocks it is necessary to understand how elements are fractionated during the production and segregation of melt. The partial melting process in the upper mantle is thought to be a dynamic one in which melt is extracted from the solid matrix at small melt fractions (e.g. McKenzie, 1985; Johnson and Dick, 1990). In this situation it is important to consider the possibility of chemical disequilibrium between the melt and the residual solid, because the time available for reaction between them is limited.

Several models have been developed recently to account for the effects of chemical disequilibrium during partial melting and melt transport (Navon and Stolper, 1987; Qin, 1992; Spiegelman and Kenyon, 1992; Hart, 1993; Iwamori, 1993a,b; Hauri, 1997; Korenaga and Kelemen, 1998; Van Orman and Grove, 1998). A limitation of each of these models is that they have treated the solid as a single phase. Many elements in upper mantle rocks are distributed in significant proportions among two or more solid phases, and to provide a complete description of the chemical evolution of the system during partial melting it is necessary to consider chemical exchanges among all phases in the system. The model developed in this chapter differs from previous disequilibrium melting models by treating the solid as a polyphase aggregate, and by accounting explicitly for mass transfer between the melt and each solid phase. The rate of chemical exchange is controlled by diffusion in the solid phases, each of which has different diffusion and partitioning properties. Based on the diffusion data presented in Chapters 1 and 2, and published data on the equilibrium partitioning of elements between minerals and basaltic melts, the model is used to predict the behavior of rare earth elements (REE) during adiabatic decompression melting in the upper mantle. We demonstrate the conditions under which diffusion may play a significant role in fractionating the REE, and show

how the melting rate, grain size, and efficiency of melt extraction influence REE abundance patterns in the solid and liquid products of partial melting.

MODEL FORMULATION

The model presented here simulates diffusion-controlled redistribution of trace elements during dynamic partial melting of a polyphase solid. The system under consideration is a representative volume of a mantle rock comprising several solid phases. Solid grains are approximated as spheres, and each solid phase is considered to have a uniform grain size. The purpose of the model is to simulate the chemical evolution of this system as it ascends at constant velocity and undergoes partial melting due to adiabatic decompression. Partial melting begins when the system encounters the solidus at a pressure P_0 and temperature T_0, and ceases at P_f and T_f. The first increment of melt is assumed to be a complete disequilibrium (modal) melt whose composition simply reflects the weighted average of the compositions of solid phases that have been dissolved. This disequilibrium melt is assumed to equilibrate instantaneously with the contact surfaces of the solid grains, inducing chemical gradients within the grains that are relaxed with time by solid-state diffusion. The extent to which the solid grains and melt are able to re-equilibrate as partial melting proceeds depends on the ratio of the diffusive relaxation time to the time required for production and extraction of melt from the solid matrix.

The model traces the chemical evolution of several reservoirs: each solid phase that hosts the trace elements of interest; the residual melt that remains within the solid matrix; and the segregated melt formed by continuous extraction of melt from the matrix. Melt is assumed to remain with the solid until a critical melt fraction is reached and thereafter is extracted so that the porosity remains constant. The extracted melt is pooled in a chemically isolated reservoir and undergoes no further chemical interaction with the solid.

The concentration of a chemical species i within a spherical grain of solid phase j is given by the following equation:

$$\frac{\partial C_j^i}{\partial t} = D_j^i\left(\frac{\partial^2 C_j^i}{\partial r_j^{\,2}} + \frac{2}{r_j}\frac{\partial C_j^i}{\partial r_j}\right). \qquad (1)$$

This is an expression of Fick's second law in spherical coordinates, where $C_j^i = C_j^i\left(r_j, t\right)$ is the concentration at a distance r_j from the center of the grain. A list of model parameters and their dimensions is given in Table 1. The diffusion coefficient D_j^i is considered to have an Arrhenian dependence on temperature and pressure,

$$D_j^i = D_{0,j}^i \exp\left(\frac{-\left(\mathcal{E}_j^i + P\mathcal{V}_j^i\right)}{\mathcal{R}T}\right). \qquad (2)$$

The boundary conditions for Eq. 1 are based on the following assumptions: (1) Before melting begins, there is no compositional zoning within the solid grains and (2) chemical species are distributed among the solid phases in equilibrium proportions; (3) during melting, chemical equilibrium between the residual melt and the *surfaces* of solid grains is maintained at all times; (4) there is no flux across the center of the solid grains (i.e. compositional zoning within each grain during melting is symmetrical). These boundary conditions are expressed by the following equations:

$$\left.\frac{\partial C_j^i}{\partial r_j}\right|_{t=0} = 0 \text{ and } \left.C_j^i\right|_{t=0} = C_{j,0}^i \qquad (3)$$

$$\frac{C_{j1,0}^i}{K_{j1}^i} = \frac{C_{j2,0}^i}{K_{j2}^i} = \cdots = \frac{C_{jn,0}^i}{K_{jn}^i}. \qquad (4)$$

$$\left.C_j^i\right|_{r_j = R_j} = K_j^i C_m^i \qquad (5)$$

$$\left.\frac{\partial C_j^i}{\partial r_j}\right|_{r_j = 0} = 0 \qquad (6)$$

where K_j^i is the equilibrium mineral/melt partition coefficient and C_m^i is the concentration of chemical species *i* in the residual melt.

The mass balance equation for a chemical species in the residual melt can be written:

$$\frac{d\left(V_m C_m^i\right)}{dt} = \sum_j -N_j 4\pi\left(R_j\right)^2 D_j^i \left.\frac{\partial C_j^i}{\partial r_j}\right|_{r_j=R_j} + \sum_j \upsilon_m \alpha_j C_j^i \Big|_{r_j=R_j} - \upsilon_e C_m^i \qquad (7)$$

$$= -\frac{d}{dt}\left\{\sum_j N_j \int_0^{R_j} 4\pi\left(r_j\right)^2 C_j^i dr_j\right\} - \upsilon_e C_m^i \qquad (8)$$

where V_m is the volume of residual melt, R_j is the time-dependent radius of a solid grain of phase j, N_j is the number of grains of phase j in the system, υ_m and υ_e are the volumetric melting and melt extraction rates, respectively, and α_j is the stoichiometric coefficient of phase j in the melting reaction. In writing Eqs. (7) and (8), density differences among the melt and solid phases have been ignored. The terms on the right-hand side of Eq. 7 represent, in order, the total diffusive current of a chemical species across the interface between the melt and each solid phase, mass transfer from solid to melt due to phase change (dissolution), and the removal of a chemical species from the residual melt by melt extraction. In Eq. 8 the diffusion and dissolution terms are combined within the integral. This equation, instead of Eq. 7, is used in the calculations because the numerical evaluation of the integral is more accurate than the evaluation of $\partial C_j^i / \partial r_j$ at $r_j = R_j$ (Navon and Stolper, 1987; Korenaga and Kelemen, 1998).

Mass balance in the pooled extracted melt is given by the equation:

$$\frac{\mathrm{d}\, V_M C_M^i}{\mathrm{d}\, t} = \upsilon_e C_m^i \qquad (9)$$

where C_M^i is the concentration of element i in the extracted melt and V_M is the volume of melt extracted. Both the residual and pooled extracted melts are assumed to be compositionally homogeneous at all times. This assumption is justified for the residual melt because chemical diffusion rates in silicate melts are much faster than in silicate minerals and because the length scale over which diffusion must take place to homogenize the melt is relatively small. Homogenization of the segregated melt is not assured, as it will depend on the geometry and size of the reservoir and on the vigor of convective mixing; but the assumption of homogeneity

for this reservoir is not critical to the model as it has no bearing on the chemical evolution of the solid phases or the residual melt.

The melting rate, in m^3/s, is given by:

$$\upsilon_m = V_0 W \frac{\partial F}{\partial z} \tag{10}$$

where V_0 is the initial solid volume, defined as $\sum_j N_j 4/3\pi\left(R_{j,0}\right)^3$, W is the upwelling velocity, and $(\partial F/\partial z)$ is the melt productivity, or the fraction of melt produced per meter of adiabatic ascent. In most calculations υ_m, was taken to be constant, but for comparison we also examined a case in which melt productivity (and consequently υ_m) increase during melting, as proposed by Asimow et al. (1997). With progressive melting, the volume of each solid phase changes according to $\frac{\mathrm{d}V_j}{\mathrm{d}t} = -\alpha_j \upsilon_m$, where α_j is the stoichiometric coefficient of phase j in the melting reaction. Solid grains are assumed to dissolve from their outer rims, preserving their spherical symmetry at all times, and the number of grains within the system is held constant (i.e. there is no formation of new grains, and no coalescence of grains). Given these assumptions, the radius of each solid grain changes with time according to:

$$R_j = R_{j,0}\left(1 - \frac{\upsilon_m \alpha_j t}{V_0 X_{j,0}}\right)^{1/3} \tag{11}$$

for constant υ_m.

The rate of extraction of melt from the solid matrix, υ_e, is initially zero and when the melt fraction exceeds the critical porosity ϕ is given by:

$$\upsilon_e = \frac{1}{1-\phi}\upsilon_m. \tag{12}$$

Thus the melt segregation rate is treated as a simple step function in which melt remains within the solid matrix until a critical porosity is reached and thereafter is removed at the rate described by Eq. 12. Although this simple functional form certainly does not represent the actual melt

segregation process, it encompasses the end-members of fractional ($\phi = 0$) and batch ($\phi = F$) melting and we believe that it captures the essence of dynamic partial melting in the upper mantle.

In general it is expected that there will be a relative flow between the residual melt and its enclosing solid matrix. However, stable elements are sensitive to differential flow between solid and melt only in two- or three-dimensional systems where the melt flow field diverges from that of the solid (e.g. Spiegelman, 1996). In situations where the melt and solid flow in one dimension the compositions of the solid and melt are essentially independent of their relative velocities (Ribe, 1985). Here we restrict ourselves to 1-D systems, such as the axial part of a mid-ocean ridge or a plume, and assume that the residual melt and the solid travel upward at the same rate. Relative flow between residual melt and solid does have an influence on the time available for chemical reaction between the two reservoirs, and therefore influences the approach of the system to equilibrium. The assumption made here that residual melt and solid travel at the same velocity maximizes the reaction time, for a given solid upwelling rate. Equilibration is enhanced relative to any case in which there is a relative flow between residual melt and solid.

Equations 1-12 are solved numerically using a fully implicit Crank-Nicolson finite difference algorithm. At each time step, the concentration of an element in the residual melt and the concentration distribution within each solid grain are calculated simultaneously. For each solid grain a fixed number of radial grid points is maintained throughout the calculation, and the moving boundary is accommodated by re-scaling the grid to the new grain radius R_j at each time step. The numerical algorithm is unconditionally stable, and at the limits of very large and very small D_j^i it successfully recovers the analytical solutions for complete equilibrium and complete disequilibrium melting, respectively. The accuracy of the calculations was assessed further by checking the mass balance of an element among the solid, residual melt, and segregated melt reservoirs at each time step, and by comparing the results of calculations using different grid spacings. Mass balance is achieved within less than 1.3% relative for the grid used in most of

the calculations (40 radial steps for each solid grain and 320 time steps). Using a finer grid changes the calculated compositions of residual melt, pooled melt, and solid phases by less than a few percent.

Assumptions

Several assumptions have been made in constructing this model, the most important of which concern the chemical exchange process, the mechanical integrity of the solid grains, and the boundary condition at the interface between solid grains and residual melt. Chemical exchange between solid and melt in this model is considered to result only from diffusion and from the incremental dissolution of mineral grains as partial melting proceeds. Solid grains are assumed to maintain their mechanical integrity at all times, with no internal deformation and no motion of grain boundaries other than that due to continuous dissolution into the melt.

Deformation must take place as the mantle ascends, and recrystallization processes associated with this deformation may significantly enhance the rate of chemical exchange. Clinopyroxene and garnet, the principal solid hosts of incompatible elements in the upper mantle, are considerably more resistant to high-temperature plastic deformation than the most abundant minerals, olivine and orthopyroxene (Karato and Wu, 1993; Karato et al., 1995; Kirby and Kronenberg, 1984; Mackwell, 1991). Most of the deformation associated with mantle upwelling may thus be accommodated by orthopyroxene and olivine, with garnet and cpx behaving as essentially rigid grains within a viscous olivine/opx matrix. Also, because of their relatively low abundances in peridotites, garnet and clinopyroxene are not susceptible to recrystallization processes that involve grain boundary migration. Most garnet and cpx grains are surrounded by olivine and orthopyroxene, and few cpx-cpx and garnet-garnet grain boundaries exist. These considerations suggest that deformation and recrystallization may not be important for clinopyroxene and garnet during mantle upwelling, and that our assumption of rigid solid grains may be a reasonable approximation. In any case the present model considers an end-member situation, and comparison of the model predictions with the compositions of

natural basalts, melt inclusions, and residual peridotites will help to determine the extent to which non-diffusive processes may enhance the redistribution of trace elements during mantle melting.

Another important assumption of the model is that the outer boundary of each solid grain is at all points in equilibrium with the residual melt. Because silicate melts probably do not wet grain boundaries in mantle rocks, residing instead along three-grain junctions (e.g. Kohlstedt, 1992), satisfying this boundary condition requires rapid grain boundary diffusion to allow all parts of the grain boundary to maintain communication with the residual melt. In the absence of grain boundary diffusion, equilibrium would be maintained only over the small portion of the surface where the grain and the melt were in physical contact, and the rate of diffusive exchange between solid and melt would be significantly reduced. The available data for polycrystalline olivine and enstatite (Farver et al., 1994; Yund, 1997) suggest that grain boundary diffusion rates are on the order of 10^{-12} m^2/s at temperatures close to the solidus of peridotite. Given this diffusivity, the time required for transport along a grain boundary that connects melt tubules separated by one centimeter is on the order of a few years. This time is short compared to typical timescales for melting and melt extraction in the mantle, and thus the assumption that solid grains are in equilibrium with residual melt over their entire boundary appears to be justified.

Rare Earth Element Fractionation During Mantle Melting

The rare earth elements are among the most widely used tracers of partial melting processes in the upper mantle. In this section we use the numerical model developed above, along with the diffusion results for clinopyroxene and garnet presented in Chapters 1 and 2, to examine the behavior of the REE during adiabatic decompression melting. Our purpose is to demonstrate the conditions under which disequilibrium fractionation of rare earth elements may take place and to show how the melting rate, solid grain size, and efficiency of melt extraction may influence REE abundance patterns in the solid and liquid products of partial melting.

Melting in the spinel stability field

We first consider models in which melting begins in the spinel stability field. High-Ca pyroxene is the primary host of rare earth elements in spinel lherzolite, and in the calculations discussed below this phase is assumed to contain all of the rare earth elements in the solid matrix, with all other solid phases having REE partition coefficients equal to zero. We have also performed calculations in which orthopyroxene and clinopyroxene are both allowed to exchange REE with the melt, and these results are not significantly different from those in which the orthopyroxene partition coefficients are equal to zero, regardless of the diffusion properties assumed for opx. Orthopyroxene contains a small proportion of the REE in upper mantle rocks and has only a minor influence on their chemical evolution during partial melting.

The partition coefficients and diffusion parameters used in making the calculations are listed in Table 2. The proportions of solid phases in the system initially, and the proportions in which the solid phases dissolve into the melt (melt reaction coefficients), are given in Table 3. We assume that the partition coefficients and melt reaction coefficient for each solid phase are constant during melting. Although cpx/melt partition coefficients are known to vary with pressure, temperature and composition (e.g. Wood and Blundy, 1997; Blundy et al., 1998; Salters and Longhi, 1999), the relative values of the partition coefficients among the REE remain nearly constant. Our primary interest is in examining the influence of diffusion on fractionation of the rare earth elements, and for this purpose the use of constant cpx/melt partition coefficients is an adequate approximation.

Although the melting reaction may change as melting progresses, clinopyroxene always dominates the melt mode (Kinzler and Grove, 1992a; Baker and Stolper, 1994; Kinzler, 1997) and while cpx remains in the residue its reaction coefficient exhibits relatively little variation. The primary effect of changes in the melting reaction is to change the relative proportions of orthopyroxene and olivine dissolving into or crystallizing from the melt with decreasing pressure (e.g. Kinzler, 1997), and this has no bearing on the present results since opx and olivine are considered to be barren of rare earth elements.

Figures 1 and 2 show the results of a series of calculations that simulate diffusive REE exchange during adiabatic decompression melting within a one-dimensional mantle column. In these calculations the solidus is intersected at a pressure of 2.0 GPa and temperature of 1400 °C, and the temperature decreases linearly at 100 °C GPa^{-1} until melting ceases at 0.4 GPa and 1240 °C. The diffusion coefficient for each element is dependent on temperature and pressure (Table 2) and decreases by approximately an order of magnitude from the bottom of the melting column to the top. In these calculations the melt productivity is assumed to have a constant value of 0.1 GPa^{-1}, leading to a total melting fraction of 16% at the top of the column. The melting rate is directly proportional to the upwelling rate *W*. We have chosen to present the results in terms of a common initial grain radius of 2 mm, and to vary the degree of disequilibrium by changing the upwelling rate. There is a direct correspondence between the upwelling rate (which controls the time scale of the calculation) and the grain size squared (which controls the length scale of diffusion), and this relation can be used to extend the results presented in the figures below to other initial grain radii. Increasing the upwelling rate by a factor of four, for example, is exactly equivalent to increasing the grain size by a factor of two.

Figure 1 shows La and Yb diffusion profiles developed within a 2 mm radius clinopyroxene grain with progressive melting. Lanthanum is the most incompatible of the rare earth elements and has the most sluggish diffusion kinetics; Yb is moderately incompatible and diffuses ~30 times more rapidly than La. At upwelling rates of 1 cm/yr (representative of passive upwelling beneath a slow spreading ridge) and 10 cm/yr (fast spreading ridge) Yb concentration profiles are nearly flat, indicating that Yb is close to equilibrium with the residual melt over the entire grain. Lanthanum is moderately zoned even at an upwelling rate of 1 cm/yr, and at an upwelling rate of 10 cm/yr is very strongly enriched in the core of the grain relative to the rim (which is in equilibrium with the residual melt). These calculations show that under conditions typical of melting beneath mid-ocean ridges, La, a representative light rare earth element, may be extracted from the solid much less efficiently than under conditions of

complete grain-scale equilibrium, while Yb (and other heavy rare earth elements) diffuse rapidly enough to be near equilibrium with the melt under the same conditions.

Figure 2 shows how the contrasting diffusivities of the light and heavy REE influence the rare earth element compositions of solid and liquid products of partial melting. Shown in figures 2*a* and *b*, as a function of upwelling rate, are the compositions of the residual solid and aggregated melt, respectively, after 16% near-fractional melting (with 1% residual porosity). Under conditions of local equilibrium, the removal of light rare earth elements from the residual solid is very efficient; after 16% melting, La is depleted by a factor of nearly 10^5 compared to the initial solid (Fig. 2*a*). Such strong depletions in light REE are unlikely to be realized during partial melting in the upper mantle if diffusion controls the rate of chemical exchange. Even at an upwelling rate as slow as 0.3 cm yr^{-1}, corresponding to a melting rate of 10^{-8} yr^{-1}, the predicted La concentration in the residual solid is nearly an order of magnitude higher than at equilibrium, and for an upwelling rate of 1 cm yr^{-1} the La concentration is two orders of magnitude higher than at equilibrium. Heavier rare earth elements are less severely affected. With increasing atomic number the difference between the equilibrium concentration and the concentration predicted by the disequilibrium model diminishes, and Yb concentrations do not increase significantly unless the upwelling rate is greater than about 10 cm yr^{-1}. At upwelling rates greater than 100 cm yr^{-1} the REE composition of the residue approaches that of a solid produced by the extraction of a complete disequilibrium ("modal") melt.

The aggregated melt is less sensitive than the residual solid to small variations in the effective partitioning of highly incompatible elements, and does not show the effects of disequilibrium at upwelling rates slower than ~3 cm yr^{-1} (Fig. 2*b*). As the upwelling rate increases, rare earth element concentrations in the aggregated melt decrease, but there is almost no change in the slope of the REE abundance pattern. This is a consequence of the increase in diffusivity across the lanthanide series, combined with the insensitivity of large degree aggregated melts to small variations in the effective partitioning of highly incompatible elements. The concentration of a highly incompatible element in the aggregated melt changes

significantly only when its effective partition coefficient exceeds the melting fraction (in this case 0.16). For the light REE such a change in effective partitioning requires a relatively large degree of local disequilibrium. The moderately incompatible heavy rare earth elements are sensitive to small variations in effective partitioning, and begin to show the effects of disequilibrium partitioning when the deviation from local equilibrium is relatively small. If diffusion rates among the REE were uniform, then with increasing upwelling rate the REE patterns in the aggregated melt would decrease in slope, simply reflecting the difference in behavior of highly and moderately incompatible elements. The increase in diffusivity across the lanthanide series is sufficient to offset this effect and keep the slope of the REE pattern nearly constant. An unfortunate consequence of this is that the shape of the REE pattern produced by disequilibrium melting is very similar to that produced by melting under conditions of local equilibrium. A disequilibrium exchange process will thus be difficult to detect in the aggregated melt. The REE composition of a disequilibrium aggregated melt is similar to that of a higher-degree equilibrium melt, or an equilibrium melt of a more depleted source.

The efficiency of melt extraction, represented by the parameter ϕ, has a strong influence on the chemical evolution of the residual solid under conditions of local equilibrium, but its importance diminishes as the deviation from equilibrium increases (Fig. 3). Incompatible elements are removed from the solid most readily if solid grains and melt are in equilibrium, and the melt is removed instantaneously as it is produced (equilibrium fractional melting). Depletion of the solid is less efficient if some or all of the melt is retained within the solid matrix, or if the magnitude of diffusional exchange is decreased—inefficient melt removal and chemical disequilibrium both impede the extraction of incompatible elements from the solid. With increasing degree of disequilibrium, the difference between instantaneous melt removal (fractional melting) and no melt removal (batch melting) on the composition of the residual solid becomes less pronounced (Fig. 3). In the end-member case of complete disequilibrium the chemical evolution of the residual solid is the same whether melt is instantaneously extracted or not removed at all.

In the calculations discussed above the melt productivity, $(\partial f/\partial P)$, is assumed to be constant. As discussed by Asimow et al. (1995) and Asimow et al. (1997) the melt productivity is likely to vary significantly during adiabatic decompression melting. For near-fractional melting beginning within the spinel stability field, the productivity is predicted to remain nearly constant up to 1.0 GPa (~30 km depth) and to increase sharply as the mantle ascends to lower pressures (Asimow et al., 1997). Such a variation in productivity will have a significant influence on diffusion-controlled chemical exchange; the approach to equilibrium will be enhanced early in the melting process when the melting rate is slow, but will diminish as the melting rate increases. To examine the influence of variable melt productivity on the distribution of the REE we have performed a set of calculations in which the productivity is held constant at 0.02 GPa^{-1} between 2.0 and 1.0 GPa, and then increases linearly at 0.717 GPa^{-2} from 1.0 to 0.4 GPa. The total degree of melting at the top of the melting column is 16%, as in the calculations above. Figure 4 shows how the evolution of the residual solid differs from the case in which the melt productivity is constant. During the early stages of melting the productivity is low and the REE are removed efficiently from the solid, but as melting progresses the degree of disequilibrium increases sharply and removal of REE from the solid becomes increasingly difficult. At shallow depths, where most of the melt is produced, melting rates are high and REE diffusivities are low; both of these factors act to limit chemical exchange between solid phases and melt. At low extents of melting (~2% or less) the solid is depleted more efficiently under the increasing productivity function than at constant productivity, but at higher degrees of melting the reverse is true. In the calculations shown in Fig. 4, the crossover in relative depletion between the two productivity functions occurs at less than 4% melting. Although the results shown in Fig. 4 are for the specific case of fractional melting of a solid with initial grain radius of 2 mm, at an upwelling rate of 1 mm yr^{-1}, the general aspects of the chemical evolution are representative. We have examined a large region of parameter space and

have found no conditions under which increasing productivity depletes the solid more effectively than constant productivity, at degrees of melting greater than ~0.1.

Melting in the garnet stability field

We now extend the model to situations in which melting begins in the garnet stability field at depths greater than ~75 km and continues into the spinel stability field at shallower depths. Before melting begins the rare earth elements are partitioned between garnet and clinopyroxene in equilibrium proportions, and after the solidus is crossed both solid phases exchange REE with the melt. When the upwelling mantle encounters the garnet–spinel facies boundary, here assumed to be located at a pressure of 2.5 GPa, garnet and olivine react to produce pyroxenes and spinel until garnet is exhausted from the residue. Clinopyroxene is likely to be a reaction product during the transformation to the spinel-facies assemblage, but in most bulk compositions the amount of cpx produced will be small. We ignore any new clinopyroxene that may be produced during the reaction to the spinel facies and consider the number of cpx grains to remain constant. All of the REE that are held within garnet when the transformation takes place are assumed to be released instantly into the residual melt. Clinopyroxene grains then attempt to re-equilibrate with this new residual melt composition via solid-state diffusion. We do not consider here the possibility that REE in the garnet are inherited by newly formed orthopyroxene grains during the garnet–spinel transformation; for a discussion of this possibility see Koga et al. (1999). Melt productivity is assumed here to remain constant across the garnet–spinel transition, although thermodynamic considerations suggest that it may drop significantly (Asimow et al., 1995).

Figures 5–7 illustrate the chemical evolution of a system undergoing near-fractional melting beginning in the garnet stability field at 2.8 GPa and 1480 °C. In this example, 3% melting takes place in the presence of garnet, and an additional 21% melting takes place in the spinel stability field. The initial grain radius is 2 mm for both clinopyroxene and garnet, and the upwelling rate is 3 cm yr^{-1}. Rare earth element diffusion rates in garnet are similar to heavy

REE diffusion rates in clinopyroxene under the *T–P* conditions of interest, and for the grain size and upwelling rate used in the calculations garnet is near equilibrium with the melt (Fig. 5). The presence of garnet has a strong influence on the chemical evolution of co-existing clinopyroxene (Fig. 6). Heavy REE are strongly partitioned into garnet, and while garnet remains in the residue clinopyroxene exhibits a characteristic "humped" REE pattern with low relative concentrations of heavy REE (Fig. 6e). When the system crosses the garnet–spinel boundary the concentrations of heavy REE in the residual melt increase abruptly, but the light REE (especially La and Ce) show little effect (Fig. 7). Clinopyroxene adjusts to the new residual melt composition to the extent that diffusion allows, and this is reflected by increased concentrations of heavy REE shortly after the garnet–spinel boundary is crossed. As melting continues in the spinel stability field, the high relative concentrations of heavy REE in clinopyroxene and in the residual melt gradually diminish.

Comparison with abyssal peridotite data

Under most conditions the residual solid is more sensitive than the aggregated melt to the effects of disequilibrium chemical exchange during partial melting. Here we assess the melting processes beneath mid-ocean ridges by comparing the predictions of the model with the rare earth element compositions of abyssal peridotites dredged from the slow-spreading America-Antarctic and Southwest Indian ridge systems (Johnson et al., 1990; Johnson and Dick, 1992). These peridotites are thought to be the residues of variable degrees of adiabatic decompression melting with efficient extraction of melt (Johnson et al., 1990). The chondrite-normalized Ce/Yb and Nd/Yb ratios of clinopyroxene grains from the abyssal peridotites are plotted in Figure 8 together with calculated residual bulk compositions for various melting conditions. Figure 8*a* shows the predicted Ce/Yb and Nd/Yb under conditions of local equilibrium for 0-20% melting in the spinel stability field. Some of the data can be explained by equilibrium melting with residual porosity between 0.003 and 0.03, but many of the data with low Nd/Yb fall below the melting trends. The concave-downward curvature of the

clinopyroxene data is not reproduced by any melting model that assumes local equilibrium between solid and melt.

Figures 8*b* and *c* show melting trends for 0-20% disequilibrium fractional melting beginning in the spinel stability field at 2.4 GPa. The upwelling rate in the calculations is 0.9 cm/yr, representative of half-spreading rates along the America-Antarctic and Southwest Indian ridges, and the curves represent melting trends for different initial grain radii varying between 0 and 3 mm. The calculations shown in Fig. 8b are for constant melt productivity, and in Fig. 8c the productivity is assumed to increase linearly between 1.0 and 0.4 GPa. As melting progresses, the effective compatibility of both Ce and Nd increase due to decreasing temperature and diffusivity. Ce, the slower diffusing element, is more severely affected, and this leads to a concave-downward curvature of the melting trend. For large grain sizes (high degrees of disequilibrium), the Ce/Yb and Nd/Yb ratios actually begin to *increase* at high melting extents, leading to a "hook" in the melting trend. This behavior is unique to disequilibrium melting and results from the large variation in diffusivity among the REE in clinopyroxene. Figure 8*d* shows melting trends for fractional disequilibrium melting beginning in the garnet stability field at 2.8 GPa. The residual solid is more severely depleted in this case, both because the melting extent is higher and because a larger proportion of the melting takes place at higher temperatures where the solid is closer to equilibrium with the melt and the REE are removed more efficiently.

Most of the abyssal peridotite data can be explained by disequilibrium fractional melting with initial grain radii of 1-3 mm, for constant melt productivity models (Figs. 8*b* and *d*), or 0.5-1 mm, for models with increasing productivity (Fig. 8*c*). Like the equilibrium models, the disequilibrium models are unable to explain the clinopyroxene data with low Nd/Yb, but unlike the equilibrium models they are able to reproduce the concave-downward curvature of the abyssal peridotite trend. We have not performed a complete search of parameter space, and it is possible that there are combinations of grain size, residual porosity, productivity function, depth of solidus intersection, and initial source composition that can account for all of the peridotite

data. It is also possible that a two-stage process is responsible for the near-vertical part of the data trend, with near-fractional melting followed by interaction with a Ce-enriched melt or fluid. If we disregard the near-vertical part of the abyssal peridotite trend and consider only samples with Nd/Yb greater than ~0.1, then the data may be explained either by melting at local equilibrium ($R_0 < 0.5$ mm) with ϕ between 0.003 and 0.03, or by perfect fractional melting ($\phi = 0$) with R_0 between 0.5 and 3 mm. The actual condition is probably between these extremes, with imperfect fractional melting and incomplete local equilibrium. In any case the residual porosity beneath the ridges must be less than ~0.03 in order to fit the data, and the effective radii of clinopyroxene grains must be less than ~3 mm.

Further constraints on the melting processes beneath mid-ocean ridges could be obtained if there were information on the spatial distribution of trace elements within individual clinopyroxene grains in abyssal peridotites. At present no such high-resolution spatial information exists. The presence of diffusional zoning profiles in residual grains would provide clear evidence of the importance of diffusion-limited exchange, and would allow more stringent constraints to be placed on the style and rate of melting beneath mid-ocean ridges.

REFERENCES

Asimow P. D., Hirschmann M. M., Ghiorso M. S., O'Hara M. J. and Stolper E. M. (1995) The effect of pressure-induced solid-solid phase transitions on decompression melting of the mantle. *Geochim. Cosmochim. Acta* **59**, 4489-4506.

Asimow P. D., Hirschmann M. M. and Stolper E. M. (1997) An analysis of variations in isentropic melt productivity. *Phil. Trans. R. Soc. Lond. A* **355**, 244-281.

Baker M. B. and Stolper E. M. (1994) Determining the composition of high-pressure mantle melts using diamond aggregates. *Geochim. Cosmochim. Acta* **58**, 2811-2828.

Blundy J. D., Robinson J. A. C. and Wood B. J. (1998) Heavy REE are compatible in clinopyroxene on the spinel lherzolite solidus. *Earth Planet. Sci. Lett.* **160**, 493-504.

Farver J. R., Yund R. A. and Rubie D. C. (1994) Magnesium grain boundary diffusion in forsterite aggregates at 1000-1300 °C and 0.1 MPa to 10 GPa. *J. Geophys. Res.* **99**, 19809-19819.

Hart S. R. (1993) Equilibration during mantle melting: A fractal tree model, *Proc. Natl. Acad. Sci.* **90**, 11,914-11,918.

Hauri E. H. (1997) Melt migration and mantle chromatography, 1: Simplified theory and conditions for chemical and isotopic decoupling. E*arth Planet. Sci. Lett.* **153**, 1-19.

Iwamori H. (1993a) Dynamic disequilibrium melting model with porous flow and diffusion controlled chemical equilibration. *Earth Planet. Sci. Lett.* **114**, 301-313.

Iwamori H. (1993b) A model for disequilibrium mantle melting incorporating melt transport by porous and channel flows. *Nature* **366**, 734-737.

Johnson K. T. M. and Dick H. J. B. (1992) Open system melting and temporal and spatial variation of peridotite and basalt at the Atlantis-II fracture-zone. *J. Geophys. Res.* **97**, 9219-9241.

Johnson K. T. M., Dick H. J. B. and Shimizu N. (1990) Melting in the oceanic upper mantle: an ion microprobe study of diopsides in abyssal peridotites. *J. Geophys. Res.* **95**, 2661-2678.

Karato S. and Wu P. (1993) Rheology of the upper mantle: a synthesis. *Science* **260**, 771-778.

Karato S., Wang Z. C., Liu B. and Fujino K. (1995) Plastic deformation of garnets: Systematics and implications for the rheology of the mantle transition zone. *Earth Planet Sci. Lett.* **130**, 13-30.

Kelemen P. B., Shimizu N. and Dunn T. (1993) Relative depletion of niobium in some arc magmas and the continental crust: Partitioning of K, Nb, La and Ce during melt/rock reaction in the upper mantle. *Earth Planet. Sci. Lett.* **120**, 111-134.

Kinzler R. J. (1997) Melting of mantle peridotite at pressures approaching the spinel to garnet transition: Application to mid-ocean ridge basalt petrogenesis. *J. Geophys. Res.* **102**, 853-874.

Kinzler R. J. and Grove T. L. (1992a) Primary magmas of mid-ocean ridge basalts, 1. Experiments and methods. *J. Geophys. Res.* **97**, 6885-6906.

Kinzler R. J. and Grove T. L. (1992b) Primary magmas of mid-ocean ridge basalts, 2. Applications. *J. Geophys. Res.* **97**, 6907-6926.

Kirby S. H. and Kronenberg A. K. (1984) Deformation of clinopyroxenite: Evidence for a transition in flow mechanisms and semi-brittle behavior. *J. Geophys. Res.* **89**, 3177-3192.

Koga K. T., Shimizu N. and Grove T. L. (1999) Disequilibrium trace element redistribution during garnet to spinel facies transition. In Gurney J. J., Gurney J. L., Pascoe M. D., and Richardson S. H., eds., Proceedings of the 7th International Kimberlite Conference, v. 1, p. 444-451.

Kohlstedt D. L. (1992) Structure, rheology and permeability of partially molten rocks at low melt fractions. In J. Phipps-Morgan et al., eds., *Mantle Flow and Melt Generation at Mid-Ocean Ridges*; *Amer. Geophys. Union Geophys. Monogr.* **71**, 103-121.

Korenaga J. and Kelemen P. B. (1998) Melt migration through the oceanic lower crust: a constraint from melt percolation modeling with finite solid diffusion. *Earth Planet. Sci. Lett.* **156**, 1-11.

Mackwell S. J. (1991) High-temperature rheology of enstatite: Implications for creep in the mantle. *Geophys. Res. Lett.* **18**, 2027-2030.

McKenzie D. (1985) ^{230}Th-^{238}U disequilibrium and the melting process beneath ridge axes. *Earth Planet. Sci. Lett.* **72**, 149-157.

Navon O. and Stolper E. M. (1987) Geochemical consequences of melt percolation: the upper mantle as a chromatographic column. *J. Geol.* **95**, 285-307.

Qin Z. (1992) Disequilibrium partial melting model and its implications for trace element fractionations during mantle melting. *Earth Planet. Sci. Lett.* **112**, 75-90.

Ribe N. M. (1985) The generation and composition of partial melts in the earth's mantle. *Earth Planet. Sci. Lett.* **73**, 361-376.

Salters V. J. M. and Longhi J. (1999) Trace element partitioning during the initial stages of melting beneath mid-ocean ridges. Earth Planet. Sci. Lett. **166**, 15-30.

Shimizu N. (1998) The geochemistry of olivine-hosted melt inclusions in a FAMOUS basalt ALV519-4-1. *Phys. Earth Planet. Inter.* **107**, 183-201.

Spiegelman M. (1996) Geochemical consequences of melt transport in 2-D: The sensitivity of trace elements to mantle dynamics. *Earth Planet. Sci. Lett.* **139**, 115-132.

Spiegelman M. and Kenyon P. (1992) The requirements for chemical disequilibrium during magma migration. *Earth Planet. Sci. Lett.* **109**, 611-620.

Van Orman J. A., Grove T. L. and Shimizu N. (1998) Uranium and thorium diffusion in diopside. *Earth Planet. Sci. Lett.* **160**, 505-519.

Walter M. J. (1998) Melting of garnet peridotite and the origin of komatiite and depleted lithosphere. *J. Petrol.* **39**, 29-60.

Wood B. J. and Blundy J. D. (1997) A predictive model for rare earth element partitioning between clinopyroxene and anhydrous silicate melt. *Contrib. Mineral. Petrol.* **129**, 166-181.

Yund R. A. (1997) Rates of grain boundary diffusion through enstatite and forsterite reaction rims. *Contrib. Mineral. Petrol.* **126**, 224-236.

Table 1. Model parameters.

Variable	Description	Dimension
C_j^i	Concentration of element i within solid phase j	kg m^{-3}
$C_{j,0}^i$	Concentration of element i within solid phase j before melting begins	kg m^{-3}
C_m^i	Concentration of element i within the residual melt	kg m^{-3}
C_M^i	Concentration of element i within the pooled extracted melt	kg m^{-3}
D_j^i	Diffusion coefficient of element i within solid phase j	m^2 s^{-1}
$D_{0,j}^i$	Pre-exponential factor for diffusion of element i within solid phase j	m^2 s^{-1}
$\mathcal{E}_j^i$	Activation energy for diffusion of element i within solid phase j	J mol^{-1}
f	Fraction of melting	None
F	Total fraction of melting at the top of the melting column	None
H	Height of melting column	m
K_j^i	Mineral/melt equilibrium partition coefficient for element i	None
N_j	Number of grains of solid phase j	None
P	Pressure	Pa
P_0	Pressure when melting begins	Pa
P_f	Pressure when melting stops	Pa
$P_{gt\rightarrow sp}$	Pressure of the garnet to spinel facies transition	Pa
r_j	Radial coordinate within solid phase j	m
$\mathcal{R}$	Gas constant	J mol^{-1} K^{-1}
R_j	Grain radius of solid phase j	m
$R_{j,0}$	Grain radius of solid phase j before melting begins	m
t	Time	s
T	Temperature	K
T_0	Temperature when melting begins	K
T_f	Temperature when melting stops	K
$T_{gt\rightarrow sp}$	Temperature of the garnet to spinel facies transition	K
V_0	Volume of solid before melting begins	m^3
V_j	Volume of solid phase j	m^3
V_m	Volume of residual melt	m^3
V_M	Volume of pooled extracted melt	m^3
$\mathcal{V}_j^i$	Activation volume for diffusion of element i within solid phase j	m^3 mol^{-1}
W	Mantle upwelling rate	m s^{-1}
X_j	Volume fraction of solid phase j	None
$X_{j,0}$	Volume fraction of solid phase j before melting begins	None
z	Vertical coordinate	m
α_j	Stoichiometric coefficient of solid phase j in melting reaction	None
ϕ	Critical porosity	None
υ_e	Melt extraction rate	m^3 s^{-1}
υ_m	Melting rate	m^3 s^{-1}

Table 2. Partition coefficients, diffusion parameters, and initial bulk concentration.

	$^1K_{cpx}$	$^1K_{opx}$	$^1K_{gt}$	$^2D_{0,cpx}$ m^2/s	$D_{0,gt}$ m^2/s	$^2E_{cpx}$ kJ/mol	E_{gt} kJ/mol	$\mathcal{V}_{cpx}$ m^3/mol	$\mathcal{V}_{gt}$ m^3/mol	$^3C_0$
La	0.054	5e-4	1e-3	4.20e-3	2.34e-9	519.3	287.7	1e-5	1e-5	0.296
Ce	0.086	9e-4	4e-3	2.20e-3	2.34e-9	508.2	287.7	1e-5	1e-5	0.361
Nd	0.19	9e-3	0.06	5.54e-4	2.34e-9	483.9	287.7	1e-5	1e-5	0.482
Sm	0.29	0.02	0.5	1.42e-4	2.34e-9	460.1	287.7	1e-5	1e-5	0.593
Dy	0.44	0.06	2.5	9.97e-6	2.34e-9	413.6	287.7	1e-5	1e-5	0.770
Er	0.44	0.07	3	2.73e-6	2.34e-9	390.9	287.7	1e-5	1e-5	0.785
Yb	0.43	0.1	4	8.83e-7	2.34e-9	371.2	287.7	1e-5	1e-5	0.800

1. Mineral/melt equilibrium partition coefficient. References: Kelemen et al. (1993), Salters and Longhi (1999).
2. D_0 and E values for cpx are interpolated using the elastic model discussed in Chapter 1.
3. Initial concentrations in the bulk solid. Relative abundances reflect the values estimated by Shimizu (1998) for depleted MORB mantle.

Table 3. Phase proportions.

phase	[1]initial solid spinel facies	initial solid garnet facies	melt mode spinel facies	[2]melt mode garnet facies
cpx	0.20	0.20	0.80	0.80
opx	0.24	—	0.30	—
garnet	0	0.08	0	0.30
other	0.56	0.72	-0.10	-0.10

1. Phase proportions for depleted MORB mantle in spinel facies (Kinzler and Grove, 1992b).
2. Garnet facies melt mode from melting reactions at 3.0 GPa (Walter,1998).

FIGURE CAPTIONS

Figure 1. Model diffusion profiles developed within a 2 mm radius clinopyroxene grain during progressive melting within the spinel stability field. Melting begins at 2.0 GPa and 1400 °C and ceases at 0.4 GPa and 1240 °C. Each panel shows rim-to-rim diffusion profiles at five equally spaced melting increments (3.2%, 6.4%, 9.6%, 12.8% and 16%). (*a*) and (*c*) show La and Yb profiles, respectively, for an upwelling rate of 1 cm yr^{-1}; (*b*) and (*d*) show La and Yb profiles for an upwelling rate of 10 cm yr^{-1}. $\partial F/\partial P = 0.1$ GPa^{-1}, $F = 0.16$, $\phi = 0.01$.

Figure 2. Influence of upwelling rate on the rare earth element compositions of the residual solid (*a*) and aggregated melt (*b*) after 16% near-fractional melting in the spinel stability field. Numbers on curves indicate upwelling rates in cm yr^{-1}. Initial grain radius is 2 mm, $\phi = 0.01$.

Figure 3. Influence of residual porosity on the composition of the residual solid after 16% melting, under the condition of local equilibrium (*a*) and for various degrees of disequilibrium (*b*, *c*, *d*). With increasing deviation from equilibrium, the solid residue of fractional melting ($\phi = 0$; instantaneous melt extraction) becomes more similar in composition to that produced by batch melting ($\phi = F$; no melt extraction). The La concentration after 16% batch melting is higher by a factor of ~10^8 than for fractional melting, if local equilibrium is achieved; the difference is less than a factor of two for disequilibrium melting at an upwelling rate of 10 cm/yr (*d*). Initial grain radius is 2 mm.

Figure 4. Influence of melt productivity $(\partial f/\partial P)$ on the chemical evolution of the residual solid. La diffusion profiles in clinopyroxene (*a, b*) and the integrated REE composition of the residual solid (*c, d*) are shown for the increasing productivity and constant productivity functions illustrated in (*e*). In the case of increasing productivity, equilibration is favored at low extents of melting (< 3%) but is hindered at higher melting degrees. The calculations shown are

for $\phi = 0$, $R_0 = 2$ mm, and $W = 1$ cm yr^{-1}, but general aspects of the chemical evolution are similar for other parameter values.

Figure 5. Chemical evolution of garnet during partial melting in the garnet stability field between 2.8 and 2.5 GPa. Diffusion profiles for La, Nd, Sm and Yb are shown in (*a–d*), and the integrated REE composition of garnet is shown in (*e*). For the upwelling rate (3 cm yr^{-1}), initial grain radius (2 mm), and residual porosity (0.01) used in the calculations, garnet is near equilibrium with the residual melt.

Figure 6. Diffusion profiles (*a–d*) and REE patterns (*e*) in clinopyroxene during progressive melting beginning in the garnet stability field at 2.8 GPa. 3% melting takes place in the presence of garnet, with an additional 21% melting in the spinel stability field. Garnet has little influence on the chemical evolution of La (*a*) and Nd (*b*), but exerts a strong control on the abundances of Sm (*c*) and Yb (*d*) in clinopyroxene. Abundances of Sm, Yb, and other middle- and heavy-REE in cpx increase abruptly at the garnet–spinel transition when all of the REE that were stored in garnet are released instantly into the residual melt. $R_0 = 2$ mm, $W = 3$ cm yr^{-1}, $\phi = 0.01$.

Figure 7. REE compositions of the residual (*a*) and aggregated melts (*b*) produced during partial melting across the garnet–spinel transition, between 2.8 and 0.4 GPa. $R_0 = 2$ mm, $W = 3$ cm yr^{-1}, $\phi = 0.01$.

Figure 8. Comparison of model predictions with the observed (Ce/Yb) and (Nd/Yb) variations in clinopyroxenes from abyssal peridotites (open circles—Johnson et al., 1990; Johnson and Dick, 1992). Concentration data are normalized to chondritic values, and all calculations assume an upwelling rate of 0.9 cm yr^{-1}. (*a*) Local equilibrium melting in spinel stability field

— $P_0 = 2.4$ GPa; $0 < \phi < 0.03$. (*b*) Disequilibrium fractional melting in spinel stability field — $P_0 = 2.4$ GPa; $(\partial f / \partial P)$ constant; $0 < R_0 < 3$ mm. (*c*) Disequilibrium fractional melting in spinel stability field — $P_0 = 2.4$ GPa; $(\partial f / \partial P)$ increasing; $0 < R_0 < 1$ mm. (*d*) Disequilibrium fractional melting beginning in garnet stability field — $P_0 = 2.8$ GPa; $(\partial f / \partial P)$ constant; $1 < R_0 < 3$ mm.

Figure 1

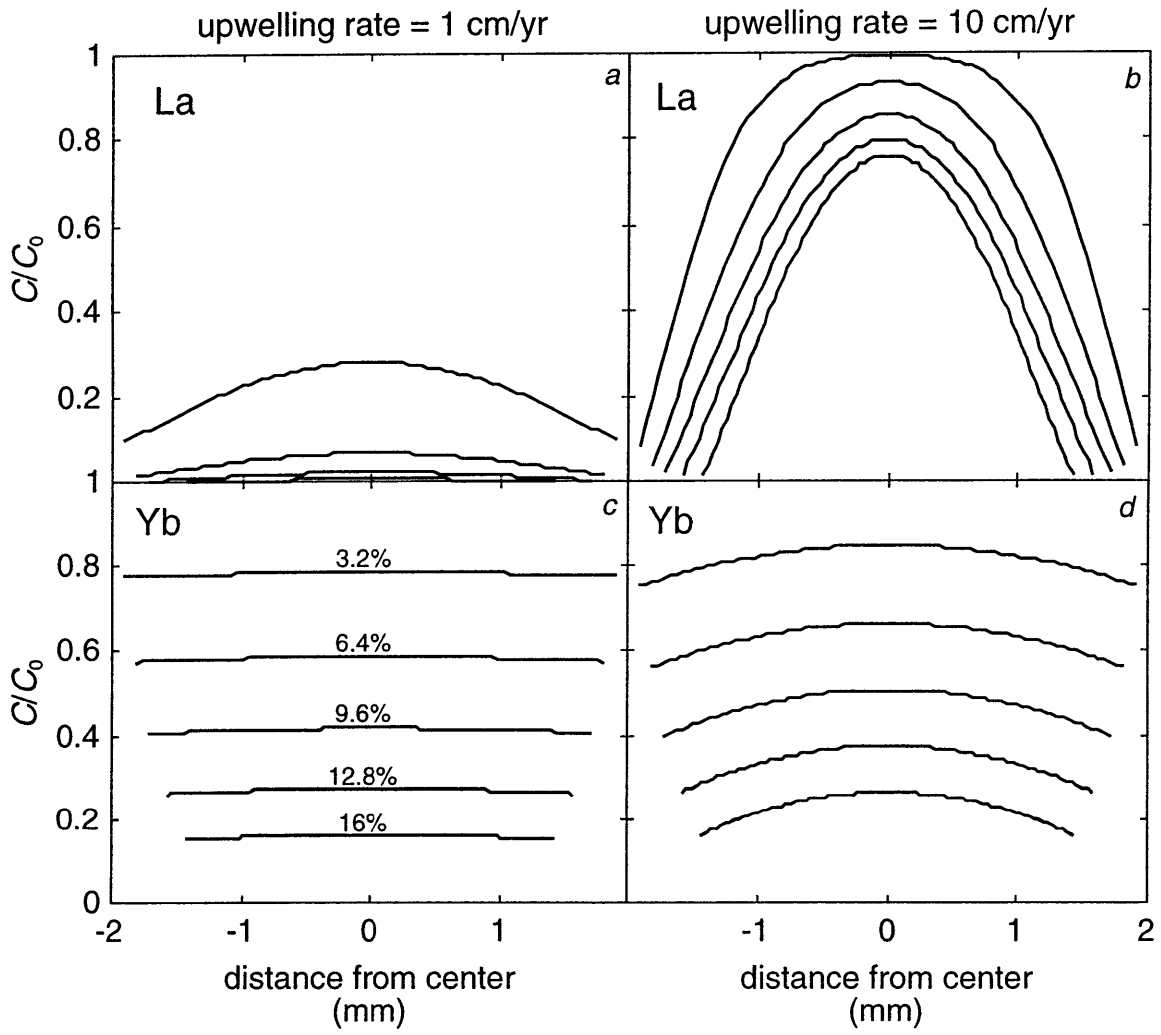
upwelling rate = 1 cm/yr
upwelling rate = 10 cm/yr
La
a
La
b
Yb
c
Yb
d
3.2%
6.4%
9.6%
12.8%
16%
C/C0
C/C0
1
0.8
0.6
0.4
0.2
0
-2
-1
0
1
2
distance from center (mm)
distance from center (mm)

Figure 2a

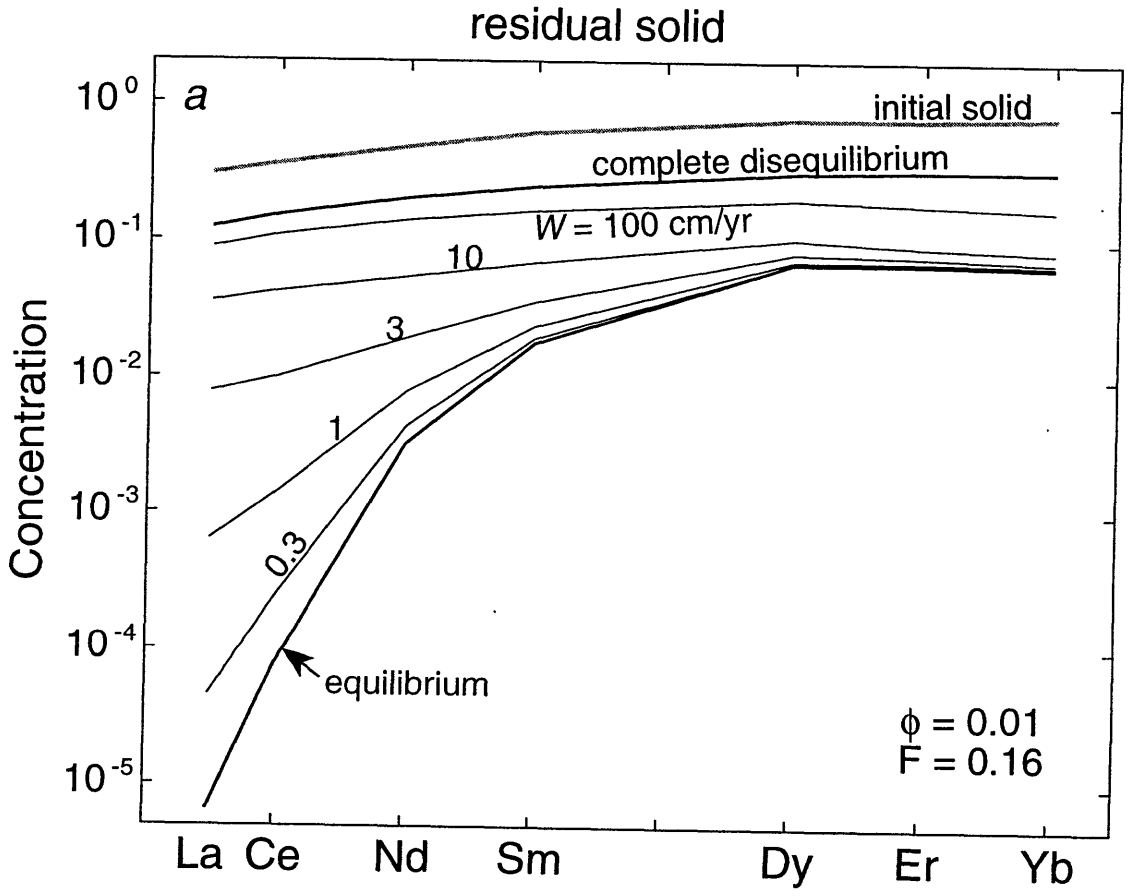
residual solid
a
initial solid
complete disequilibrium
W = 100 cm/yr
10
3
1
0.3
equilibrium
ϕ = 0.01
F = 0.16
Concentration
10^0
10^-1
10^-2
10^-3
10^-4
10^-5
La
Ce
Nd
Sm
Dy
Er
Yb

Figure 2b

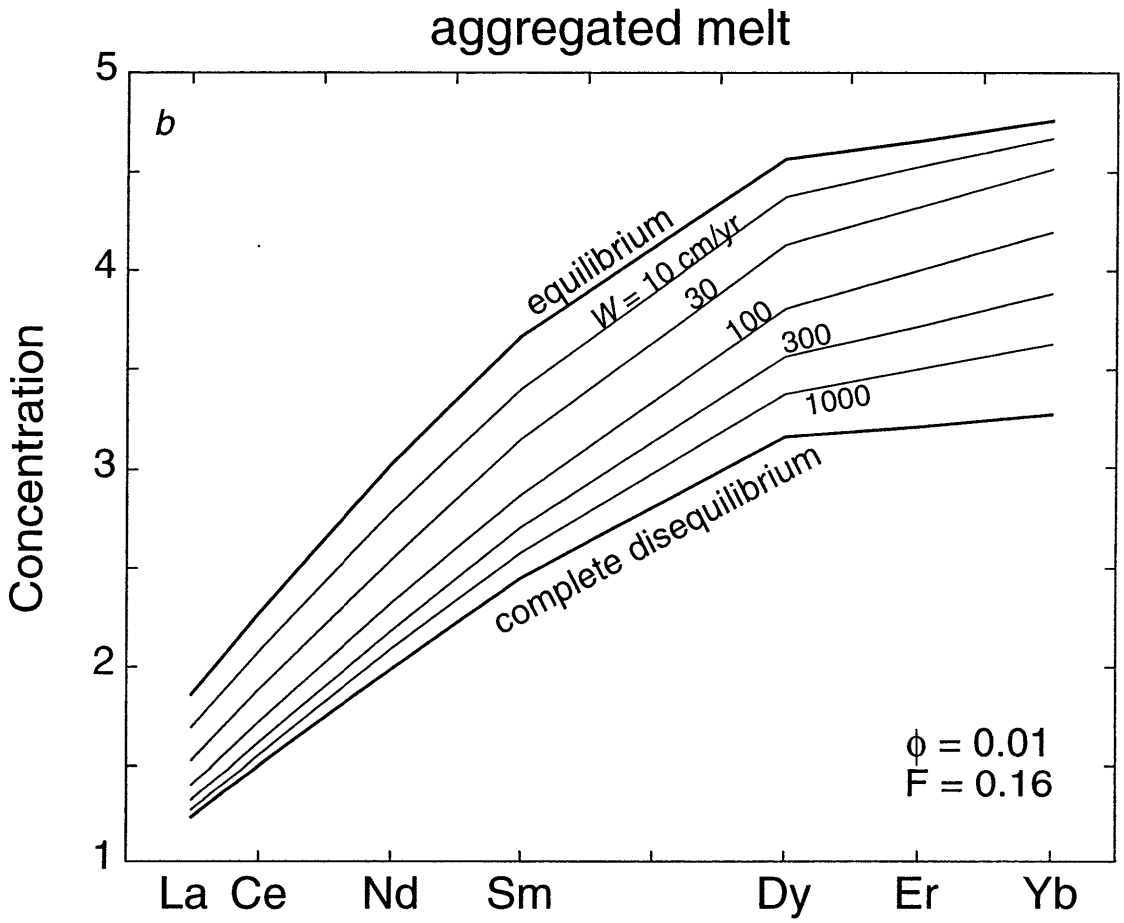
aggregated melt
b
Concentration
5
4
3
2
1
La
Ce
Nd
Sm
Dy
Er
Yb
equilibrium
W = 10 cm/yr
30
100
300
1000
complete disequilibrium
ϕ = 0.01
F = 0.16

Figure 3

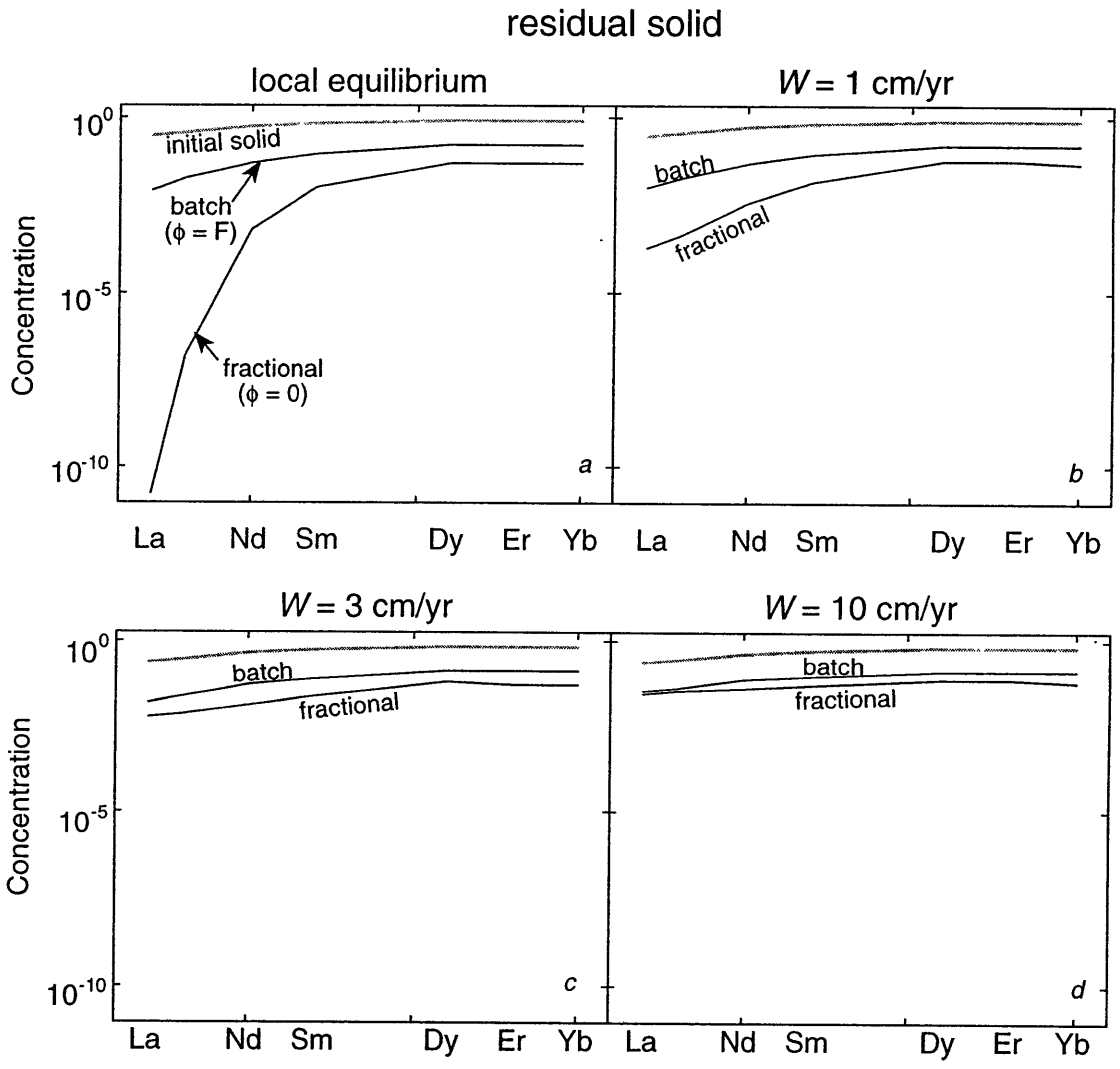
residual solid
local equilibrium
W = 1 cm/yr
W = 3 cm/yr
W = 10 cm/yr
Concentration
10^0
10^-5
10^-10
initial solid
batch
(ϕ = F)
fractional
(ϕ = 0)
a
b
c
d
La
Nd
Sm
Dy
Er
Yb

Figure 4

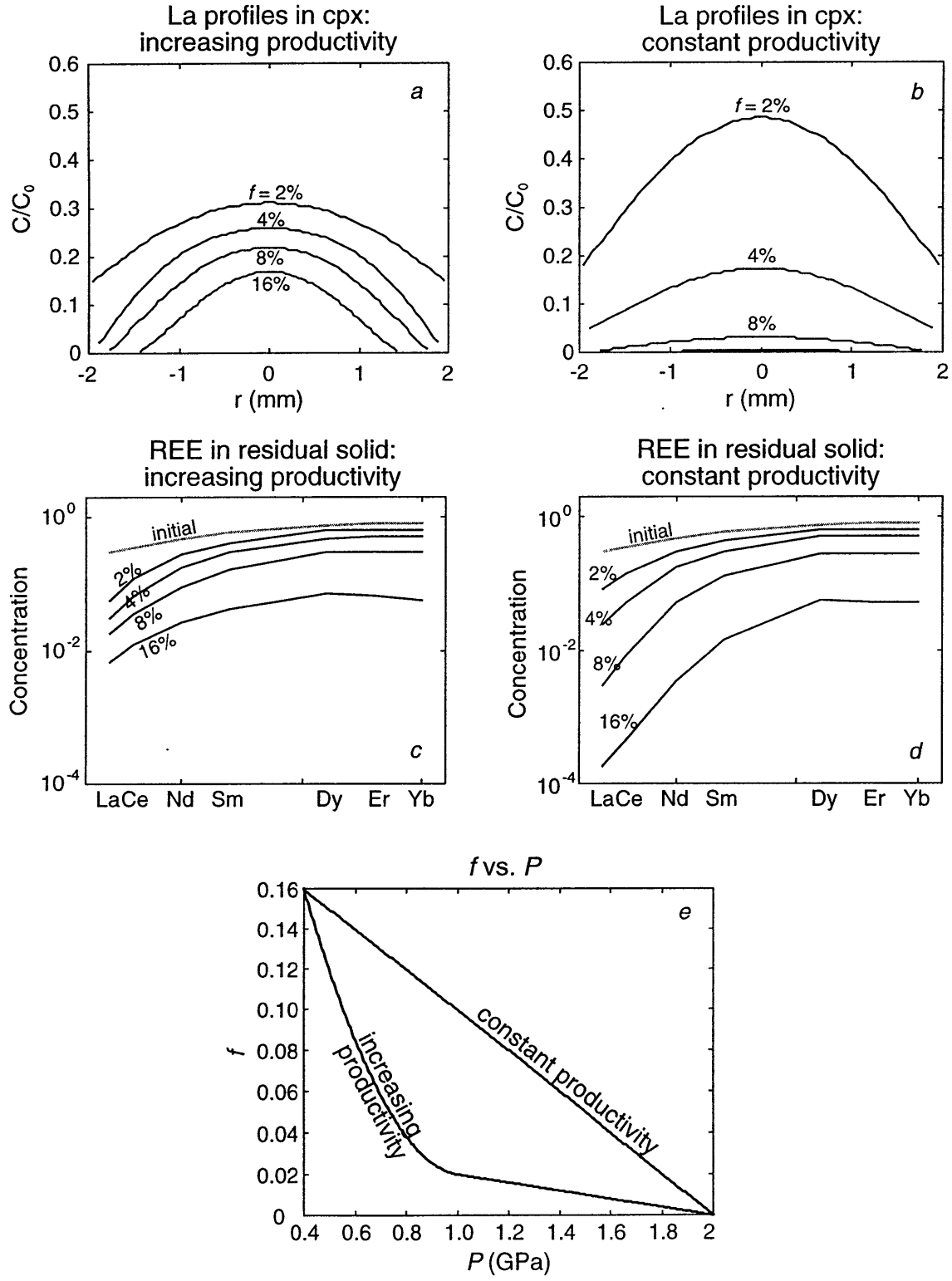
La profiles in cpx:
increasing productivity
a
C/C0
f = 2%
4%
8%
16%
r (mm)
La profiles in cpx:
constant productivity
b
f = 2%
4%
8%
r (mm)
REE in residual solid:
increasing productivity
c
Concentration
initial
2%
4%
8%
16%
LaCe Nd Sm Dy Er Yb
REE in residual solid:
constant productivity
d
f vs. P
e
f
constant productivity
increasing productivity
P (GPa)

Figure 5

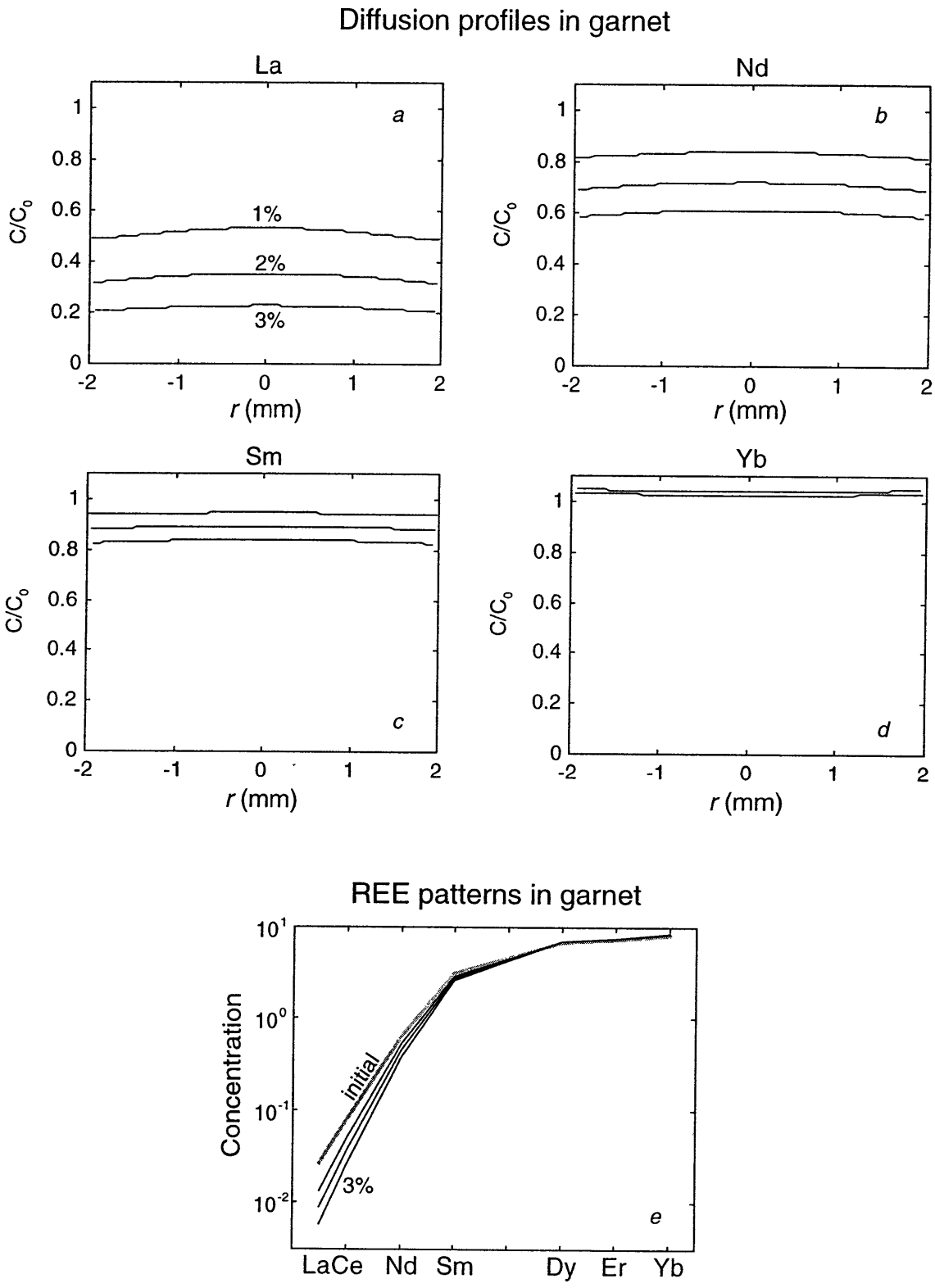
Diffusion profiles in garnet
La
Nd
Sm
Yb
a
b
c
d
1%
2%
3%
C/C0
r (mm)
REE patterns in garnet
Concentration
initial
3%
e
LaCe
Nd
Sm
Dy
Er
Yb

Figure 6

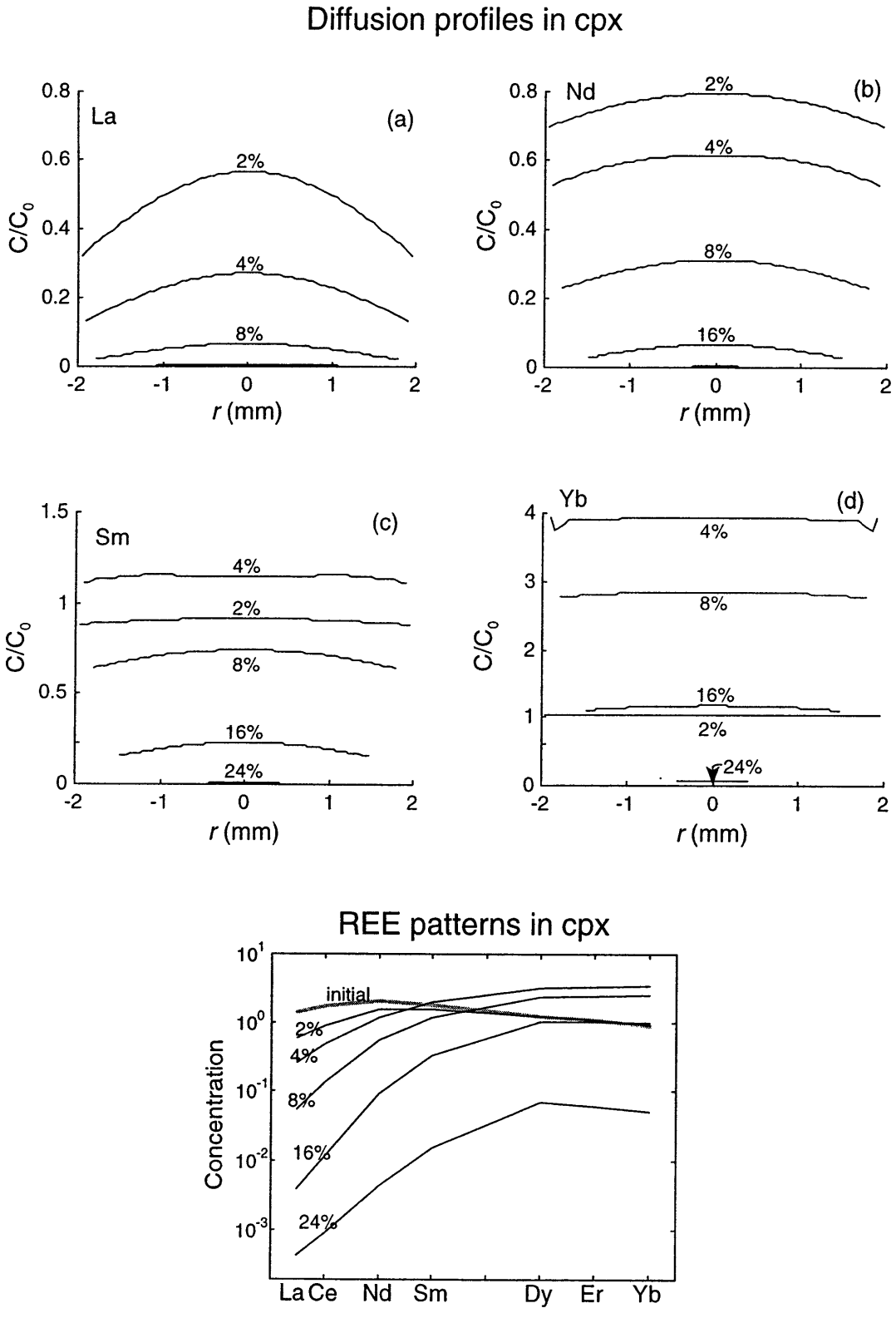
Diffusion profiles in cpx
La
(a)
2%
4%
8%
Nd
(b)
2%
4%
8%
16%
Sm
(c)
4%
2%
8%
16%
24%
Yb
(d)
4%
8%
16%
2%
24%
C/C0
r (mm)
REE patterns in cpx
Concentration
initial
2%
4%
8%
16%
24%
La Ce Nd Sm Dy Er Yb

Figure 7

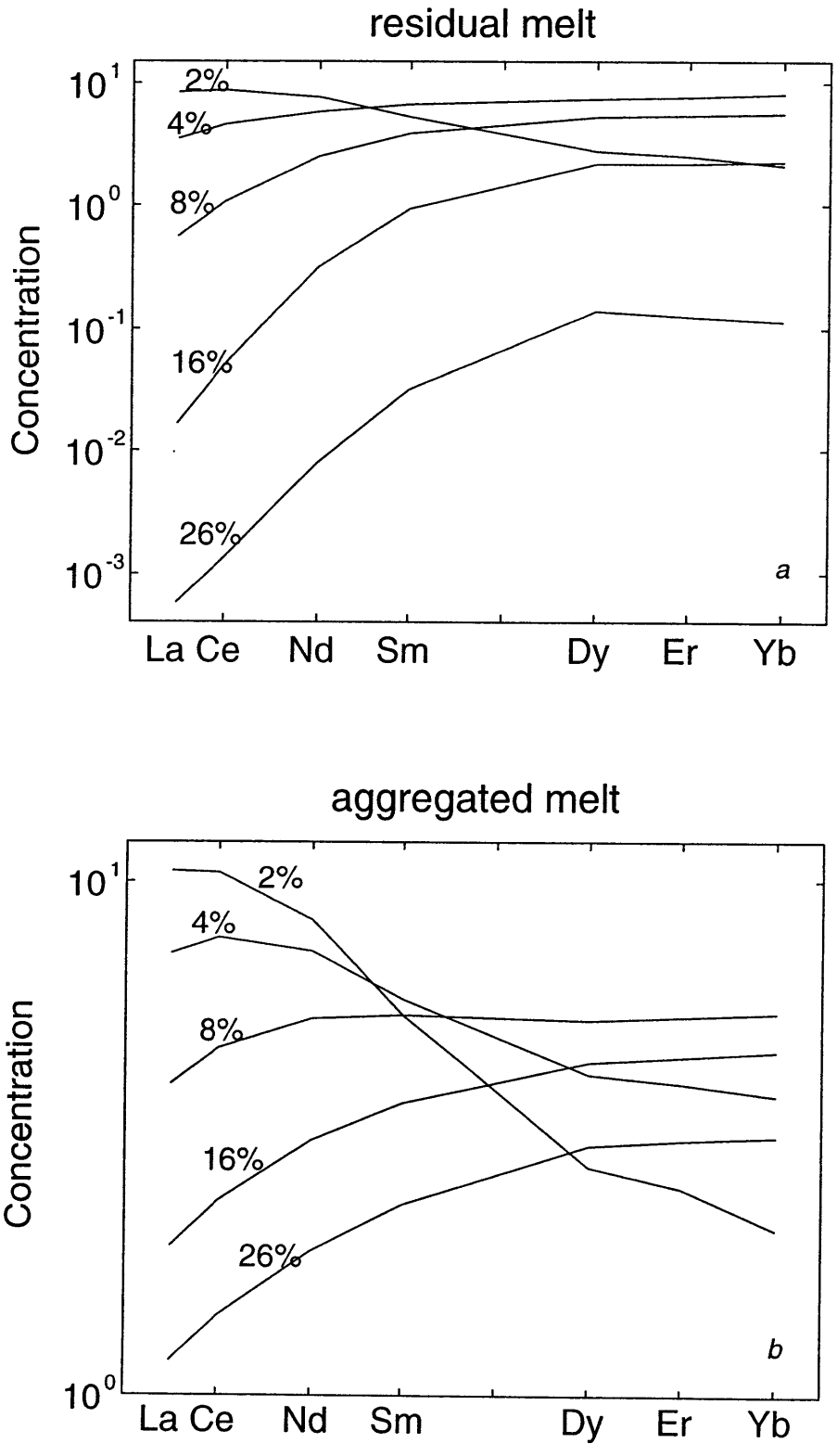
residual melt
Concentration
10^{1}
10^{0}
10^{-1}
10^{-2}
10^{-3}
2%
4%
8%
16%
26%
a
La Ce Nd Sm Dy Er Yb
aggregated melt
Concentration
10^{1}
10^{0}
2%
4%
8%
16%
26%
b
La Ce Nd Sm Dy Er Yb

Figure 8

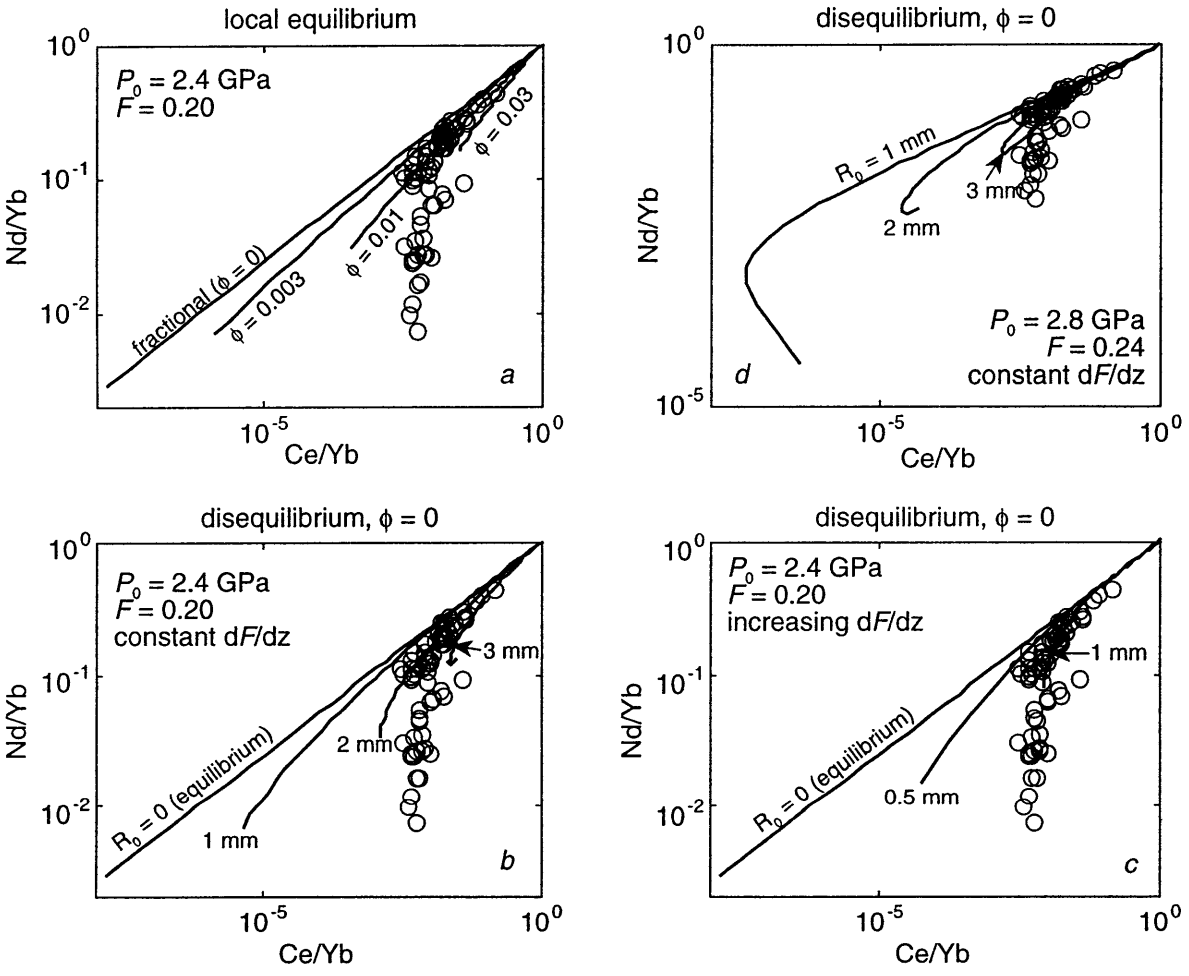
local equilibrium
P_0 = 2.4 GPa
F = 0.20
fractional (ϕ = 0)
ϕ = 0.003
ϕ = 0.01
ϕ = 0.03
a
disequilibrium, ϕ = 0
P_0 = 2.8 GPa
F = 0.24
constant dF/dz
R_0 = 1 mm
2 mm
3 mm
d
disequilibrium, ϕ = 0
P_0 = 2.4 GPa
F = 0.20
constant dF/dz
R_0 = 0 (equilibrium)
1 mm
2 mm
3 mm
b
disequilibrium, ϕ = 0
P_0 = 2.4 GPa
F = 0.20
increasing dF/dz
R_0 = 0 (equilibrium)
0.5 mm
1 mm
c
Nd/Yb
Ce/Yb
10^0
10^{-1}
10^{-2}
10^{-5}

CHAPTER 4.

URANIUM AND THORIUM DIFFUSION IN DIOPSIDE: IMPLICATIONS FOR U-SERIES DISEQUILIBRIUM IN MORB

ABSTRACT

This paper presents new experimental data on the tracer diffusion rates of U and Th in diopside at 1 atm and 1150-1300 °C. Diffusion couples were prepared by depositing a thin layer of U-Th oxide onto the polished surface of a natural diopside single crystal, and diffusion profiles were measured by ion microprobe depth profiling. For diffusion parallel to [001] the following Arrhenius relations were obtained:

$$\log_{10} D_U = (-5.75 \pm 0.98) - (418 \pm 28 \text{ kJ/mol})/2.303RT$$
$$\log_{10} D_{Th} = (-7.77 \pm 0.92) - (356 \pm 26 \text{ kJ/mol})/2.303RT$$

The diffusion data are used to assess the extent to which equilibrium is obtained during near fractional melting of a high-Ca pyroxene bearing mantle peridotite. We find that the diffusion rates for both elements are slow and that disequilibrium between solid and melt will occur under certain melting conditions. For near-fractional adiabatic decompression melting at ascent rates > 3 cm/yr, high-Ca pyroxene will exhibit disequilibrium effects. High-Ca pyroxene will become zoned in U and Th and the melts extracted will be depleted in these incompatible elements relative to melts produced by equilibrium fractional melting. U and Th diffusivities in high-Ca pyroxene are similar, and diffusive fractionation of these elements will be limited. Numerical solutions to a dynamic melting model with diffusion-controlled chemical equilibration indicate that the activity ratio [^{230}Th/^{238}U] in a partial melt of spinel peridotite will be slightly less than 1 for a broad range of melting parameters. This result reinforces the conclusion that melting of spinel peridotite cannot account for ^{230}Th excesses in mid-ocean ridge and ocean island basalts, and that garnet must therefore be present over part of the melting column.

INTRODUCTION

Radioactive disequilibrium between ^{238}U and ^{230}Th is widely used to infer the rate and style of melting and melt transport in the mantle (McKenzie, 1984; Williams and Gill, 1989; Spiegelman and Elliott, 1993; Qin, 1993; Iwamori, 1994; Richardson and McKenzie, 1994; Lundstrom et al., 1995; Elliott, 1997). Making full use of the ^{238}U-^{230}Th system requires knowing in which minerals and at what depths in the mantle U and Th are fractionated from each other. Clinopyroxene (cpx) and garnet are the principal hosts of U and Th in upper mantle rocks and control the fluxes of these elements during melting. Equilibrium mineral/melt partition coefficients for U and Th between clinopyroxene and basaltic melt are small (~10^{-3} to 10^{-2}) and differ by only about a factor of 2, with U being the more incompatible element (LaTourrette and Burnett, 1992; Beattie, 1993a; Hauri et al., 1994; Lundstrom et al., 1994; Salters and Longhi, 1996). The similarity between U and Th partition coefficients implies that clinopyroxene has little ability to fractionate these elements. Even if significant fractionation were possible it would be in the wrong sense to explain the ^{230}Th excesses observed in nearly all recently erupted mid-ocean ridge basalts (MORB) (Condomines et al., 1988; Bourdon et al., 1996). On the other hand, U and Th partition coefficients between garnet and basaltic melt differ by nearly an order of magnitude (Beattie, 1993b; LaTourrette et al., 1993; Hauri et al., 1994), with Th being the more incompatible element. The equilibrium partitioning data, then, appear to require melting in the presence of garnet to explain the excess ^{230}Th in MORB. This is an important conclusion because it requires that melting begins at depths greater than ~75 km, where garnet becomes the stable aluminous phase in peridotite (Takahashi and Kushiro, 1983; Takahashi, 1986) or, alternatively, that garnet pyroxenite is an important component of the MORB source (Hirschmann and Stolper, 1996).

The conclusion that clinopyroxene cannot deliver excess ^{230}Th to the melt is valid if chemical equilibrium between cpx and melt is maintained during melting. If, however, diffusion in clinopyroxene is slow relative to the melting rate, then equilibrium may not be achieved. In this case fractionation between U and Th depends strongly on the relative diffusion rates of

these elements (Qin, 1992; Iwamori 1993a,b). A reversal in the effective compatibility order of two elements is possible if the more compatible element diffuses significantly faster than the incompatible element (Qin, 1992). To produce excess ^{230}Th in the melt by a disequilibrium mechanism would require that (1) U diffuses slowly enough in clinopyroxene that equilibrium between cpx and melt is not achieved, and (2) Th diffuses significantly faster than U. To determine whether disequilibrium melting can influence U and Th partitioning, we performed a series of experiments to measure the diffusion rates of U and Th in diopside in the temperature range 1150-1300 °C.

EXPERIMENTAL METHODS

Sample preparation

Diffusion experiments were performed on gem-quality natural diopside crystals from the Kunlun Mts., China (American Museum of Natural History samples #100242 and #104501). The crystals were light green, transparent, free of cracks and visible inclusions, and had major element compositions very near pure diopside (Table 1). Each crystal was sectioned perpendicular to the *c* crystallographic axis into slabs ~0.5 mm thick. One side of each slab was polished to 0.06 μm alumina grit and then cut into pieces 1-2 mm on a side. These pieces were cleaned ultrasonically in deionized water and then pre-annealed for 2 days at 1200 °C, with oxygen fugacity controlled near the quartz-fayalite-magnetite (QFM) buffer.

The diffusion source material was deposited as an aqueous solution onto the polished surface of the diopside. A dilute (0.05 M) nitric acid solution that contained dissolved U, Th, and Al in 1:1:4 molar proportions was prepared from 10,000 μg/ml ICP standard solutions and diluted with purified water to 270 μg U/ml. Approximately 1 μl of this solution was deposited onto the polished surface of the diopside, along with a small amount of methanol to reduce surface tension and allow the solution to spread uniformly over the sample surface. The solution was evaporated in air at 120 °C, which left a thin layer of nitrates with concentration $\sim 5\times10^{-10}$ mol/mm^2. At the conditions of the diffusion anneal, with f_{O_2} at the QFM buffer, the

nitrates decompose to Al_2O_3 and nearly stoichiometric $UThO_4$ (Levin et al., 1964; Chapman et al., 1964). Because U and Th have the same formal charge in the oxide (+4) that they presumably have in diopside, no further redox reactions are necessary to introduce these elements into the diopside lattice. There was no evidence in any of the experiments that the tracer layer reacted with the diopside. We calculate that less than 0.01% of the U and Th diffused into the diopside crystal during any of the experiments, and thus the tracer layer provided an effectively infinite reservoir of U and Th.

Al was added to the tracer solution as a possible charge-balancing species. However, as discussed below in the *Analyses* section, we were unable to detect Al diffusion profiles in any of our samples, and it is unclear whether Al was actually transported into the crystal during any of the diffusion anneals.

Diffusion anneals

Diffusion anneals were performed at constant temperature in open Pt crucibles placed in the hotspot of a Deltech DT31VT vertical gas mixing furnace, with anneal times ranging from 2 to 24 days. Run temperature was attained within approximately 5 minutes after introducing the charge into the furnace and was continuously monitored using a Pt-$Pt_{90}Rh_{10}$ thermocouple calibrated against the melting points of NaCl, Au, and Pd. Fluctuation in temperature over the course of each anneal was generally within ± 2 °C, with the exception of a single experiment (UTh1200b) in which the thermocouple degraded during the anneal; temperature for this experiment was assigned an uncertainty of ± 5 °C. Oxygen fugacity was controlled near the QFM buffer by mixing CO_2 and H_2 gases and was continuously monitored with a solid ZrO_2-CaO electrolyte oxygen sensor calibrated against the Fe-FeO, Ni-NiO, and Cu-Cu_2O buffers. Variation in f_{O_2} over the course of each experiment was within ± 0.1 log unit. Experiments were quenched by removing the sample from the furnace and allowing it to cool in air. Heating and cooling times were insignificant compared to the anneal durations, and therefore no attempt was made to account for diffusion during run-up or quenching.

In addition to the diffusion anneals, we performed "zero-time" experiments in order to evaluate systematic errors associated with analysis of the diffusion profiles. Diffusion couples were prepared as above, taken to 1200 °C and held there for approximately five minutes, then quenched in air.

After quenching, samples were rinsed ultrasonically in deionized water, then ethanol. They were then mounted in epoxy with the diffusion source layer facing up and coated with a thin layer of gold, which provided a conductive surface for ion microprobe depth profiling.

Analyses

Concentration profiles in the annealed samples were measured using the Cameca IMS 3f ion microprobe at the Woods Hole Oceanographic Institution. A primary beam of O^- ions was focused onto the surface of the sample, producing secondary ions that were continuously analyzed in a mass spectrometer. In this procedure successively deeper layers are sampled as the primary beam sputters through the sample, allowing concentrations to be measured as functions of depth. The primary beam was accelerated under a potential of ~8.2 kV and was focused to a diameter of ~20-30 μm, with beam currents usually in the range 10-20 nA. By analyzing "zero-time" experiments, we found that optimum resolution was achieved by rastering the primary beam over a square area 150-200 μm on a side and inserting a circular mechanical aperture 68 μm in diameter into the secondary optics. The aperture was centered over the sputtered area so that secondary ions were collected only from the central, flat portion of the pit. This configuration optimized depth resolution and minimized contamination of the diffusion profile with material from the tracer layer. In analyses of "zero-time" experiments, U and Th counts dropped sharply after penetration of the tracer layer, and fell to background levels at a depth of approximately 40 nm.

Secondary ions were measured in a series of cycles in which electron multiplier counts were collected in sequence on masses ^{27}Al (3 s), ^{44}Ca (5 s), ^{232}Th (15-30 s) and ^{238}U (15-30 s). The ^{44}Ca signal was monitored to determine the position of the interface between the tracer layer

and the diopside. ^{44}Ca counts increased sharply after the tracer layer was penetrated, which was usually within the first two or three cycles, and then decreased very gradually due to charging of the sample surface. To correct for the charging effect and for small fluctuations in primary beam intensity, ^{232}Th and ^{238}U counts were normalized to ^{44}Ca, and the ratios $^{232}Th/^{44}Ca$ and $^{238}U/^{44}Ca$ were used in place of raw Th and U counts to model diffusion coefficients.

Aluminum concentration profiles in annealed samples were indistinguishable from those from "zero-time" experiments: Al counts dropped sharply over the upper 20-30 nm and were nearly constant over the remaining depth interval.

Analysis "Reversals"

In order to be certain that the ion microprobe depth profiling technique was measuring the true concentration profile in the sample, we devised an analysis "reversal." We wanted to determine whether the diffusion profile was contaminated during the analysis by material from the tracer layer. Therefore, we reanalyzed one experiment (UTh1200a) from the reverse direction. The sample was extracted from its epoxy mount and remounted in high-strength thin section epoxy on a glass slide, with the tracer layer facing down. It was then carefully ground to a thickness of ~7 μm. After grinding, the thin section was polished with diamond and alumina pastes (to 0.06 μm alumina) and prepared as described above for SIMS depth profiling. Sputtering began on the polished surface and proceeded through the diopside crystal to the tracer layer. A higher primary beam current (30 nA) and smaller raster area (100 μm X 100 μm) were used for this analysis so that the relatively thick sample could be penetrated in a reasonable time (approximately 10 hours). In the discussion below, results of this analysis are referred to as a reversal.

Depth measurement

The depth of each sputtered pit was measured with a Sloan Dektak 8000 surface-contact profilometer equipped with a 2.5 μm diamond-tipped stylus. Prior to making the depth measurements, the gold coat was removed from the sample by ultrasonic rinsing in a KI

solution. At least two orthogonal scans were made for each pit, and in each we considered the mean depth over the central ~70 μm. Pits produced under the same primary beam conditions yielded consistent sputtering rate estimates, confirming that the sputtering rate during each analysis was constant. Although the profilometer is capable of measuring depth to a precision of ~1 nm, the uncertainty in the depth measurement was considerably greater, being controlled primarily by the roughness of the sample surface. In most cases the vertical relief at the bottom of the sputtered pit was between 10 and 40 nm.

Determination of diffusion coefficients

Diffusion in these experiments is well described by the equation for one-dimensional diffusion in a semi-infinite medium, with constant interface concentration (Crank, 1975):

$$\frac{C(x,t) - C_0}{C_i - C_0} = erf\left(\frac{x}{2\sqrt{Dt}}\right) \qquad (1)$$

where C is the concentration at depth x after annealing time t, C_0 is the concentration at the interface, C_i is the initial concentration in the diopside crystal (essentially zero for both U and Th), and D is the diffusion coefficient. A typical diffusion profile is shown in Fig. 1a. The first few points in the profile were sometimes high due to contamination from the tracer layer, and these points were disregarded in the fitting procedure. To extract a diffusion coefficient from the data, each profile was linearized by plotting the inverse error function of the left-hand side of Eq. 1 against depth (Fig. 1b). The diffusion coefficient was then calculated from the relation $D = (4m^2t)^{-1}$, where m is the slope of the least-squares line fit to the inverted data. On the inverse error function plot, the data scatter and tail off slightly at the deep end of the profile as the concentration drops toward the detectability limit. We fit only the shallower part of the concentration profile and stopped including points when count rates approached background levels. Small adjustments in the interface concentration, C_0, were made in the fitting procedure to force the line through the origin.

RESULTS

Error Analysis

There are two types of uncertainty in our data set, one associated with intra-run variability and the second associated with reproducibility of diffusion coefficients for multiple experiments run at similar conditions. The source of uncertainty in the first is associated with error in measurement of the depth profile. In the second case there is the additional source of systematic error associated with our ability to exactly reproduce the conditions of the experiment.

The uncertainties associated with measurement of the diffusion profile can be assessed by comparing diffusion coefficients extracted from individual diffusion profiles from the same experiment. The uncertainty in the reported value of D for each profile was estimated from a combination of the error in the crater depth measurement and the formal uncertainty from the linear fit to the erf-inverted diffusion profile. When multiple diffusion profiles were measured on a single sample, these yielded diffusion coefficients that in nearly all cases were identical within error (Table 2). A single diffusion coefficient for each experiment was calculated by taking the weighted average of the results from each diffusion profile, with the weights being equal to the inverse square of the uncertainty in each measurement (Bevington and Robinson, 1992). These are the uncertainties reported in bold type in Table 2 and shown in the Arrhenius plots in Figure 4. An independent assessment of the diffusion coefficient measured in the "forward" profiles is given by our "reverse" profile measurement. Diffusion coefficients extracted from the reverse concentration profile were in excellent agreement with the forward measurements of the same experiment, and the quality of the profiles was very similar (Fig. 2). A measure of the inter-run reproducibility can be inferred by comparing experiments that were performed under the same temperature conditions. The range of values among duplicate runs is similar to that determined from separate profiles in a single sample (Table 2).

Time series

If volume diffusion is the mechanism responsible for U and Th transport, then the calculated diffusion coefficients should be independent of the duration of the experiment. We ran three experiments at 1200 °C that ranged in duration from 71 to 278 hours (nearly a factor of 4). U and Th diffusion coefficients in these experiments agreed within less than a factor of two (Fig. 3). Two experiments at 1300 °C also were in excellent agreement, although they covered a much smaller range in time (56-86 hours).

Temperature dependence

The diffusion coefficients calculated for each experiment were used to assess the temperature dependence of U and Th diffusion, which can be described by the Arrhenius equation:

$$D = D_0 e^{-H_a / RT} \qquad (2)$$

where D_0 is a frequency factor, H_a is the activation enthalpy, R is the gas constant and T is absolute temperature. Both U and Th show good Arrhenian behavior, exhibiting linear trends on a plot of log$D$ vs. inverse temperature (Fig. 4). Linear least-squares regressions of the data (York, 1969) yield the following Arrhenius relations:

$$\log D_U = (-5.75 \pm 0.98) - (418 \pm 28 \text{ kJ/mol})/2.303RT \qquad (3)$$

$$\log D_{Th} = (-7.77 \pm 0.92) - (356 \pm 26 \text{ kJ/mol})/2.303RT \qquad (4)$$

where the diffusion coefficients are in units of m^2/s and the uncertainties quoted are $\pm 1\sigma$. Uranium and thorium diffusivities converge with increasing temperature and are very similar near the melting point of diopside (~1390 °C).

DISCUSSION

Comparison with other diffusion data in diopside

Seitz (1973) reported a U tracer diffusion coefficient for diopside of 10^{-16} m^2/s at 1240 °C, which is four orders of magnitude higher than our results for U diffusion. His experiments

involved diopside crystals annealed in a diopside-albite-anorthite melt, and it is possible that growth of the crystals during the experiment accounts for the high apparent diffusivity.

Experimental measurements of tracer-, self-, and inter-diffusion coefficients have been reported for several other cations in natural diopside, and these are in good general agreement with our results (Fig. 5). The tracer diffusion data for cations that partition onto the M2 site are broadly consistent with trends observed in other minerals: diffusion rates increase with decreasing ionic charge and with decreasing ionic radius. The influence of ionic radius on tetravalent and trivalent cation diffusion rates in diopside is of the same order of magnitude as that observed in zircon (Cherniak et al., 1997a,b). In diopside, for example, the diffusion coefficient for Yb (0.985 Å radius in VIII-fold coordination; Shannon, 1976) is a factor of ~16 higher than for Ce (1.14 Å) at 1300 °C. In zircon, the diffusion coefficient for Yb is a factor of ~19 higher than Sm (1.08 Å) at the same temperature. In contrast, ionic charge appears to be much less important in diopside than in zircon, particularly for the +3 and +4 ions. In diopside the diffusion coefficients for U^{4+} (1.00 Å) and Yb^{3+} (0.985 Å) differ by about an order of magnitude. In zircon the effect of ionic charge is much greater, with Yb diffusivity being about 5 orders of magnitude faster than U (Cherniak et al., 1997a,b). This difference may be a consequence of the relatively small energy of the divalent M2 lattice site in diopside compared to that of the tetravalent VIII-fold site in zircon.

Early Partial Melting?

Several studies have observed that Fe-bearing pyroxenes exsolve a silica-enriched melt phase at temperatures far below their nominal melting temperatures (Ingrin et al., 1991; Doukhan et al., 1993). This phenomenon, termed early partial melting (EPM), appears to be related to cation vacancies associated with Fe^{3+} impurities (Jaoul and Raterron, 1994) and is sensitive to the Fe content of the pyroxene and the f_{O_2} of the surrounding atmosphere. The diopside we used has less Fe (less than half by mole) than pyroxenes in which EPM has so far

been observed, and it is unclear whether EPM would be expected under the conditions of our experiments. Optical inspection of our samples revealed no evidence for EPM, and if present, melt precipitates must be quite small in size. We note that where EPM has been unambiguously observed it has little effect on cation diffusion because the precipitates do not form an interconnected network. Dimanov et al. (1996) observed abundant glassy precipitates under the optical microscope in their experiments on Ca self-diffusion in Fe-bearing diopside, yet observed only a very small (one might argue unresolvable) inflection in the Arrhenius curve at the onset of EPM. We consider EPM effects absent in our data.

EQUILIBRATION DURING MELTING AND MELT TRANSPORT

In this section we use the U and Th diffusion data presented above to estimate the time scale of chemical equilibration during melting and melt transport. We first develop a scaling argument which shows that equilibrium between melt and the interiors of cpx grains is unlikely under most conditions appropriate to melting beneath mid-ocean ridges. We then use a numerical melting model to assess the degree of fractionation between U and Th during disequilibrium near-fractional melting.

Scaling argument

We follow the scaling approach adopted by Spiegelman and Kenyon (1992) and Hart (1993) to evaluate equilibration between clinopyroxene and melt during melt transport. The question we address is whether partitioning of U and Th between clinopyroxene and melt will approach equilibrium under conditions relevant to the production and transport of mid-ocean ridge basalts.

For melt percolating upward through an upwelling porous matrix, diffusive equilibration is governed by the Peclet number, which is equal to the ratio of the characteristic time required for diffusive transport in the solid grains of the matrix to the time required for melt to move through the system. For melt flowing across a layer of thickness H, which for our purposes

can be taken to be the height of the mantle melting column, the characteristic advection time can be written:

$$t_{adv} \approx \frac{H}{w} \qquad (6)$$

where w is the melt velocity.

As discussed by Hart (1993), the characteristic diffusion time, or more specifically the time required for the concentration of an element in the melt to reach 83% of its ultimate equilibrium value, is approximately:

$$t_D \approx \frac{r^2}{D(K)^{1.5}} \qquad (7)$$

where r is the radius of a cylinder of melt, D is the diffusion coefficient in the solid, and K is the solid/melt equilibrium partition coefficient. In this expression, the characteristic diffusion time depends on the compatibility of the element being considered. An incompatible element ($K < 1$) requires longer diffusion times than a compatible element because a larger volume of solid must be tapped in order to provide its higher relative abundance in the melt.

In a grain-scale porous network with wetting angle ~50°, the radius of a melt tubule is related to the grain size d and porosity ϕ by (Hart, 1993; von Bargen and Waff, 1986):

$$r \approx 0.13d(\phi)^{1/2} \qquad (8)$$

Conservation of mass in a one-dimensional upwelling column requires that (Spiegelman, 1993):

$$\phi = \frac{WF}{w} \qquad (9)$$

where W is the solid velocity, w is the melt velocity, and F is the melting degree. Combining Eqs. 6-9, the Peclet number can be written:

$$Pe = \frac{t_D}{t_{adv}} \approx \frac{d^2WF}{59D(K)^{1.5}H}. \qquad (10)$$

For a Peclet number >1, equilibration will be <83%.

Equation 10 is equivalent to the expression derived by Hart (1993) (his Eq. 6), who considered the time scale for growth of a melt tubule lying along grain boundaries rather than the time scale for porous flow through a network of melt tubules. These two time scales are the same because mass balance requires that the melt production and extraction rates are equal.

At 1400 °C, a temperature relevant to melting beneath mid-ocean ridges (Klein et al., 1987; McKenzie and Bickle, 1988; Kinzler and Grove, 1992), the diffusion coefficients for U and Th in clinopyroxene are both approximately 1.5×10^{-19} m^2/s, extrapolating from the Arrhenius relations given in Eqs. 3 and 4. Both U and Th have cpx/melt partition coefficients in the range 0.001-0.01 (LaTourrette and Burnett, 1992; Beattie, 1993a; Hauri et al., 1994; Lundstrom et al., 1994; Salters and Longhi, 1996). Taking a partition coefficient of 0.005, cpx grain diameter of 5 mm, mantle upwelling rate of 3 cm/yr, melting degree of 15%, and melting column height of 60 km, the Peclet number is ~20, which is within the disequilibrium domain. Figure 6 explores a more complete range of parameter values and shows that partitioning of U and Th between clinopyroxene and melt will be a disequilibrium process except at very slow spreading ridges. For example, a 5 mm grain at peridotite solidus temperatures (~1400-1500 °C) will approach partitioning equilibrium only at upwelling rates of ~1 cm/yr or slower. In contrast to the usual assumption (Spiegelman and Elliott, 1993; Lundstrom et al., 1995; Hart, 1993), we conclude that equilibrium may not be achieved during melting or grain-scale porous flow for highly incompatible and slowly-diffusing elements.

Numerical model

The scaling argument developed above allows us to estimate the conditions under which disequilibrium is expected during near-fractional melting, but it does not allow us to quantitatively predict the degree to which elements are fractionated due to their different diffusion rates. Numerical models have shown that the extent of elemental fractionation during disequilibrium melting is sensitive to the relative diffusion rates (e.g. Qin, 1992; Iwamori, 1993a,b). We adopt the disequilibrium melting model of Qin (1992), modified to allow for

non-modal melting and for temperature-dependent (and therefore time-dependent) diffusion coefficients, in order to evaluate whether U and Th can be fractionated significantly by clinopyroxene, and in particular whether there are any conditions under which their compatibility order may be reversed.

The model we adopt is a near-fractional melting model modified to account for diffusion-controlled chemical equilibration between solid and its enclosing melt. The solid is assumed to be composed of spherical grains of equal size which retain their spherical symmetry during melting. These grains are assumed to be homogeneous in composition when melting begins, with ^{238}U and ^{230}Th in radioactive equilibrium. During melting, the interface between the solid and melt is always in chemical equilibrium, and concentrations in the interiors of grains are controlled by diffusion. Melt remains with the residue until a critical melt fraction is reached and is thereafter removed at the rate that keeps the porosity constant. Extracted melt is pooled in a chemically isolated reservoir, and both residual and extracted melts are assumed to homogenize continuously and instantaneously, an excellent approximation considering that U and Th diffusion in silicate melts is ~8 orders of magnitude faster than in clinopyroxene (LaTourrette and Wasserburg, 1997).

For simplicity, the melting rate is assumed to be constant, but clinopyroxene is allowed to dissolve at a rate different from that of the bulk rock, that rate depending on the stoichiometric coefficient for cpx in the melting reaction and on the abundance of cpx in the rock. We consider U and Th fluxes between clinopyroxene and melt only; in other words, we assume that when melting begins all of the U and Th in the system reside in cpx and that the solid/liquid partition coefficients for other solid phases are equal to zero.

The concentrations of ^{238}U and ^{230}Th in a cpx grain are expressed by:

$$\frac{\partial C_{cpx}^{U}}{\partial t} = D_U(t)\left(\frac{\partial^2 C_{cpx}^{U}}{\partial r^2} + \frac{2}{r}\frac{\partial C_{cpx}^{U}}{\partial r}\right) - \lambda_U C_{cpx}^{U}$$
$$\frac{\partial C_{cpx}^{Th}}{\partial t} = D_{Th}(t)\left(\frac{\partial^2 C_{cpx}^{Th}}{\partial r^2} + \frac{2}{r}\frac{\partial C_{cpx}^{Th}}{\partial r}\right) + \lambda_U \frac{m_{Th}}{m_U} C_{cpx}^{U} - \lambda_{Th} C_{Cpx}^{Th} \qquad (11)$$

where C_{cpx}^{U} and C_{cpx}^{Th} are concentrations of ^{238}U and ^{230}Th at time t and radial distance r. λ_U and λ_{Th} are the decay constants and m_U and m_{Th} the masses of ^{238}U and ^{230}Th, respectively. These are expressions of Fick's second law in spherical coordinates, modified to account for decay of ^{238}U and ^{230}Th. The diffusion coefficients D_U and D_{Th} depend on the temperature-time path followed during melting and are thus functions of time. We assume that temperature decreases linearly with time and specify initial and final temperatures T_i and T_f.

Initial and boundary conditions for Eqs. (11) are:

$$\begin{aligned} C_{cpx}^{U}(r,0) &= C_o^U \\ C_{cpx}^{Th}(r,0) &= \frac{\lambda_U}{\lambda_{Th}} C_o^U \end{aligned} \qquad (12)$$

$$\begin{aligned} C_{cpx}^{U}(R(t),t) &= K_U C_m^U(t) \\ C_{cpx}^{Th}(R(t),t) &= K_{Th} C_m^{Th}(t) \end{aligned} \qquad (13)$$

where C_0^U is the initial concentration of ^{238}U in the clinopyroxene and K_U and K_{Th} are the equilibrium cpx/melt partition coefficients for U and Th. The first pair of equations describes the initial condition, in which ^{238}U and ^{230}Th are assumed to be in radioactive equilibrium and distributed homogeneously in a grain of clinopyroxene. The second states that the clinopyroxene rim is at all times in equilibrium with the residual melt.

Concentrations in the residual melt are described by:

$$\begin{aligned} \frac{d\left(V_m C_m^U\right)}{dt} &= -4\pi R(t)^2 D_U(t) \left.\frac{\partial C_{cpx}^U}{\partial r}\right|_{r=R(t)} + \upsilon_m \gamma C_{cpx}^U(R(t),t) - \upsilon_e C_m^U - \lambda_U V_m C_m^U \\ \frac{d\left(V_m C_m^{Th}\right)}{dt} &= -4\pi R(t)^2 D_{Th}(t) \left.\frac{\partial C_{cpx}^{Th}}{\partial r}\right|_{r=R(t)} + \upsilon_m \gamma C_{cpx}^{Th}(R(t),t) - \upsilon_e C_m^{Th} + V_m\left(\lambda_U \frac{m_{Th}}{m_U} C_m^U - \lambda_{Th} C_m^{Th}\right) \end{aligned} \qquad (14)$$

where C_m^U and C_m^{Th} are concentrations in the residual melt, V_m is the volume of residual melt, $R(t)$ is the radius of a clinopyroxene grain, υ_m and υ_e are the volumetric melting and melt extraction rates, respectively, and γ is the stoichiometric coefficient of clinopyroxene in the melting reaction. The terms on the right-hand side of Eq. (14) represent, in order, (1) the total diffusive current across the cpx/melt

interface at time t, (2) the U or Th mass flux out of the clinopyroxene by melting, (3) the mass flux out of the system by melt extraction, and (4) changes in mass due to decay of ^{238}U and ^{230}Th.

In the pooled extracted melt, concentrations are given by:

$$\frac{d\left(V_M C_M^U\right)}{dt} = \upsilon_e C_m^U - \lambda_U V_M C_M^U$$
$$\frac{d\left(V_M C_M^{Th}\right)}{dt} = \upsilon_e C_m^{Th} + V_M\left(\lambda_U \frac{m_{Th}}{m_U} C_M^U - \lambda_{Th} C_M^{Th}\right) \qquad (15)$$

where C_M^U and C_M^{Th} are concentrations in the extracted melt and V_M is the volume of melt extracted.

The melting rate, υ_m, is taken to be constant and is equal to:

$$\upsilon_m = \frac{V_0 WF}{H} \qquad (16)$$

where W is the solid upwelling velocity, F is the total degree of melting, and H is the height of the melting column. V_0 is the initial solid volume, defined as $V_0=4/3\pi R_0^3/X_{cpx}$, where X_{cpx} is the volume fraction of clinopyroxene in the solid. The melt extraction rate, υ_e, is initially zero and is equal to:

$$\upsilon_e = \frac{1}{1-\phi_{crit}}\upsilon_m \qquad (17)$$

when the melt fraction exceeds the critical value, ϕ_{crit}. The radius of a clinopyroxene grain, $R(t)$, changes with time according to:

$$R(t) = R_0\left(1 - \frac{\upsilon_m \gamma t}{V_0 X_{cpx}}\right)^{1/3}. \qquad (18)$$

Equations 11-18 were solved numerically using an implicit Crank-Nicolson finite difference scheme. The moving boundary between clinopyroxene and melt was accommodated by keeping a fixed number of radial grid points and rescaling the grid to the new grain radius at each time step.

We performed a series of model runs using the parameter values listed in Table 3. In each, the radial distribution of ^{238}U and ^{230}Th in cpx spheres and their concentrations in the

residual and aggregated melts are calculated as functions of time. Figure 7a illustrates the evolution of Th and U distributions in a cpx sphere under melting conditions typical for fast spreading ridges. Note that the interior of the crystal maintains high relative concentrations of U and Th and is far from equilibrium with the residual melt even at high degrees of melting. In contrast, at slow spreading ridges (Fig. 7b) clinopyroxene crystals approach equilibrium with the residual liquid. The upwelling rate at which disequilibrium becomes important depends on several factors, most importantly the grain size. The examples shown in Fig. 7 both used an initial grain diameter of 5 mm. This is within the range of cpx grain sizes (~2-10 mm diameter) in fertile peridotite xenoliths from Pali-Aike, Chile, which geochemically and isotopically resemble MORB-source mantle (Stern et al., 1989). Clinopyroxene grains from abyssal peridotites are typically smaller, with diameters up to 2-3 mm (Komor et al., 1990; Dick and Natland, 1996), but these rocks represent melting residues and are more appropriate for estimating the final, rather than initial, cpx radii. The actual size of cpx grains in MORB mantle is not well known, but a range of 2-10 mm provides a realistic lower limit. In model runs using an initial cpx diameter of 2 mm (not shown), cpx is in moderate disequilibrium with residual melt for fast spreading ridges (upwelling rate of 10 cm/yr). For an initial diameter of 10 mm, strong disequilibrium develops even at upwelling rates as slow as 1 cm/yr.

Deformation of high-Ca pyroxene during mantle upwelling

It is reasonable to question whether the model presented above is realistic for describing a solid mantle that deforms as it ascends. The model considers spherical high-Ca pyroxene grains that remain undeformed during decompression melting. Deformation of these grains would decrease the net diffusion length, thereby increasing the degree of equilibration between solid and melt. The degree to which high-Ca pyroxene is deformed during upwelling depends on its viscosity relative to the viscosities of olivine and orthopyroxene. Under typical upper mantle conditions of $T = 1400$ °C, $P = 1.5$ GPa and $\sigma = 0.3$ MPa, the viscosities of olivine and orthopyroxene are similar at approximately 5×10^{19} Pa s (Karato and Wu, 1993; Mackwell,

1991). Diopside is several orders of magnitude stiffer than either of these minerals, having a viscosity of about 4 x 10^{25} Pa s under the same conditions (Kirby and Kronenberg, 1984). Olivine and orthopyroxene, being much weaker than cpx, are expected to accommodate most of the strain associated with upwelling. The assumption in our model that high-Ca pyroxene grains remain undeformed during adiabatic decompression melting therefore seems reasonable.

Implications for $^{230}Th/^{238}U$ disequilibrium in MORB

It is clear that under certain melting conditions solid-state diffusion may exert strong control on the fluxes of U and Th between cpx and melt. Can excess ^{230}Th in the melt be generated under these conditions? Figure 8a shows activity ratios [^{230}Th/^{238}U] in the aggregated melt for a model run with cpx diameter of 5 mm and upwelling rate of 10 cm/yr. The solid curve was generated using the Arrhenius relations for U and Th given in Eqs. (3) and (4). The activity ratio is always below 1 and gradually converges on a steady-state value of ~0.97 as melting progresses. ^{230}Th excesses never occur because during the early stages of melting, at high temperature, U has a higher diffusivity than Th and is thus released more quickly into the melt. The dashed curves reflect the uncertainty in the relative diffusivity of U and Th, and were generated by running the model with U and Th Arrhenius lines rotated within their 1σ uncertainty limits. The upper curve pairs the steepest Th Arrhenius line with the shallowest U Arrhenius line, and the lower curve vice versa. The uncertainty envelope covers a moderate range of activity ratios at small melting degrees, including a region of small ^{230}Th excesses, but at higher degrees of melting becomes quite narrow and does not overlap the region with [^{230}Th/^{238}U] > 1.

Figure 8b shows a similar plot for an upwelling rate of 1 cm/yr. In this case cpx is close to equilibrium with the melt, and varying the U and Th Arrhenius parameters within their uncertainty limits has little effect on the activity curves. The activity ratio has a nearly constant value of ~0.96 for melting degrees above ~2%.

We conclude that it is highly unlikely that high-Ca pyroxene could be responsible for generating the ^{230}Th excesses observed in MORB. Most MORB lavas have [^{230}Th/^{238}U] activity ratios of 1.1-1.4 (e.g. Condomines et al., 1988; Bourdon et al., 1996), well outside the uncertainty limits defined by the upper and lower curves in Figs. 8a or 8b. Even at a very high degree of chemical disequilibrium, with a cpx diameter of 10 mm and an upwelling rate of 10 cm/yr, the uncertainty envelope never extends to an activity ratio above 1.15. Clinopyroxene can therefore be ruled out as the source of the ^{230}Th excess signal observed in ocean floor basalts, as it is unable to produce significant ^{230}Th excesses under either equilibrium or disequilibrium conditions.

Implications for ^{226}Ra/^{230}Th disequilibrium in MORB

The slow diffusivities of U and Th in high-Ca pyroxene have important consequences for the production of ^{226}Ra/^{230}Th disequilibrium in basalts. Radium is highly incompatible in both the garnet and spinel stability fields, and ^{226}Ra excesses in the melt may be produced at any depth within the melting column. However, during near-fractional melting under conditions of local equilibrium U, Th and Ra are efficiently stripped from the solid residue, and most of the ^{226}Ra excess must be produced near the bottom of the melting column. If ^{226}Ra excesses are produced at great depths, in the garnet stability field, then the rate of melt transport from these depths must be very rapid. To preserve the large Ra excesses that are observed in many MORB and OIB the melt transport time must be on the order of the half-life of ^{226}Ra (~1600 years) or less. For ^{226}Ra excesses produced at 80 km depth, the average rate of melt transport to the surface must be at least ~50 m yr^{-1}. Such rapid melt transport requires efficient channelized flow, with melt channels extending to depths near the site of excess ^{226}Ra production.

The constraint on minimum melt transport rates is relaxed if melting takes place under conditions of incomplete local equilibrium. Under disequilibrium conditions the effective compatibility of U and Th is increased, and because U and Th are stripped less efficiently from the solid ^{226}Ra can be produced at higher degrees of melting, and at shallower depths. In this

case the minimum melt transport rate is reduced, and channelized melt transport need not extend into the garnet stability field. Fractionation of Ra and Th is likely to be more efficient under disequilibrium conditions than under conditions of local equilibrium. Large divalent cations like Pb (Cherniak, 1998) and Sr (Sneeringer et al., 1984) diffuse several orders of magnitude more rapidly than Th. If Ra diffusion is similarly fast, then Ra will locally equilibrate during melting under conditions relevant to melting beneath ridges, and its effective partition coefficient will remain very low. As discussed above, Th is not expected to approach equilibrium under many conditions, and its effective partition coefficient will increase as the deviation from equilibrium increases. Thus, with increasing upwelling rate (and/or increasing grain size) the effective partition coefficients of Th and Ra diverge, and Ra/Th fractionation becomes increasingly efficient. If disequilibrium fractionation during melting has an important role in $^{226}Ra/^{230}Th$ disequilibrium, then the magnitude of ^{226}Ra disequilibrium should be higher at fast spreading ridges than at slow spreading ridges. Because less time is available for ingrowth, the magnitude of ^{230}Th excess decreases with increasing upwelling rate; therefore, if disequilibrium fractionation of Ra and Th is responsible for Ra excess there should be a negative correlation between ^{226}Ra excess and ^{230}Th excess. Such a correlation is indeed observed in the MORB data set (Kelemen et al., 1997), and may indicate disequilibrium fractionation. As Kelemen et al. (1997) point out, however, there are other ways to explain this trend. A more definitive test of the disequilibrium fractionation hypothesis awaits further $^{226}Ra/^{230}Th$ data from ridges covering a large range of spreading rates.

Partial melting is not the only process that can lead to secular disequilibrium of $^{226}Ra/^{230}Th$; excess ^{226}Ra may also be produced by chromatographic fractionation during melt transport (e.g. Spiegelman and Elliott, 1993). While slow diffusion of Th may increase the efficiency of Ra/Th fractionation during partial melting, the opposite is true during melt transport. During melt transport, the effective compatibility of Th *decreases* as the rate of chemical exchange between melt and solid decreases. With increasing deviation from equilibrium the effective mineral/melt partition coefficient tends toward 0, in contrast to melting

where the effective partition coefficient tends toward 1. During melt transport under conditions of incomplete local equilibrium, the Th partition coefficient will decrease, approaching that of Ra, and fractionation of the two elements will be less efficient than at local equilibrium. The model results presented above suggest that Th will not be in local equilibrium beneath mid-ocean ridges even at the relatively long time-scales over which the solid mantle moves through the melting regime. Considering that the melt must move upward even more rapidly than the solid given its greater intrinsic buoyancy, it is doubtful that Th will be able to achieve equilibrium with the solid during melt transport by a diffusive chemical exchange process. As a consequence, it is doubtful that large ^{226}Ra excesses can be produced by chromatographic fractionation.

That the slow diffusion of Th enhances the production of excess ^{226}Ra during melting, but inhibits ^{226}Ra/^{230}Th disequilibrium during melt transport, may help to resolve an important paradox that exists in the combined ^{238}U/^{230}Th/^{226}Ra data set. The presence of ^{230}Th excesses in MORB requires melting in the presence of garnet. To avoid chromatographic fractionation in the spinel stability field that will tend to erase ^{230}Th excesses, much of the melt must be transported in chemical disequilibrium. In contrast, the presence of ^{226}Ra excesses in MORB has usually been thought to require equilibrium transport of melt, and associated chromatographic fractionation of Ra and Th, because of the unrealistically rapid melt transport rates that are required to explain ^{226}Ra excesses by a melting process. Kelemen et al. (1997) have suggested that melt is transported in a two porosity regime, with some melt transported in channels (and contributing the ^{230}Th excess), and the rest transported by equilibrium porous flow (leading to ^{226}Ra excess). Alternatively, our results suggest that both the ^{230}Th and ^{226}Ra data may be explained by disequilibrium chemical fractionation during melting, without the need for chromatographic fractionation. Whether the U-series data are best explained in terms of a two porosity flow regime or by disequilibrium fractionation during melting can be tested by demonstrating whether there is a positive correlation between spreading rate and ^{226}Ra excess. Such a correlation should exist if disequilibrium melting is responsible for the production of

^{226}Ra excesses. If equilibrium porous flow is instead responsible for Ra/Th disequilibrium there should be no positive correlation between spreading rate and ^{226}Ra excess, unless the proportion of melt that occupies a grain-scale porous network increases with the solid upwelling rate.

REFERENCES

Beattie P. (1993a) The generation of uranium series disequilibria by partial melting of spinel peridotite: Constraints from partitioning studies. *Earth Planet. Sci. Lett.* **117**, 379-391.

Beattie P. (1993b) Uranium-thorium disequilibria and partitioning on melting of garnet peridotite. *Nature* **363**, 63-65.

Bevington P. R. and Robinson D.K. (1992) *Data Reduction and Error Analysis for the Physical Sciences, 2nd ed.*, McGraw-Hill.

Bourdon B., Zindler A., Elliott T. and Langmuir C. H. (1996) Constraints on mantle melting at mid-ocean ridges from global ^{238}U-^{230}Th disequilibrium data. *Nature* **385**, 231-235.

Chapman A. T. and Meadows R. E. (1964) Volatility of $UO_{2\pm x}$ and phase relations in the system uranium-oxygen. *J. Amer. Ceram. Soc.* **47**, 614-621.

Cherniak D. J. (1998) Pb diffusion in clinopyroxene. *Chem. Geol.* **150**, 105-117.

Cherniak D. J., Hanchar J. M. and Watson, E. B. (1997a) Rare-earth diffusion in zircon. *Chem. Geol.* **134**, 289-301.

Cherniak D. J., Hanchar J. M. and Watson, E. B. (1997b) Diffusion of tetravalent cations in zircon. *Contrib. Mineral. Petrol.* **127**, 383-390.

Condomines M., Hemond Ch., and Allègre C. J. (1988) U-Th-Ra radioactive disequilibria and magmatic processes. *Earth Planet. Sci. Lett.* **90**, 243-262.

Crank J. (1975) *The Mathematics of Diffusion, 2nd ed.* Oxford Univ. Press, Oxford.

Dick H. J.B. and Natland J. H. (1996) Late-stage melt evolution and transport in the shallow mantle beneath the East Pacific Rise. *In* C. Mevel, K.M. Gillis, J.F. Allan, and P.S. Meyer, eds., *Proc. ODP, Sci. Results* **147**, 103-134.

Dimanov A., Jaoul O., and Sautter V. (1996) Calcium self-diffusion in natural diopside single crystals. *Geochim. Cosmochim. Acta* **60**, 4095-4106.

Doukhan N., Doukhan J. C., Ingrin J., Jaoul O. and Raterron P. (1993) Early partial melting in pyroxenes. *Amer. Mineral.* **78**, 1247-1257.

Elliott T. (1997) Fractionation of U and Th during mantle melting: A reprise. *Chem. Geol.* **139**, 165-183.

Grove T. L. and Wagner T. P. (1993) Is adiabatic melting of oceanic mantle a disequilibrium process? Constraints from experimental measurement of element diffusion rates in high-Ca pyroxene. *EOS Trans. AGU* **74**, 284.

Hart S. R. (1993) Equilibration during mantle melting: A fractal tree model, *Proc. Natl. Acad. Sci.* **90**, 11,914-11,918.

Hauri E. H., Wagner T. P. and Grove T. L. (1994) Experimental and natural partitioning of Th, U, Pb and other trace elements between garnet, clinopyroxene and basaltic melts. *Chem. Geol.* **117**, 149-166.

Hirschmann M. M. and Stolper E. M. (1996) A possible role for garnet pyroxenite in the origin of the "garnet signature" in MORB. *Contrib. Mineral. Petrol.* **124**, 185-208.

Ingrin J., Doukhan N. and Doukhan J. C. (1991) High temperature deformation of diopside single crystal: 2. TEM investigation of the defect microstructures. *J. Geophys. Res.* **96**, 14287-14297.

Iwamori H. (1993a) Dynamic disequilibrium melting model with porous flow and diffusion controlled chemical equilibration. *Earth Planet. Sci. Lett.* **114**, 301-313.

Iwamori H. (1993b) A model for disequilibrium mantle melting incorporating melt transport by porous and channel flows. *Nature* **366**, 734-737.

Iwamori H. (1994) ^{238}U-^{230}Th-^{226}Ra and ^{235}U-^{231}Pa disequilibria produced by mantle melting with porous and channel flows. *Earth Planet. Sci. Lett.* **125**, 1-16.

Jaoul O. and Raterron P. (1994) High-temperature deformation of diopside crystal 3. Influences of pO_2 and SiO_2 precipitation. *J. Geophys. Res.* **99**, 9423-9439.

Karato S. and Wu P. (1993) Rheology of the upper mantle: a synthesis. *Science* **260**, 771-778.

Kelemen P. B., Hirth G., Shimizu N., Spiegelman M., and Dick H. J. B. (1997) A review of melt migration processes in the adiabatically upwelling mantle beneath ocean spreading ridges. *Phil. Trans. R. Soc. Lond. A* **355**, 283-318.

Kinzler R. J. and Grove T. L. (1992) Primary magmas of mid-ocean ridge basalts, 2. Applications. *J. Geophys. Res.* **97**, 6907-6926.

Kirby S. H. and Kronenberg A. K. (1984) Deformation of clinopyroxenite: Evidence for a transition in flow mechanisms and semi-brittle behavior. *J. Geophys. Res.* **89**, 3177-3192.

Klein E. M. and Langmuir C. H. (1987) Global correlations of ocean ridge basalt chemistry with axial depth and crustal thickness. *J. Geophys. Res.* **92**, 8089-8115.

Komor S. C., Grove T. L., and Hebert R. (1990) Abyssal peridotites from ODP Hole 670A (21°10'N, 45°02'W): Residues of mantle melting exposed by non-constructive axial divergence. *In* R. Detrick, J. Honnorez, W.B. Bryan, T. Juteau, et al., eds., *Proc. ODP, Sci. Results* **106/109**, 85-99.

LaTourrette T. Z. and Burnett D. S. (1992) Experimental determination of U and Th partitioning between clinopyroxene and natural and synthetic basaltic liquid. *Earth Planet. Sci. Lett.* **110**, 227-244.

LaTourrette T. and Wasserburg G. J. (1997) Self diffusion of europium, neodymium, thorium, and uranium in haplobasaltic melt: The effect of oxygen fugacity and the relationship to melt structure. *Geochim. Cosmochim. Acta* **61**, 755-764.

LaTourrette T. Z., Kennedy A. K. and Wasserburg G. J., (1993) Thorium-uranium fractionation by garnet: Evidence for a deep source and rapid rise of oceanic basalts. *Science* **261**, 739-742.

Levin E. M., Robbins C. R. and McMurdie H. F. (1964) *Phase Diagrams for Ceramists*, American Ceramic Society, Columbus, Ohio.

Lundstrom C. C., Gill J., Williams Q., and Perfit M. R (1995) Mantle melting and basalt extraction by equilibrium porous flow. *Science* **270**, 1958-1961.

Lundstrom C. C., Shaw H. F., Ryerson F. J., Phinney D. L., Gill J. B., and Williams Q. (1994) Compositional controls on the partitioning of U, Th, Ba, Pb, Sr, and Zr between clinopyroxene and haplobasaltic melts: Implications for uranium series disequilibria in basalts. *Earth Planet. Sci. Lett.* **128,** 407-423.

Mackwell S. J. (1991) High-temperature rheology of enstatite: Implications for creep in the mantle. *Geophys. Res. Lett.* **18**, 2027-2030.

McKenzie D. (1985) ^{230}Th-^{238}U disequilibrium and the melting process beneath ridge axes. *Earth Planet. Sci. Lett.* **72**, 149-157.

McKenzie D. and Bickle M. J. (1988) The volume and composition of melt generated by extension of the lithosphere. *J. Petrol.* **29**, 625-679.

Qin Z. (1992) Disequilibrium partial melting model and its implications for trace element fractionations during mantle melting. *Earth Planet. Sci. Lett.* **112**, 75-90.

Qin Z. (1993) Dynamics of melt generation beneath mid-ocean ridge axes: Theoretical analysis based on ^{238}U-^{230}Th-^{226}Ra and ^{235}U-^{231}Pa disequilibria. *Geochim. Cosmochim. Acta* **57**, 1629-1634.

Richardson C. and McKenzie D. (1994) Radioactive disequilibria from 2D models of melt generation by plumes and ridges. *Earth Planet. Sci. Lett.* **128**, 425-437.

Salters V. J. M. and Longhi J. (1996) Partitioning of trace elements during primary melting of MORB mantle. *J. Conf. Abstr.* **1**, 529.

Seitz M. G. (1973) Uranium and thorium diffusion in diopside and fluorapatite. *Carnegie Inst. Wash. Yrbk.* **72**, 586-588.

Shannon R. D. (1976) Revised effective ionic radii and systematic studies of interatomic distances in halides and chalcogenides. *Acta Crystall.* **A32**, 751-767.

Sneeringer M., Hart S. R. and Shimizu N. (1984) Strontium and samarium diffusion in diopside. *Geochim. Cosmochim. Acta* **48**, 1589-1608.

Spiegelman M. (1993) Physics of melt extraction: Theory, implications, and applications. *Phil. Trans. R. Soc. Lond. A* **342**, 23-41.

Spiegelman M. and Elliott T. (1993) Consequences of melt transport for uranium series disequilibrium in young lavas. *Earth Planet. Sci. Lett.* **118**, 1-20.

Spiegelman M. and Kenyon P. (1992) The requirements for chemical disequilibrium during magma migration. *Earth Planet. Sci. Lett.* **109**, 611-620.

Stern C. R., Saul S., Skewes M. A. and Futa K. (1989) Garnet peridotite xenoliths from the Pali-Aike alkali basalts of southernmost South America. *Geol. Soc. Australia Spec. Pub.* **14**, 735-744.

Takahashi E. (1986) Melting of a dry peridotite KLB-1 up to 14 GPa: Implication on the origin of peridotitic upper mantle. *J. Geophys. Res.* **91**, 9367-9382.

Takahashi E. and Kushiro I. (1983) Melting of a dry peridotite at high pressures and basalt magma genesis. *Am. Mineral.* **68**, 859-879.

Williams R. W. and Gill J. B. (1989) Effects of partial melting on the uranium decay series. *Geochim. Cosmochim. Acta* **53**, 1607-1619.

von Bargen N. and Waff H. S. (1986) Permeabilities, interfacial areas, and curvatures of partially molten systems: Results of numerical computations of equilibrium microstructures. *J. Geophys. Res.* **91**, 9261-9276.

York D. (1969) Least squares fitting of a straight line with correlated errors. *Earth Planet. Sci. Lett.* **3**, 320-324.

Table 1. Kunlun Mts. diopside composition.

Oxide	Weight %
SiO_2	55.5
TiO_2	0.06
Al_2O_3	0.88
FeO^{tot}	0.55
MgO	18.1
CaO	24.7
Na_2O	0.53
Total	100.3

Table 2. Run conditions and experimental results.

ID	T (°C)	anneal time (hr)	$D_{Th} \pm 1\sigma$ (m^2/s)	$D_U \pm 1\sigma$ (m^2/s)
UTh1150a	1150	576.80	$1.59 \pm 0.31 \times 10^{-21}$	$4.54 \pm 1.55 \times 10^{-22}$
UTh1150b	1150	456.61	$1.18 \pm 0.21 \times 10^{-21}$	$9.52 \pm 1.69 \times 10^{-22}$
			$1.55 \pm 1.09 \times 10^{-21}$	$5.78 \pm 6.98 \times 10^{-22}$
			$1.20 \pm 0.20 \times 10^{-21}$	**$9.44 \pm 1.66 \times 10^{-22}$**
UTh1200a	1200	70.65	$4.56 \pm 1.21 \times 10^{-21}$*	$3.33 \pm 7.27 \times 10^{-21}$*
			$6.38 \pm 2.37 \times 10^{-21}$	$2.54 \pm 1.99 \times 10^{-21}$
			$5.06 \pm 1.00 \times 10^{-21}$	$2.39 \pm 0.70 \times 10^{-21}$
			$6.87 \pm 3.33 \times 10^{-21}$	$4.53 \pm 2.28 \times 10^{-21}$
			$5.26 \pm 0.72 \times 10^{-21}$	**$2.90 \pm 0.69 \times 10^{-21}$**
UTh1200d	1200	199.50	$4.49 \pm 1.05 \times 10^{-21}$	$5.46 \pm 2.10 \times 10^{-21}$
			$2.87 \pm 0.78 \times 10^{-21}$	$2.44 \pm 0.94 \times 10^{-21}$
			$3.80 \pm 0.67 \times 10^{-21}$	**$3.95 \pm 1.08 \times 10^{-21}$**
UTh1200b	1200	277.67	$2.82 \pm 0.94 \times 10^{-21}$	$2.29 \pm 0.82 \times 10^{-21}$
			$3.45 \pm 0.87 \times 10^{-21}$	$2.40 \pm 0.85 \times 10^{-21}$
			$3.22 \pm 0.65 \times 10^{-21}$	**$2.35 \pm 0.59 \times 10^{-21}$**
UTh1	1300	56.22	$1.32 \pm 0.62 \times 10^{-20}$	$1.06 \pm 0.50 \times 10^{-20}$
			$1.39 \pm 0.75 \times 10^{-20}$	$1.84 \pm 0.86 \times 10^{-20}$
			$2.70 \pm 0.83 \times 10^{-20}$	$2.88 \pm 0.74 \times 10^{-20}$
			$2.12 \pm 0.49 \times 10^{-20}$	**$2.35 \pm 0.48 \times 10^{-20}$**
UTh2	1300	86.10	$1.97 \pm 0.81 \times 10^{-20}$	$1.36 \pm 0.69 \times 10^{-20}$
			$3.98 \pm 2.06 \times 10^{-20}$	$3.30 \pm 1.95 \times 10^{-20}$
			$2.75 \pm 0.89 \times 10^{-20}$	**$2.18 \pm 0.84 \times 10^{-20}$**

Values in bold type are weighted averages for each experiment.

* This profile was measured in the reverse direction.

Table 3. Model Parameters and Values.

Parameter	Value(s)
ϕ, critical melt fraction	0.001-0.01
K_U, U Cpx/liq partition coefficient	0.005
K_{Th}, Th Cpx/liq partition coefficient	0.01
γ, Cpx coefficient in melting reaction	0.80
X_{Cpx}, volume fraction Cpx	0.15
R_0, Cpx initial radius, mm	1-5
H, melting column height, km	33-63
F, melting degree	0.10-0.20
W, mantle upwelling rate, cm/yr	1-10
T_i, initial temperature, K	1588-1748
T_f, final temperature, K	1506-1514

FIGURE CAPTIONS

Figure 1. A typical diffusion profile (a) and its error function inversion (b). The diffusion coefficient is calculated from the slope of the line fit to the inverted data, which is equal to $(2\sqrt{Dt})^{-1}$. The error function curve shown in (a) is a solution to Eq. (1) using the diffusion coefficient calculated from the linear inverse error function fit.

Figure 2. Comparison of diffusion profiles measured from opposite directions on the same sample. The circles represent a concentration profile measured in the "forward" direction, through the surface diffusant layer. The squares represent a depth profile made in the reverse direction.

Figure 3. Time series at 1200 °C and 1300 °C for U and Th diffusion anneals. The horizontal dashes represent individual measurements of a single experiment, and circles indicate the weighted average. Squares indicate diffusion coefficients extracted from "reverse" profiles.

Figure 4. Arrhenius plots of U and Th diffusivity between 1150 and 1300 °C. The circles represent average diffusion coefficients for each experiment, and the solid lines are weighted least-squares fits to the data. Activation enthalpies and pre-exponential factors are given in the text.

Figure 5. Summary of cation diffusion data in natural, near end-member diopside. The dashed line labeled "CATS-Di" refers to interdiffusion of $CaAl_2SiO_6$ and diopside (Grove and Wagner, 1993). The dotted line shows Ca self-diffusion coefficients (Dimanov et al., 1996). Solid lines refer to tracer diffusion coefficients for Sr (Sneeringer et al., 1984), Pb (Cherniak et al., 1998), Yb and Ce (Chapter 1), and U and Th (this chapter).

Figure 6. Plot of cpx grain diameter vs. temperature showing the conditions under which U and Th partitioning equilibrium may be obtained during adiabatic melting. The curves represent solutions to Eq. (10), with $t_D/t_{adv} = 1$, for upwelling rates of 1 and 10 cm/yr. Each curve separates regions of greater than (above the curve) and less than 83% equilibration.

Figure 7. Model Th and U diffusion profiles developed across a 2.5 mm clinopyroxene grain during progressive melting. (a) For a mantle upwelling rate of 10 cm/yr cpx is in strong disequilibrium with the melt, even after 15% melting. (b) In contrast, at 1 cm/yr cpx is near equilibrium with the melt after only ~3% melting. Both figures show elemental rather than isotopic concentrations. $\phi = 1\%$, $T_i = 1395$ °C, $T_f = 1240$ °C, $H = 48$ km.

Figure 8. [^{230}Th/^{238}U] activity ratios in the aggregated melt. The dashed curves define an uncertainty envelope that is based on the error in the Arrhenius parameters for U and Th. Uranium and thorium are not efficiently fractionated under either (a) disequilibrium or (b) near-equilibrium melting conditions, and in both cases the activity ratio is near 1 throughout most of the melting interval. Parameter values are the same as those used in the calculations shown in Fig. 7.

Figure 1

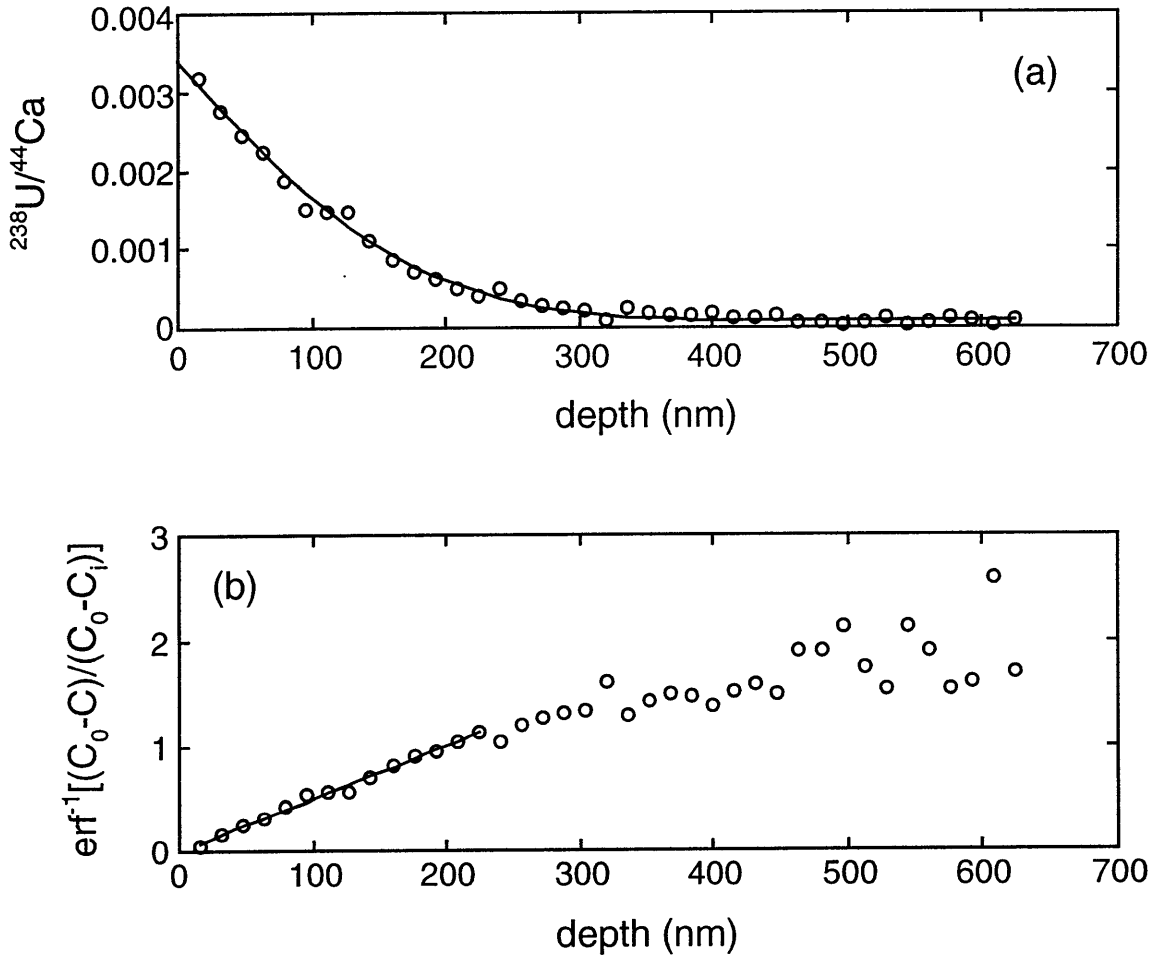
0.004
0.003
0.002
0.001
0
$^{238}U/^{44}Ca$
(a)
0
100
200
300
400
500
600
700
depth (nm)
3
2
1
0
$erf^{-1}[(C_0-C)/(C_0-C_i)]$
(b)
0
100
200
300
400
500
600
700
depth (nm)

Figure 2

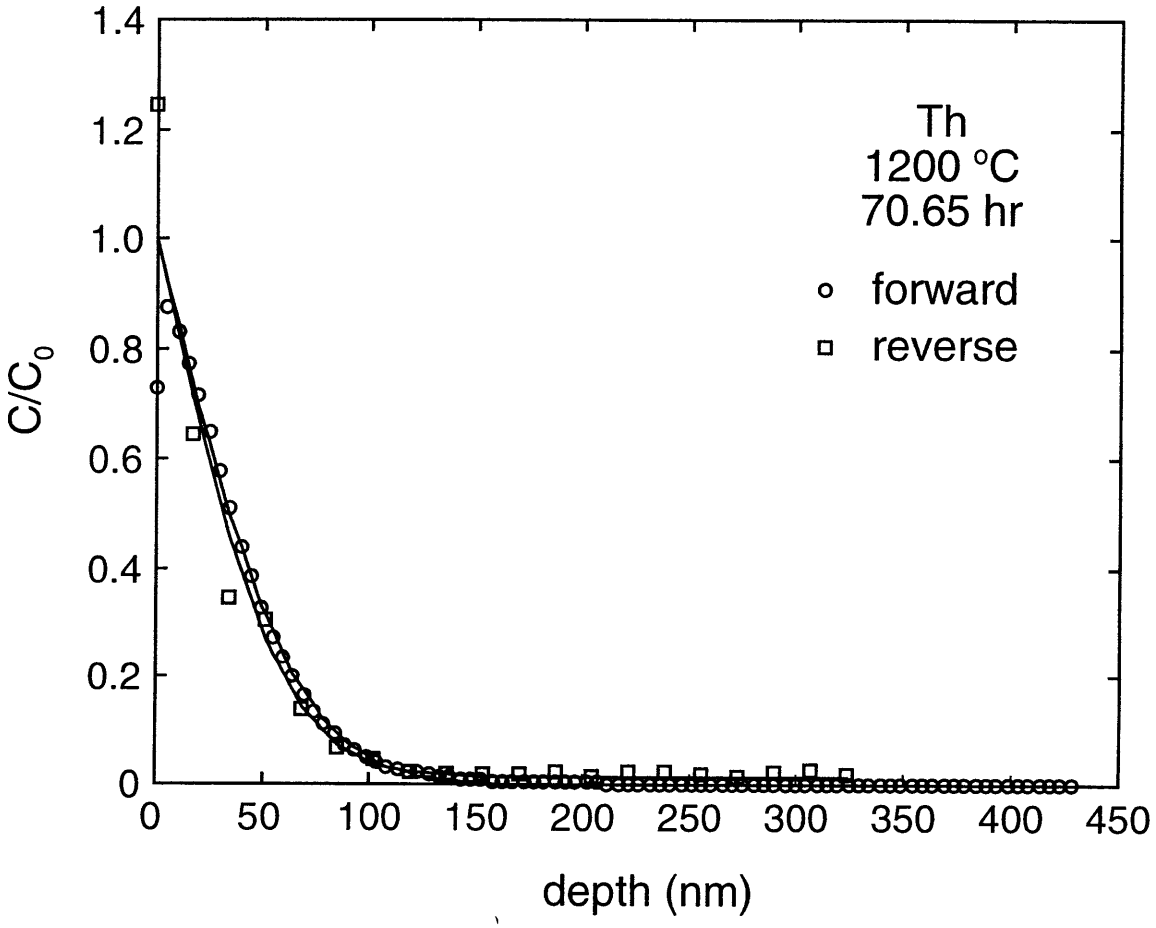
1.4
1.2
1.0
0.8
0.6
0.4
0.2
0
C/C0
0
50
100
150
200
250
300
350
400
450
depth (nm)
Th
1200 °C
70.65 hr
forward
reverse

Figure 3a

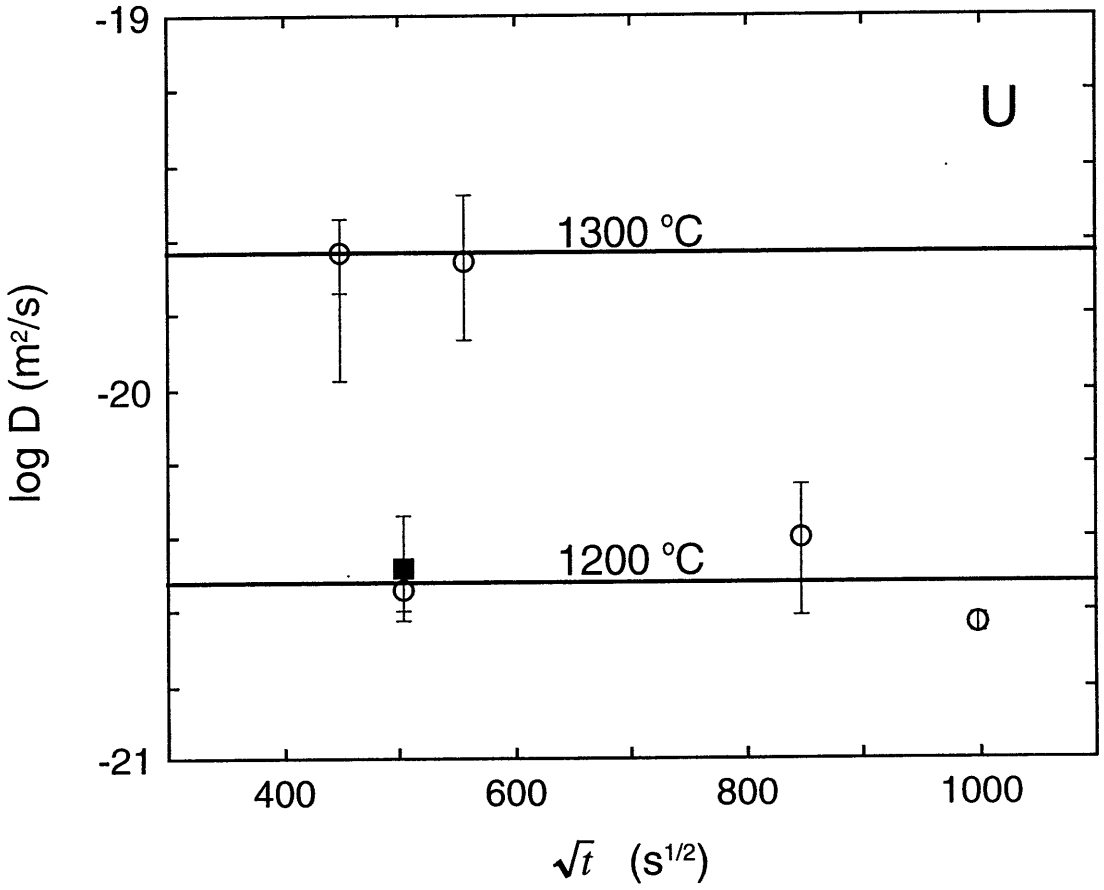

Figure 3b

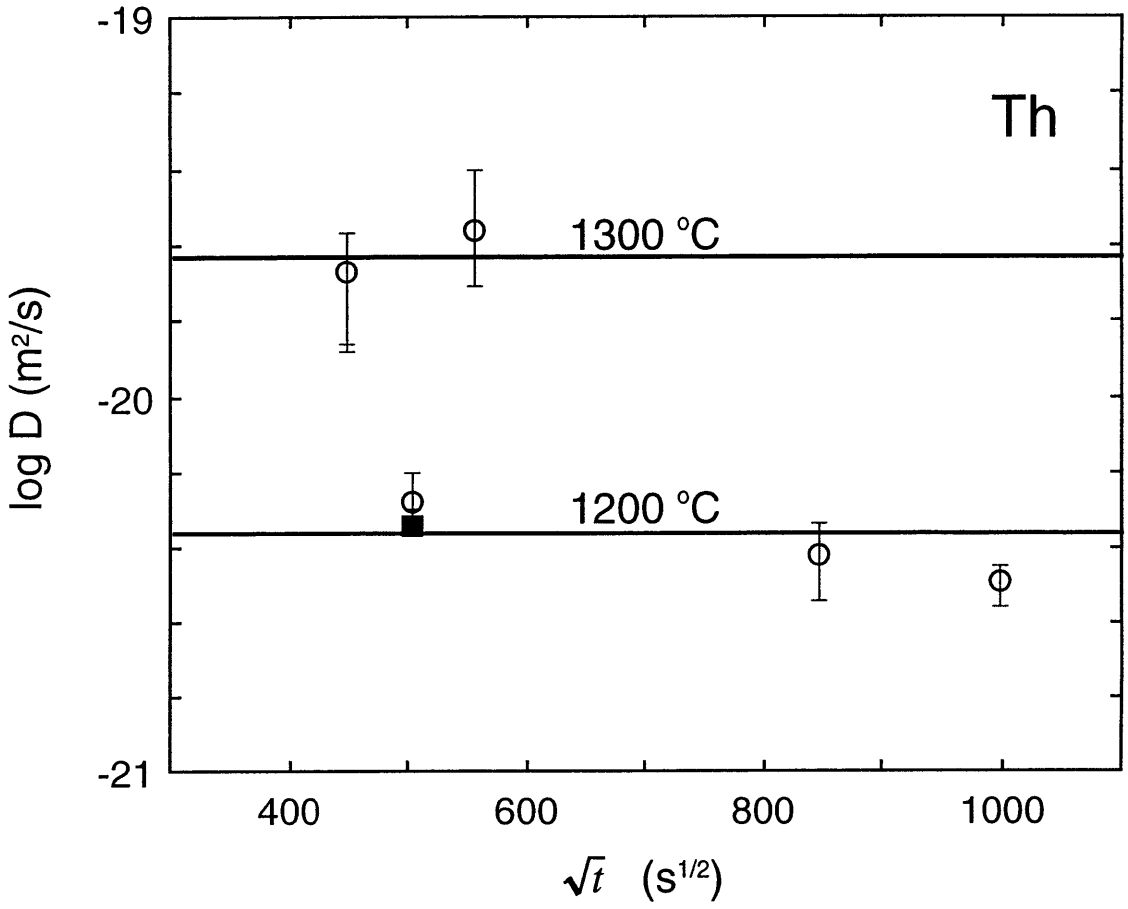

Figure 4a

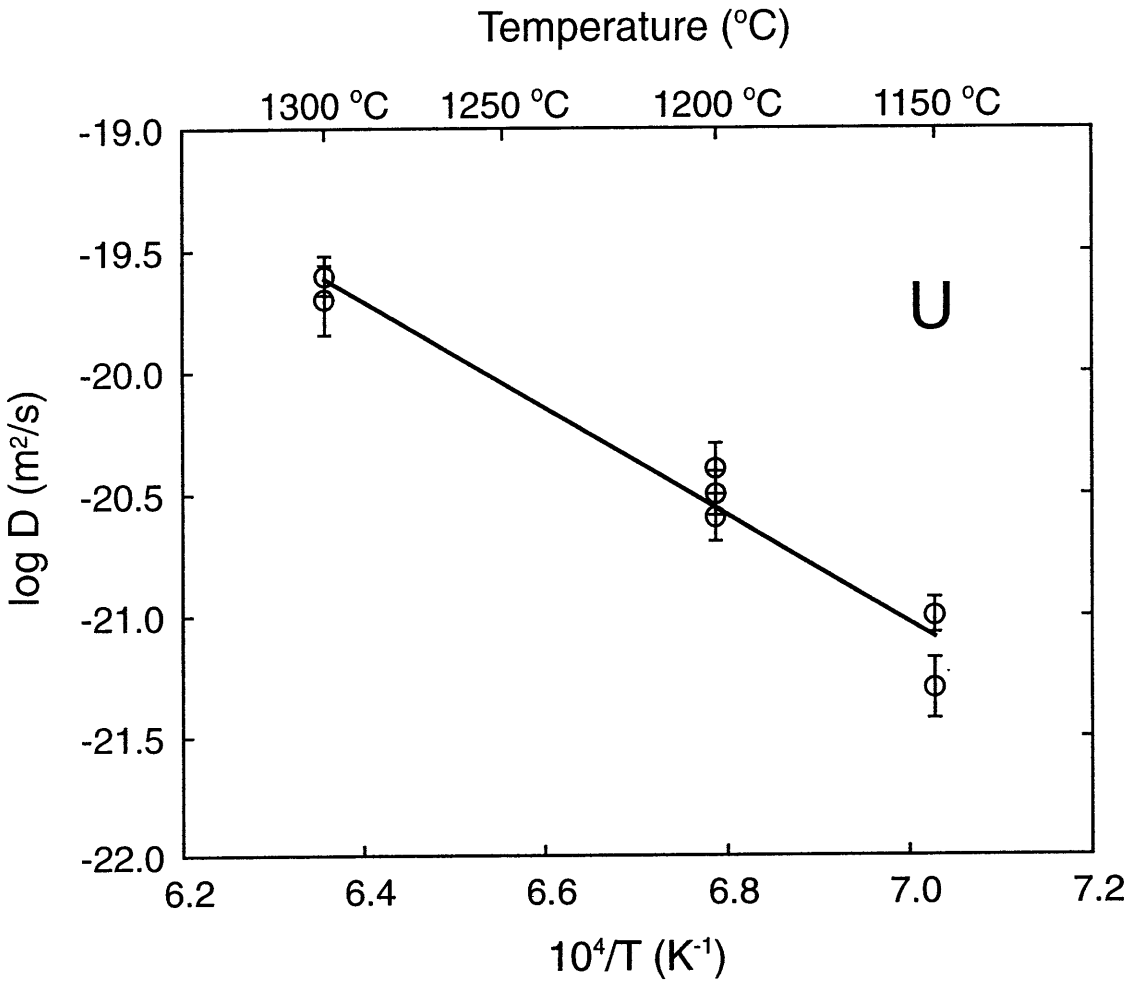
Temperature (°C)
1300 °C
1250 °C
1200 °C
1150 °C
-19.0
-19.5
-20.0
-20.5
-21.0
-21.5
-22.0
log D (m²/s)
U
6.2
6.4
6.6
6.8
7.0
7.2
10⁴/T (K⁻¹)

Figure 4b

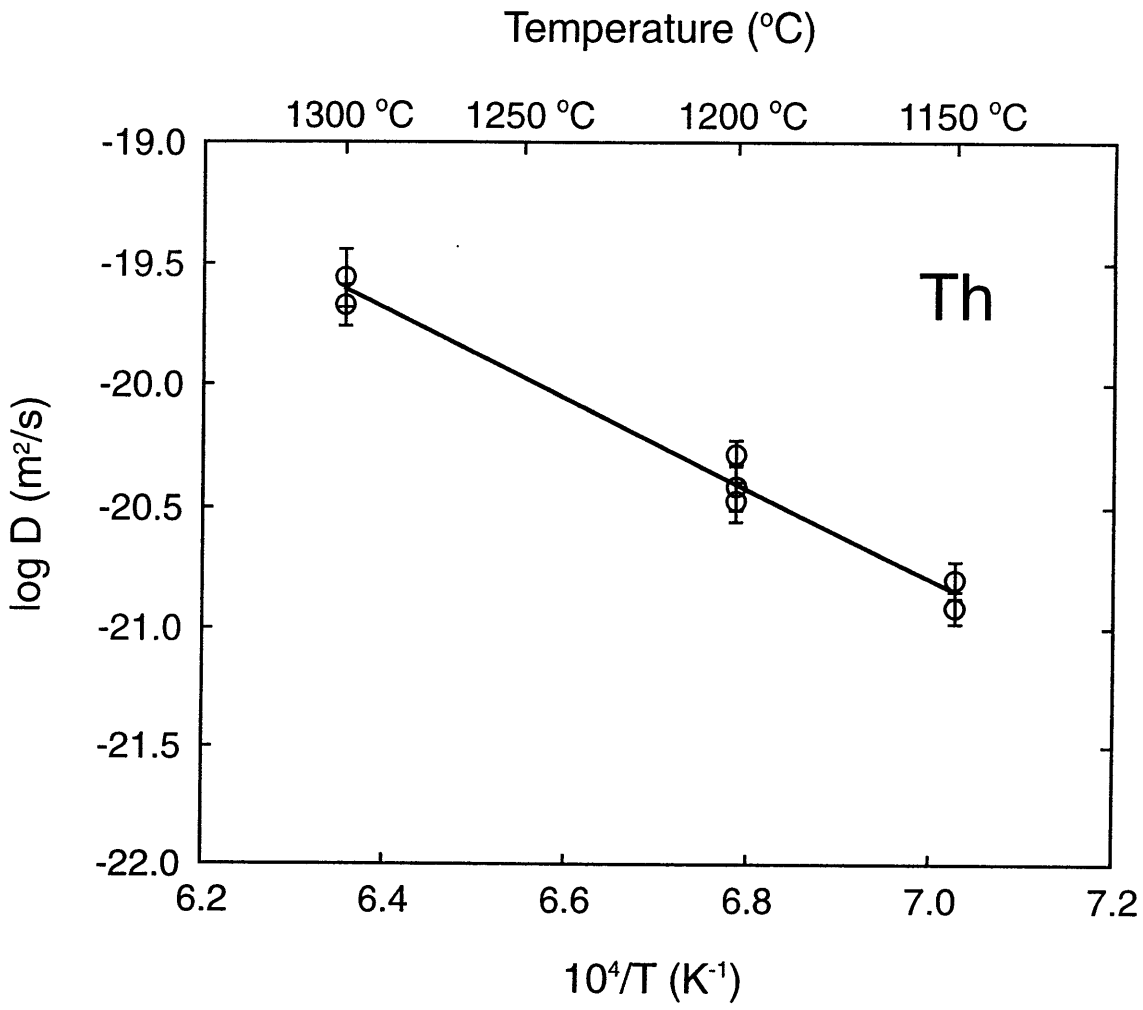
Temperature (°C)
1300 °C
1250 °C
1200 °C
1150 °C
-19.0
-19.5
-20.0
-20.5
-21.0
-21.5
-22.0
log D (m²/s)
Th
6.2
6.4
6.6
6.8
7.0
7.2
10⁴/T (K⁻¹)

Figure 5

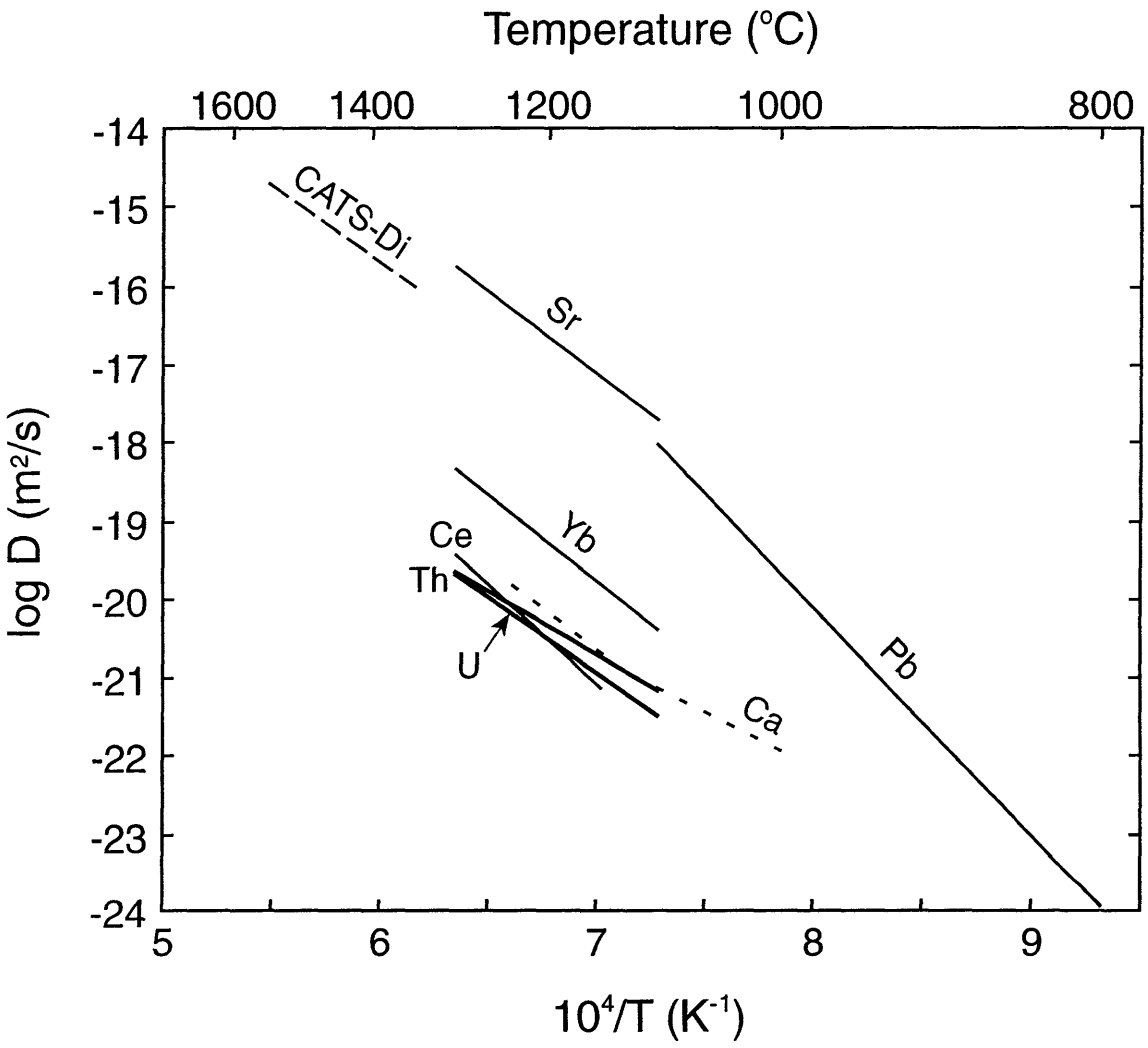
Temperature (°C)
1600
1400
1200
1000
800
-14
-15
-16
-17
-18
-19
-20
-21
-22
-23
-24
log D (m²/s)
CATS-Di
Sr
Yb
Ce
Th
U
Ca
Pb
5
6
7
8
9
10⁴/T (K⁻¹)

Figure 6

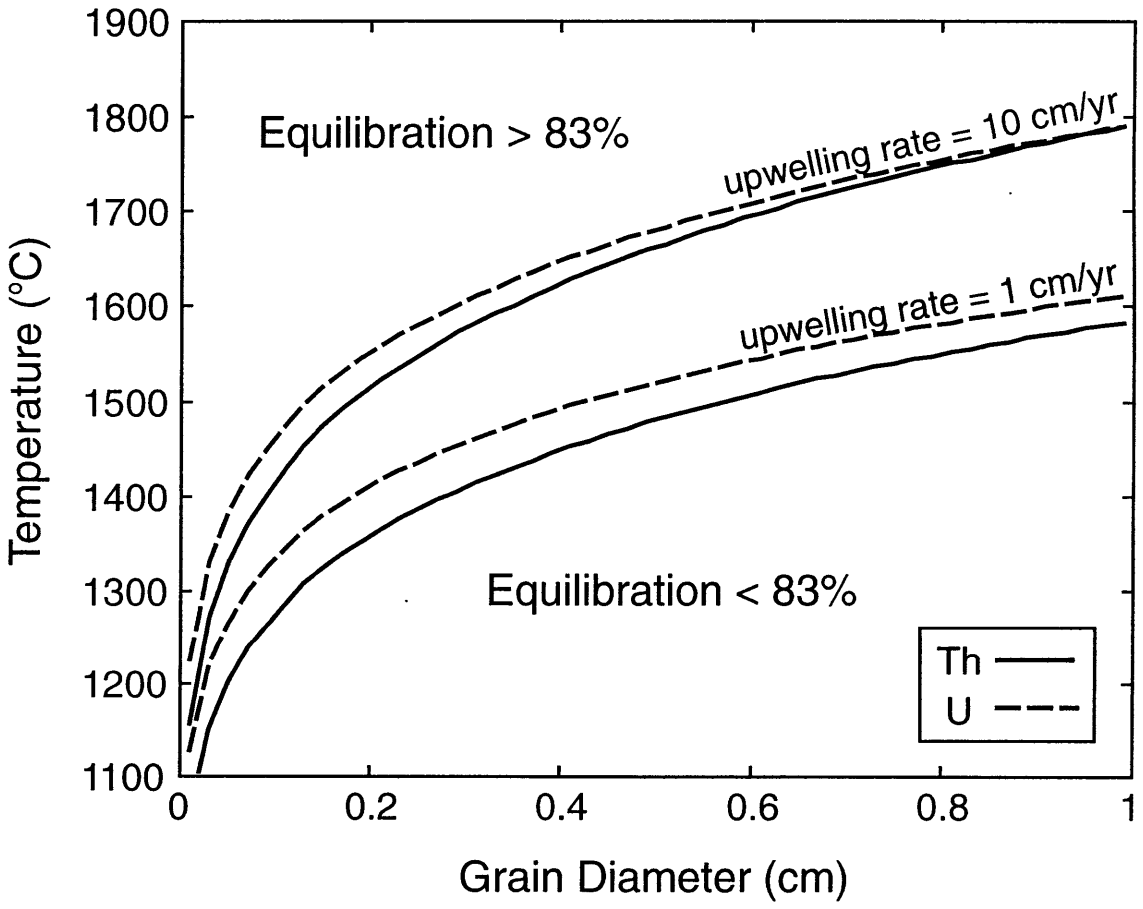
1900
1800
1700
1600
1500
1400
1300
1200
1100
Temperature (°C)
0
0.2
0.4
0.6
0.8
1
Grain Diameter (cm)
Equilibration > 83%
Equilibration < 83%
upwelling rate = 10 cm/yr
upwelling rate = 1 cm/yr
Th
U

Figure 7

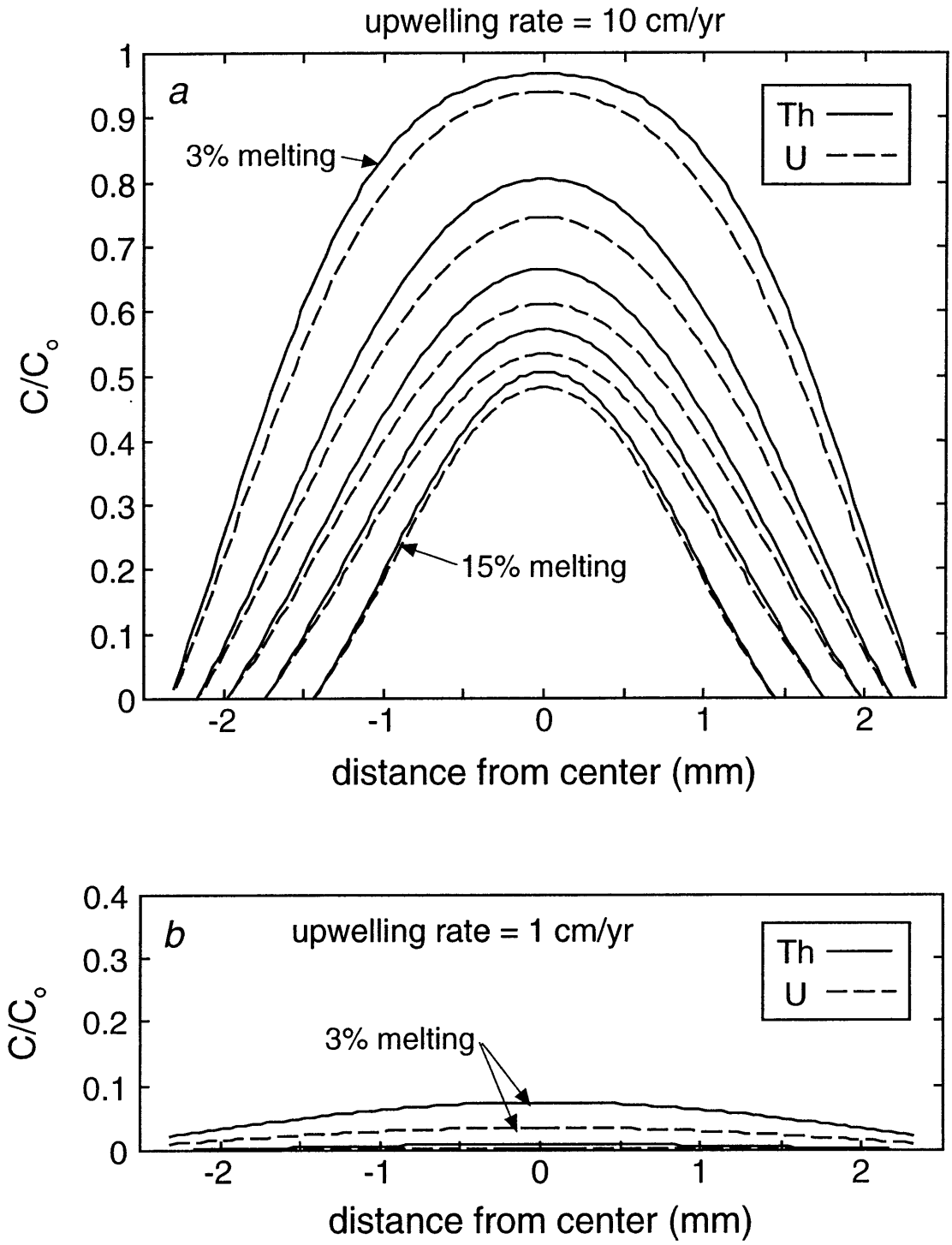
upwelling rate = 10 cm/yr
a
3% melting
15% melting
Th
U
C/C$_o$
distance from center (mm)
b
upwelling rate = 1 cm/yr
3% melting
Th
U
C/C$_o$
distance from center (mm)

Figure 8

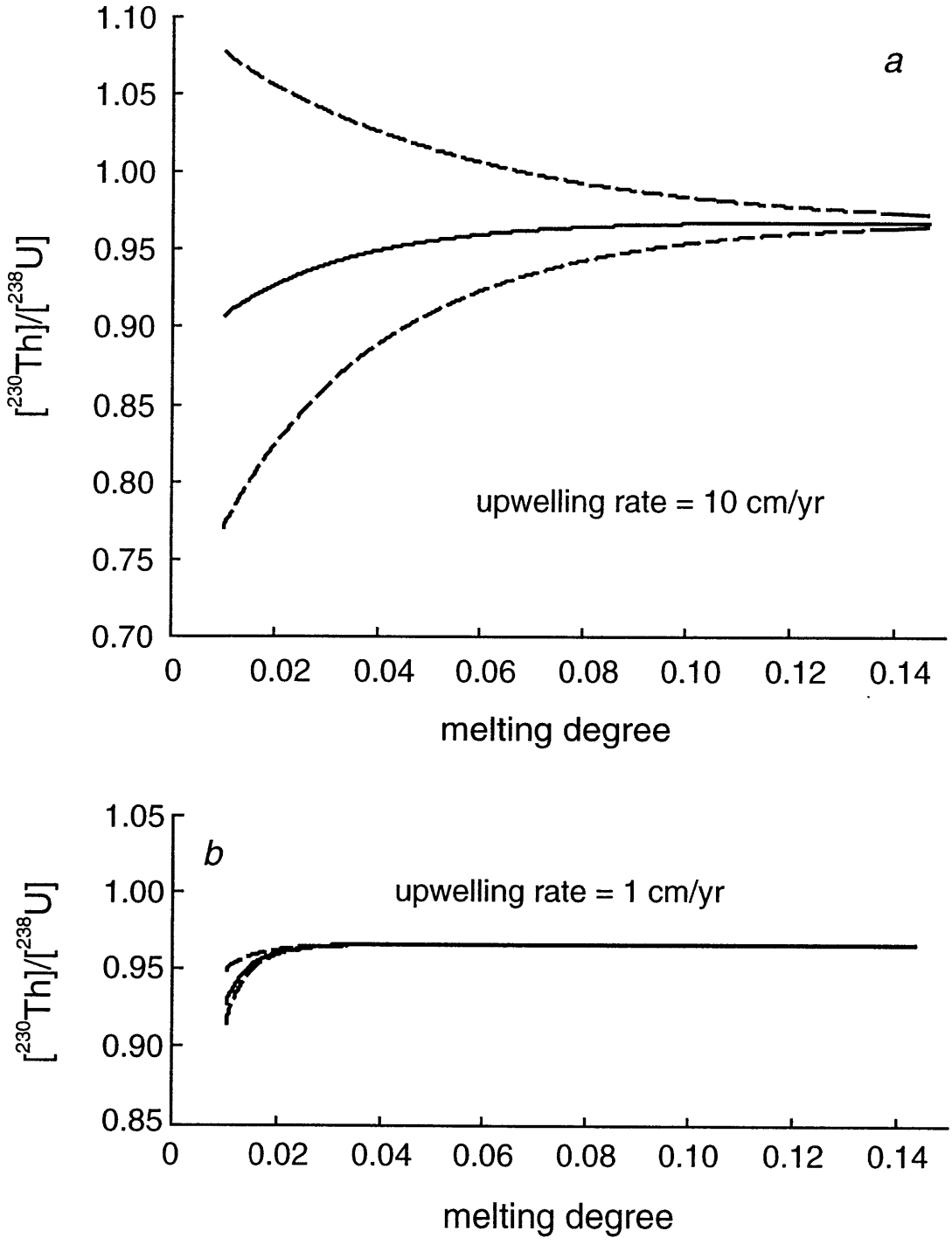
1.10
1.05
1.00
0.95
0.90
0.85
0.80
0.75
0.70
[230Th]/[238U]
a
upwelling rate = 10 cm/yr
0
0.02
0.04
0.06
0.08
0.10
0.12
0.14
melting degree
1.05
1.00
0.95
0.90
0.85
[230Th]/[238U]
b
upwelling rate = 1 cm/yr
0
0.02
0.04
0.06
0.08
0.10
0.12
0.14
melting degree

CHAPTER 5.

ORIGIN OF LUNAR HIGH-TI ULTRAMAFIC GLASSES: CONSTRAINTS FROM PHASE RELATIONS AND DISSOLUTION KINETICS OF CLINOPYROXENE-ILMENITE CUMULATES

ABSTRACT

Phase equilibrium and dissolution kinetics experiments on synthetic late stage magma ocean cumulates are used to place constraints on hypotheses for the origin of lunar high-Ti ultramafic glasses. Models for the production of high-Ti lunar magmas have called for either (1) assimilation of late stage clinopyroxene-ilmenite cumulates at shallow levels or (2) sinking of cpx-ilmenite cumulates to form a hybrid mantle source. To satisfy the constraints of our experiments, we propose an alternative model that involves shallow level reaction and mixing of cumulates, followed by sinking of hybrid high-Ti materials. This model can fulfill compositional requirements imposed by the pristine lunar glass suite that are difficult to satisfy in assimilation models. It also avoids difficulties that arise in overturn models from the low solidus temperatures of cpx-ilmenite cumulates. Partially molten cpx-ilmenite cumulates become gravitationally unstable with respect to underlying mafic cumulates only when they have cooled to within about 30 °C of their solidus (~1125 °C at 100 km depth), and at these temperatures the viscosity of mafic cumulates is too high to allow for growth and descent of cpx-ilmenite diapirs on the appropriate time scale. Reaction and mixing between late stage liquids and mafic cumulates at shallow levels would produce a refractory hybrid material that is negatively buoyant at higher temperatures, and could sink more efficiently to the depths inferred for production of high-Ti ultramafic glasses.

INTRODUCTION

Lunar volcanic glasses vary widely in composition, particularly in their content of titanium (0.26-16.4 wt.% TiO_2; Delano, 1986). The high Ti contents of these glasses are usually attributed to ilmenite bearing cumulates that crystallized during late stages of magma ocean differentiation (e.g. Anderson, 1971; Taylor and Jakes, 1974; Hubbard and Minear, 1975; Ringwood and Kesson, 1976; Hess, 1991; Snyder et al., 1992; Shearer and Papike, 1993; Hess and Parmentier, 1995; Wagner and Grove, 1997; Shearer and Papike, 1999b). The role of late stage cumulates in lunar volcanism remains a subject of debate. Different models have called for assimilation of these cumulates by ascending low-Ti magmas (e.g. Hubbard and Minear, 1975; Wagner and Grove, 1997) or global scale overturn of the magma ocean cumulate pile to produce a heterogeneous mantle source (e.g. Ringwood and Kesson, 1976; Hess and Parmentier, 1995). Each of these models implies a different chemical distribution within the lunar mantle following magma ocean solidification, and each may have different consequences for the subsequent thermal evolution of the Moon (Hess and Parmentier, 1995). The experiments in this paper place constraints on hypotheses for high-Ti ultramafic magma production by providing information on the melting behavior of clinopyroxene-ilmenite source materials.

Models for the origin of lunar ultramafic glasses begin with the concept of an early magma ocean differentiation event, as originally proposed by Smith et al. (1970) and Wood et al. (1970). Crystallization of the magma ocean produced a layered pile of chemically diverse cumulate zones, with olivine and orthopyroxene forming the base of the pile and plagioclase floating upward to form the anorthositic crust (Taylor and Jakes, 1974; Walker et al., 1975; Longhi, 1977; Snyder et al., 1992). Cumulates produced late in the crystallization sequence, after ~95% crystallization, were enriched in Ti, Fe and other incompatible elements, and crystallized as a ~20 km thick layer near the base of the crust (at ~100 km depth). These late stage cumulates are thought to be composed primarily of clinopyroxene (cpx) and ilmenite (ilm).

Early models called for production of low- and high-Ti magmas from different levels within the layered cumulate pile. Low-Ti liquids were thought to be produced from mafic cumulates at lower levels, and high-Ti liquids were thought to be formed by melting of late stage cumulates at shallow depths (Taylor and Jakes, 1974; Walker et al., 1975). This conception proved inconsistent with later experimental results. Both low- and high-Ti ultramafic glass compositions are saturated with olivine + orthopyroxene at similar pressures (Green et al., 1975; Delano, 1980; Chen et al., 1982; Chen and Lindsley, 1983; Wagner and Grove, 1997), suggesting a similar depth of origin for all ultramafic glasses (~400 km). Also, neither cpx nor ilmenite is saturated on the liquidus of any pristine high-Ti ultramafic glass at any pressure (Kesson, 1975; Delano, 1980; Wagner and Grove, 1997), and this rules out a high-Ti magma source that is composed predominantly of cpx and ilmenite. Subsequent models have had to take into account these experimental restrictions.

One set of models involves in situ assimilation of clinopyroxene-ilmenite cumulates by low-Ti ultramafic liquids (Anderson, 1971; Hubbard and Minear, 1975; Wagner and Grove 1997). In these models the cumulate pile maintains its original layered structure. Low-Ti liquids are produced at depth by partial melting of mafic cumulates, and these magmas assimilate late stage cumulates on their way to the surface to produce high-Ti magmas. Assimilation models have had difficulty accounting for some of the compositional traits of high-Ti ultramafic glasses. To satisfy major element mass balance (in particular the CaO/TiO_2 ratio), the proportions of ilmenite and cpx entering the liquid must be approximately 3:1 (Wagner and Grove, 1997; Shearer and Papike, 1999a). In contrast, the relative abundance of ilmenite and cpx in late stage cumulates is thought to be 1:5 to 1:6 (e.g. Snyder et al., 1992). Severe non-modal assimilation, favoring ilmenite over cpx, is therefore required. Wagner and Grove (1997) suggested that a disequilibrium dissolution process might lead to selective assimilation of ilmenite, but did not have the experimental data to evaluate this model in detail. Our experiments provide a test of the cpx-ilmenite assimilation model, and show that

assimilation processes, whether equilibrium or disequilibrium, can not account for the compositions of lunar high-Ti ultramafic glasses.

A second model for high-Ti magma production involves overturn of the gravitationally unstable magma ocean cumulate pile to produce a mixed, hybrid lunar mantle (Ringwood and Kesson, 1976; Herbert, 1980; Hess, 1991; Spera, 1992; Hess and Parmentier, 1995). Partial melting within this heterogeneous mantle is thought to account for the compositions of low- and high-Ti ultramafic glasses. An important constraint on overturn models is the temperature at which the high-Ti layer becomes negatively buoyant with respect to underlying mafic cumulates. Residual high-Ti liquids are less dense than mafic cumulates, and must partially solidify before the high-Ti layer becomes gravitationally unstable. Our experiments on the phase relations of cpx-ilmenite cumulates allow us to predict the temperature at which cpx-ilmenite cumulates become denser than mafic cumulates. Estimates of the viscosity at this temperature allow us to calculate rates of growth and descent of cpx-ilmenite cumulate diapirs.

EXPERIMENTAL METHODS

The experiments in this paper were designed to characterize the melting and dissolution behavior of cpx-ilmenite cumulates under lunar mantle conditions. The solidus to liquidus phase relations of a synthetic high-Ti cumulate composition were determined under dry, reducing conditions in the pressure range 0.1 MPa to 1.8 GPa. These experiments yield information on the proportions and compositions of solid and liquid phases as functions of temperature and pressure, and provide a test for petrogenetic models that involve mixing between partial melts of cpx-ilmenite cumulates and low-Ti ultramafic liquids. We also performed two groups of dissolution experiments to determine the behavior of cpx-ilm cumulates during disequilibrium melting and/or dissolution. The first group of experiments was designed to measure the rate of clinopyroxene dissolution into a low-Ti lunar basalt, for comparison with ilmenite dissolution rates determined by Wagner and Grove (1997). The second group was designed to measure the rate of melt production at the interface between cpx

and ilmenite single crystals, and the relative rates of dissolution of cpx and ilmenite into the growing melt layer.

Phase Equilibrium Experiments

Starting materials

Phase equilibrium experiments were performed on a model high-Ti cumulate composition (TiCum; see Table 1) similar to that proposed by Snyder et al. (1992) for the solid assemblage that would precipitate after ~95% crystallization of the lunar magma ocean. In the Snyder et al. (1992) model, most of the plagioclase floats upward to form the lunar crust, but a small amount (2-5% of the total) remains with the denser mush, and this bit of entrained plagioclase accounts for the modest Al_2O_3 content of the composition. A mechanical mixture of the TiCum composition was prepared from high-purity oxides and silicates ground in an agate mortar under ethanol for 6 hours.

0.1 MPa experiments

Experiments at 0.1 MPa pressure were performed under a controlled atmosphere at temperatures that spanned the solidus and liquidus of the high-Ti cumulate composition. A pressed pellet of TiCum powdered mix was sintered onto a 0.8 mm diameter Pt_{91-93}-Fe_{7-9} loop that was chosen to minimize Fe exchange with the TiCum composition. The loop and pellet were suspended in the hotspot of a Deltech DT31VT vertical gas-mixing furnace. Oxygen fugacity was controlled near the quartz-fayalite-magnetite (QFM) buffer by mixing CO_2 and H_2 gases and was continuously monitored with a solid ZrO_2-CaO electrolyte oxygen sensor calibrated against the Fe-FeO, Ni-NiO, and Cu-Cu_2O buffers. Temperature was monitored using a Pt-$Pt_{90}Rh_{10}$ thermocouple calibrated against the melting points of NaCl, Au, and Pd on the IPTS 1968 temperature scale. The thermocouple junction was placed immediately adjacent to the experimental charge, and temperatures are believed to be accurate within ± 2 °C. Experiments were run at constant temperature for 24 to 148 hours and were terminated by drop-quenching the charge into a water bath.

High pressure experiments

The starting material for the high pressure experiments was prepared by pressing approximately 0.5 g of TiCum powdered mix into a large pellet. The pellet was hung on 0.1 mm Pt wire and conditioned below the solidus for 39 hours at 1050 °C and oxygen fugacity corresponding to the Fe-FeO buffer, using the same furnace and techniques employed for the 0.1 MPa experiments. The sintered pellet was then ground to a fine powder in an agate mortar. Approximately 10 mg of the conditioned starting material was loaded into a graphite crucible and then placed in a Pt outer capsule that was open at one end. After drying for 12-48 hours at 120 °C, the Pt outer capsule was welded shut, placed into a high-density Al_2O_3 sleeve, and centered in a straight-walled graphite furnace using crushable MgO spacers. The pressure medium consisted of a sintered $BaCO_3$ sleeve. Pressure for this assembly was calibrated using the Ca-Tschermakite breakdown reaction (Hays, 1966). The pressure correction was found to be < 0.1 GPa at 1.3 GPa and 1350 °C, and the values reported in Table 2 do not include a friction correction. Temperature was monitored and controlled using a $W_{97}Re_3$-$W_{75}Re_{25}$ thermocouple that was separated from the Pt capsule by a thin crushable MgO wafer. The temperature difference between the position of the thermocouple junction and the hotspot was determined to be 20 °C using offset thermocouples, and temperatures reported in Table 2 are corrected for this difference. No correction for the effect of pressure on thermocouple emf has been applied. Runs were pressed cold to 0.7 GPa and then heated at 100 °C/min to 865 °C, where they were held for 6 minutes. They were then pumped to the desired run pressure and heated to run temperature at 50 °C/min. Experiments were held at constant temperature and pressure for 10 to 24 hours and were quenched by shutting off the power.

Analyses

Experimental run products were analyzed using either a 4- or 5-spectrometer JEOL 733 electron microprobe at the Massachusetts Institute of Technology (Table 3). A 10 nA beam current and 15 kV accelerating potential were used for all analyses. A 2 μm beam diameter was

used for analysis of solid phases, and a 10 μm beam diameter was used for glass analyses. Data were reduced using the phi-rho-z correction scheme.

Clinopyroxene Dissolution Experiments

Dissolution of clinopyroxene in a synthetic analog of Luna 24 low-Ti basalt was measured at temperatures between 1270 and 1450 °C and pressures of 1.0 to 1.3 GPa (Table 5). The design of the experiments was similar to those of Zhang et al. (1989) and Wagner and Grove (1997). A single crystal of gem quality diopside from the Kunlun Mts., China (Table 1), was cut perpendicular to the *c* axis into wafers ~1 mm thick using a low-speed diamond wafering saw. The Kunlun Mts. diopside is higher in CaO and MgO and lower in FeO than pyroxenes expected to precipitate during late stages of magma ocean crystallization. As discussed below, dissolution of Kunlun Mts. diopside in basaltic magmas is probably slower than dissolution of a more Fe-rich pyroxene, and thus the rates we report below are probably lower limits for the assimilation process under consideration. The diopside wafers were drilled into cylindrical disks using a 2.8 mm inner diameter diamond coring bit, and the thickness of each disk was measured with a micrometer to a precision of ~10 μm.

Each disk was sandwiched between equally thick layers of a synthetic Luna 24 basalt analog powder (Table 1) in a tightly fitting graphite capsule 6.5 mm long. This sample geometry was designed to minimize convection in the liquid portion of the charge and to provide for one-dimensional diffusive dissolution of the crystal into Luna 24 basalt melt reservoirs on either side of the disk. The thickness of the melt reservoir was effectively infinite compared to the lengths of diffusion profiles developed during each of the runs.

The experimental charge was placed directly into a high-density alumina sleeve without a Pt outer capsule, then loaded into a piston cylinder apparatus using the techniques described above for the phase equilibrium experiments. A more rapid heating rate (200 °C/min) was used for the dissolution experiments to minimize dissolution during the approach to run conditions. Experiments were held at constant temperature for times ranging from 1000 seconds to 24

hours and were quenched by shutting off the power. The sample assembly was cut into two pieces perpendicular to the crystal-melt interface, and the thickness of the partially dissolved disk was determined using a Zeiss reflected light microscope with an ocular scale accurate to 10 μm (Table 4). No attempt was made to account for dissolution during heating or quenching of the experiment, as this effect was small compared to the precision of the thickness measurements. In one experimental charge (B547), concentration profiles in the glass perpendicular to the crystal-melt interface were measured, using the electron microprobe, as an independent means of estimating the mass of diopside that had dissolved into the melt.

Melting Kinetics Experiments

The rate of melt production at the interface between diopside and ilmenite single crystals was determined at 1.3 GPa and temperatures of 1300-1350 °C (Table 6). Kunlun Mts. diopside and Frank Smith ilmenite single crystals (Table 1) were cut with a diamond wafering saw into parallelepipeds of approximately equal size. One side of each piece was polished with diamond pastes to 0.3 μm grit. The polished face of the diopside crystal was oriented perpendicular to the *c* axis; polished ilmenite faces were oriented randomly. Ilmenite and diopside pieces were placed together, with their polished surfaces in contact, in a tightly fitting graphite capsule (Fig. 1), and were held at constant temperature and pressure in a piston cylinder device. As with the single crystal diopside dissolution experiments, the assembly was pressed cold and brought quickly to run temperature (at 200 °C/min), and was quenched by shutting off the power. The initial and final thickness of the ilmenite and diopside crystals were measured using the techniques described above for the cpx single crystal dissolution experiments. Quench crystallization was especially pervasive in these experiments, due to the highly depolymerized nature of the melt produced, making it difficult to measure concentration profiles in quenched glass between the ilmenite and diopside crystals. In one experiment (B634) that preserved a few large pools of glass it was possible to measure a portion of the concentration profile using the electron microprobe.

EXPERIMENTAL RESULTS

Phase Equilibrium Experiments

The subsolidus to near-liquidus phase relations of the synthetic high-Ti cumulate were determined up to 1.3 GPa (Fig. 2). The sequence of phase appearances with decreasing temperature was similar at all pressures investigated. Clinopyroxene is the only phase saturated on the liquidus up to at least 1.3 GPa. Ilmenite is the next phase to crystallize with decreasing temperature, followed by trace amounts of tridymite and ulvospinel at 0.1 MPa, and quartz at 1.3 GPa. The subsolidus assemblage at 0.1 MPa is cpx+ilm+plag; at 1.3 GPa plagioclase has disappeared and the subsolidus phases are cpx+ilm. A single experiment at 1.8 GPa and 1290 °C, which produced liq+cpx, suggests that the phase relations are similar at higher pressure (Fig. 2).

Our results can be compared with those of Wyatt (1977), who performed experiments between 2.0 and 4.8 GPa on starting material consisting of 29 wt.% ilmenite and 71 wt.% cpx, with molar Mg# = 0.638 (our high-Ti cumulate composition, in contrast, contains ~14 wt.% ilmenite and 86 wt.% cpx, with Mg# = 0.311). Wyatt (1977) reported a nearly constant melting interval of ~140 °C between 2.0 and 4.8 GPa, with cpx being the liquidus phase in all but one case. The liquidus and solidus of Wyatt's bulk composition, extrapolated to lower pressure, coincide with our liquidus and solidus within ~20 °C. The similarity between our results and those of Wyatt (1977) suggests that the general aspects of the phase equilibria in cpx-ilmenite assemblages are not very sensitive to changes in bulk composition and pressure.

The near-solidus melting reactions for our high-Ti cumulate composition are given in Table 4. We ignore the trace amounts of ulvospinel and tridymite or quartz that are produced in experiments just above the solidus and consider the simplified melting equation: $\alpha\, cpx + \beta\, ilm = 1\, melt$. Within the uncertainty limits, the stoichiometric coefficients for cpx and ilm in the melting reaction do not appear to change between 0.1 MPa and 1.3 GPa. However, the TiO_2 content in the melt near the ilmenite-out phase boundary is ~3 wt.% higher at 1.3 GPa than at

0.1 MPa (Table 3), suggesting that there is actually a slight increase in the ratio of ilmenite to cpx entering the melt with increasing pressure.

Clinopyroxene Dissolution Experiments

The results of the experiments on diopside dissolution in synthetic Luna 24 basaltic liquid are summarized in Table 5. Dissolution rates are given in terms of mass dissolved per square root run duration per m^2 interfacial area between crystal and melt. The mass dissolved during the experiment was calculated from the change in thickness of the single crystal disk, assuming a diopside density of 3300 kg/m^3. Dissolution rates are expressed in terms of mass, rather than distance, to facilitate comparison with ilmenite dissolution rates measured by Wagner and Grove (1997). Dissolution rates are given with respect to the square root of the run duration because diffusion controlled dissolution proceeds linearly with $\sqrt{t}$.

The dissolution rate can be estimated independently, and chemical diffusion in the melt verified to be the rate-controlling mechanism, by examining concentration profiles in the glass adjacent to the diopside disk. Figure 3 shows SiO_2, TiO_2, Al_2O_3 and MgO concentration profiles from a dissolution experiment performed at 1350 °C and 1.3 GPa (B547). These components all appear to display normal diffusion behavior; there is no evidence for multicomponent coupling effects such as uphill diffusion. Not shown are concentration profiles for CaO and FeO, which were nearly flat over the interval measured and could not be used to extract effective binary diffusion coefficients nor to estimate the dissolution rate. The curves in Fig. 3 are fits to the data of an analytical solution for one-dimensional diffusion controlled dissolution into a semi-infinite melt reservoir (Zhang et al., 1989):

$$C(x,t) = C_\infty + \frac{(C_0 - C_\infty)}{erfc(-a)} erfc\left(\frac{x}{2\sqrt{Dt}} - a\right), \qquad (1)$$

where C_∞ is the concentration in the melt at infinite distance from the interface, C_0 is the concentration in the melt at the interface, x is distance from the interface, t is run duration, and D is the effective binary diffusion coefficient in the melt. The parameter a satisfies (Zhang et al., 1989):

$$\frac{C_0 - C_\infty}{C_s - C_0} = \sqrt{\pi} a e^{a^2} erfc(-a), \qquad (2)$$

where C_s is the concentration in the diopside crystal. The interface concentration C_0 is assumed to be constant throughout the duration of the experiment. This appears to be a very good approximation, at least in the case of diopside. Zhang et al. (1989) have shown, using interface reaction rates for diopside inferred from the experiments of Kuo and Kirkpatrick (1985), that the interfacial melt will attain a constant saturation condition in less than 1 second.

Effective binary diffusion coefficients obtained from fits to the SiO_2, TiO_2, Al_2O_3 and MgO concentration profiles are given in Table 6. These provide an independent means of estimating the dissolution rate, using the relation (Zhang et al., 1989):

$$rate = a\rho\sqrt{D}, \qquad (3)$$

where ρ is diopside density and the rate is in units of g m^{-2} $s^{-1/2}$ (Table 6). The mean value of dissolution rates calculated from each of the four diffusion profiles is 1.67 ± 0.46 g m^{-2} $s^{-1/2}$ which agrees with the value of 2.18 ± 0.59 g m^{-2} $s^{-1/2}$ obtained from the measured change in thickness of the diopside disk. Agreement between these two completely independent dissolution rate estimates confirms that our experiments are well described by diffusive dissolution into an infinite melt reservoir with constant interfacial melt composition.

Temperature dependence

The dissolution rate for Kunlun Mts. diopside at 1.3 GPa increases strongly with temperature (Fig. 4). This dependence is due to the influence of temperature on chemical diffusivity in the melt and on the temperature dependence of the parameter a. Referring to Eqn. (3), the temperature dependence of the dissolution rate can be written (neglecting thermal expansion of the diopside):

$$\frac{\partial(\ln rate)}{\partial(1/T)} = \frac{1}{2}\frac{\partial(\ln D)}{\partial(1/T)} + \frac{\partial(\ln a)}{\partial(1/T)}. \qquad (4)$$

The first term on the right hand side represents the temperature dependence of chemical diffusivity in the melt. According to the Arrhenius equation, $D = D_0 \exp(-H_a / RT)$, this term

is equal to $-H_a/2R$, where R is the molar Boltzmann constant and H_a is the activation enthalpy for diffusion.

The second term in Eqn. (4) is nonlinear and more difficult to express in simple form. We can estimate the magnitude of this term using Eqn. (2), provided that we can estimate the values of C_s and C_∞ and the temperature dependence of the interface melt composition, C_0. C_s, C_∞ and C_0 are proportional to the equilibrium activity of a component with Kunlun Mts. diopside stoichiometry in the crystal, Luna 24 basaltic liquid, and the saturated interface melt, respectively. C_s by this definition is equal to 1, and C_∞ can be calculated given an activity model for the melt. A value of 0.307 for C_∞ is obtained using the solution model of Ghiorso and Sack (1995; available online as the MELTS Supplemental Calculator at http://gneiss.geology.washington.edu/~ghiorso/MELTSWWW/Melts.html). The temperature dependence of C_0 is expressed as $\partial(\ln C_0)/\partial(1/T) = H_f/R$, where H_f is the enthalpy of fusion of Kunlun Mts. diopside. We used the MELTS Supplemental Calculator to calculate H_f and C_0 for Kunlun Mts. diopside at the conditions of our experiments. H_f has values between 111 and 127 kJ/mol at temperatures of 1270 to 1450 °C and 1.3 GPa, and C_0 has values between 0.33 and 0.75 at the same conditions. Given values for C_s and C_∞ of 1 and 0.307, Eqn. 2 gives the relation between a and C_0. This relation is approximately log linear, except when C_0 approaches C_∞. For $0.33<C_0<0.75$ the average value of $\partial \ln a / \partial \ln C_0$ is ~3.4. Combined with the temperature dependence for C_0 given above, this gives $\partial \ln a / \partial \ln(1/T) \cong 3.4 H_f / R$. From Eqn. (4), an expression for the temperature dependence of Kunlun Mts. diopside dissolution in Luna 24 basalt at 1.3 GPa and 1270-1450 °C is then given by:

$$\frac{\partial(\ln rate)}{\partial(1/T)} \cong \frac{1}{R}\left(\frac{1}{2}H_a + 3.4H_f\right). \qquad (5)$$

This expression is an approximation of a more complicated functional form, and the factor of 3.4 multiplying the enthalpy of fusion holds only over the range of parameters we have estimated here.

The activation enthalpy for diffusion of network-forming components in andesitic to basaltic melts is typically 200-300 kJ/mol (e.g. Baker, 1990; Zhang et al., 1989). Taking a value of 250 kJ/mol for the diffusion activation enthalpy and 120 kJ/mol for the enthalpy of fusion of diopside, $\partial \ln rate / \partial(1/T)$ for our experiments at 1.3 GPa is predicted from (5) to have a value of -533 (kJ/mol)/R. This is in good agreement with the value of -503 (kJ/mol)/R determined from the fit to our experimental data (Fig. 4).

Pressure dependence

The dissolution rate for diopside at 1350 °C is significantly greater at 1.0 GPa than at 1.3 GPa (Table 5, Fig. 4). Brearley and Scarfe (1986) observed a similar increase in dissolution rate with decreasing pressure in their experiments on clinopyroxene dissolution in alkali basalt. Diffusion of network forming cations in silicate melts has a modest pressure dependence (e.g. Baker, 1990; Shimizu and Kushiro, 1991) which is not sufficient, and may be in the wrong sense, to explain the pressure dependence of diopside dissolution rates. The pressure dependence is probably due mostly to the increase in diopside solubility with decreasing pressure. Using MELTS (Ghiorso and Sack, 1995) as above to calculate the "saturated" activity of diopside in a melt at 1350 °C and 1.0-1.3 GPa, we find that the parameter a is expected to increase from ~0.15 at 1.3 GPa to ~0.24 at 1.0 GPa. This corresponds to a ratio of dissolution rates at 1.0 and 1.3 GPa of ~1.6, which is in reasonable agreement with the measured ratio of 2.25 ± 0.79 (Table 5).

Comparison of diopside and ilmenite dissolution rates

The dissolution rates reported here for diopside at 1.3 GPa are significantly slower than ilmenite dissolution rates measured by Wagner and Grove (1997) in low-Ti lunar basalts at 1.0 GPa (Fig. 5). Part of this difference in dissolution rates may be attributed to pressure; the dashed line in Figure 5 shows diopside dissolution rates shifted upward to pass through our data point at 1.0 GPa and 1350 °C. At low temperatures there is still a significant difference in dissolution rates, even with the correction for pressure. However, at temperatures

corresponding to the liquidus of lunar high-Ti glasses (~1400 °C for Apollo 14 black glass at 1.0 GPa; Wagner and Grove, 1997) there is expected to be very little difference in the dissolution rates of ilmenite and diopside. Pyroxenes in high-Ti cumulates may dissolve even faster than the nearly pure diopside used in our experiments, because they are closer in composition to the liquid they are dissolving into, particularly in terms of FeO, CaO and MgO. In general, the smaller the compositional difference between mineral and melt, the faster the dissolution rate (Zhang et al., 1989). Thus our results for nearly pure diopside probably represent a lower limit for the dissolution rate of clinopyroxene in high-Ti cumulates.

Melting Kinetics Experiments

A summary of the results of diopside-ilmenite melting kinetics experiments is given in Table 7. Dissolution rates for ilmenite and diopside were estimated by measuring the initial and final thickness of the two crystals perpendicular to their interface. Densities of 3300 and 4600 kg/m^3 for diopside and ilmenite, respectively, were used to convert the change in thickness to a change in mass.

Backscattered electron images of run products from two experiments at 1350 °C are shown in Figure 6. In the longer experiment (B634; 6 hr) the configuration is gravitationally stable, with diopside on top of ilmenite. The configuration is reversed in the shorter duration experiment (B653; 1 hr), with ilmenite on top of diopside. In this case there is a driving force for convective mixing between dense ilmenite-enriched melts at the top of the growing melt layer and diopside-enriched melts below. If convection were an important mechanism for mass transport in this experiment, one would expect the dissolution rate to be significantly more rapid than in the gravitationally stable experiment. The ilmenite dissolution rate is slightly higher in experiment B653, but the diopside dissolution rate is the same within the uncertainty of the measurement. Convection thus appears not to have a large influence on dissolution rates in these experiments.

In the melting kinetics experiments the interface between ilmenite and melt is always observed to be smooth (Fig. 6). The diopside-melt interface is more rugged, and relict blocks of diopside are suspended in the interstitial pool of melt. These blocks were probably the result of dissolution along cleavage cracks that formed during pressurization and heating of the experimental charge, as has been observed also by Greenwood and Hess (1998) in melting of superheated albite. Relict blocks were not observed in the experiments on diopside dissolution into Luna 24 basalt, probably because the diopside was surrounded by soft glass powder which absorbed most of the deformation during pressurization and prevented cleavage cracks from forming. In any case the relict blocks represent a significant volume of undissolved material, and this was accounted for in estimating the amount of diopside that dissolved during the experiments.

Figure 7 shows a plot of ilmenite and diopside dissolution distances versus the square root of the run duration for melting kinetics experiments run at 1350 °C. The linear dependence of dissolution distance on $\sqrt{t}$ suggests that melting is controlled by diffusion. It is presumed that a saturation condition is maintained at each interface, such that the melt is saturated with diopside at the diopside-melt interface and with ilmenite at the ilmenite-melt interface. Growth of the melt layer is limited by diffusive transport of Ca, Si and Mg away from the diopside interface and by complementary diffusive transport of Fe and Ti away from the ilmenite interface. In one experimental charge (B634) a significant portion of the concentration profile could be measured in quenched glass (Fig. 8). SiO_2 and CaO concentrations increase smoothly across the melt layer from ilmenite to diopside, and TiO_2 and FeO profiles have the opposite trend.

An Arrhenius plot showing the dissolution rates of ilmenite and diopside in the melting kinetics experiments is shown in Figure 9. Diopside dissolves significantly faster than ilmenite at the conditions of the experiments. The trend of the data suggests that at higher temperatures (above ~1380 °C) the order of dissolution rates may reverse. The temperatures at which melting of high-Ti cumulates may take place in the Moon are bracketed by the solidus of the

high-Ti cumulate and the liquidus of lunar ultramafic liquids. At temperatures near the solidus of the high-Ti cumulate (~1200 °C at 1.3 GPa), ilmenite is predicted to dissolve an order of magnitude more slowly than diopside with which it is in contact. At ultramafic glass liquidus temperatures (~1400-1500 °C at 1.3 GPa) the melting rate will be very fast and dissolution rates of ilmenite and diopside will be similar. At 1400 °C, cm-sized grains will dissolve completely within hours.

DISCUSSION

Assimilation Model for High-Ti Magma Genesis

The cumulate assimilation model must meet two requirements: there should be sufficient heat available to allow for assimilation, and the resulting melts must be similar in composition to those represented in the lunar ultramafic glass suite. Wagner and Grove (1997) evaluated the heat budget and found that it was sufficient to allow significant assimilation of cpx-ilmenite cumulates by low-Ti ultramafic magmas. Here we focus on the compositional constraints and ask whether an assimilation process can reproduce the compositional trend displayed by the pristine lunar ultramafic glasses.

Partial fusion of clinopyroxene-ilmenite cumulates

One mechanism for the chemical interaction of low-Ti magmas with late stage cpx-ilmenite cumulates involves heating and partial fusion of the cumulates. Do mixtures of cpx-ilmenite cumulate partial melts and low-Ti ultramafic magmas resemble high-Ti ultramafic glass compositions? The compositions of partial melts produced in our phase equilibrium experiments are compared with the compositions of pristine lunar glasses on a plot of CaO vs. TiO_2 (Fig. 10). The lunar glasses, shown as filled circles, form a trend of decreasing CaO with increasing TiO_2. Partial melts of the cpx-ilmenite cumulate (open symbols) do not lie on this trend or its extension; they have significantly lower TiO_2 and higher CaO concentrations than the highest TiO_2 glasses. Thus simple mixing of equilibrium partial melts of a cpx-ilmenite cumulate with a low-Ti parent liquid can not reproduce the compositional trend of the high-Ti

glasses. Increasing the pressure of melting does not move cpx-ilmenite partial melts toward the compositions of the lunar glasses; the TiO_2 content increases and CaO content decreases somewhat with pressure, but the shift in composition is small and more or less parallel to the lunar glass array. Neither can fractional crystallization cause hybrid liquids to evolve toward lunar glass compositions. Fractional crystallization of olivine or orthopyroxene will increase both the TiO_2 and CaO concentrations, moving melts along a trajectory away from and nearly orthogonal to the trend of the lunar glasses. Fractionation of high-Ca pyroxene or plagioclase would move melts in the right direction, but this is not an option because pristine lunar glass liquids are not saturated with either of these phases at any pressure (Kesson, 1975; Delano, 1980; Wagner and Grove, 1997).

For assimilation to meet the compositional constraints provided by the pristine lunar glass suite, a significantly higher ratio of ilmenite to cpx must enter the melt, on the order of ~3:1. Can a rapid disequilibrium melting process accomplish this? Our melting kinetics experiments indicate that it can not. Clinopyroxene dissolves more rapidly than ilmenite with which it is in contact, particularly at lower temperatures. At temperatures above 1350 °C cpx may dissolve more rapidly than ilmenite, but the melting rate at these temperatures is so fast that solid cumulates are unlikely to be preserved at all. At 1400 °C, a 1 cm cpx grain in contact with ilmenite is predicted to dissolve completely in only a few hours. It is doubtful that a melting and mixing process could take place on such a short time scale.

Selective contamination may take place by diffusive fractionation in the melt (e.g. Watson, 1982), but this is unlikely to increase the TiO_2/CaO ratio beyond that for simple binary mixing between the assimilating magma and the cpx-ilmenite partial melt. Ti diffuses more slowly than Ca in basaltic liquids (e.g. LaTourrette et al., 1996), and thus diffusive fractionation would be likely to decrease rather than increase the TiO_2/CaO ratio in the assimilating magma. Uphill diffusion could complicate matters, but is unlikely to play a major role in chemical fractionation of TiO_2 and CaO because both species have similar preferences for less polymerized liquids (Zhang et al., 1989).

Dissolution of clinopyroxene and ilmenite into low-Ti magmas

Another possible mechanism for assimilation of late stage cumulates involves dissolution of cpx and ilmenite directly into low-Ti magmas. This is unlikely to be a significant mechanism for assimilation of cpx-ilmenite cumulates, because dissolution at the boundary between cpx and ilmenite crystals is more rapid than dissolution of these minerals into low-Ti melts. At 1400 °C the melting rate is predicted to be a factor of ~3 faster than the dissolution rates of cpx and ilmenite into low-Ti melts (compare Figs. 5 and 9). Thus, a cpx-ilmenite xenolith entrained in an ascending low-Ti magma would melt internally, at interfaces between cpx and ilmenite, faster than the individual minerals would dissolve into the entraining low-Ti magma. Dissolution of cpx and ilmenite into low-Ti liquids would be important only if cpx and ilmenite were not in physical contact. Even in this case, the dissolution rates of ilmenite and cpx are expected to be similar at ultramafic glass liquidus temperatures (see Fig. 5), making selective assimilation of ilmenite unlikely. Selective assimilation could only take place at lower temperatures, where ilmenite does dissolve significantly faster than cpx. The assimilating liquid in this case would need to have a significantly lower liquidus temperature than any of the ultramafic glasses.

Hybrid source models

Assimilation of cpx-ilmenite cumulates by the processes described above does not account for the compositions of lunar high-Ti ultramafic glasses. An alternative is that the high-Ti glasses were generated during partial melting of a hybrid source region at depth. Arguments similar to those given above rule out simple mixing of melts from separate cpx-ilmenite and olivine-orthopyroxene cumulate sources. Mixing between cpx-ilmenite partial melts and low-Ti ultramafic magmas will lead to hybrid liquids deficient in TiO_2 and enriched in CaO relative to high-Ti ultramafic glasses (see Fig. 10). Instead, high-Ti lunar magmas must have equilibrated with a source that contained olivine ± orthopyroxene in addition to cpx and ilmenite.

The prevailing model for creating such a source involves overturn of the gravitationally unstable magma ocean cumulate pile. Several variants of this model have been proposed. Ringwood and Kesson (1976) envisioned cpx-ilmenite pods decoupling from overlying crust, sinking into the lunar mantle and partially melting and reacting with mafic cumulates at depth. The heterogeneous hybrid mantle resulting from this process was considered to be the source for high- and low-Ti ultramafic magmas and mare basalts. Hess and Parmentier (1995) proposed that large cpx-ilmenite cumulate diapirs could have descended to the center of the Moon, carrying with them a significant complement of the Moon's radionuclides. In this version of the overturn model, the source region for high-Ti lunar magmas is thought to lie within a convectively mixed layer just above the radioactively heated cpx-ilmenite core.

The dynamics of cumulate pile overturn depend on viscosity, which is strongly dependent on temperature. The temperature during overturn is constrained by the phase relations of cpx-ilmenite cumulates. The high-Ti layer becomes gravitationally unstable when the temperature has fallen near the solidus; more than ~30 °C above the solidus, the high-Ti layer will be mostly molten (see Table 2) and less dense than underlying mafic cumulates. Thus, when cpx-ilmenite diapirs begin to sink through underlying cumulates, the temperature cannot be far above 1125 °C (the solidus at 100 km depth). The viscosity of mafic cumulates at this temperature can be estimated using flow laws for dry olivine given by Karato and Wu (1993). The viscosity in the power law creep regime is calculated to be in the range 1×10^{21} to 5×10^{23} Pa s, assuming that stresses are similar to those in Earth's convecting mantle (1 MPa to 0.1 MPa). Similar viscosities are obtained for diffusion (Newtonian) creep; 1×10^{22} to 6×10^{23} Pa s for olivine grain sizes of 1 to 5 mm. These viscosities are much higher than have been used in models of cumulate pile overturn, where the temperature constraint has not been taken into account. Hess and Parmentier (1995), for example, assumed a viscosity for mafic cumulates of $\sim 10^{19}$ Pa s. This is a reasonable value for the early evolution of the magma ocean, when the temperature is near the solidus of mafic cumulates, but is too low to apply during

sinking of the high-Ti layer, when the temperature is constrained to be near the cpx-ilmenite solidus.

The rate of settling of cpx-ilmenite diapirs through mafic cumulates can be calculated from Stokes' law. If the temperature gradient within the lunar mantle is adiabatic (~0.15 °C/km; Finilla et al., 1994), there will be little change in the viscosity with depth. For a viscosity of 3×10^{22} Pa s (corresponding to power law creep with 0.3 MPa stress), and a density difference between cpx-ilm and mafic cumulates of 350 kg/m^3, the settling rate in meters per second is calculated to be $\sim 1 \times 10^{-21} d^2$, where d is the diameter of the diapir (assumed here to be spherical) in meters. Given this relation for the settling rate, we can calculate how far diapirs could descend into the lunar mantle in the ~400 million years available between complete solidification of the magma ocean and the onset of high-Ti volcanism on the Moon at ~3.9 Ga. A cumulate diapir 40 km in diameter is calculated to fall only 20 km in this time. Only diapirs larger than about 180 km could descend to depths of several hundred kilometers where lunar ultramafic glasses are thought to be produced, and ~360 km diapirs are required if cumulates are to descend to the lunar core.

A high-Ti cumulate layer evenly distributed beneath the lunar crust would be only about 20 kilometers thick (Snyder et al., 1992; Hess and Parmentier, 1995), so diapirs would have to grow considerably to reach the ~180 km size that is probably necessary for descent deep into the lunar mantle. Whether diapirs can grow large enough depends critically on the viscosity of the cpx-ilmenite cumulate layer. Analytical expressions for the growth time and characteristic wavelength of Rayleigh-Taylor instabilities (Whitehead, 1988; Hess and Parmentier, 1995) indicate that the viscosity of cpx-ilmenite cumulates must be ~300 times less than the viscosity of mafic cumulates in order to grow diapirs 180 km in diameter within 100 My. Such a low viscosity seems unlikely, because clinopyroxene-dominated rocks in general are even stronger than olivine rocks (e.g. Kirby and Kronenberg, 1984). Hess and Parmentier (1995) suggested that a liquid phase that wets grain boundaries in the cpx-ilmenite cumulate might lower the viscosity enough to generate very large diapirs. Grain boundary wetting is rare in silicates

(Kohlstedt and Zimmerman, 1996) but whether it may occur in cpx-ilmenite rocks remains an open question. If melts do not wet grain boundaries, then it probably is not possible to generate cpx-ilmenite diapirs of the size required to transport cpx-ilmenite cumulates hundreds of kilometers into the lunar mantle.

The preceding analysis illustrates an essential problem in redistributing cpx-ilmenite cumulates to deep levels within the Moon. At the low temperatures that are needed to keep the cpx-ilmenite cumulates negatively buoyant, settling of diapirs through the cold, stiff mafic cumulates is difficult. This difficulty can be eased if the solidus of high-Ti material is increased so that overturn can take place at higher temperatures, where settling is more efficient. We suggest that physical mixing and chemical reaction between high-Ti liquids and mafic cumulates produced a refractory hybrid material at shallow levels, during late stages of magma ocean solidification. Large scale transport of this hybrid material could be accomplished more easily than in the case of pure cpx-ilmenite cumulates. Calculations using the MELTS algorithm (Ghiorso and Sack, 1995) indicate that the addition of as little as 20 wt.% Fo70 olivine to our TiCum composition would raise the solidus by ~80 °C. The viscosity at this temperature would be an order of magnitude lower than at the solidus of cpx-ilmenite cumulates. The density of this material would be at least 200 kg/m^3 greater than that of mafic cumulates, and we calculate that diapirs as small as ~60 km in diameter could descend several hundred kilometers into the lunar mantle within a few hundred million years. The time required for diapirs to develop would be on the order of ~10 million years.

Shallow level hybridization is probably a natural consequence of the very long solidification time inferred for late stage magma ocean liquids. Complete crystallization of late stage liquids, after the formation of a stable anorthosite crust, is predicted to take 200 My or more (Solomon and Longhi, 1977). During the long solidification process, late stage liquids will react chemically with the mafic products of earlier fractional crystallization. Cumulates also may mix physically over short length scales, driven by gravitational instabilities that develop during crystallization (e.g. Snyder et al., 1992; Hess and Parmentier, 1995). Reaction and

mixing among late stage liquids and mafic cumulates may have been enhanced by radioactive heating in the crust. It has been shown recently that a large proportion of the Moon's budget of radioactive elements may reside within a single crustal province on the nearside (e.g. Haskin, 1998). Heat produced in this highly radiogenic crust may significantly slow the crystallization of late stage liquids (Wieczorek and Phillips, 1999), allowing more time for their interaction with mafic cumulates.

CONCLUSIONS

The implications of our experiments for the origin of lunar high-Ti ultramafic glasses can be summarized as follows:

1. Assimilation of late stage cumulates does not appear to be a viable mechanism for the production of lunar high-Ti magmas. Assimilation processes involving equilibrium or disequilibrium partial melting of cpx-ilmenite cumulates, followed by mixing with low-Ti magmas, are not able to produce liquids with the appropriate compositions. Selective contamination, either by diffusive fractionation in the melt or by preferential dissolution of ilmenite into the assimilating magma, also is unlikely to lead to magmas similar in composition to lunar high-Ti ultramafic glasses.

2. The low temperature (near 1125 °C at 100 km depth) at which the solidifying high-Ti layer becomes gravitationally unstable with respect to underlying cumulates places severe restrictions on the rate of settling of cpx-ilmenite cumulates through the lunar mantle. The viscosity at this temperature is probably too high for cpx-ilmenite diapirs to descend to the depths inferred for production of high-Ti ultramafic magmas within the appropriate time frame.

Chemical reaction and physical mixing between high Ti liquids and mafic cumulates at shallow levels may have produced a hybrid material negatively buoyant at higher temperatures, and able to descend to hundreds of kilometers depth before the onset of high-Ti volcanism on the Moon. We suggest that shallow level hybridization, followed by sinking, may have been the

process that created the heterogeneous mantle source for lunar ultramafic glasses and mare basalts.

REFERENCES

Anderson A. T. (1971) Exotic armalcolite and the origin of Apollo 11 ilmenite basalts. *Geochim. Cosmochim. Acta* **35**, 969-973.

Baker D. R. (1990) Chemical interdiffusion of dacite and rhyolite: Anhydrous measurements at 1 atm and 10 kbar, application of transition state theory, and diffusion in zoned magma chambers. *Contrib. Mineral. Petrol.* **104**, 407-423.

Brearley M. and Scarfe C. M. (1986) Dissolution rates of upper mantle minerals in an alkali basalt melt at high pressure: An experimental study and implication for ultramafic xenolith survival. *J. Petrol.* **27**, 1157-1182.

Chen H.-K. and Lindsley D. H. (1983) Apollo 14 very low-titanium glasses: Melting experiments in iron-platinum alloy capsules. *J. Geophys. Res.* **88**, B335-B342.

Chen H.-K., Delano J. W., and Lindsley D. H. (1982) Chemistry and phase relations of VLT volcanic glasses from Apollo 14 and Apollo 17. *J. Geophys. Res.* **87**, A171-A181.

Delano J. W. (1980) Chemistry and liquidus relations of Apollo 15 red glass: Implications for the deep lunar interior. *Proc. 11th Lunar Planet. Sci. Conf.*, 251-288.

Delano J. W. (1986) Pristine lunar glasses: Criteria, data, and implications. *J. Geophys. Res.* **91**, D201-D213.

Finilla A. B., Hess P. C., and Rutherford M. J. (1994) Assimilation by lunar mare basalts: Melting of crustal material and dissolution of anorthite. *J. Geophys. Res.* **99**, 14,677-14,690.

Ghiorso M. S. and Sack R. O. (1995) Chemical mass transfer in magmatic processes IV. A revised and internally consistent thermodynamic model for the interpolation and extrapolation of liquid-solid equilibria in magmatic systems at elevated temperatures and pressures. *Contrib. Mineral. Petrol.* **119**, 197-212.

Green D. H., Ringwood A. E., Hibberson W. O., and Ware N. G. (1975) Experimental petrology of the Apollo 17 mare basalts. *Proc. 11th Lunar Sci. Conf.*, 871-893.

Greenwood J. P. and Hess P. C. (1998) Congruent melting kinetics of albite: Theory and experiment. *J. Geophys. Res.* **103**, 29815-29828.

Haskin, L. A., The Imbrium impact event and the thorium distribution at the lunar highlands surface. *J. Geophys. Res.* **103**, 1679-1689.

Hays J. F. (1966) Lime-alumina-silica. *Carnegie Inst. Wash. Yearbk.* **65**, 234-236.

Herbert F. (1980) Time dependent lunar density models. *Proc. 11th Lunar Planet. Sci. Conf.*, 2015-2030.

Hess P. C. (1991) Diapirism and the origin of high TiO_2 mare glasses. *Geophys. Res. Lett.* **18**, 2069-2072.

Hess P. C. and Parmentier E. M. (1995) A model for the thermal and chemical evolution of the Moon's interior: Implications for the onset of mare volcanism. *Earth Planet. Sci. Lett.* **134**, 501-514.

Hubbard N. J. and Minear J. W. (1975) A chemical and physical model for the genesis of lunar rocks: Part II. Mare basalts. *Lunar Sci.* **VI**, 405-407.

Karato S. and Wu P. (1993) Rheology of the upper mantle: a synthesis. *Science* **260**, 771-778.
Kesson S. E. (1975) Mare basalts: Melting experiments and petrogenetic interpretations. *Proc. 6th Lunar Sci. Conf.*, 921-941.

Kirby S. H. and Kronenberg A. K. (1984) Deformation of clinopyroxenite: Evidence for a transition in flow mechanisms and semi-brittle behavior. *J. Geophys. Res.* **89**, 3177-3192.

Kohlstedt D. L. and Zimmerman M. E. (1996) Rheology of partially molten mantle rocks. *Annu. Rev. Earth Planet. Sci.* **24**, 41-62.

Kuo L. C. and Kirkpatrick R. J. (1985) Kinetics of crystal dissolution in the system diopside-forsterite-silica. *Am. J. Sci.* **285**, 51-90.

LaTourrette T., Wasserburg G. J. and Fahey A. J. (1996) Self diffusion of Mg, Ca, Ba, Nd, Yb, Ti, Zr, and U in haplobasaltic melt. *Geochim. Cosmochim. Acta* **60**, 1329-1340.

Longhi J. (1977) Magma oceanography 2: Chemical evolution and crustal formation. *Proc. 8th Lunar Sci. Conf.*, 601-621.

Ringwood A. E. and Kesson S. E. (1976) A dynamic model for mare basalt petrogenesis. *Proc. 7th Lunar Sci. Conf.*, 1697-1722.

Shearer C. K. and Papike J. J. (1993) Basaltic magmatism on the Moon: A perspective from volcanic picritic glass beads. *Geochim. Cosmochim. Acta* **57**, 4785-4812.

Shearer C. K. and Papike J. J. (1999a) Origin of lunar mare high-titanium basalts: Melting of a deep hybridized source or shallow assimilation of high-Ti cumulates? *Lunar Planet. Sci.* **XXX**, 1365.

Shearer C. K. and Papike J. J. (1999b) Magmatic evolution of the Moon. *Am. Mineral.* **84**, 1469-1494.

Shimizu N. and Kushiro I. (1991) The mobility of Mg, Ca, and Si in diopside-jadeite liquids at high pressures. In *Physical Chemistry of Magmas* (eds. L. L. Perchuk and I. Kushiro) pp. 192-212. Springer-Verlag, New York, New York, USA.

Smith J. V., Anderson A. T., Newton R. C., Olsen E. J., Wyllie P. J., Crewe A. V., Isaacson M. S., and Johnson D. (1970) Petrologic history of the Moon inferred from petrography, mineralogy, and petrogenesis of Apollo 11 rocks. *Proc. 1st Lunar Sci. Conf.*, 897-925.

Snyder G. A., Taylor L. A., and Neal C. R. (1992) A chemical model for generating the sources of mare basalts: Combined equilibrium and fractional crystallization of the lunar magmasphere. *Geochim. Cosmochim. Acta* **56**, 3809-3823.

Solomon S. C. and Longhi J. (1977) Magma oceanography: 1. Thermal evolution. *Proc. 8th Lunar Sci. Conf.*, 583-599.

Spera F. J. (1992) Lunar magma transport phenomena. *Geochim. Cosmochim. Acta* **56**, 2253-2265.

Taylor S. R. and Jakes P. (1974) The geochemical evolution of the Moon. *Proc. 5th Lunar Sci. Conf.*, 1287-1305.

Wagner T. P. and Grove T. L. (1997) Experimental constraints on the origin of lunar high-Ti ultramafic glasses. *Geochim. Cosmochim. Acta* **61**, 1315-1327.

Walker D., Longhi J., and Hays J. F. (1975a) Differentiation of a very thick magma body and implications for the source regions of the mare basalts. *Proc. 6th Lunar Sci. Conf.*, 1103-1120.

Walker D., Longhi J., Stolper E. M., Grove T. L., and Hays J. F. (1975b) Origin of titaniferous lunar basalts. *Geochim. Cosmochim. Acta* **39**, 1219-1235.

Watson E. B. (1982) Basalt contamination by continental crust: Some experiments and models. *Contrib. Mineral. Petrol.* **80**, 73-87.

Whitehead J. A. (1988) Fluid models of geological hotspots. *Ann. Rev. Fluid Mech.* **20**, 61-87.

Wieczorek M. A. and Phillips R. J. (1999) Thermal modeling of mare volcanism and the "Procellarum KREEP Terrane". *Lunar Planet. Sci.* **XXX**, 1547.

Wood J. A., Dickey J. S., Marvin U. B., and Powell B. N. (1970) Lunar anorthosites and a geophysical model of the Moon. *Proc. 1st Lunar Sci. Conf.*, 965-988.

Wyatt B. A. (1977) The melting and crystallization behavior of a natural clinopyroxene-ilmenite intergrowth. *Contrib. Mineral. Petrol.* **61**, 1-9.

Zhang Y., Walker D., and Lesher C. E. (1989) Diffusive crystal dissolution. *Contrib. Mineral. Petrol.* **102**, 492-513.

Table 1. Compositions of starting materials used in phase equilibrium and kinetics experiments.

Material	SiO_2	TiO_2	Al_2O_3	Cr_2O_3	FeO	MnO	MgO	CaO	Na_2O	K_2O
High-Ti Cumulate (TiCum)[a]	41.61	9.1	2.8	0	29.6	0	7.5	8.2	0	0
Diopside, Kunlun Mts.[b]	54.92	0.03	0.64	0	0.76	0.06	18.35	25.2	0.42	0
Ilmenite, Frank Smith Mine[b]	0.13	51.8	0.64	1.7	33.2	0.17	11.4	0.07	0	0
Luna 24 Ferrobasalt[a]	47.1	0.88	12.6	0.23	20.2	0.25	6.31	12.8	0.2	0.02

Values are given in weight percent.
a Compositions determined by combining weighed amounts of synthetic oxides.
b Compositions determined by electron microprobe.

Table 2. Conditions and results of phase equilibrium experiments on synthetic high-Ti cumulate composition (TiCum).

Run #	P (GPa)	T (°C)	t (hr)	Run Products[a]	Phase Proportions[b] (mass)	$^{c}\Sigma r^{2}$
TiCum 2	0.0001	1220	51	gl	-	-
TiCum 3	0.0001	1200	25	gl,cpx	96:4	0.2
TiCum 8	0.0001	1185	44	gl,cpx	91:9	0.55
TiCum 5	0.0001	1175	24	gl,cpx	89:11	0.74
TiCum 4	0.0001	1150	46	gl,cpx	82:18	0.54
TiCum 6	0.0001	1125	148	gl,cpx,ilm	72:25:3	0.01
TiCum 18	0.0001	1100	34	gl,cpx,ilm,trid,usp	49:40:11:tr:tr	0.04
TiCum 9	0.0001	1050	63	cpx,ilm,plag	79:14:7	1.1
TiCum 17	1.3	1340	17	gl,cpx	94:06	0.89
TiCum 16	1.3	1300	11	gl,cpx	78:22	0.04
TiCum 15	1.3	1280	10	gl,cpx	73:27	0.69
TiCum 14	1.3	1260	20	gl,cpx	64:36	0.05
TiCum 12	1.3	1240	23	gl,cpx,ilm	53:45:2	0.13
TiCum 11	1.3	1220	22	gl,cpx,ilm,qtz	35:56:9:tr	0.16
TiCum 10	1.3	1200	19	cpx,ilm	86:14	2.2
TiCum20	1.8	1290	24	gl,cpx	62:38	0.11

a Abbreviations are: gl, glass; cpx, clinopyroxene; ilm, ilmenite; trid, tridymite; usp, ulvospinel; plag, plagioclase; qtz, quartz.
b Phase proportions listed in same order as in Run Products column, estimated by unweighted multiple linear regression of the phase compositions (Table 3) against the bulk composition (Table 1).
c Sum of squared residuals for the multiple regression

Table 3. Compositions of run products from experiments on synthetic high-Ti cumulate (TiCum).

Run #	Phase[a]	N[b]	SiO_2[c]	TiO_2	Al_2O_3	FeO	MgO	CaO	Total
TiCum 3	gl	7	41.7(0.4)	9.29(0.15)	2.98(0.04)	30.5(0.2)	6.85(0.11)	8.37(0.13)	99.7
	cpx	9	53.8(0.3)	0.58(0.07)	0.10(0.03)	22.9(0.4)	21.8(0.6)	1.84(0.09)	101
TiCum 8	gl	7	40.8(0.2)	9.69(0.14)	3.08(0.08)	31.2(0.2)	6.42(0.07)	8.64(0.09)	99.8
	cpx	5	52.7(1.4)	0.60(0.10)	0.11(0.03)	22.6(1.0)	22.6(1.0)	2.03(0.13)	101
TiCum 5	gl	7	40.4(0.3)	9.82(0.20)	3.11(0.04)	31.3(0.3)	6.25(0.13)	8.71(0.12)	99.6
	cpx	6	53.2(0.3)	0.62(0.10)	0.13(0.06)	23.7(0.7)	21.2(0.4)	2.10(0.05)	101
TiCum 4	gl	7	39.4(0.2)	10.6(0.2)	3.32(0.05)	31.6(0.3)	5.26(0.04)	9.24(0.08)	99.4
	cpx	8	52.5(0.4)	0.78(0.11)	0.17(0.05)	25.3(0.4)	19.3(0.4)	2.82(0.35)	101
TiCum 6	gl	8	40.5(0.2)	10.1(0.05)	3.80(0.04)	30.2(0.2)	4.49(0.04)	10.1(0.1)	99.2
	cpx	8	51.3(0.2)	0.85(0.05)	0.31(0.09)	26.6(0.6)	17.2(0.2)	4.31(0.47)	101
	ilm	3	n.d.	54.0(0.1)	0.20(0.01)	44.2(0.3)	3.74(0.06)	0.13(0.02)	102
TiCum 18	gl	6	42.5(0.2)	7.50(0.29)	5.59(0.34)	30.2(0.2)	2.89(0.62)	10.6(0.1)	99.2
	cpx	5	49.9(1.0)	1.31(0.91)	0.54(0.14)	27.9(1.5)	14.2(0.4)	6.90(1.80)	101
	ilm	3	n.d.	50.3(0.4)	0.25(0.01)	47.8(0.3)	2.51(0.05)	0.33(0.06)	100
	trid	1	96.7	0.44	0.10	0.75	0.02	0.10	98.1
	usp	3	0.08(0.07)	25.3(0.1)	1.72(0.05)	69.8(0.28)	1.99(0.05)	0.29(0.02)	99.2
TiCum 9	cpx	8	48.8(1.0)	1.51(0.49)	1.04(0.42)	29.9(1.7)	9.41(0.34)	9.69(1.74)	100
	ilm	3	0.02(0.02)	52.6(0.5)	n.d.	45.6(0.2)	1 67(0.06)	0.39(0.04)	100
	plag	5	45.0(0.3)	n.d.	31.8(1.1)	4.87(1.29)	0.35(0.14)	18.1(0.5)	100
TiCum 17	gl	3	41.4(0 07)	10.1(0.11)	3.07(0.02)	29.3(0.2)	6.53(0.09)	8.88(0.15)	99.4
	cpx	3	52.7(0.3)	0.53(0.06)	0.32(0.04)	23.8(0.2)	20.4(0.2)	3.35(0.14)	101
TiCum 16	gl	3	39.5(0.1)	11.5(0.05)	3.56(0.05)	31.3(0.1)	4.95(0.02)	9.18(0 08)	99.9
	cpx	4	52.2(0.3)	0.72(0.12)	0.51(0.02)	26.2(0.4)	17.1(0.3)	4.93(0.12)	102
TiCum 15	gl	3	39.1(0.3)	12.8(0.2)	3.76(0.06)	30.3(0.2)	4.38(0.11)	9.43(0.02)	99.8
	cpx	7	51.3(0.4)	0.76(0.11)	0.60(0.08)	26.3(0.2)	15.9(0.2)	5.73(0.34)	101
TiCum 14	gl	8	37.4(0.2)	13.7(0.09)	4.01(0.06)	32.1(0.2)	3.78(0.16)	9.01(0.12)	99.9
	cpx	8	50.5(0.4)	0.90(0.07)	0.81(0.06)	26.6(0.4)	14.5(0.4)	6.92(0.41)	100
TiCum 12	gl	8	36.9(0.2)	13.7(0.1)	4.48(0.04)	31.9(0.2)	3.24(0.05)	9.05(0.05)	99.3
	cpx	8	49.8(0.6)	1.02(0.09)	1.04(0.07)	27.1(0.6)	13.1(0.24)	7.98(0.47)	100
	ilm	3	0.05(0.01)	53.4(0.3)	0.39(0.03)	45.0(0.4)	2.67(0.08)	0 29(0.01)	102
TiCum 11	gl	7	41.2(0.5)	10.8(0.1)	6.30(0.06)	28.3(0.1)	2.47(0.14)	9.30(0.13)	98.4
	cpx	8	49.5(0.2)	1.00(0.09)	1.51(0.16)	28.1(0.5)	11.7(0.15)	8.46(0.48)	100
	ilm	3	0.06(0.01)	52.3(0.2)	0.42(0.03)	46.3(0.05)	2.26(0.03)	0.31(0.03)	102
	qtz	1	99.6	0.15	0.07	0.31	n.d.	n.d.	100
TiCum 10	cpx	11	48.4(0.5)	1.46(0.11)	3.08(0.57)	28.9(0.8)	8.96(0.47)	9.67(0.65)	100
	ilm	2	0.05(0.04)	52.7(0.5)	0.52(0.03)	45.8(0.5)	1.67(0.06)	0.36(0.05)	101
TiCum20	gl	5	36.7(0.3)	14.2(0.2)	4.00(0.08)	32.2(0.3)	3.98(0.17)	9.15(0.04)	100
	cpx	1	50.9	0.85	1.06	27.2	13.6	6.86	100

a Abbreviations are as in Table 2.
b Number of analyses.
c Values in parentheses represent one standard deviation of replicate analyses.

Table 4. Stoichiometric coefficients for high-Ti cumulate melting reaction.

Experiment T1-T2	P (GPa)	ΔF	ΔT (°C)	Melting Rate (%/°C)	α	β
TiCum18-TiCum6	0.0001	0.24(0.02)	25	0.94	0.66(0.07)	0.34(0.03)
TiCum11-TiCum12	1.3	0.18(0.03)	20	0.91	0.63(0.18)	0.37(0.09)

Stoichiometric coefficients refer to the reaction α cpx + β ilm = 1 melt and were calculated from the change in phase proportions between experiments conducted at different temperatures. The values in parentheses are 1 σ, calculated by propagating the errors in estimation of phase proportions.

Table 5. Conditions and results of experiments on dissolution of diopside single crystals in Luna 24 basalt.

Run #	T (°C)	P (GPa)	t (s)	Initial length (μm)	Final length (μm)	Diss. rate (g m^{-2} $s^{-1/2}$)
B552	1270	1.3	87600	1333(10)	1277(9)	0.312(0.064)
B547	1350	1.3	9250	958(10)	831(33)	2.18(0.59)
C211	1350	1.0	3600	1085(10)	907(35)	4.90(1.1)
B548	1450	1.3	1000	1328(10)	970(39)	18.7(2.1)

Values in parentheses represent one standard deviation.

Table 6. Effective binary diffusion coefficients (EBDC) of SiO_2, TiO_2, Al_2O_3 and MgO for diopside dissolution into Luna 24 basalt at 1350 °C, 1.3 GPa. Dissolution rates were calculated using the EBDC for each component and Eqn. 3.

	SiO_2	TiO_2	Al_2O	MgO	CaO	FeO
EBDC ($\mu m^2/s$)	25.4(9.0)	28.7(10)	25.0(6.3)	192(77)	--	--
Co	48.8	0.68	10.45	8.10	14.1	17.4
a	0.12(0.01)	0.12(0.01)	0.068(0.01)	0.032(0.005)	--	--
Dissolution Rate ($g\ m^{-2}\ s^{-1/2}$)	2.01(0.55)	2.09(0.59)	1.13(0.31)	1.46(0.52)	--	--

Values in parentheses represent one standard deviation.

Table 7. Conditions and results of diopside-ilmenite melting kinetics experiments.

Run #	Mineral	T (°C)	P (GPa)	t (s)	Pos[a]	Initial length (μm)	Final length (μm)	Diss. rate ($g\ m^{-2}\ s^{-1/2}$)
B653	diopside	1350	1.3	3560	bot	1085(10)	832(13)	14.0(0.88)
	ilmenite				top	1049(10)	903(9)	11.5(1.1)
B634	diopside	1350	1.3	21600	top	1097(10)	501(10)	13.4(0.31)
	ilmenite				bot	1095(10)	812(10)	9.05(0.45)
B669	diopside	1300	1.3	21800	bot	1080(10)	915(10)	3.68(0.31)
	ilmenite				top	1062(10)	1013(7)	1.56(0.39)

Values in parentheses represent one standard deviation.
a. Position in the experimental charge.

FIGURE CAPTIONS

Fig. 1. Piston cylinder assembly used for ilmenite-diopside melting kinetics experiments. The interface between ilmenite and diopside is centered in the hotspot of the graphite furnace.

Fig. 2. Pressure-temperature phase diagram for synthetic high-Ti cumulate composition. Data are from Table 2.

Fig. 3. Concentration profiles (wt.%) in quenched glass from diopside dissolution experiment (B547; T = 1350 °C, P = 1.3 GPa), where x is distance from the diopside-melt interface. Compositions near the interface could not be measured due to the presence of a ~150 μm thick layer of quench crystals adjacent to the diopside. The curves are fits of Eqn. 1 to the data.

Fig. 4. Arrhenius plot showing the dissolution rate of Kunlun Mts. diopside in Luna 24 basalt vs. inverse temperature. Dissolution rates at 1.3 GPa can be described by: $R = 3.24*10^{16}\exp(-6.05*10^4/T)$, where T is temperature in K and R is the dissolution rate in g m^{-2} $s^{-1/2}$.

Fig. 5. Comparison of diopside and ilmenite dissolution rates in low-Ti lunar basaltic liquids. Diopside dissolution rates are from this work, and ilmenite dissolution rates are from Wagner and Grove (1996). The arrows and dashed line show the increase in dissolution rate of diopside when pressure decreases from 1.3 to 1.0 GPa.

Fig. 6. Backscattered electron images of run products from diopside-ilmenite melting kinetics experiments performed at 1350 °C and 1.3 GPa. a) Expt. B653, 1 hr run duration, ilmenite on top of diopside. b) Expt. B634, 6 hr run duration, diopside on top of ilmenite. The field of view in each micrograph is approximately 1.7 x 2.0 mm.

Fig. 7. Dissolution distance vs. square root of run duration for diopside-ilmenite melting kinetics experiments run at 1350 °C and 1.3 GPa. Data are from Table 7. Diopside--circles; ilmenite--squares.

Fig. 8. Concentration profiles (wt.%) across quenched melt layer in diopside-ilmenite melting kinetics experiment B634. At the left of the diagram is the ilmenite-melt interface (x = 0); the diopside-melt interface is at the right of the diagram, at x = 760 μm.

Fig. 9. Arrhenius plot showing rates of dissolution of ilmenite and diopside into the melt layer formed at their mutual boundary, at 1.3 GPa. Ilmenite and diopside dissolution rates at 1.3 GPa can be described by: R_{ilm} (g m^{-2} $s^{-1/2}$) = $4.72*10^{26}\exp(-9.59*10^4/T)$; R_{di} = $1.17*10^{19}\exp(-6.71*10^4/T)$.

Fig. 10. Comparison of lunar ultramafic glass and high-Ti cumulate partial melt compositions, on a plot of TiO_2 vs. CaO (wt.%). Solid circles represent the most primitive lunar glasses from each of the 26 groups defined by Delano (1986). Open symbols show the highest TiO_2 partial melts of the TiCum composition, at 0.1 MPa (squares) and 1.3 to 1.8 GPa (circles). The X symbol shows the composition of the TiCum starting material.

Figure 1

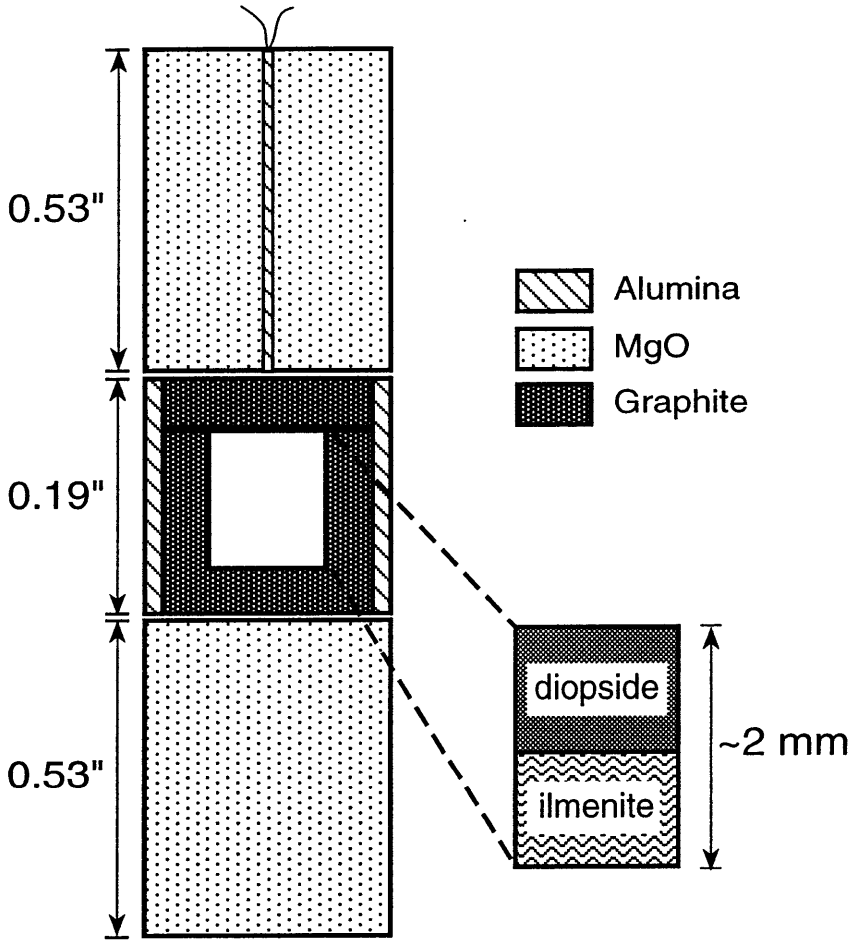

Figure 2

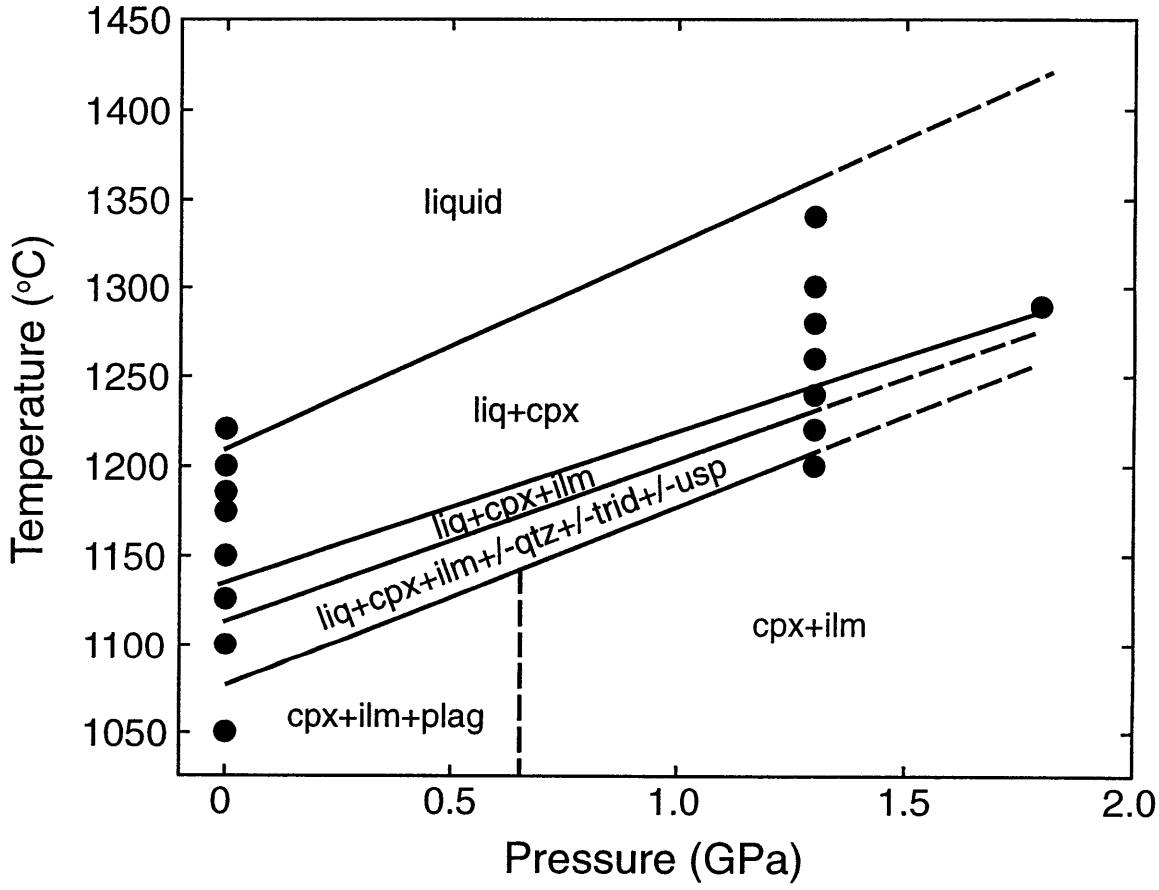
1450
1400
1350
1300
1250
1200
1150
1100
1050
Temperature (°C)
liquid
liq+cpx
liq+cpx+ilm
liq+cpx+ilm+/-qtz+/-trid+/-usp
cpx+ilm
cpx+ilm+plag
0
0.5
1.0
1.5
2.0
Pressure (GPa)

Figure 3

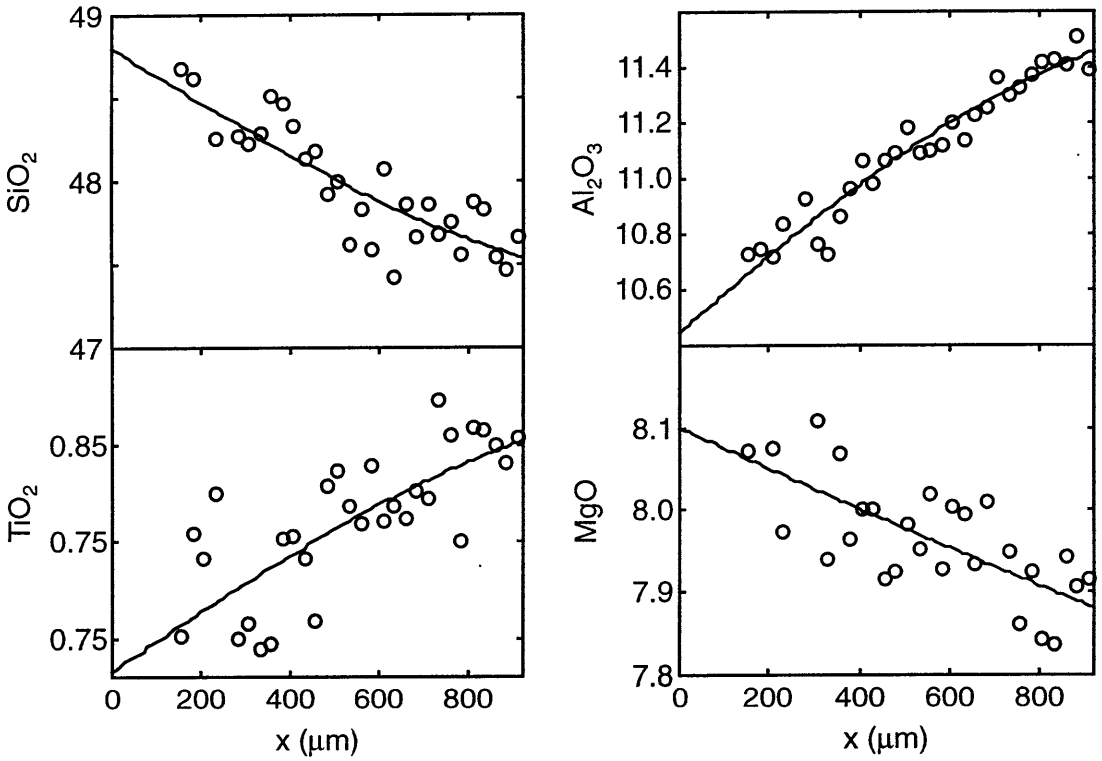
SiO2
49
48
47
TiO2
0.85
0.75
0.75
0
200
400
600
800
x (μm)
Al2O3
11.4
11.2
11.0
10.8
10.6
MgO
8.1
8.0
7.9
7.8
0
200
400
600
800
x (μm)

Figure 4

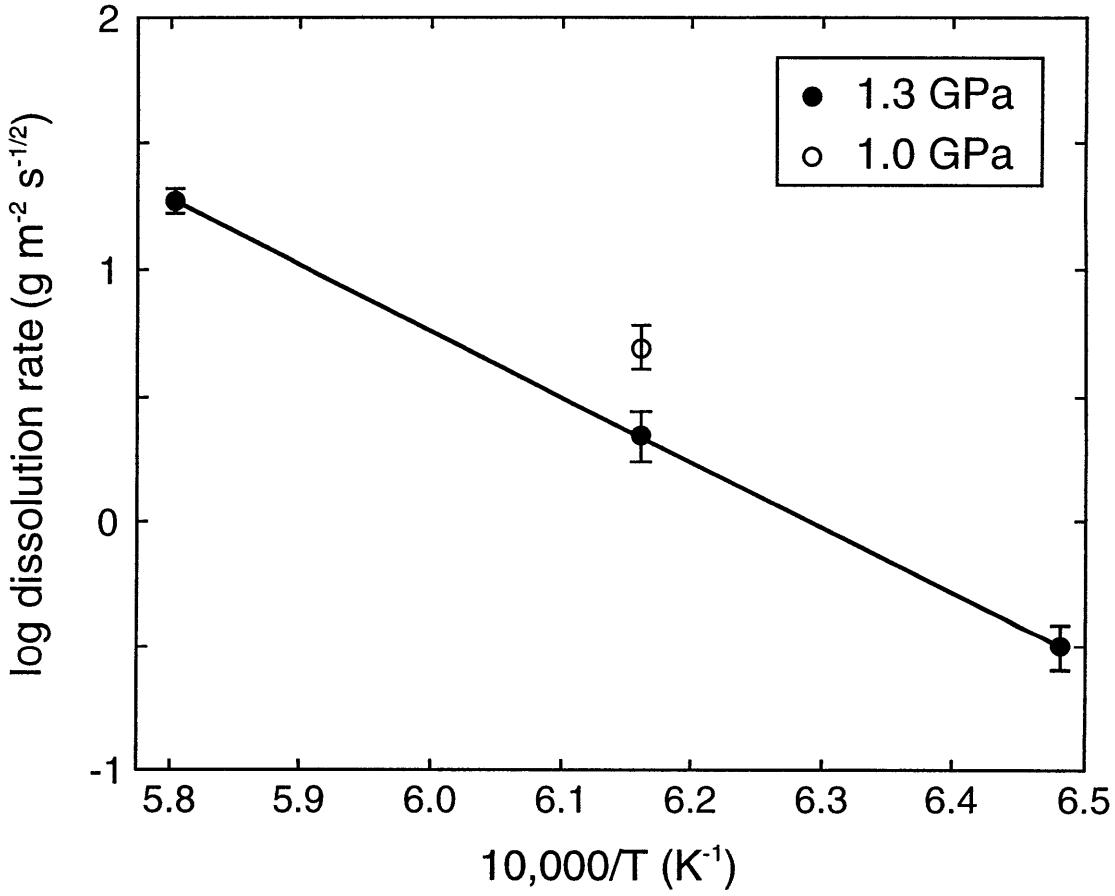
2
1
0
-1
5.8
5.9
6.0
6.1
6.2
6.3
6.4
6.5
log dissolution rate (g m-2 s-1/2)
10,000/T (K-1)
1.3 GPa
1.0 GPa

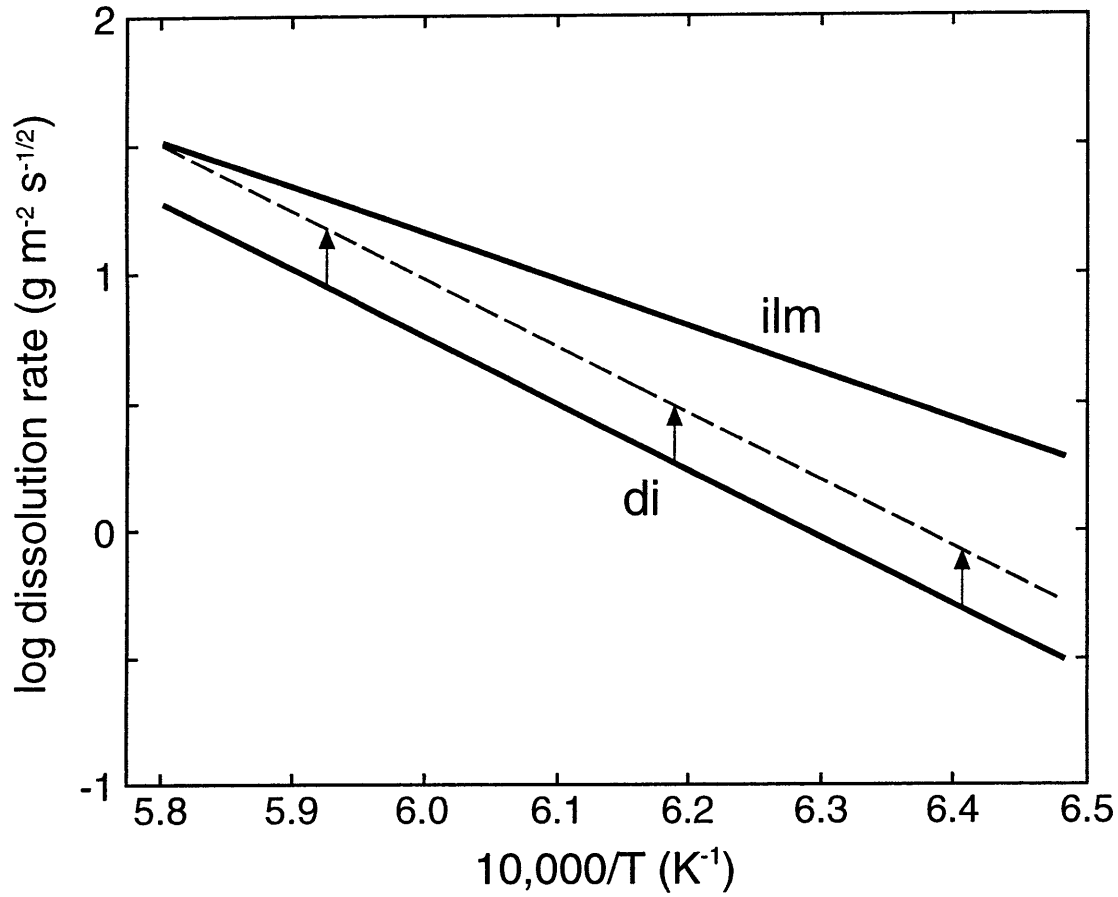
2
1
0
-1
log dissolution rate (g m-2 s-1/2)
ilm
di
5.8
5.9
6.0
6.1
6.2
6.3
6.4
6.5
10,000/T (K-1)

Figure 6a

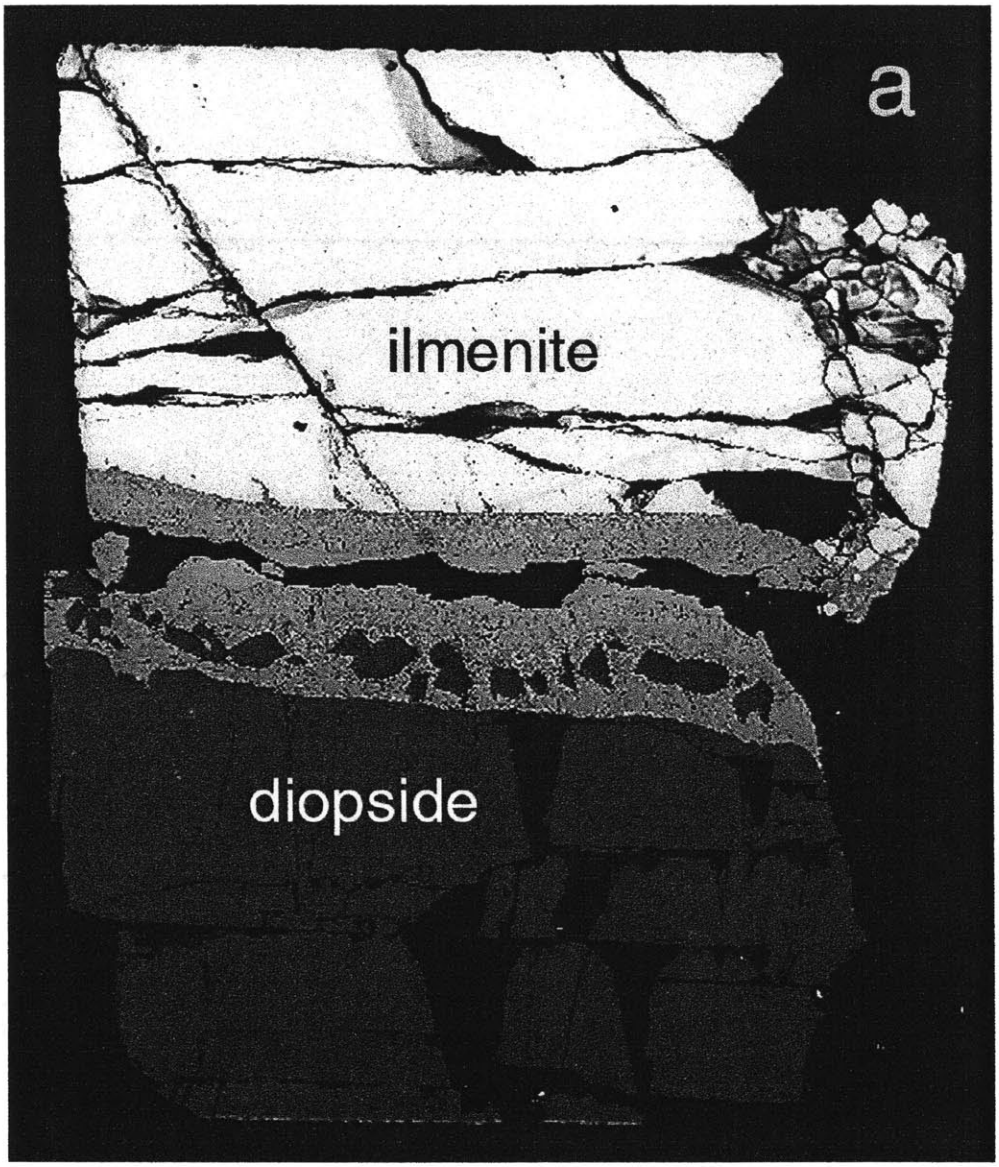

Figure 6b

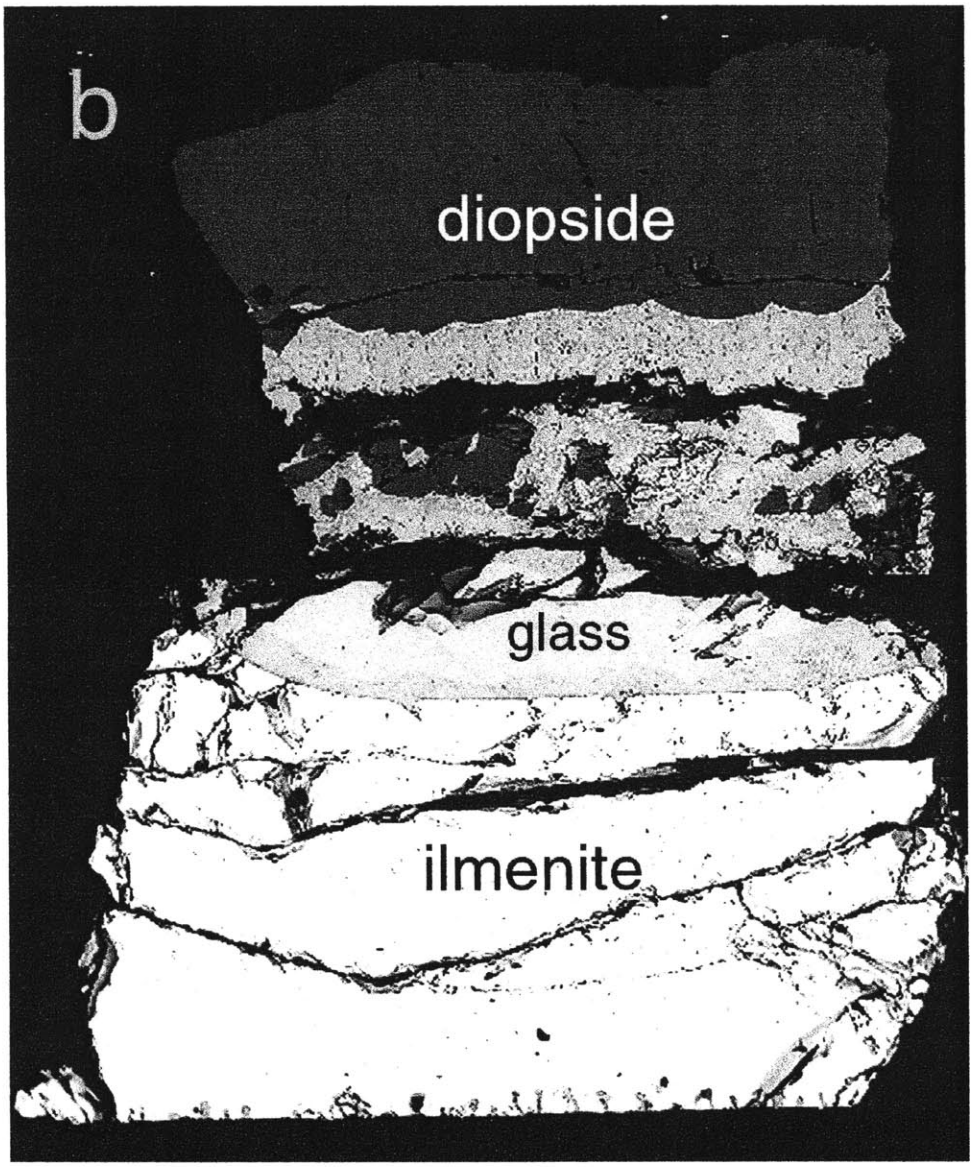

Figure 7

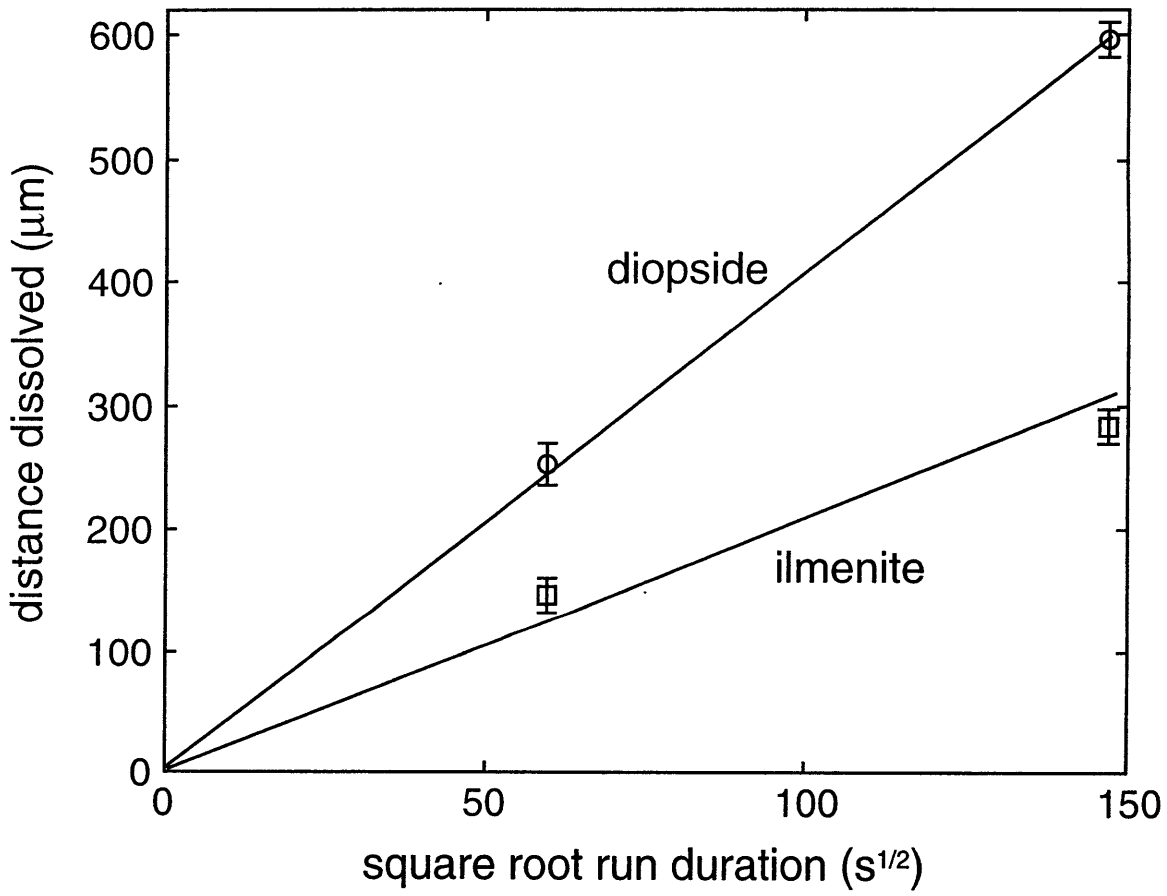
600
500
400
300
200
100
0
distance dissolved (μm)
diopside
ilmenite
0
50
100
150
square root run duration (s1/2)

Figure 8

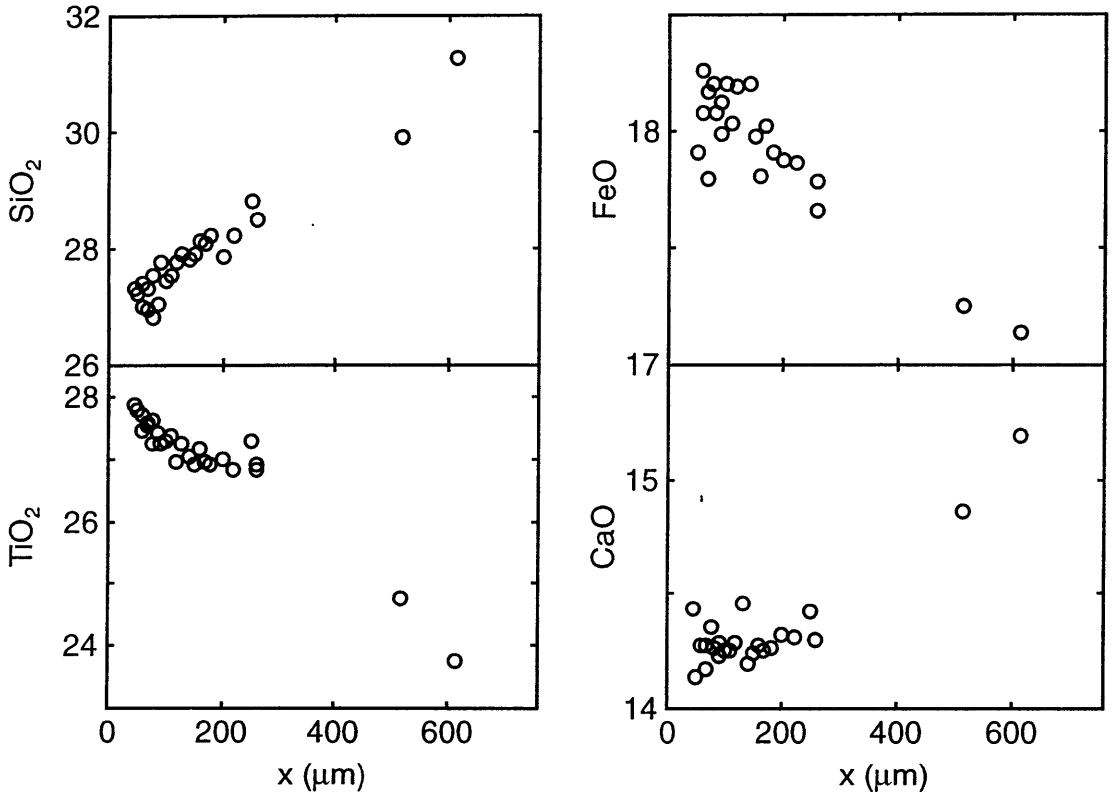
SiO2
32
30
28
26
TiO2
28
26
24
0
200
400
600
x (μm)
FeO
18
17
CaO
15
14
0
200
400
600
x (μm)

Figure 9

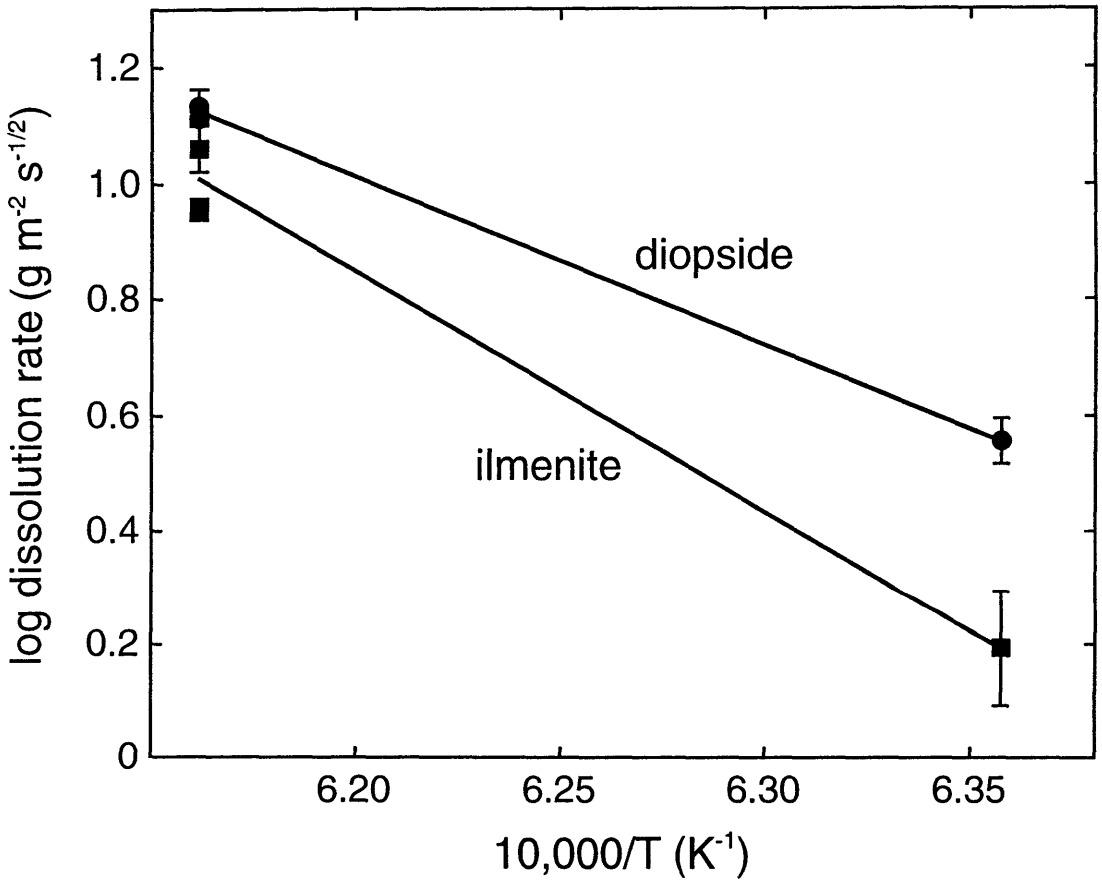
log dissolution rate (g m^{-2} s$^{-1/2}$)
1.2
1.0
0.8
0.6
0.4
0.2
0
diopside
ilmenite
6.20
6.25
6.30
6.35
10,000/T (K^{-1})

Figure 10

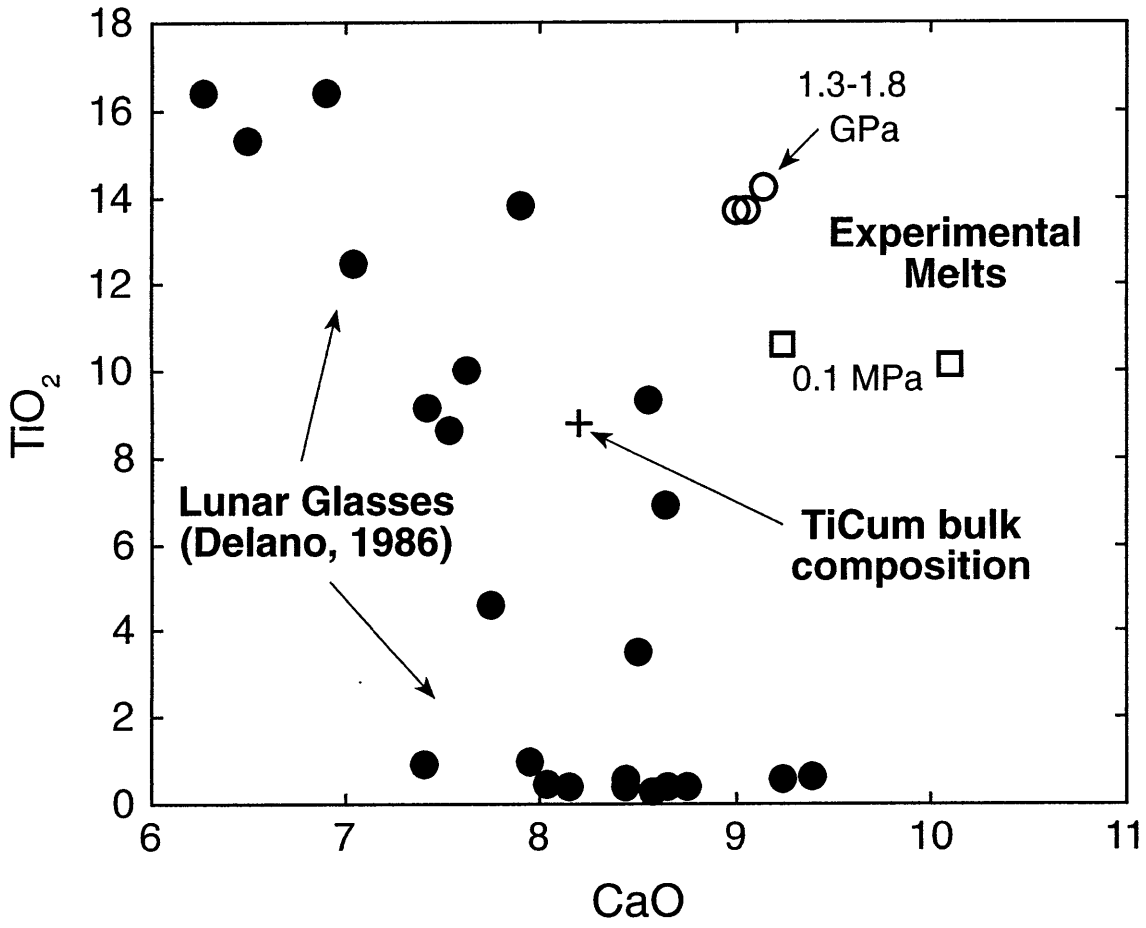
18
16
14
12
10
8
6
4
2
0
6
7
8
9
10
11
TiO2
CaO
1.3-1.8
GPa
Experimental
Melts
0.1 MPa
Lunar Glasses
(Delano, 1986)
TiCum bulk
composition